PHD

The role of structural disorder in crystalline, glassy and liquid materials

Rowlands, Ruth

Award date:
2016

Awarding institution:
University of Bath

The role of structural disorder in crystalline, glassy and liquid materials

submitted by

Ruth F. Rowlands

for the degree of Doctor of Philosophy

of the

University of Bath

Department of Physics

March 15, 2016

COPYRIGHT

Signature of Author ....Ruth Rowlands........

Ruth F. Rowlands

Abstract

The method of neutron diffraction with isotope substitution (NDIS) was employed to measure the structures of crystalline ice-Ih, amorphous $GeSe_3$ and $GeSe_4$ and a 5 molal solution of NaCl in D_2O.

For crystalline ice-Ih, the complete set of partial structure factors was measured at temperatures of 15 K and 123 K using hydrogen/deuterium isotope substitution to help clarify the nature of the proton disorder associated with the hydrogen bond network. The disorder manifests itself in the asymmetric profiles of the intra-molecular H-H peak and first inter-molecular O-H peak, in both ice-Ih and low density amorphous ice. The measured partial pair-distribution functions show that each oxygen molecule is hydrogen bonded to two others and indicates that the hydrogen bond is bent, with an average O-H$\cdots$O angle of $160.1(4.4)^\circ$ at 15 K and $177.2(2.4)^\circ$ at 123 K.

In the work on the prototypical network forming glasses $GeSe_3$ and $GeSe_4$, the full set of partial structure factors were measured using the NDIS technique. A comparison of the structures of glassy $GeSe_2$, $GeSe_3$ and $GeSe_4$ shows that whilst $GeSe_3$ and $GeSe_4$ are chemically ordered continuous random network glasses, the intrinsic chemical order of glassy $GeSe_2$ is broken by the existence of Ge-Ge and Se-Se homopolar bonds. There are some discrepancies associated with the pair-correlation functions calculated using first-principles molecular dynamics simulations, particularly with respect to the Ge-Ge correlations, which indicates scope for improvement in these simulations.

In situ high pressure neutron diffraction experiments using Cl isotope subtitution were performed on a 5 molal solution of NaCl in D_2O at 150°C. The O-D bond distances and coordination numbers did not change over the measured pressure range of 0.24 GPa – 3.38 GPa. Site specific information of the Cl^- coordination environment was obtained from the difference functions, which showed that as the pressure increases the nearest-neighbour Cl-D coordination number decreases from 7.1(5) to 6.3(5), as the associated Cl-D distance decreases from 2.21(4) Å to 2.18(4) Å.

Acknowledgements

Firstly I would like to thank my supervisor Phil Salmon for his support and guidance throughout my PhD. I would also like to thank my colleagues within the Liquids and Amorphous Materials group: Anita Zeidler, Kamil Wezka, Keiron Pizzey and Annalisa Polidori for their friendship, training, and extensive support on experiments.

From the University of Bath I would like to thank Harry Bone, Wendy Lambson, Simon Dodd, Paul Reddish and Phil Jones for all their help and technical expertise. I would like to thank Dan Wolverson for being my secondary supervisor and for his assistance in building and setting up a UV-Vis spectrometer.

At the University of Göttingen, I would like to thank Werner Kuhs for his assistance in preparing the ice samples and for his excellent advice on that experiment and with the subsequent data analysis.

At the ILL, I would like to thank Henry Fischer, Alain Bertoni, Claude Payre and Jean-Luc Laborier for all their advice, guidance and technical support during many difficult experiments. I would also like to thank Juan Rodriguez-Carvajal for his assistance with the crystallographic ice data. I would like to thank Stefan Klotz for his excellent scientific advice and assistance on particularly difficult pressure experiments at the ILL and LLB.

At the LLB, I would like to thank Marie-Claire Bellissent-Funel, Burkhard Annighöfer, Jacques Darpentigny and Josselin Dupont for their assistance in the assembly of the Ti-Zr pressure cell and in the subsequent experiment and data analysis. I would also like to thank Louis Hennet for his technical and scientific assistance in this experiment.

From ISIS I would like to thank Alex Hannon for his support during various GEM experiments on chalcogenide glasses. I would also like to thank Craig Bull, Matt Tucker and Phil Hawkins for their help and advice on all the PEARL experiments. I would also like to thank James Drewitt for his assistance in the SiO_2 and AsSe PEARL experiments.

I would like to thank the University of Bath for providing me with funding, and the ILL, LLB and ISIS for granting beamtime to run these experiments. I also thank the organisers of the Oxford neutron training school and the ISIS neutron training course for the practical and theoretical training they provided.

Finally I would like to thank to my parents and the rest of the Rowlands clan for their unending love and support.

List of publications

Published articles:

- A. Zeidler, K. Wezka, R. F. Rowlands, D. A. J. Whittaker, P. S. Salmon, A. Polidori. J. W. E. Drewitt, S. Klotz, H. E. Fischer, M. C. Wilding, C. L. Bull, M. G. Tucker and M. Wilson. High-Pressure Transformation of SiO_2 from a Tetrahedral to an Octahedral Network: A Joint Approach Using Neutron Diffraction and Molecular Dynamics. *Phys. Rev. Lett.* , **113** 135501, 2014

Contents

1. Introduction

Accurate information on the structure of disordered systems is a fundamental requirement for understanding both the physical and chemical properties of these materials. Disordered materials have a wide range of scientific and technological applications in fields that range from optics [1–6] and geophysics [7, 8] to complex biological systems [9, 10]. Historically, the field of structural analysis in materials science has been separated into the crystalline and non-crystalline worlds, each relying on different techniques with little overlap between the two [11]. However atomic disorder occurs in all materials, including crystalline systems, and the techniques typically applied to amorphous materials can provide invaluable insight into the nature of this disorder.

Disorder in crystalline materials typically occurs in the form of lattice defects or interstitials disrupting the perfect periodicity of the crystal lattice. In crystallography, the atomic structure can be described by one of 230 unique space groups, which fully reflect the symmetry of the structure [11]. However, deviations from this perfect symmetry often characterise complex crystals and are frequently crucial to their properties [11]. Therefore, it is essential that these deviations are well characterized to obtain a complete understanding of the structure. A combination of crystallographic and spectroscopic techniques may suffice to characterise these deviations if the density of defects is low. However, when the density of defects is high or where there are overlapping defects, it may be more useful to consider the system to be locally non-crystalline. Thus, on the level of a specific unit cell, the time and ensemble averaged symmetry of the crystal may not be retained, and the static or dynamic disorder produces local configurations with lower symmetry [12].

In contrast, liquid and glassy materials do not exhibit the long range atomic ordering seen in crystalline systems, making them challenging materials to study. However, the chemical bonding constraints produce structural motifs that have well-defined short range order (≤ 5 Å), and these structural motifs connect to produce intermediate range order (~ 10 Å). Glasses are usually formed when a liquid is quenched sufficiently quickly through its glass transition temperature, so that crystallisation cannot occur. Therefore, the atomic structure of glass is similar to that of a supercooled liquid that has been frozen into the solid state [13].

A number of techniques can be used to determine the bulk structure of disordered materials, and a complete description will often involve contributions from multiple experiments and simulations. For example, information about the atomic distributions in a disordered material can be obtained by using diffraction techniques such as x-ray and neutron diffraction. Complementary structural information can also be obtained from spectroscopic techniques such as magic angle spinning nuclear magnetic resonance (MAS-NMR) or Raman spectroscopy. However, spectroscopy experiment often require *a priori* structural information to aid in the interpretation of the results. The work presented in this thesis makes use of neutron diffraction with isotope substitution (NDIS) to obtain new information on the structure of crystalline, glassy and liquid materials.

Neutrons are a very useful probe for studying the atomic structure of materials, as the neutrons scatter mostly from the nuclei of atoms. Different isotopes of the same chemical species can have different scattering cross-section for neutrons, and it is this fact that is exploited in the NDIS technique, which was first introduced by Enderby *et al.* [14]. The measured diffraction patterns are dependent on the magnitude of the scattering vector Q, and for a multi-component system containing n different chemical species the diffraction pattern is comprised of $n(n+1)/2$ partial structure factors $S_{\alpha\beta}(Q)$, which describe the pair-correlations between atoms of chemical species α and β. The corresponding real space information is contained within the partial pair-distribution functions $g_{\alpha\beta}(r)$ which are obtained via Fourier transformation. These $g_{\alpha\beta}(r)$ functions represent the maximal amount of information that can be obtained from a diffraction experiment, and they can be used to find parameters such as coordination numbers and bond distances. As a result the NDIS technique is an extremely powerful tool for solving the atomic structure of crystalline, glassy and liquid materials.

Thesis outline

The content of this thesis is organised as follows:

- Chapter 2 - The essential theory for neutron diffraction experiments on disordered materials is presented. This includes the basic properties of the neutron, the theoretical background for neutron scattering, and an introduction to the method of neutron diffraction with isotope substitution (NDIS).

- Chapter 3 - The D4c diffractometer based at the Insitut Laue-Langevin neutron source is introduced and the data analysis procedures are discussed. Experimental details of (i) the Paris-Edinburgh large-volume press for liquids and (ii) D4c's cryostat are presented.

- Chapter 4 - The NDIS method is used to measure the full set of partial structure factors for ice-Ih at temperatures of 15 K and 123 K. The results are compared to information obtained on the structure using crystallographic techniques, and to the structure of low-density amorphous ice and water [15].
- Chapter 5 - The NDIS method is used to measure the full set of partial structure factors for glassy $GeSe_3$ and glassy $GeSe_4$. The results are compared to those obtained on the structure of glassy $GeSe_2$ [16] from previous NDIS experiments, and from recent first-principals molecular dynamics simulations [17–19].
- Chapter 6 - The coordination environment of the Cl^- ion in a 5 molal aqueous NaCl – D_2O solution is investigated at pressures up to 3.38 GPa. The D4c results make use of NDIS to provide information on the structure at the first-order difference function level. The results are compared to previous work at ambient and low pressure.
- Chapter 7 - An overall summary is presented along with suggestions for further work.

2. Theory

In this chapter the essential theory of neutron diffraction for disordered materials is presented, including the basic properties of the neutron and how isotope substitution techniques can be used to obtain a maximal amount of structural information from diffraction patterns. The formalism is based on the description given by Fischer *et al* [13], but a more in depth explanation of neutron scattering theory can be found in references [20, 21].

2.1 Properties of a neutron

The neutron is a versatile probe that is used widely in condensed matter physics to study both the structure and dynamics of materials. The neutron's lack of charge allows it to interact directly with the nucleus of a material via the strong force as there is no Coulomb barrier to overcome. The de Broglie wavelength of thermal neutrons is comparable to inter-atomic spacings, thus the resulting interference effects yield information on the structure of the scattering system.

The kinetic energy E of a neutron with mass m_n is given by

$$E = \frac{m_n|\mathbf{v}|^2}{2} = \frac{|\mathbf{p}|^2}{2m_n}, \tag{2.1}$$

where $\mathbf{v}$ is the neutron's velocity and $\mathbf{p}$ is its momentum. The neutron's de Broglie wavelength is defined as

$$\lambda = \frac{h}{|\mathbf{p}|} = \frac{h}{m_n|\mathbf{v}|}, \tag{2.2}$$

where h is Planck's constant. The magnitude of a wavevector $\mathbf{k}$ in the direction specified by a velocity $\mathbf{v}$ is given by

$$|\mathbf{k}| = \frac{2\pi}{\lambda}. \tag{2.3}$$

Thus, the neutron's energy can be rewritten as

$$E = \frac{h^2}{2m_n\lambda^2}, \tag{2.4}$$

which can be usefully expressed in terms of the wavelength, speed v and temperature T for a thermal neutron by using $\frac{1}{2}mv^2 = \frac{1}{2}kT$ and inserting the values for the elementary constants:

$$E = \frac{81.81}{\lambda^2} = 5.227\, v^2 = 0.08617\, T, \tag{2.5}$$

with units of energy in meV, wavelength in Å, speed in km s^{-1} and temperature in Kelvin.

2.2 Neutron scattering

Consider an event where an incident neutron with a wavevector $\mathbf{k_i}$ and energy E_i undergoes scattering from a sample such that the scattered neutron has a wavevector $\mathbf{k_f}$ and energy E_f. The resulting change in the neutron's momentum is given by

$$\Delta\mathbf{p} = \hbar\mathbf{k_i} - \hbar\mathbf{k_f} = \hbar\mathbf{Q}, \tag{2.6}$$

where $\hbar = h/2\pi$ and the scattering vector $\mathbf{Q}$, which forms the scattering triangle shown in figure 2-1, is defined as

$$\mathbf{Q} = \mathbf{k_i} - \mathbf{k_f}. \tag{2.7}$$

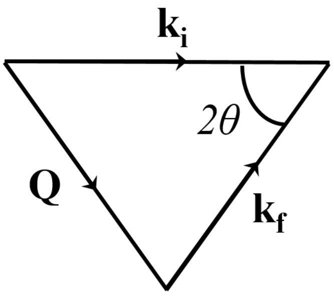

Figure 2-1: The scattering triangle relating the vectors $\mathbf{k_i}$, $\mathbf{k_f}$ and $\mathbf{Q}$ to the scattering angle 2θ.

The energy transfer in the scattering event is given by,

$$\Delta E = E_i - E_f = \frac{\hbar^2|\mathbf{k_i}|^2}{2m_n} - \frac{\hbar^2|\mathbf{k_f}|^2}{2m_n}. \tag{2.8}$$

By applying the cosine rule to the scattering triangle in figure 2-1, it follows that

$$Q^2 = k_i^2 + k_f^2 - 2k_ik_f\cos(2\theta), \tag{2.9}$$

where 2θ is the scattering angle.

2.3 The static approximation

In the static approximation, the assumption is made that the energy exchange between a neutron and a sample $\Delta E = \hbar\omega$ is much smaller than the incident energy $E_i = \hbar\omega_i$, such that $\Delta E/E_i \ll 1$. Then it follows from equation 2.8 that,

$$|\mathbf{k_i}| = \frac{2\pi}{\lambda_i} \approx |\mathbf{k_f}| = \frac{2\pi}{\lambda_f}, \tag{2.10}$$

and if this is applied to equation 2.9 then the magnitude of the scattering vector becomes

$$Q = \frac{4\pi}{\lambda}\sin(\theta). \tag{2.11}$$

It is important to emphasise that the static approximation does not correspond to purely elastic scattering. In elastic scattering there is no change in energy during a scattering event $\Delta E = 0$, and the structural information obtained from the diffraction experiment corresponds to the time-averaged atomic positions in the sample. This outcome can be seen by considering the Heisenberg uncertainty principle

$$\Delta E \Delta t \sim \hbar. \tag{2.12}$$

If a scattering event is elastic then $\Delta E = 0$, such that an infinite time scale is associated with the scattering event. In terms of the van Hove formalism, the time-dependent pair-correlation function $G(r, t = \infty)$ corresponds to elastic scattering whereas $G(r, t = 0)$ corresponds to the static approximation [13].

In a diffraction experiment each incident neutron samples the structure over all pairs of atoms in its coherence volume and the diffraction pattern is built up by summing the scattered intensity from each of these coherence volumes. Thus, a diffraction experiment made in the static approximation corresponds to taking an average of instantaneous snapshots of the system's structure.

For liquids the atoms do not have static equilibrium positions [21] and elastic scattering does not occur. The structure measured in a diffraction experiment corresponds to an average over the instantaneous snapshots. For a glass or disordered crystal it is possible to view the structure in terms of the thermal motion of atoms about time-independent equilibrium positions and purely elastic scattering can occur. In this case the thermal motion about the mean atomic position, leads to Debye-Waller factors [21, 22] in the diffracted intensity.

2.4 Neutron diffraction

Figure 2-2 shows the scattering geometry in a neutron diffraction experiment. A collimated beam of incident neutrons with flux Φ is scattered by a sample centred at the origin of coordinates. The scattered neutrons are counted by a detector of area $\mathrm{d}S$ at a distance R from the origin, where the detector counts all neutrons irrespective of their final energy. The solid angle subtended by the detector is $\mathrm{d}\Omega = \mathrm{d}S/R^2$. The differential scattering cross-section can be defined as

$$\frac{\mathrm{d}\sigma}{\mathrm{d}\Omega} = \frac{\text{Number of neutrons scattered into } \mathrm{d}\Omega \text{ per second}}{\Phi\, \mathrm{d}\Omega}. \tag{2.13}$$

Neutrons interact with the atomic nuclei in a sample via the nuclear strong force. As this short range interaction ($\sim 10^{-14}$ m) is significantly smaller than the wavelength of a thermal neutron ($\sim 10^{-10}$ m), the neutrons will scatter isotropically. The neutron scattering length b gives a measure of the probability that the atomic nucleus will scatter any given neutron that is incident upon it, and depends on the orientation of the nuclear spin relative to the spin of the incident neutron. Figure 2-3 shows the variation in neutron scattering lengths with atomic weight. There is currently no exact theory to predict the value of b for an element, and the values are all measured empirically. The scattering cross-section for a single spin-less bound nucleus is given

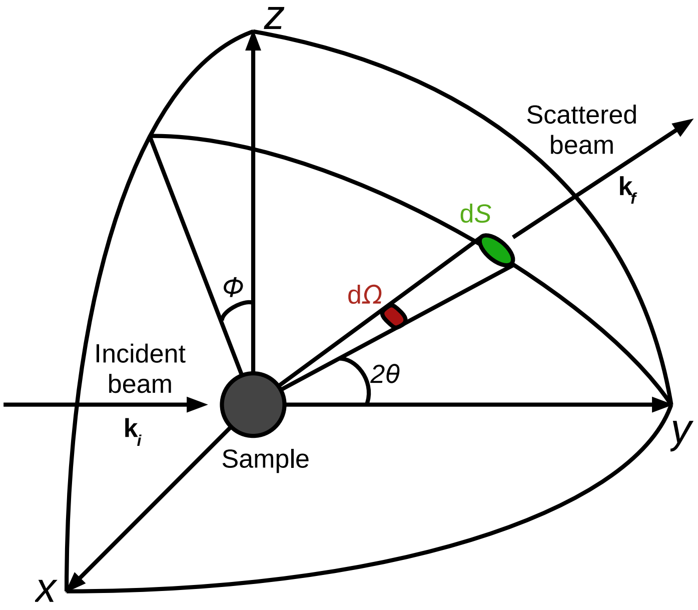

Figure 2-2: Diagram showing the scattering of neutrons by a sample into a detector of surface area $\mathrm{d}S$. Reproduced from [23]

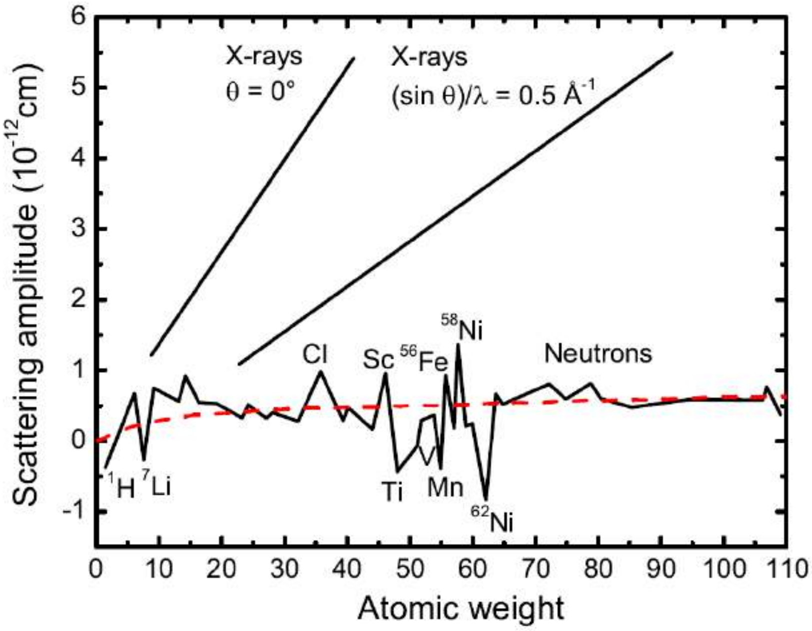

Figure 2-3: The variation in coherent scattering lengths as a function of the atomic weight for neutrons and X-rays (reproduced from reference [24]). The X-ray scattering length is dependent on $Q \propto \sin(\theta)/\lambda$ and scales with atomic number. The neutron scattering length has no such dependence, and can vary significantly between isotopes of the same element. The dashed red curve indicates the potential scattering for neutrons.

by

$$\sigma = 4\pi b^2. \tag{2.14}$$

For an isotropic system containing N scattering centres, the differential scattering cross-section can be written as:

$$\frac{\mathrm{d}\sigma}{\mathrm{d}\Omega}(Q) = \left\langle \sum_{i=1}^{N} \sum_{j=1}^{N} \bar{b_i} \bar{b_j^*} e^{i\mathbf{Q}\cdot(\mathbf{r_i}-\mathbf{r_j})} \right\rangle \tag{2.15}$$

where b_i is the bound neutron scattering length of atom i and b_j^* is the complex conjugate of the bound neutron scattering length of atom j. The brackets $\langle\rangle$ denote a thermal average. The horizontal bar is the average of the b_i values over the positions of the scattering centres, where the scattering length for a site depends on the isotope at that site and the relative orientation of the nuclear and neutron spins.

For a system of n different chemical species, the differential scattering cross-section is given by

$$\begin{aligned}\frac{1}{N}\frac{\mathrm{d}\sigma}{\mathrm{d}\Omega}(Q) &= F(Q) + P_{\mathrm{self}}(Q) + P_{\mathrm{distinct}}(Q) \\ &= F(Q) + \sum_{\alpha=1}^{n} c_\alpha \left(b_\alpha^2 + b_{\mathrm{inc},\alpha}^2\right) \left[1 + P_\alpha\left(Q\right)\right] + P_{\mathrm{distinct}}(Q), \qquad (2.16)\end{aligned}$$

where b_α, $b_{\mathrm{inc},\alpha}$ and c_α are the coherent neutron scattering length, incoherent neutron scattering length and the atomic fraction of chemical species α, respectively. The total structure factor is given by $F(Q)$ and contains information on the relative positions of pairs of distinct nuclei. The inelasticity correction terms $P(Q) = P_{\mathrm{self}}(Q) + P_{\mathrm{distinct}}(Q)$ are introduced to account for a breakdown of the static approximation due to the recoil of nuclei in a scattering event. It contains a contribution from the inelastic scattering that is associated with both the self and distinct ($P_{\mathrm{distinct}}(Q)$) parts of $\frac{\mathrm{d}\sigma}{\mathrm{d}\Omega}(Q)$ for which there is no exact theory [13]. For heavier elements the Placzek correction can be used [25], and the distinct term is usually neglected. For lighter elements such as hydrogen, deuterium and lithium there is currently no method for calculating these corrections exactly.

2.4.1 Faber-Ziman formalism

The total structure factor can be re-written in terms of the Faber-Ziman partial structure factors $S_{\alpha\beta}(Q)$, which describe the correlations between pairs of nuclei of chemical species α and β [26]:

$$F(Q) = \sum_{\alpha=1}^{n}\sum_{\beta=1}^{n} c_\alpha c_\beta b_\alpha b_\beta \left[S_{\alpha\beta}(Q) - 1\right]. \qquad (2.17)$$

The corresponding real-space information $G(r)$ can be obtained by taking the Fourier transform of $F(Q)$:

$$\begin{aligned}G(r) &= \frac{1}{2\pi^2 r\rho}\int_0^\infty QF(Q)\sin(Qr)\,\mathrm{d}Q \\ &= \sum_{\alpha=1}^{n}\sum_{\beta=1}^{n} c_\alpha c_\beta b_\alpha b_\beta \left[g_{\alpha\beta}(r) - 1\right], \qquad (2.18)\end{aligned}$$

where ρ is the atomic number density of the sample, and $g_{\alpha\beta}(r)$ is a partial pair-distribution function. At distances shorter than the minimum separation between atoms, the total pair-distribution function tends to the limit:

$$G(r \to 0) = -\sum_{\alpha=1}^{n}\sum_{\beta=1}^{n} c_\alpha c_\beta b_\alpha b_\beta. \tag{2.19}$$

The sum-rule relation derived by Enderby *et al.* [14] should also be satisfied. This relation is given by

$$\int\limits_0^\infty F(Q)Q^2\,\mathrm{d}Q = 2\pi^2\rho G(0), \tag{2.20}$$

where $G(0) = G(r \to 0)$. The sum rule can be derived from equation 2.18 by considering the limit as $r \to 0$.

The Faber-Ziman partial structure factors are related to the partial pair-distribution functions through the Fourier transform relations:

$$S_{\alpha\beta}(Q) - 1 = \frac{4\pi\rho}{Q}\int\limits_0^\infty r\left[g_{\alpha\beta}(r) - 1\right]\sin(Qr)\,\mathrm{d}r, \tag{2.21}$$

and

$$g_{\alpha\beta}(r) - 1 = \frac{1}{2\pi^2 r\rho}\int\limits_0^\infty Q\left[S_{\alpha\beta}(Q) - 1\right]\sin(Qr)\,\mathrm{d}Q. \tag{2.22}$$

The partial pair-distribution function $g_{\alpha\beta}(r)$ can be used to find the coordination number $\overline{n}_\alpha^\beta$, which gives the mean number of atoms of chemical species β contained within a spherical shell of radii r_1 and r_2 centred on an atom of chemical species α

$$\overline{n}_\alpha^\beta = 4\pi\rho c_\beta \int\limits_{r_1}^{r_2} r^2 g_{\alpha\beta}(r)\,\mathrm{d}r. \tag{2.23}$$

2.4.2 Bhatia-Thornton formalism

An alternative method for describing a binary system is to decompose the total structure factor into the Bhatia-Thornton partial structure factors,

$$\begin{aligned} F(Q) = \langle b\rangle^2 &\left[S_{\mathrm{NN}}^{\mathrm{BT}}(Q) - 1\right] + \\ &c_\alpha c_\beta \left(b_\alpha - b_\beta\right)^2 \left\{\left[\frac{S_{\mathrm{CC}}^{\mathrm{BT}}(Q)}{c_\alpha c_\beta}\right] - 1\right\} + \\ &2\langle b\rangle \left(b_\alpha - b_\beta\right) S_{\mathrm{NC}}^{\mathrm{BT}}(Q), \end{aligned} \tag{2.24}$$

where $\langle b \rangle = c_\alpha b_\alpha + c_\beta b_\beta$ is the average neutron scattering length. $S_{\mathrm{NN}}^{\mathrm{BT}}(Q)$ describes the global structure of the material and treats all atomic sites as equal. $S_{\mathrm{CC}}^{\mathrm{BT}}(Q)$ contains information on the chemical ordering of species α and β, and $S_{\mathrm{NC}}^{\mathrm{BT}}(Q)$ is the cross term giving the correlation between atomic sites and their chemical occupancy. The Bhatia-Thornton partial structure factors are related to their corresponding partial pair-distribution function via the Fourier transformation relations

$$S_{\mathrm{NN}}^{\mathrm{BT}}(Q) - 1 = \frac{4\pi\rho}{Q} \int_0^\infty \left[g_{\mathrm{NN}}^{\mathrm{BT}}(r) - 1 \right] r \sin(Qr)\, \mathrm{d}r, \tag{2.25}$$

$$\frac{S_{\mathrm{CC}}^{\mathrm{BT}}(Q)}{c_\alpha c_\beta} - 1 = \frac{4\pi\rho}{Q} \int_0^\infty g_{\mathrm{CC}}^{\mathrm{BT}}(r) r \sin(Qr)\, \mathrm{d}r, \tag{2.26}$$

$$\frac{S_{\mathrm{NC}}^{\mathrm{BT}}(Q)}{c_\alpha c_\beta} = \frac{4\pi\rho}{Q} \int_0^\infty g_{\mathrm{NC}}^{\mathrm{BT}}(r) r \sin(Qr)\, \mathrm{d}r, \tag{2.27}$$

or

$$g_{\mathrm{NN}}^{\mathrm{BT}}(r) - 1 = \frac{1}{2\pi^2 r\rho} \int_0^\infty \left[S_{\mathrm{NN}}^{\mathrm{BT}}(Q) - 1 \right] Q \sin(Qr)\, \mathrm{d}Q, \tag{2.28}$$

$$g_{\mathrm{CC}}^{\mathrm{BT}}(r) = \frac{1}{2\pi^2 r\rho} \int_0^\infty \left[\frac{S_{\mathrm{CC}}^{\mathrm{BT}}(Q)}{c_\alpha c_\beta} - 1 \right] Q \sin(Qr)\, \mathrm{d}Q, \tag{2.29}$$

$$g_{\mathrm{NC}}^{\mathrm{BT}}(r) = \frac{1}{2\pi^2 r\rho} \int_0^\infty \left[\frac{S_{\mathrm{NC}}^{\mathrm{BT}}(Q)}{c_\alpha c_\beta} \right] Q \sin(Qr)\, \mathrm{d}Q. \tag{2.30}$$

For a system in which $b_\alpha = b_\beta$ it follows from equation 2.24 that the weighting factors for $S_{\mathrm{CC}}^{\mathrm{BT}}(Q)$ and $S_{\mathrm{NC}}^{\mathrm{BT}}(Q)$ are zero such that

$$F(Q) = \langle b \rangle^2 \left[S_{\mathrm{NN}}^{\mathrm{BT}}(Q) - 1 \right], \tag{2.31}$$

i.e $S_{\mathrm{NN}}^{\mathrm{BT}}(Q)$ is measured directly. The coordination number obtained from $g_{\mathrm{NN}}^{\mathrm{BT}}(r)$ is an average over all chemical species and gives the mean number of atoms at a distance between r_1 and r_2 centred on an atom at the origin of coordinates:

$$\overline{n} = 4\pi\rho \int_{r_1}^{r_2} r^2 g_{\mathrm{NN}}^{\mathrm{BT}}(r)\, \mathrm{d}r = c_\alpha \left(\bar{n}_\alpha^\alpha + \bar{n}_\alpha^\beta \right) + c_\beta \left(\bar{n}_\beta^\beta + \bar{n}_\beta^\alpha \right). \tag{2.32}$$

2.5 Isotopic substitution

The method of isotope substitution in neutron diffraction is a powerful tool for solving the structure of materials, and relies on the difference in the coherent neutron scattering lengths between isotopes of a particular element. Contrasting diffraction patterns can be measured for samples that are identical except for the isotopic composition of one (or more) of the elements. Consider a sample containing n chemical species that is described by $m = (n+1)n/2$ partial structure factors. A complete determination of all of the $S_{\alpha\beta}(Q)$ functions requires diffraction patterns to be measured for m samples. In the simplest case of a binary system, $n = 2$ such that a minimum of $m = 3$ total structure factors $F_1(Q)$, $F_2(Q)$ and $F_3(Q)$ must be measured. These functions can be written in matrix form as

$$\begin{pmatrix} F_1(Q) \\ F_2(Q) \\ F_3(Q) \end{pmatrix} = \begin{pmatrix} c_\alpha^2 b_{\alpha,1}^2 & c_\beta^2 b_{\beta,1}^2 & 2c_\alpha c_\beta b_{\alpha,1} b_{\beta,1} \\ c_\alpha^2 b_{\alpha,2}^2 & c_\beta^2 b_{\beta,2}^2 & 2c_\alpha c_\beta b_{\alpha,2} b_{\beta,2} \\ c_\alpha^2 b_{\alpha,3}^2 & c_\beta^2 b_{\beta,3}^2 & 2c_\alpha c_\beta b_{\alpha,3} b_{\beta,3} \end{pmatrix} \cdot \begin{pmatrix} S_{\alpha\alpha}(Q) - 1 \\ S_{\beta\beta}(Q) - 1 \\ S_{\alpha\beta}(Q) - 1 \end{pmatrix} \tag{2.33}$$

where $b_{\alpha,1}$ is the coherent neutron scattering length of chemical species α for sample 1, which corresponds to the total structure factor $F_1(Q)$. These functions can be written in a more concise form as,

$$\mathbf{F} = \mathbf{A} \cdot \mathbf{S}, \tag{2.34}$$

where $\mathbf{F}$ and $\mathbf{S}$ are column vectors and $\mathbf{A}$ is a matrix of weighting factors. This equation can be inverted to solve for the partial structure factors

$$\mathbf{S} = \mathbf{A}^{\mathbf{-1}} \cdot \mathbf{F}. \tag{2.35}$$

For a square matrix, the determinant $|A|$ normalised by dividing each row i by $\sum_\alpha \sum_\beta c_\alpha c_\beta b_{\alpha,i} b_{\beta,i}$ gives an indication of the robustness of the determination of the $S_{\alpha\beta}(Q)$ functions [27].

In the case where more than $m = 3$ structure factors have been measured for a binary system, the method of singular value decomposition (SVD) can be used to compute the pseudoinverse of the matrix $\mathbf{A}$ making use of all available information on the structure. The mathematical details are well established [27], and an example of this procedure as applied to liquid and glassy zinc chloride is given by Zeidler *et al* [28].

2.6 Difference functions

Measuring the full set of partial structure factors in a neutron diffraction experiment is not always feasible. However site-specific information can be obtained by considering a pair of isotopically enriched samples and measuring the first-order difference functions. In particular a single partial structure factor can be eliminated from $F(Q)$ to reduce the overall complexity of correlations associated with a single diffraction pattern, and it is possible to choose the partial structure factor to be removed. For example if two total structure factors $F_1(Q)$ and $F_2(Q)$ are measured for two samples, that are identical in every aspect except for the isotopic composition of chemical species β, then the difference function,

$$\begin{aligned}\Delta F_{\text{no }\alpha\alpha}(Q) &= F_1(Q) - F_2(Q)\\ &= c_\beta^2\left(b_{\beta,1}^2 - b_{\beta,2}^2\right)\left[S_{\beta\beta}(Q)-1\right] + 2c_\alpha c_\beta b_\alpha\left(b_{\beta,1}-b_{\beta,2}\right)\left[S_{\alpha\beta}(Q)-1\right],\end{aligned} \tag{2.36}$$

removes the $S_{\alpha\alpha}(Q)$ partial structure factor. Alternatively the $S_{\beta\beta}(Q)$ partial structure factor can be eliminated by constructing the difference function

$$\begin{aligned}\Delta F_{\text{no }\beta\beta}(Q) &= F_1(Q) - \frac{b_{\beta,1}^2}{b_{\beta,2}^2}F_2(Q)\\ &= c_\alpha^2 b_\alpha^2\left(1-\frac{b_{\beta,1}^2}{b_{\beta,2}^2}\right)\left[S_{\alpha\alpha}(Q)-1\right] + 2c_\alpha c_\beta b_\alpha\left(b_{\beta,1}-\frac{b_{\beta,1}^2}{b_{\beta,2}}\right)\left[S_{\alpha\beta}(Q)-1\right].\end{aligned} \tag{2.37}$$

Finally the $S_{\alpha\beta}(Q)$ partial structure factor can be removed by constructing the difference function

$$\begin{aligned}\Delta F_{\text{no }\alpha\beta}(Q) &= F_1(Q) - \frac{b_{\beta,1}}{b_{\beta,2}}F_2(Q)\\ &= c_\alpha^2 b_\alpha^2\left(1-\frac{b_{\beta,1}}{b_{\beta,2}}\right)\left[S_{\alpha\alpha}(Q)-1\right] + c_\beta^2\left(b_{\beta 1}^2 - b_{\beta,2}b_{\beta,1}\right)\left[S_{\beta\beta}(Q)-1\right].\end{aligned} \tag{2.38}$$

The corresponding real-space information for each difference function can be obtained by Fourier transformation. For example, in the case of the $\Delta F_{\text{no }\alpha\beta}(Q)$ difference function

$$\begin{aligned}\Delta G_{\mathrm{no}\ \alpha\beta}(r) &= \frac{1}{2\pi^2 r\rho}\int_0^\infty Q\Delta F_{\mathrm{no}\ \alpha\beta}(Q)\sin(Qr)\,\mathrm{d}Q \\ &= G_1(Q) - \frac{b_{\beta,1}}{b_{\beta,2}}G_2(Q) \\ &= c_\alpha^2 b_\alpha^2\left(1-\frac{b_{\beta,1}}{b_{\beta,2}}\right)g_{\alpha\alpha}(r) + c_\beta^2\left(b_{\beta,1}^2 - b_{\beta,2}b_{\beta,1}\right)g_{\beta\beta}(r) + \Delta G_{\mathrm{no}\ \alpha\beta}(r\to 0),\end{aligned} \tag{2.39}$$

where the low-r limit is given by

$$\Delta G_{\mathrm{no}\ \alpha\beta}(r\to 0) = -\left[c_\alpha^2 b_\alpha^2\left(1-\frac{b_{\beta,1}}{b_{\beta,2}}\right) + c_\beta^2\left(b_{\beta,1}^2 - b_{\beta,2}b_{\beta,1}\right)\right]. \tag{2.40}$$

2.7 Modification functions

In practice, a measured total structure factor will be truncated by the maximum Q-value (Q_{max}) that can be accessed by the diffractometer used in an experiment. This defines a modification function

$$M(Q) = \begin{cases} 1 & \text{if } Q \le Q_{\mathrm{max}} \\ 0 & \text{if } Q > Q_{\mathrm{max}}, \end{cases} \tag{2.41}$$

which accounts for the finite Q_{max}. Let's define the density correlation function

$$D_{\mathrm{exp}}(r) = \frac{2}{\pi}\int_0^\infty Q\frac{F(Q)}{|G(0)|}\sin(Qr)M(Q)\,\mathrm{d}Q, \tag{2.42}$$

where the normalisation by $|G(0)|$ ensures that the weighting factors of $g_{\alpha\beta}(r)$ sum to unity. The Fourier transform of the modification function $M(Q)$ is given by

$$\begin{aligned}P(r) &= \frac{1}{\pi}\int_0^{Q_{\mathrm{max}}}\cos(Qr)\,\mathrm{d}Q \\ &= \frac{Q_{\mathrm{max}}}{\pi}\mathrm{sinc}(Q_{\mathrm{max}}r).\end{aligned} \tag{2.43}$$

from which it follows that

$$
\begin{aligned}
D_{\mathrm{exp}}(r) &= 4\pi\rho r \frac{G(r)}{|G(0)|} \otimes P(r) \\
&= 4\pi\rho \sum_{\alpha=1}^{n} \sum_{\beta=1}^{n} \frac{c_\alpha c_\beta b_\alpha b_\beta}{|G(0)|} r g_{\alpha\beta}(r) \otimes P(r) - 4\pi\rho r,
\end{aligned}
\tag{2.44}
$$

where $\otimes$ denotes the 1–D convolution operator.

Let each real-space peak i in $rg_{\alpha\beta}(r)$ be represented by a Gaussian function centred at $r_{\alpha\beta}(i)$ with a standard deviation $\sigma_{\alpha\beta}(i)$ and an area that corresponds to a coordination number $\overline{n}_{\alpha}^{\beta}(i)$. Then the measured density correlation function can be fitted by using a sum of weighted Gaussians as given by [29]

$$
\begin{aligned}
D_{\mathrm{fit}}(r) = \sum_i \Bigg\{ & w_{\alpha\beta}(i) \frac{\overline{n}_{\alpha}^{\beta}(i)}{c_\beta(i) r_{\alpha\beta}(i)} \frac{1}{\sqrt{2\pi}\sigma_{\alpha\beta}(i)} \\
& \times \exp\left(\frac{-[r - r_{\alpha\beta}(i)]^2}{2[\sigma_{\alpha\beta}(i)]^2} \right) \otimes P(r) \Bigg\} - 4\pi\rho r,
\end{aligned}
\tag{2.45}
$$

where $w_{\alpha\beta} = 2c_\alpha c_\beta b_\alpha b_\beta / |G(0)|$ for $\alpha \neq \beta$ and $w_{\alpha\beta} = c_\alpha^2 b_\alpha^2 / |G(0)|$ for $\alpha = \beta$. The fitted density correlation function $D_{\mathrm{fit}}(r)$ can be optimised by minimising the R_χ-factor [30] defined by

$$
R_\chi = \sqrt{\frac{\sum_i [D_{\mathrm{exp}}(r_i) - D_{\mathrm{fit}}(r_i)]^2}{\sum_i D_{\mathrm{exp}}^2(r_i)}}. \tag{2.46}
$$

Once the fit is optimised, the peak positions and coordination numbers follow from the fitted parameters.

If Q_{max} is suitably large that $M(Q)$ has a negligible effect on $F(Q)$, then $D(r)$ can be written in terms of its partial pair-density correlation functions $d_{\alpha\beta}(r)$ [31],

$$
D(r) = \sum_{\alpha=1}^{n} \sum_{\beta=1}^{n} c_\alpha c_\beta b_\alpha b_\beta d_{\alpha\beta}(r), \tag{2.47}
$$

where

$$
d_{\alpha\beta}(r) = 4\pi r\rho \left[g_{\alpha\beta}(r) - 1 \right]. \tag{2.48}
$$

3. Instrumentation and diffraction data treatment

In this chapter, an outline is given of the experimental methods that were employed for the work described in this thesis. The chapter describes the production of neutrons from a fission reactor source and the instrumentation used to obtain diffraction pattern, and a summary is given of the data analysis procedures.

3.1 Fission neutron sources

Research reactors such as the Institut Laue-Langevin (ILL) in Grenoble, France produce neutrons through the nuclear fission of enriched uranium. At the ILL the principle raw material is ^{235}U, which becomes unstable when a nucleus captures a neutron n and decays producing energy E and an average of 2.4 neutrons per event [32]. An example of a typical mechanism for this decay is:

$$n +^{235} \mathrm{U} \rightarrow^{141} \mathrm{Ba} +^{92} \mathrm{K} + 3n + E. \tag{3.1}$$

Neutrons produced from fission reactions are very energetic but are slowed down by a moderator before they are used in a scattering experiment, where the kinetic energy of the neutrons is reduced through a series of collisions with the nuclei of the moderating material. The neutrons emerge from the moderator with a Maxwell-Boltzmann distribution of energies, with a peak position that depends on the temperature of the moderator. The ILL has several moderators, namely a hot graphite source at 2400 K, a thermal D_2O source at 300 K and two cold D_2 sources at 20 K, providing a range of energies and hence wavelengths for scattering experiments.

Figure 3-1 shows the layout for a typical diffraction experiment. The neutrons from the moderator impinge on a monochomator, where a single neutron wavelength is selected through Bragg reflection by the monochromator crystals. These monochromatic neutrons are focused onto the sample by the curvature of the monochromator, and the scattered neutrons are detected at an angle of 2θ. Collimation is provided by neutron absorbing materials to reduce background scattering.

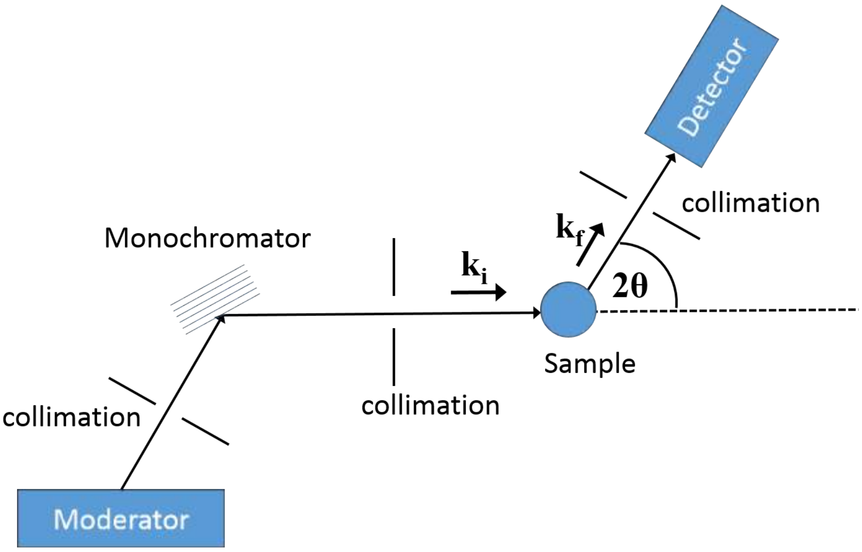

Figure 3-1: Schematic of a typical diffraction experiment at a reactor source with neutrons of incident wavevector $\mathbf{k_i}$ and scattered wavevector $\mathbf{k_f}$.

The diffractometer measures the differential scattering cross-section $\frac{\mathrm{d}\sigma}{\mathrm{d}\Omega}$ of a sample, by integrating over all possible neutron energy exchanges with the sample at constant scattering angle. For reactor sources, equation 2.11 gives the relation between the scattering angle 2θ and scattering vector Q.

3.2 The D4c diffractometer

D4c is a high-precision diffractometer dedicated to the study of the structure of disordered materials [33]. The diffractometer faces the hot graphite moderator, which is kept at 2400 K and therefore employs high-flux short-wavelength neutrons. Monochromatic neutrons are selected using Bragg diffraction from the (331), (220) or (200) lateral faces of a Cu monochromator, producing neutrons with wavelengths of 0.35 Å, 0.5 Å or 0.7 Å, respectively. Harmonic $\lambda/2$ contamination at λ =0.5 Å or λ =0.7 Å, is removed using either an Ir or a Rh filter, respectively.

The incident neutron flux is measured using a monitor which is positioned between the monochromator and the beam-defining slits before the sample position, and is used for normalising the incident beam intensity. The sample is placed within an evacuated belljar (diameter = 46 cm, height 55 cm) which has a wide-angle thin aluminium window facing the detectors.

D4c has nine 1D ^{3}He microstrip detectors that cover a large angular range, where

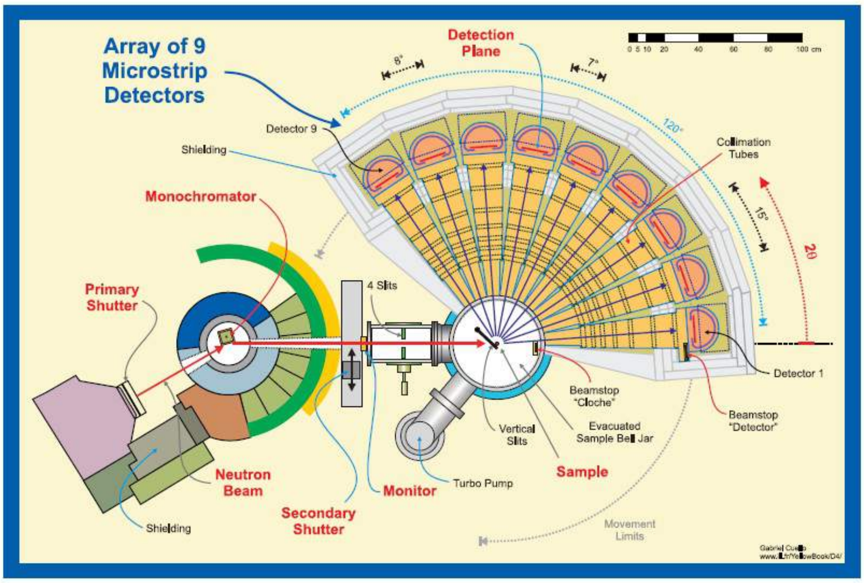

Figure 3-2: Schematic of the D4c diffractometer at the ILL [33]

each individual detector covers a range of 8° in 2θ, and the entire detector assembly is able to rotate around the sample position to cover the 7° gaps between detectors. This produces a total angular range of $1.5^\circ \leq 2\theta \leq 137^\circ$. The microstrip detectors provide the high counting rate stability that is required for isotope substitution experiments on disordered materials. The Q-range covered by the detector depends on the wavelength of the incident neutrons and can be calculated using equation 2.11 as,

$$0.5\,\text{Å}^{-1} \leq Q \leq 33\,\text{Å}^{-1} \quad \text{for } \lambda = 0.35 \text{ Å},$$
$$0.3\,\text{Å}^{-1} \leq Q \leq 23\,\text{Å}^{-1} \quad \text{for } \lambda = 0.5 \text{ Å},$$

or

$$0.2\,\text{Å}^{-1} \leq Q \leq 17\,\text{Å}^{-1} \quad \text{for } \lambda = 0.7 \text{ Å}. \tag{3.2}$$

D4c can accommodate many different sample environments for making *in situ* structural measurements. The measurements presented in this thesis required a low-temperature cryostat, a Paris-Edinburgh high-pressure press, and vanadium cans at ambient conditions.

3.3 The Paris-Edinburgh press for liquid samples

The Paris-Edinburgh (PE) press is a large-volume pressure cell that is often used to study the *in situ* high pressure structure of liquid and glassy samples. The press applies pressure through two identical opposed anvils, where the sample is encapsulated by an annular gasket arrangement. The maximum pressure that can be applied to the sample generally depends on the anvil material, together with the geometry and size of the sample and its gasket.

On the D4c instrument, the VX5 variant of the PE press with two support pillars and sintered cubic boron nitride (BN) anvils is used to study liquids under pressures up to 9 GPa. Figure 3-3 shows a diagram of the anvils that apply pressure to a sample that is contained within encapsulated hemispherical titanium-zirconium (Ti-Zr) gaskets [34] (figures 3-4 and 3-5). The boron nitride die of the anvil is supported by a steel binding ring and has a hemispherical sample chamber and a toroidal groove to accommodate the outer ring of the gasket. Boron nitride is used for the die, as it is a strong neutron absorber which reduces the background scattering. 80 W cartridge heaters are inserted into a 12.5 mm bore in the back of each of the anvils, and make it possible to run experiments at temperatures up to $\sim$ 200 °C. Figure 3-6 shows a side view of the anvil and gasket set-up within the press. To minimise the heat loss, a 4 mm sleeve of zirconia ceramic [35] is placed between the BN die and the steel binding ring. The backing seat for the anvils has a die made from zirconia, surrounded by a steel supporting ring. The anvil and backing seat fit into a stainless steel binding ring, which contains a channel for a cooling fluid to be circulated. The temperature of the sample is measured and controlled by two thermocouples attached to the front face of the BN die, about $\sim$ 2 mm from the gasket. The thermocouples are placed such that they are out of the incident neutron beam, and do not contribute to the measured intensity.

The sample gaskets are made from a titanium-zirconium alloy with the composition $\mathrm{Ti}_{0.676}\mathrm{Zr}_{0.324}$, which is chosen because the average coherent scattering length is zero, i.e this composition is said to be null scattering. However due to some preference for like-atom bonding, the Ti-Zr does not form a perfect random substitutional alloy, resulting in some Q-dependent structure in the measured diffraction patterns. More details on the pressure dependent structure of $\mathrm{Ti}_{0.676}\mathrm{Zr}_{0.324}$ can be found in reference [36].

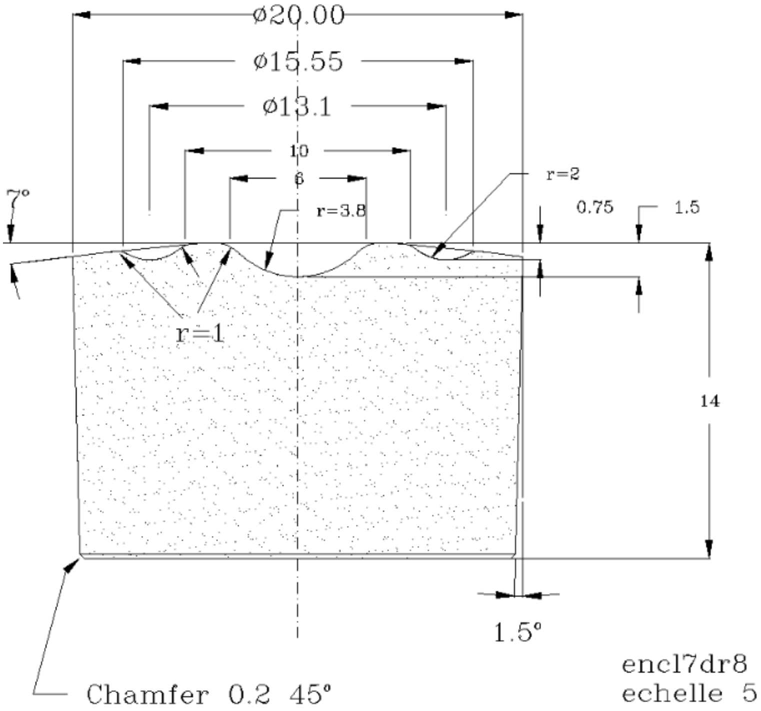

Figure 3-3: Schematic of the boron nitride die for a single toroid anvil used on D4c with encapsulated Ti-Zr gaskets. The dimensions are in units of mm.

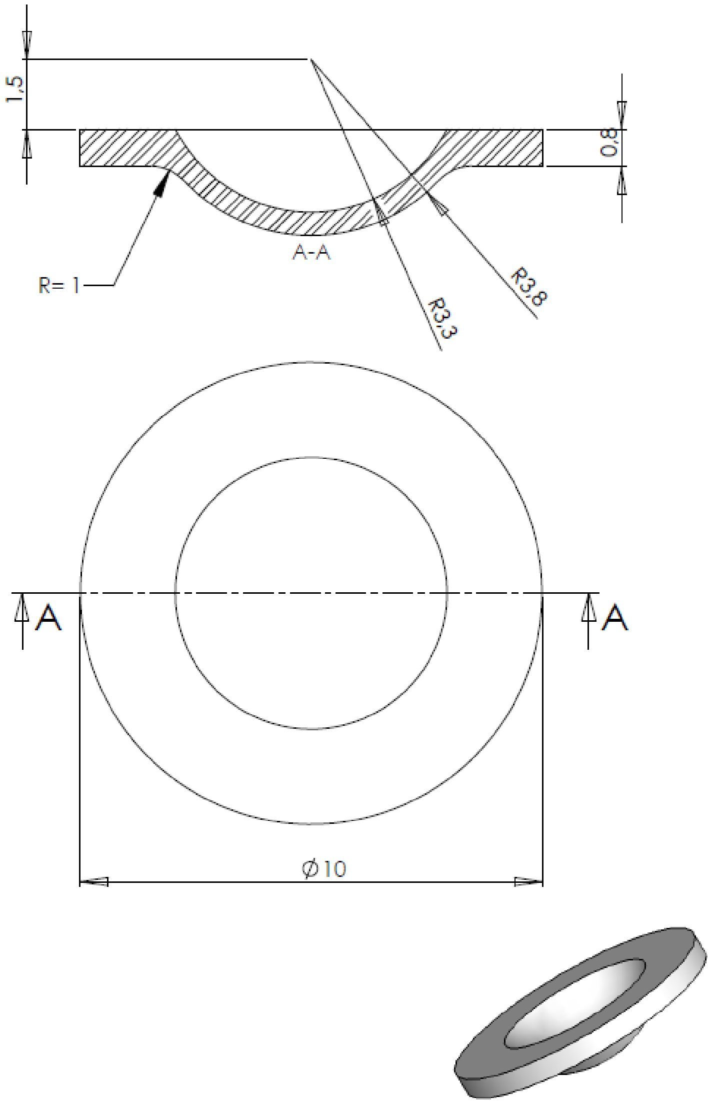

Figure 3-4: Schematic of hemispherical encapsulated Ti-Zr gaskets, where a pair of these are required for each sample, along with the outer ring shown in figure 3-5. The dimensions are in units of mm.

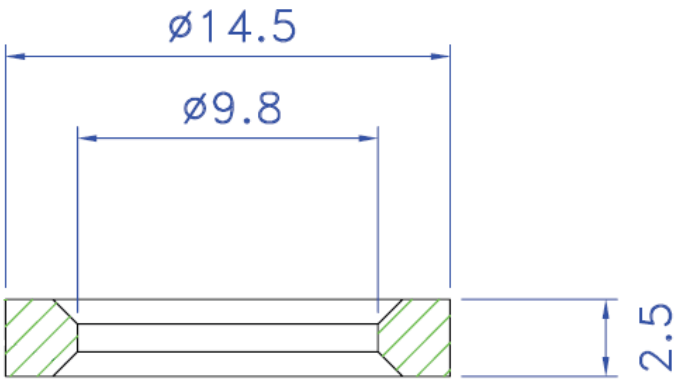

Figure 3-5: Schematic of the outer ring for the encapsulated Ti-Zr gaskets shown in figure 3-4. The dimensions are in units of mm. The outer gasket is pre-compressed and then turned out to ensure a close fit with the two hemispherical gaskets.

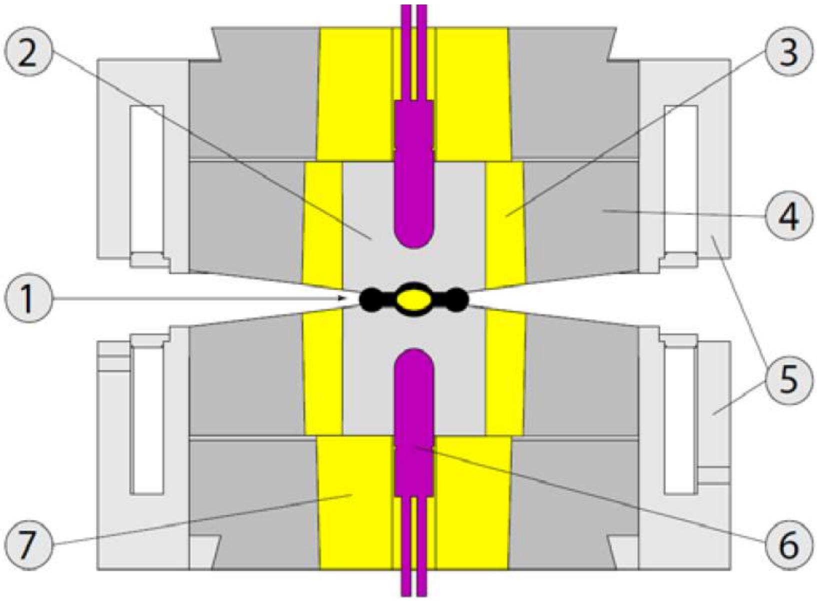

Figure 3-6: Cross-section of the gasket-anvil set-up used on D4c with encapsulated Ti-Zr gaskets (reproduced from reference [35]). Shown in the diagram are (1) the encapsulated Ti-Zr gaskets containing a sample (2) cubic boron nitride anvil (3) zirconia ceramic sleeve, (4) steel binding ring, (5) cooling ring, (6) cartridge heaters and (7) backing seat with zirconia die and steel supporting ring.

3.3.1 Producing pressure

In a PE press experiment, pressure is applied to the anvils of the press using a hydraulic pump. One anvil is held immobile, whilst a force is a applied to the other anvil, creating pressure at the sample position. The force on an anvil is given by

$$F = P_{\text{oil}} A = Lg, \tag{3.3}$$

where P_{oil} is the oil pressure of the hydraulic system, $A = 66.5\ \text{cm}^2$ is the area of the anvil for the VX5 variant of the PE press, L is the applied load and $g = 9.81\ \text{ms}^{-2}$. The pressure at the sample position can be determined from the load applied to the anvils through a calibration curve. The calibration curve for encapsulated gaskets in a VX5 varient of the PE press is given in figure 3-7.

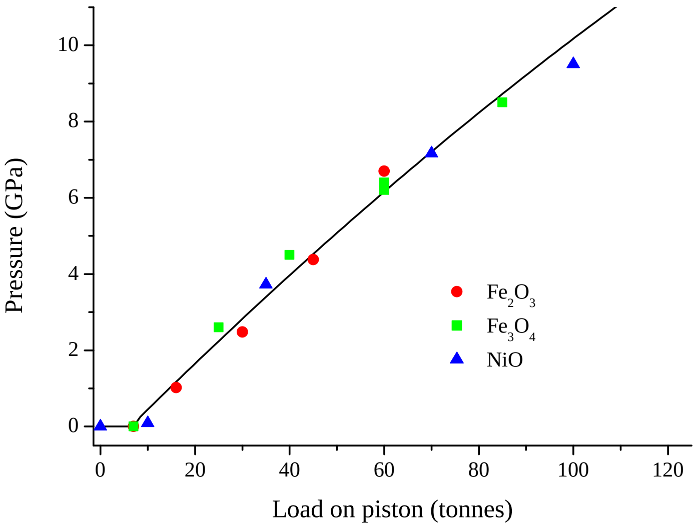

Figure 3-7: Calibration curve giving the load applied to the piston of a VX5 variant of the PE press versus the pressure at the sample position for single toroid encapsulated gaskets. The data points were obtained from the diffraction patterns measured for crystalline NiO (red circle), Fe_2O_3 (green square) and Fe_3O_4 (blue triangle). The solid calibration curve corresponds to the measured data points. Figure reproduced from reference [37].

3.4 The D4c cryostat

The D4c cryostat is an orange cryostat that has been specially adapted for use within D4c's belljar. The main features of the orange cryostat include a large-sample top-loading capability, isolated sample area with static exchange gas, low helium consumption and fast sample cycling times. The orange cryostat has helium and nitrogen level monitors with an auto-fill capability and a helium pumping system [32]. D4c's orange cryostat has a temperature range of 1.8 K – 320 K. A schematic of the cryostat tail within the belljar is given in figure 3-8. Figure 3-9 shows pictures of the D4c cryostat highlighting the position of the vanadium cryostat tail and incident beam collimation.

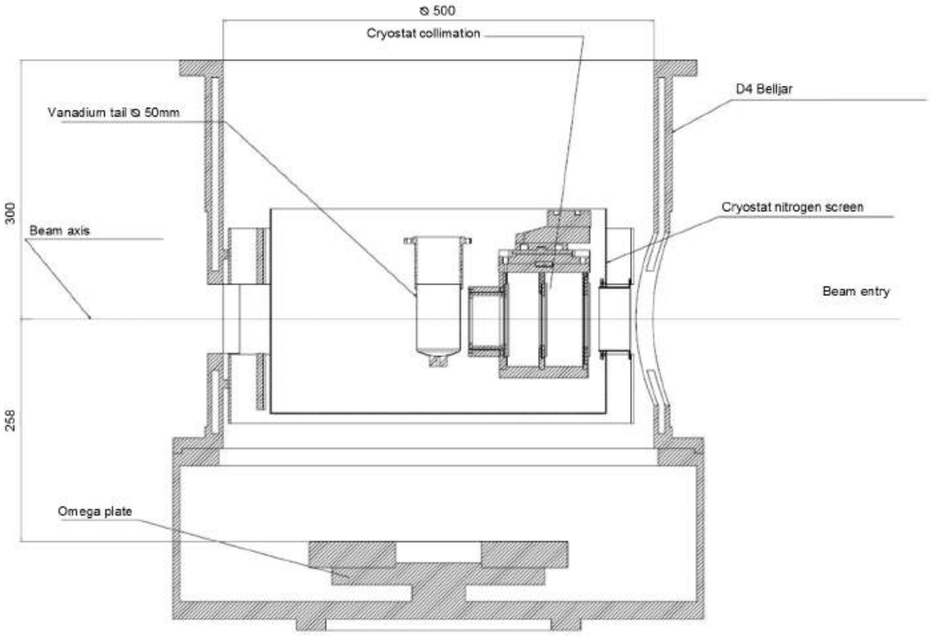

Figure 3-8: Schematic of the D4c cryostat tail within the belljar, indicating the position of the vanadium cryostat tail, and the incident beam collimation within D4c's belljar as shown in the photograph figure 3-9a. The dimensions are in units of mm.

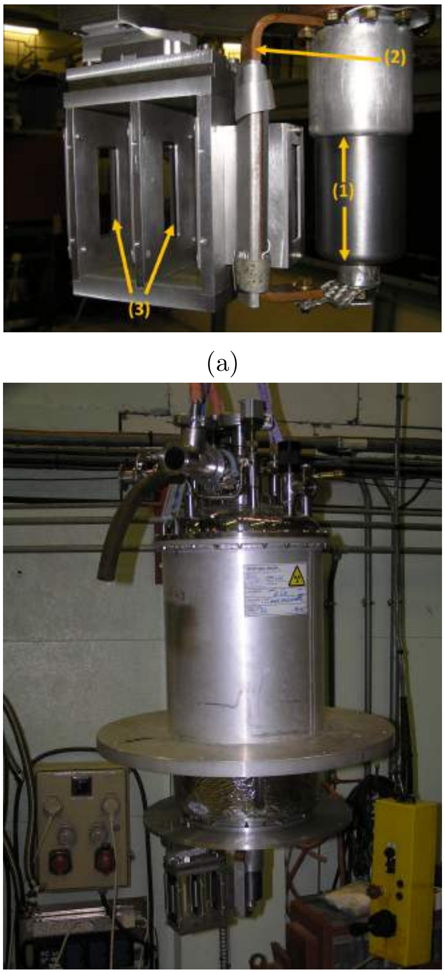

(a)

(b)

Figure 3-9: (a) Photographs showing (1) the vanadium cryostat tail adapted for use within D4c's belljar, (2) the cold-finger that reduces the temperature gradient across the vanadium cryostat tail and (3) the collimation for the incident neutron beam. (b) Photograph showing a full view of the D4c cryostat, including the collimation and cryostat tail.

3.5 Neutron diffraction data analysis

Chapter 2 outlines basic diffraction theory in the small sample limit, where neutrons are not attenuated by the sample and there are no multiple scattering events. In this case the single scattered intensity $I_{\mathrm{S}}(\theta)$ measured for N_{S} sample scattering centres illuminated by the neutron beam is given by

$$I_{\mathrm{S}}(\theta) = a(\theta) N_{\mathrm{S}} \left.\frac{\mathrm{d}\sigma}{\mathrm{d}\Omega}\right|_{\mathrm{S}}, \tag{3.4}$$

where $a(\theta)$ is the diffractometer calibration coefficient which converts cross-sections into measured intensities, and $\left.\frac{\mathrm{d}\sigma}{\mathrm{d}\Omega}\right|_{\mathrm{S}}$ is the differential scattering cross-section for the sample.

In practice the small sample limit is not met, so it is necessary to correct the measured datasets for beam attenuation and multiple scattering from the sample. For most experiments, the sample is also held within a container, such as a vanadium can or Ti-Zr gaskets, so additional corrections have to be made for the container scattering.

3.5.1 Attenuation and multiple scattering corrections

In a diffraction experiment, neutron absorption and scattering events lead to an attenuation of the overall scattered intensity. For a sample with cylindrical geometry the attenuation coefficient can be calculated using the method of Paalman and Pings [38]. The attenuation coefficient $A_{i,j}(\theta)$ corresponds to events where a neutron that is scattered from medium i is attenuated in medium j, and is dependent on the scattering angle. Corrections also have to be made for multiple scattering events within the sample, which can be calculated within the quasi-isotropic approximation [39]. In the simplest case, the multiple scattering cross-section $M_{\mathrm{S}}(\theta)$ for a container-less sample S is given by

$$M_{\mathrm{S}}(\theta) = N_{\mathrm{S}} A_{\mathrm{S,S}}(\theta) \frac{\sigma_{\mathrm{S}}}{4\pi} \Delta_{\mathrm{S}}(\theta) \left[1 + P_{\mathrm{S}}(\theta)\right], \tag{3.5}$$

where $\Delta_{\mathrm{S}}(\theta)$ is the ratio of multiple scattering to single scattering, $P_{\mathrm{S}}(\theta)$ is an inelasticity correction and

$$\sigma_{\mathrm{S}} = 4\pi \left(b_{\mathrm{S}}^2 + b_{\mathrm{S,inc}}^2\right) \tag{3.6}$$

is the total scattering cross-section of the sample.

3.5.2 Container and background corrections

Let's consider a measurement made using the D4C diffractometer. The scattered intensity measured by the D4c detectors is normalised to the incident monitor count. The sample S is measured within its container C and gives a measured intensity denoted by $I^{\mathrm{E}}_{\mathrm{SC}}(\theta)$. The measured background intensity is denoted by $I^{\mathrm{E}}_{\mathrm{B}}(\theta)$. Therefore the background corrected intensity is given by

$$\begin{aligned} I^{\mathrm{E}'}_{\mathrm{SC}}(\theta) &= I^{\mathrm{E}}_{\mathrm{SC}}(\theta) - I^{\mathrm{E}}_{\mathrm{B}}(\theta) \\ &= A_{\mathrm{S,SC}}(\theta) I_{\mathrm{S}}(\theta) + A_{\mathrm{C,SC}}(\theta) I_{\mathrm{C}}(\theta) + a(\theta) M_{\mathrm{SC}}(\theta). \end{aligned} \tag{3.7}$$

In this equation $I_{\mathrm{S}}(\theta)$ and $I_{\mathrm{C}}(\theta)$ are the single scattered intensities for a bare sample and an empty container, respectively, and $M_{\mathrm{SC}}(\theta)$ is the multiple scattering cross-section for the sample in its container. Similarly the background-corrected intensity measured for the empty container is given by

$$\begin{aligned} I^{\mathrm{E}'}_{\mathrm{C}}(\theta) &= I^{\mathrm{E}}_{\mathrm{C}}(\theta) - I^{\mathrm{E}}_{\mathrm{B}}(\theta) \\ &= A_{\mathrm{C,C}}(\theta) I_{\mathrm{C}}(\theta) + a(\theta) M_{\mathrm{C}}(\theta). \end{aligned} \tag{3.8}$$

where $M_{\mathrm{C}}(\theta)$ is the multiple scattering cross-section for the empty container. By using equations 3.4, 3.7, and 3.8 and rearranging, the differential scattering cross-section can be expressed in terms of the measured intensities as

$$\left.\frac{\mathrm{d}\sigma}{\mathrm{d}\Omega}\right|_{\mathrm{S}} = \frac{1}{N_{\mathrm{S}} A_{\mathrm{S,SC}}(\theta)} \left\{ \left[\frac{I^{\mathrm{E}'}_{\mathrm{SC}}(\theta)}{a(\theta)} - M_{\mathrm{SC}}(\theta) \right] - \frac{A_{\mathrm{C,SC}}(\theta)}{A_{\mathrm{C,C}}(\theta)} \left[\frac{I^{\mathrm{E}'}_{\mathrm{C}}(\theta)}{a(\theta)} - M_{\mathrm{C}}(\theta) \right] \right\}. \tag{3.9}$$

3.5.3 Vanadium normalisation

The normalisation factor $a(\theta)$ used to convert cross-sections into experimental intensities can be calculated by measuring a calibrant of known scattering cross-section. Vanadium is the commonly used standard in neutron scattering, as it has a very small coherent scattering length but a large incoherent scattering length, such that neutrons are scattered isotropically. As a result the distinct term in the scattering cross-section is negligible such that

$$\left.\frac{\mathrm{d}\sigma}{\mathrm{d}\Omega}\right|_{\mathrm{V}} = b^2_{\mathrm{V,inc}} \left[1 + P_{\mathrm{V}}(Q)\right]. \tag{3.10}$$

where $b_{\mathrm{V,inc}}$ is the incoherent scattering length of vanadium. The single scattered intensity for vanadium is then given by

$$\begin{aligned} I_{\mathrm{V}}(\theta) =& a(\theta) N_{\mathrm{V}} \left.\frac{\mathrm{d}\sigma}{\mathrm{d}\Omega}\right|_{\mathrm{V}} \\ =& a(\theta) N_{\mathrm{V}} \left[\frac{\sigma_{\mathrm{V}}}{4\pi} \left(1 + P_{\mathrm{V}}(Q)\right) \right] \end{aligned} \tag{3.11}$$

where $\sigma_{\rm V} = 4\pi b^2_{\rm V,inc}$. If the vanadium is held within a container then, by following the same procedure that led to equation 3.9, it follows that

$$\left.\frac{{\rm d}\sigma}{{\rm d}\Omega}\right|_{\rm V} = \frac{1}{N_{\rm V}A_{\rm V,VC}(\theta)}\left\{\left[\frac{I^{\rm E'}_{\rm VC}(\theta)}{a(\theta)} - M_{\rm VC}(\theta)\right] - \frac{A_{\rm C,VC}(\theta)}{A_{\rm C,C}(\theta)}\left[\frac{I^{\rm E'}_{\rm C}(\theta)}{a(\theta)} - M_{\rm C}(\theta)\right]\right\}, \tag{3.12}$$

where $N_{\rm V}$ is the number of vanadium nuclei illuminated by the incident beam. By rearranging equations 3.10 and 3.12, it follows that the normalisation coefficient is given by

$$a(\theta) = \frac{I^{\rm E'}_{\rm VC}(\theta)}{N_{\rm V}A_{\rm V,VC}(\theta)b^2_{\rm V,inc}\left[1+P_{\rm V}(Q)\right] + M_{\rm VC}(\theta) - \frac{A_{\rm C,VC}(\theta)}{A_{\rm C,C}(\theta)}M_{\rm C}(\theta)}. \tag{3.13}$$

3.5.4 Data analysis flow chart

In figure 3-10, a flow chart is given that outlines the data analysis procedure for isotopic substitution experiments on disordered materials using the D4c diffractometer.

For r values smaller than the first nearest neighbour distance in a sample $g_{\alpha\beta}(r) = 0$, which leads to the expression for $G(r \to 0)$ given by equation 2.19 [40]. However when $G(r)$ is obtained by Fourier transforming a measured $F(Q)$ function, there are always low-r oscillations, which should oscillate about the $G(r \to 0)$ limit. As these oscillations do not arise from the structure of the material, the back Fourier transform of $G(r)$ with the low-r oscillations set to the theoretical $G(r \to 0)$ limit should reproduce the measured $F(Q)$ exactly. A large discrepancy between the measured $F(Q)$ and the back Fourier transform in the low-Q region usually indicates that either the data set is incorrectly normalised, or that the background scattering has not been completely subtracted [40, 41]. Hence the criteria given in the flow chart in figure 3-10 for deciding when the data corrections are suitably well applied. The same argument also applies to the measured first-order difference functions and partial structure factors.

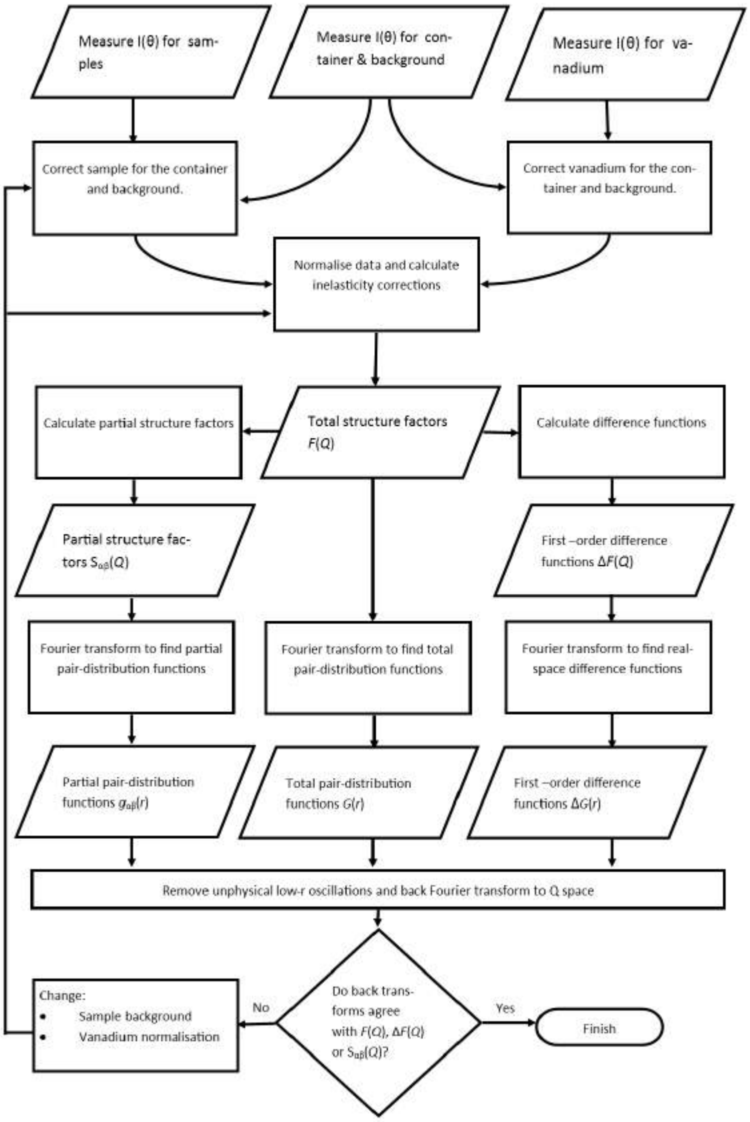

Figure 3-10: A flow diagram for the data analysis procedure applied to D4c diffraction data.

4. The structure of Ice-Ih

4.1 Introduction

Ice is a material that has fascinated scientists for centuries, and as methods of studying materials have progressed, it is often among the first compounds to be studied with a new technology or technique. The interest in ice research is hardly surprising given that it plays a significant role in the Earth's atmosphere and geological processes. Indeed it is so familiar to us on our planet, it is often forgotten that it is present in other forms on many other celestial bodies in our solar system, and in interstellar space [42]. A better understanding of its structure is therefore fundamental to answering current questions in astrophysics, cryophysics, atmospheric and environmental science [12, 43–46].

Ice exists in as many as sixteen different phases [43], and new phases are still being discovered [47, 48]. The phase diagram given in figure 4-1 shows some of the stable forms of ice, and indicates the variety in structure that occurs. The structure of most of these phases is known thanks largely to crystallographic neutron and x-ray diffraction studies. Ice-Ih is the common form of ice formed when water freezes at atmospheric pressure. The 'h' is commonly added to distinguish the normal stable hexagonal phase from its metastable cubic variant ice-Ic [49].

Ice-Ih is one of the most disordered crystalline materials [12, 45], where the symmetry elements of the crystallographic space group ($P6_3/mmc$) apply to the time and space averaged atomic positions [12, 43, 45]. On the level of a specific unit cell this symmetry is not retained, and static or dynamic disorder produces local configurations with lower symmetry [12]. Whilst the oxygen atoms in ice-Ih are related to an underlying lattice structure, the hydrogen atoms are not [50], and it has been found that all of the phases of ice which share a boundary with the liquid phase are orientationally disordered [43]. To understand this feature it is important to recall that the ice network must fulfil the Bernal-Fowler rules [51]: Each molecule forms four hydrogen bonds with its neighbours, and there is only one hydrogen atom participating in each bond. Therefore the molecule has six allowed possible orientations, and given that each crystallographic oxygen site also has a certain degree of positional disorder, local molecular

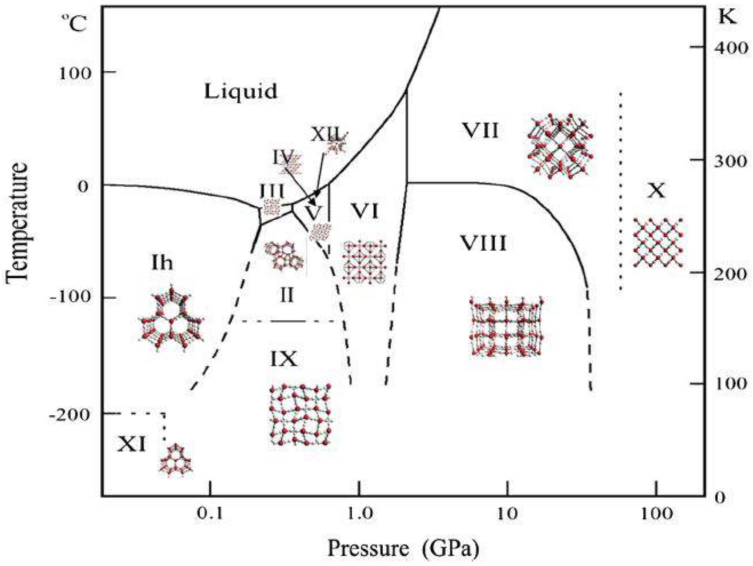

Figure 4-1: The solid-liquid phase diagram of ice, showing most of the known stable phases of ice on a logarithmic pressure scale, with representations of their structures. The thick lines represent measured transitions and the dashed lines are extrapolation of known transitions to low temperatures [43, 44].

geometries are actually very different to the global average. It is the time and ensemble averaging that makes it difficult to deduce the nature of the local disorder from the Bragg scattering in a crystallographic neutron or x-ray experiment. To build a more complete picture of the local configurations, it is necessary to combine spectroscopy and nuclear magnetic resonance data with the results from diffraction [12].

The resulting picture of the hydrogen bonding in ice-Ih is inconsistent. Nuclear quadrupole resonance experiments estimate a first inter-molecular oxygen-hydrogen distance of 1.80(1) Å but as the distance is measured indirectly from the deuteron quadrupole coupling the accuracy of this result is questionable [12, 52]. A standard crystallographic analysis finds a much shorter O-H distance of 1.751(4) Å [12] and although this value is precise, its accuracy is uncertain due to the oxygen and hydrogen disorder.

A pair distribution function (PDF) experiment is the method that is typically used to study structurally disordered materials such as liquids and glasses, where the local structure is probed directly. A crystallographic analysis only takes into account the Bragg (elastic) scattering producing a time and ensemble average of the system related to the van Hove correlation function $G(r, t = \infty)$ [13, 53]. However the PDF method also includes the information underneath the Bragg peaks in the form of diffuse scattering which is usually removed as background in a crystallographic analysis [11]. The result is that the local structure is probed directly by taking an average over a series of quasi-instantaneous snapshots of the system [13]. The PDF method measures the total scattering which is the sum of the Bragg scattering and the diffuse scattering. As ice-Ih is such a thoroughly disordered crystalline system, a PDF analysis will provide vital information on the structure and clarify the nature of the hydrogen bonds.

The work presented in this chapter makes use of neutron diffraction with isotope substitution (NDIS) to measure the full set of partial structure factors for ice-Ih using D4c. Two sets of partial structure factors were measured at both 15 K and 123 K in order to asses the Debye-Waller broadening of the r-space peaks. The results are compared to data from a standard crystallographic analysis to clarify the nature of the hydrogen bond network in ice-Ih. Finally the results are compared to the partial structure factors measured for low density amorphous ice, and water.

This chapter is organised as follows. The essential theory for the neutron diffraction experiment is discussed in section 4.2. The experimental procedure for the work is given in section 4.3. The results and accompanying discussion are presented in sections 4.4 and 4.5. Finally the conclusions are summarised in section 4.6.

4.2 Theory

The differential scattering cross-section for a system of N scattering centres is given by

$$\begin{aligned}\frac{1}{N}\frac{\mathrm{d}\sigma}{\mathrm{d}\Omega}(Q) &= F(Q) + P_{\mathrm{self}}(Q) + P_{\mathrm{distinct}}(Q) \\ &= F(Q) + \sum_{\alpha=1}^{n} c_\alpha \left(b_\alpha^2 + b_{\mathrm{inc},\alpha}^2\right)\left[1 + P_\alpha\left(Q\right)\right] + P_{\mathrm{distinct}}(Q), \qquad (4.1)\end{aligned}$$

where c_α is the concentration of chemical species α that has a coherent neutron scattering length b_α and an incoherent neutron scattering length $b_{\mathrm{inc},\alpha}$. The total structure factor is given by $F(Q)$ and contains information on the relative positions of pairs of distinct nuclei. The $P(Q) = P_{\mathrm{self}}(Q) + P_{\mathrm{distinct}}(Q)$ terms contain the self scattering from individual nuclei and a contribution from the inelastic scattering that is associated with both the self ($P_{\mathrm{self}}(Q)$) and distinct ($P_{\mathrm{distinct}}(Q)$) parts of $\frac{\mathrm{d}\sigma}{\mathrm{d}\Omega}(Q)$ for which there is no exact theory [13].

The total structure factor $F(Q)$ can be expressed as the weighted sum of Faber-Ziman partial structure factors $S_{\alpha\beta}(Q)$:

$$F(Q) = \sum_{\alpha=1}^{n}\sum_{\beta=1}^{n} c_\alpha c_\beta b_\alpha b_\beta \left[S_{\alpha\beta}(Q) - 1\right]. \qquad (4.2)$$

The corresponding real-space information $G(r)$ can be obtained by taking the Fourier transform of $F(Q)$:

$$\begin{aligned} G(r) &= \frac{1}{2\pi^2 r\rho} \int\limits_0^\infty QF(Q)\sin(Qr)\,\mathrm{d}Q \\ &= \sum_{\alpha=1}^{n}\sum_{\beta=1}^{n} c_\alpha c_\beta b_\alpha b_\beta \left[g_{\alpha\beta}(r) - 1\right], \end{aligned} \tag{4.3}$$

where ρ is the atomic number density of the sample. The partial pair-distribution function $g_{\alpha\beta}(r)$ can be used to find the coordination number $\overline{n}_\alpha^\beta$, which gives the mean number of chemical species β contained within a spherical shell of radii r_1 and r_2 centred on an atom of species α

$$\overline{n}_\alpha^\beta = 4\pi\rho c_\beta \int\limits_{r_1}^{r_2} r^2 g_{\alpha\beta}(r)\,\mathrm{d}r. \tag{4.4}$$

If a peak in $g_{\alpha\beta}(r)$ is asymmetric it can be useful to find its weighted peak position

$$\bar{r}_{\alpha\beta} = \frac{\int_{r_\mathrm{min}}^{r_\mathrm{max}} r g_{\alpha\beta}(r)\,\mathrm{d}r}{\int_{r_\mathrm{min}}^{r_\mathrm{max}} g_{\alpha\beta}(r)\,\mathrm{d}r} \tag{4.5}$$

where the integration range over the peak is chosen by the limits r_min and r_max.

A multiple-component system can be decomposed into its partial structure factors using the method of neutron diffraction with isotope substitution [26]. A two component system, such as ice, requires the measurement of three total structure factors if the full set of partial structure factors is to be obtained. In the case where more than three total structure factors are measured the solution is overconstrained and, to make use of all available data, a singular value decomposition (SVD) analysis can be used to find the partial structure factors. The mathematical details are well established, and an example of this procedure as applied to liquid and glassy zinc chloride is given by Zeidler *et al* [28]. When applying the method of hydrogen (H/D) isotope substitution it is convenient to refer to individual samples by the average bound coherent scattering length for hydrogen. For example, ${}^{\mathrm{bH0}}F(Q)$ will then refer to the total structure factor measured for a sample with a hydrogen scattering length labelled by bH0 = 0. The values of the bound coherent scattering lengths $\bar{b}_\mathrm{H}$ for the isotopically enriched ice samples used in the present work are given in table 4.1.

Table 4.1: Table of the mean bound coherent scattering lengths $\bar{b}_\mathrm{H}$ for the isotopically enriched ice samples that were used in the present work. The values were calculated using b_H= -3.7406(11) fm and b_D= 6.6741(4) fm [54].

Sample	$\bar{b}_\mathrm{H}$/fm
bH0	0.0000(5)
bH1	1.387(5)
bH2	2.908(1)
bH4	4.384(2)
bH5	5.810(5)
bH6	6.660(5)

In the present work, the matrix equation to be solved is

$$\begin{pmatrix} {}^{\mathrm{bH0}}F(Q) \\ {}^{\mathrm{bH1}}F(Q) \\ {}^{\mathrm{bH2}}F(Q) \\ {}^{\mathrm{bH4}}F(Q) \\ {}^{\mathrm{bH5}}F(Q) \\ {}^{\mathrm{bH6}}F(Q) \end{pmatrix} = \mathbf{A} \cdot \begin{pmatrix} S_\mathrm{HH}(Q) - 1 \\ S_\mathrm{OO}(Q) - 1 \\ S_\mathrm{OH}(Q) - 1 \end{pmatrix}, \tag{4.6}$$

where the matrix of weighting factors $\mathbf{A}$ is given by

$$\mathbf{A} = \begin{pmatrix} c_\mathrm{H}^2 b_\mathrm{H0}^2 & c_\mathrm{O}^2 b_\mathrm{O}^2 & 2c_\mathrm{H}c_\mathrm{O}b_\mathrm{H0}b_\mathrm{O} \\ c_\mathrm{H}^2 b_\mathrm{H1}^2 & c_\mathrm{O}^2 b_\mathrm{O}^2 & 2c_\mathrm{H}c_\mathrm{O}b_\mathrm{H1}b_\mathrm{O} \\ c_\mathrm{H}^2 b_\mathrm{H2}^2 & c_\mathrm{O}^2 b_\mathrm{O}^2 & 2c_\mathrm{H}c_\mathrm{O}b_\mathrm{H2}b_\mathrm{O} \\ c_\mathrm{H}^2 b_\mathrm{H4}^2 & c_\mathrm{O}^2 b_\mathrm{O}^2 & 2c_\mathrm{H}c_\mathrm{O}b_\mathrm{H4}b_\mathrm{O} \\ c_\mathrm{H}^2 b_\mathrm{H5}^2 & c_\mathrm{O}^2 b_\mathrm{O}^2 & 2c_\mathrm{H}c_\mathrm{O}b_\mathrm{H5}b_\mathrm{O} \\ c_\mathrm{H}^2 b_\mathrm{H6}^2 & c_\mathrm{O}^2 b_\mathrm{O}^2 & 2c_\mathrm{H}c_\mathrm{O}b_\mathrm{H6}b_\mathrm{O} \end{pmatrix}. \tag{4.7}$$

The numerical values of the matrix elements for the pseudo-inverse of $\mathbf{A}$ are given by

$$\frac{\mathbf{A}^{-1}}{\text{barn}^{-1}} = \begin{pmatrix} 11.5031 & -3.2373 & -10.6082 & -8.9779 & 0.8189 & 10.5014 \\ 22.3662 & 8.2934 & -1.0905 & -4.1597 & -1.4727 & 2.7710 \\ -17.4681 & 1.2587 & 11.5892 & 11.4222 & 1.7203 & -8.5223 \end{pmatrix}. \tag{4.8}$$

The Bhatia-Thornton formalism gives an alternative method for considering the partial structure factors of a binary system. Here, the total structure factor $F(Q)$ can be written in terms of the number-number $S_{\mathrm{NN}}^{\mathrm{BT}}(Q)$, concentration-concentration $S_{\mathrm{CC}}^{\mathrm{BT}}(Q)$ and number-concentration $S_{\mathrm{NC}}^{\mathrm{BT}}(Q)$ partial structure factors such that

$$\begin{aligned} F(Q) = \langle b\rangle^2 & \left[S_{\mathrm{NN}}^{\mathrm{BT}}(Q) - 1\right] + \\ & c_\alpha c_\beta \left(b_\alpha - b_\beta\right)^2 \left\{\left[\frac{S_{\mathrm{CC}}^{\mathrm{BT}}(Q)}{c_\alpha c_\beta}\right] - 1\right\} + \\ & 2\langle b\rangle \left(b_\alpha - b_\beta\right) S_{\mathrm{NC}}^{\mathrm{BT}}(Q), \end{aligned} \tag{4.9}$$

where $\langle b\rangle = c_\alpha b_\alpha + c_\beta b_\beta$ is the average neutron scattering length. $S_{\mathrm{NN}}^{\mathrm{BT}}(Q)$ describes the global structure of the material and treats all atomic sites as equal, i.e. irrespective of the chemical species at a particular site. $S_{\mathrm{CC}}^{\mathrm{BT}}(Q)$ contains information on the chemical ordering of species α and β, and $S_{\mathrm{NC}}^{\mathrm{BT}}(Q)$ is a cross term that gives the correlation between atomic sites and their chemical occupancy.

A singular value decomposition (SVD) analysis can also be used to calculate the Bhatia-Thornton partial structure factors using all six of the measured total structure factors. In this case, the matrix equation that must be solved is

$$\begin{pmatrix} {}^{\mathrm{bH0}}F(Q) \\ {}^{\mathrm{bH1}}F(Q) \\ {}^{\mathrm{bH2}}F(Q) \\ {}^{\mathrm{bH4}}F(Q) \\ {}^{\mathrm{bH5}}F(Q) \\ {}^{\mathrm{bH6}}F(Q) \end{pmatrix} = \mathbf{B} \cdot \begin{pmatrix} S_{\mathrm{NN}}^{\mathrm{BT}}(Q) - 1 \\ \dfrac{S_{\mathrm{CC}}^{\mathrm{BT}}(Q)}{c_{\mathrm{H}} c_{\mathrm{O}}} - 1 \\ S_{\mathrm{NC}}^{\mathrm{BT}}(Q) \end{pmatrix}, \tag{4.10}$$

where the matrix of weighting factor coefficients is given by

$$\mathbf{B} = \begin{pmatrix} \left(c_{\rm H} b_{\rm H0} + c_{\rm O} b_{\rm O}\right)^2 & c_{\rm H} c_{\rm O} \left(b_{\rm H0} - b_{\rm O}\right)^2 & 2\left(c_{\rm H} b_{\rm H0} + c_{\rm O} b_{\rm O}\right)\left(b_{\rm H0} - b_{\rm O}\right) \\ \left(c_{\rm H} b_{\rm H1} + c_{\rm O} b_{\rm O}\right)^2 & c_{\rm H} c_{\rm O} \left(b_{\rm H1} - b_{\rm O}\right)^2 & 2\left(c_{\rm H} b_{\rm H1} + c_{\rm O} b_{\rm O}\right)\left(b_{\rm H1} - b_{\rm O}\right) \\ \left(c_{\rm H} b_{\rm H2} + c_{\rm O} b_{\rm O}\right)^2 & c_{\rm H} c_{\rm O} \left(b_{\rm H2} - b_{\rm O}\right)^2 & 2\left(c_{\rm H} b_{\rm H2} + c_{\rm O} b_{\rm O}\right)\left(b_{\rm H2} - b_{\rm O}\right) \\ \left(c_{\rm H} b_{\rm H4} + c_{\rm O} b_{\rm O}\right)^2 & c_{\rm H} c_{\rm O} \left(b_{\rm H4} - b_{\rm O}\right)^2 & 2\left(c_{\rm H} b_{\rm H4} + c_{\rm O} b_{\rm O}\right)\left(b_{\rm H4} - b_{\rm O}\right) \\ \left(c_{\rm H} b_{\rm H5} + c_{\rm O} b_{\rm O}\right)^2 & c_{\rm H} c_{\rm O} \left(b_{\rm H5} - b_{\rm O}\right)^2 & 2\left(c_{\rm H} b_{\rm H5} + c_{\rm O} b_{\rm O}\right)\left(b_{\rm H5} - b_{\rm O}\right) \\ \left(c_{\rm H} b_{\rm H6} + c_{\rm O} b_{\rm O}\right)^2 & c_{\rm H} c_{\rm O} \left(b_{\rm H6} - b_{\rm O}\right)^2 & 2\left(c_{\rm H} b_{\rm H6} + c_{\rm O} b_{\rm O}\right)\left(b_{\rm H6} - b_{\rm O}\right) \end{pmatrix}. \tag{4.11}$$

The numerical values of the matrix elements for the pseudo-inverse are given by

$$\frac{\mathbf{B}^{-1}}{\text{barn}^{-1}} = \begin{pmatrix} -0.16597 & 0.042120 & 0.31481 & 0.62419 & 0.96489 & 1.18750 \\ 15.29011 & 0.56418 & -7.75046 & -7.99599 & -0.90988 & 6.73710 \\ 1.34134 & -1.18716 & -2.34927 & -1.86802 & 0.102978 & 1.98177 \end{pmatrix}. \tag{4.12}$$

Site specific structural information can also be obtained by measuring first-order difference functions. In these functions, one of the pair correlation functions is eliminated, thus reducing the overall complexity of correlations associated with a single diffraction pattern. It is possible to choose the pair-correlation function to be removed. For example, let us consider the total structure factors ${}^{\rm bHX}F(Q)$ and ${}^{\rm bHY}F(Q)$. Then the difference function

$$\begin{aligned} {}^{\rm bHY-bHX}\Delta F_{\rm no\ OO}(Q) &\equiv {}^{\rm bHY}F(Q) - {}^{\rm bHX}F(Q) \\ &= c_{\rm H}^2 \left(b_{\rm HY}^2 - b_{\rm HX}^2\right)\left[S_{\rm HH}(Q) - 1\right] + \\ &\quad 2 c_{\rm O} c_{\rm H} b_{\rm O} \left(b_{\rm HY} - b_{\rm HX}\right)\left[S_{\rm OH}(Q) - 1\right], \end{aligned} \tag{4.13}$$

removes the O-O correlations. Alternatively the H-H correlations can be removed by constructing the difference function

$$\begin{aligned} {}^{\rm bHX-bHY}\Delta F_{\rm no\ HH}(Q) &\equiv \left(\frac{b_{\rm HY}^2}{b_{\rm HX}^2}\right) {}^{\rm bHX}F(Q) - {}^{\rm bHY}F(Q) \\ &= c_{\rm O}^2 b_{\rm O}^2 \left(\frac{b_{\rm HY}^2}{b_{\rm HX}^2} - 1\right)\left[S_{\rm OO}(Q) - 1\right] + \\ &\quad 2 c_{\rm O} c_{\rm H} b_{\rm O} \left(\frac{b_{\rm HY}^2}{b_{\rm HX}} - b_{\rm HY}\right)\left[S_{\rm OH}(Q) - 1\right]. \end{aligned} \tag{4.14}$$

Similarly, the O-H correlations can be removed by constructing the difference function

$$\begin{aligned}{}^{\mathrm{bHY-bHX}}\Delta F_{\mathrm{no\ OH}}(Q) &\equiv {}^{\mathrm{bHY}}F(Q) - \left(\frac{b_{\mathrm{HY}}}{b_{\mathrm{HX}}}\right) {}^{\mathrm{bHX}}F(Q) \\ &= c_{\mathrm{O}}^2 b_{\mathrm{O}}^2 \left(1 - \frac{b_{\mathrm{HY}}}{b_{\mathrm{HX}}}\right) \left[S_{\mathrm{OO}}(Q) - 1\right] + \\ & c_{\mathrm{H}}^2 \left(b_{\mathrm{HY}}^2 - b_{\mathrm{HX}} b_{\mathrm{HY}}\right) \left[S_{\mathrm{HH}}(Q) - 1\right]. \end{aligned} \tag{4.15}$$

The weighting factors for each difference function are given in table 4.2. The corresponding real space information can be obtained by Fourier transformation e.g. for the no O-O difference function

$$\begin{aligned}{}^{\mathrm{bHY-bHX}}\Delta G_{\mathrm{no\ OO}}(r) &= \frac{1}{2\pi^2 r\rho} \int_0^\infty Q\ {}^{\mathrm{bHY-bHX}}\Delta F_{\mathrm{no\ OO}}(Q) \sin(Qr)\,\mathrm{d}Q \\ &= {}^{\mathrm{bHY}}G(r) - {}^{\mathrm{bHX}}G(r) \\ &= c_{\mathrm{H}}^2 \left(b_{\mathrm{HY}}^2 - b_{\mathrm{HX}}^2\right) g_{\mathrm{HH}}(r) + \\ & 2c_{\mathrm{O}}c_{\mathrm{H}}b_{\mathrm{O}} \left(b_{\mathrm{HY}} - b_{\mathrm{HX}}\right) g_{\mathrm{OH}}(r) + \Delta G_{\mathrm{no\ OO}}(r \to 0), \end{aligned} \tag{4.16}$$

where the low-r limit is given by

$${}^{\mathrm{bHY-bHX}}\Delta G_{\mathrm{no\ OO}}(r \to 0) = -\left\{c_{\mathrm{H}}^2 \left(b_{\mathrm{HY}}^2 - b_{\mathrm{HX}}^2\right) + 2c_{\mathrm{O}}c_{\mathrm{H}}b_{\mathrm{O}} \left(b_{\mathrm{HY}} - b_{\mathrm{HX}}\right)\right\}. \tag{4.17}$$

Similarly for the no H-H difference function

$$\begin{aligned}{}^{\mathrm{bHX-bHY}}\Delta G_{\mathrm{no\ HH}}(r) &= \frac{1}{2\pi^2 r\rho} \int_0^\infty Q\ {}^{\mathrm{bHX-bHY}}\Delta F_{\mathrm{no\ HH}}(Q) \sin(Qr)\,\mathrm{d}Q \\ &= \left(\frac{b_{\mathrm{HY}}^2}{b_{\mathrm{HX}}^2}\right) {}^{\mathrm{bHX}}G(r) - {}^{\mathrm{bHY}}G(r) \\ &= c_{\mathrm{O}}^2 b_{\mathrm{O}}^2 \left(\frac{b_{\mathrm{HY}}^2}{b_{\mathrm{HX}}^2} - 1\right) g_{\mathrm{OO}}(r) + \\ & 2c_{\mathrm{O}}c_{\mathrm{H}}b_{\mathrm{O}} \left(\frac{b_{\mathrm{HY}}^2}{b_{\mathrm{HX}}} - b_{\mathrm{HY}}\right) g_{\mathrm{OH}}(r) + \Delta G_{\mathrm{no\ HH}}(r \to 0), \end{aligned} \tag{4.18}$$

and for the no O-H difference function

$$\begin{aligned}
{}^{\mathrm{bHY-bHX}}\Delta G_{\mathrm{no\ OH}}(r) &= \frac{1}{2\pi^2 r\rho}\int_0^\infty Q\ {}^{\mathrm{bHY-bHX}}\Delta F_{\mathrm{no\ OH}}(Q)\sin(Qr)\,\mathrm{d}Q \\
&= {}^{\mathrm{bHY}}G(r) - \left(\frac{b_{\mathrm{HY}}}{b_{\mathrm{HX}}}\right){}^{\mathrm{bHX}}G(r) \\
&= c_{\mathrm{O}}^2 b_{\mathrm{O}}^2\left(1-\frac{b_{\mathrm{HY}}}{b_{\mathrm{HX}}}\right)g_{\mathrm{OO}}(r)+ \\
& c_{\mathrm{H}}^2\left(b_{\mathrm{HY}}^2 - b_{\mathrm{HX}}b_{\mathrm{HY}}\right)g_{\mathrm{HH}}(r)+\Delta G_{\mathrm{no\ OH}}(r\to 0). \qquad (4.19)
\end{aligned}$$

Table 4.2: The weighting factors in units of barns (10^{-28} m^2) for the first-order difference functions as defined by equations 4.13 to 4.15. The numerical values take into account the isotopic enrichments of the samples used in the experiment. Note that the samples are referred to by the approximate coherent scattering length of the hydrogen that is present, as given in table 4.1.

$\Delta F_{\mathrm{no}\ \alpha\beta}(Q)$	${}^{\mathrm{bHX}}F(Q)$	${}^{\mathrm{bHY}}F(Q)$	$S_{\mathrm{OO}}(Q)$(barn)	$S_{\mathrm{OH}}(Q)$(barn)	$S_{\mathrm{HH}}(Q)$(barn)
$\Delta F_{\mathrm{no\ OO}}(Q)$	bH0	bH6	0.0000(5)	0.1718(2)	0.1971(5)
	bH1	bH6	0.0000(5)	0.1360(2)	0.1886(5)
	bH2	bH6	0.0000(5)	0.0968(2)	0.1595(5)
	bH0	bH5	0.0000(5)	0.1499(1)	0.1500(5)
	bH1	bH5	0.0000(5)	0.1141(2)	0.1415(5)
	bH2	bH5	0.0000(5)	0.0748(2)	0.1124(5)
	bH0	bH4	0.0000(6)	0.1131(2)	0.0854(5)
$\Delta F_{\mathrm{no\ HH}}(Q)$	bH1	bH6	0.8252(15)	0.6530(11)	0.0000(8)
	bH1	bH5	0.6191(15)	0.4778(11)	0.0000(8)
	bH1	bH4	0.3363(15)	0.2442(11)	0.0000(8)
	bH2	bH6	0.1589(13)	0.2217(10)	0.0000(8)
	bH2	bH5	0.1120(13)	0.1496(10)	0.0000(8)
$\Delta F_{\mathrm{no\ OH}}(Q)$	bH1	bH6	-0.1422(12)	0.0000(7)	0.1276(10)
	bH1	bH5	-0.1193(12)	0.0000(7)	0.1142(10)
	bH1	bH4	-0.0808(12)	0.0000(7)	0.0583(10)
	bH2	bH6	-0.0483(11)	0.0000(6)	0.1110(9)
	bH2	bH5	-0.0373(11)	0.0000(6)	0.0749(9)

(a) (b)

Figure 4-2: (a) The nitrogen filled glove-box used for preparing the ice samples at the University of Göttingen and (b) top down view of the inside of the glove-box showing the sample preparation equipment.

4.3 Experiment

4.3.1 Sample preparation

The ice-Ih samples were made from water with the desired isotopic composition of D_2O (99.9% D from Sigma Aldrich) and H_2O (99.985% H LC-MS CROMASOLV from Sigma Aldrich). The ice samples were made at the University of Göttingen, using a dry nitrogen glovebox, as shown in figure 4-2. Water was sprayed into liquid nitrogen producing ice spheres with a mean diameter of $\sim 20\ \mu$m. The ice samples were annealed at 245 K for 2.67 hours to remove stacking faults prior to transport to the ILL. The hydrogen coherent scattering length for the samples are given in table 4.3, and the datasets are referred to by their approximate b_{H} values. The isotopically enriched samples range from null water (bH0) to pure D_2O (bH6). The bH0 sample was chosen to have an H/D ratio that produces a mean coherent neutron scattering length of zero for hydrogen.

4.3.2 Neutron diffraction experiment

The neutron diffraction experiment on ice-Ih was carried out using the D4c diffractometer at the Institut Laue-Langevin. Diffraction patterns were measured for each of the six ice samples (see table 4.3) at 15 K and 123 K with an incident neutron wavelength of 0.4985(1) Å. These two temperatures were chosen as previous crystallographic work has been published on ice-Ih at 15 K [56] and 123 K [12].

The ice samples were loaded into a 5 mm diameter vanadium can inside a specially designed nitrogen filled glove-box (figure 4-3a), to prevent any change in composition

Table 4.3: Table giving the isotopic compositions for the ice-Ih samples as expressed in terms of the mean scattering length for hydrogen. $b_{\mathrm{H}x} = xb_{\mathrm{H}} + (1-x)b_{\mathrm{D}}$ $0 \leq x \leq 1$ where x is the fraction of hydrogen that is light hydrogen H (equivalent to the mole fraction of H_2O present) and $1-x$ is the fraction of hydrogen that is heavy hydrogen D (equivalent to the mole fraction of D_2O present). The set scattering lengths were calculated using b_{H}= -3.7406(11) fm and b_{D}= 6.6741(4) fm [54]. Also listed is the total scattering cross-section $\sigma_{\mathrm{H_2O}}$ for each sample at an incident wavelength of $\lambda = 0.5$ Å, calculated from the measured values for pure H_2O and D_2O given in the Barn book [55].

Sample	x	$\bar{b}_{\mathrm{H}}$/fm	$\sigma_{\mathrm{H_2O}}$/barn($\lambda = 0.5$ Å)
bH0	0.640(7)	0.0000(5)	11.240(2)
bH1	0.507(4)	1.387(5)	9.652(7)
bH2	0.361(4)	2.908(1)	7.952(5)
bH4	0.219(6)	4.384(2)	6.301(9)
bH5	0.082(6)	5.810(5)	4.707(2)
bH6	0.001(1)	6.660(5)	3.756(6)

from exchange with water in the atmosphere. The sample, vanadium can and loading equipment were kept below 273 K during the procedure by partially submerging the vanadium can in liquid nitrogen as shown in figure 4-3b, and by periodically cooling the loading equipment. Once the sample had been transferred to the cryostat the excess nitrogen was boiled off prior to any measurement runs.

Diffraction patterns were taken for the samples in their vanadium can in the cryostat at 123 K and 15 K. Measurements of the empty vanadium container in the cryostat and the empty cryostat were taken at 300 K, 123 K and 15 K. Two vanadium rods in the cryostat (with diameters of 5.0 mm and 6.37 mm) were measured for normalisation purposes at 300 K. Two different absorbing samples, one powdered ^{10}B within the vanadium can, and a slab of $^{10}B_4C$ were also measured at 300 K, 123 K and 15 K in the cryostat to account for the effect of the sample's attenuation on the background signal at low scattering angles.

4.3.3 Background correction at small scattering angles

The data correction procedures for neutron diffraction from a reactor source are well documented [13, 57]. In this experiment a few additional effects made the background subtraction more complicated, as shown in figure 4-4. Stepping occurs at low angles in all of the datasets, and is due to the movement of the D4c detectors out of the incident neutron beam. However, the diffraction patterns for the vanadium rod, the empty

(a) (b)

Figure 4-3: (a) The nitrogen filled glove-box used for loading samples at the ILL and (b) top down view of loading ice-Ih into the vanadium can via an aluminium funnel.

cryostat and both of the $^{10}B_4C$ patterns also had a slope at low angles that covered most of the first detector.

The slope is shown in figure 4-4 where the empty cryostat diffraction pattern has been subtracted from the vanadium rod diffraction pattern. This slope at low angles also occurs in the scattering from the ice data, but as the raw data is dominated by the self scattering at low angles it is difficult to observe in the diffraction patterns. The low angle slope is sample dependent and occurs because the cryostat tail has a diameter that is much larger than the sample (sample diameter = 5 mm versus the cryostat tail diameter = 50 mm). The width (7mm) of the incident neutron beam is wider than the sample diameter, but smaller than the diameter of the cryostat tail. The geometry of the detector collimation means that different parts of a given detector see a different amount of the scattering from the cryostat tail. The hydrogen in the ice samples is very strongly scattering and as a result the scattered neutrons from the sample will also go on to scatter from the cryostat tail. This multiple scattering effect means that additional sections of the cryostat tail are now illuminated compared to the incident beam. The detector collimation means that this multiple scattering is not uniformly observed by all of the cells of a given detector. It is this effect that is though to cause the slope seen in the datasets. The empty cryostat diffraction pattern does not show this effect, as there is nothing at the sample position to scatter the incident neutrons. As a result each of the datasets has a different sample dependent background that depends on the scattering power of each sample, which cannot be corrected for by subtracting the empty cryostat measurement. So the slope that occurs in the 5 mm vanadium rod diffraction pattern is different to the slope for the fully deuterated ice sample (bH6) diffraction pattern, which is again different to the slope for the most hydrogenated ice sample (bH0) diffraction pattern.

Often a linear combination of the empty cryostat with an absorbing sample such as boron can be used to correct a low angle slope. However both of the measured boron patterns had a different slope, which started at a higher angle to that seen for the vanadium, and so could not be used to correct effectively for the slope.

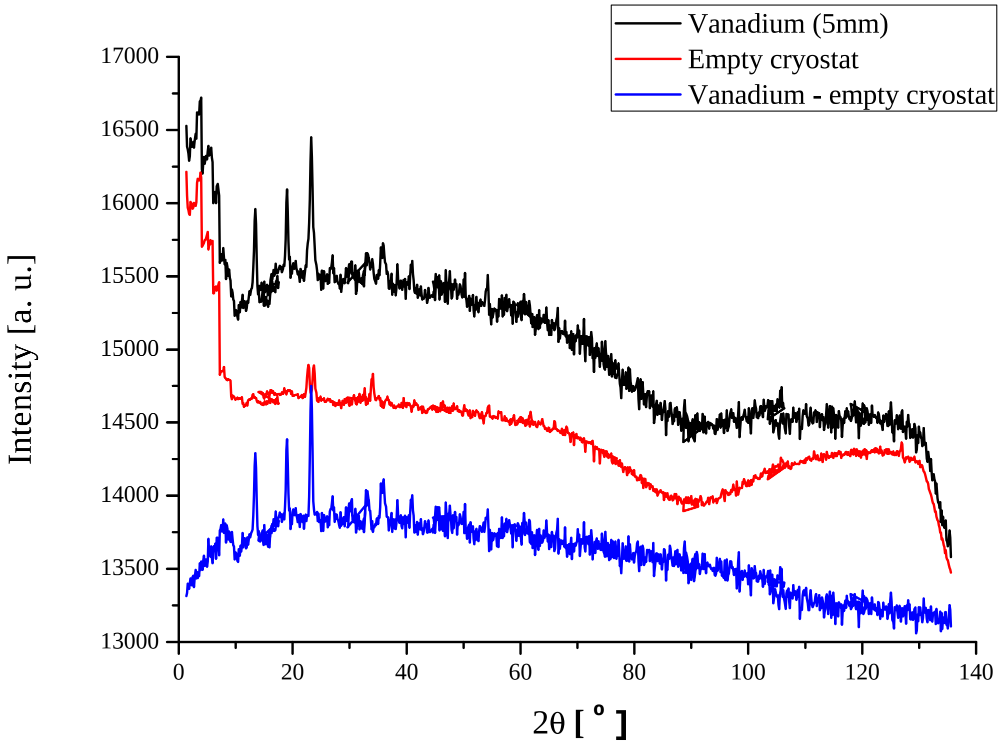

Figure 4-4: Measured intensities for the 5.0 mm diameter vanadium rod and empty cryostat at 300 K, and a direct subtraction of the cryostat from the vanadium. The vanadium rod and empty cryostat datasets illustrate the stepping at low angles and the corrected dataset shows a residual slope at low angles.

Several empirical slope correction methods were considered in the process of the data analysis. It was found that the best method was firstly to remove the stepping by subtracting the empty cryostat pattern. Then the scattering angle range used to fit the vanadium data for normalising the first detector data was restricted to include only the lowest 10 degrees for the first detector bank. This led to a re-normalisation of the low-Q region for the first detector, which in turn lead to an overall change to the normalisation of the data to ensure agreement between the back Fourier transform of $G(r)$ and the final $F(Q)$ function. The final $g_{\alpha\beta}(r)$ functions that resulted from the data analysis gave coordination numbers and peak positions that were consistent with the existence of complete water molecules i.e two intramolecular O-H bonds and one intramolecular H-H bond.

4.4 Results

4.4.1 Inelasticity corrections for hydrogen and deuterium

For lighter elements such as hydrogen and deuterium, the standard methods of calculating the inelasticity corrections for neutron diffraction experiments are not valid [13, 25, 58], as the mass of hydrogen is approximately equal to the mass of a neutron. Instead empirical schemes are used to correct for the Q-dependent inelasticity slope [15]. Figures 4-5 and 4-6 show the measured differential scattering cross-sections $\frac{\mathrm{d}\sigma}{\mathrm{d}\Omega}(Q)$ at 15 K and 123 K. The correction for the Q-dependent inelastic slopes was obtained by first fitting a 5th order polynomial to $Q\frac{\mathrm{d}\sigma}{\mathrm{d}\Omega}(Q)$ for the bH0 and bH6 samples. These can be written as

$$\begin{aligned} \phi_{\mathrm{bH0}}(Q) &= x_{\mathrm{bH0}}\phi_{\mathrm{H_2O}}(Q) + (1 - x_{\mathrm{bH0}})\phi_{\mathrm{D_2O}}(Q) \\ \phi_{\mathrm{bH6}}(Q) &= x_{\mathrm{bH6}}\phi_{\mathrm{H_2O}}(Q) + (1 - x_{\mathrm{bH6}})\phi_{\mathrm{D_2O}}(Q), \end{aligned} \tag{4.20}$$

where $\phi_{\mathrm{bH0}}(Q)$ and $\phi_{\mathrm{bH6}}(Q)$ are the fitted 5th order polynomials to $Q\frac{\mathrm{d}\sigma}{\mathrm{d}\Omega}(Q)$ for the bH0 and bH6 samples. $\phi_{\mathrm{H_2O}}(Q)$ and $\phi_{\mathrm{D_2O}}(Q)$ are the components of the Q-dependent inelasticity slope that correspond to light water and heavy water respectively. x is the mole fraction of hydrogen that is light hydrogen H in the sample, as given in table 4.3, and the subscript relates to the relevant sample. As this is a system of two linear equations with two unknowns it can be solved as,

$$\begin{pmatrix} \phi_{\mathrm{H_2O}}(Q) \\ \phi_{\mathrm{D_2O}}(Q) \end{pmatrix} = \begin{pmatrix} x_{\mathrm{bH0}} & (1 - x_{\mathrm{bH0}}) \\ x_{\mathrm{bH6}} & (1 - x_{\mathrm{bH6}}) \end{pmatrix}^{-1} \begin{pmatrix} \phi_{\mathrm{bH0}}(Q) \\ \phi_{\mathrm{bH6}}(Q) \end{pmatrix}. \tag{4.21}$$

The slopes for the other four compositions were calculated from a linear combination of these two polynomials $\phi_{\mathrm{H_2O}}(Q)$ and $\phi_{\mathrm{D_2O}}(Q)$ [15], and are given by

$$\begin{aligned} \phi_{\mathrm{bH1}}(Q) &= x_{\mathrm{bH1}}\phi_{\mathrm{H_2O}}(Q) + (1 - x_{\mathrm{bH1}})\phi_{\mathrm{D_2O}}(Q) \\ \phi_{\mathrm{bH2}}(Q) &= x_{\mathrm{bH2}}\phi_{\mathrm{H_2O}}(Q) + (1 - x_{\mathrm{bH2}})\phi_{\mathrm{D_2O}}(Q) \\ \phi_{\mathrm{bH4}}(Q) &= x_{\mathrm{bH4}}\phi_{\mathrm{H_2O}}(Q) + (1 - x_{\mathrm{bH4}})\phi_{\mathrm{D_2O}}(Q) \\ \phi_{\mathrm{bH5}}(Q) &= x_{\mathrm{bH5}}\phi_{\mathrm{H_2O}}(Q) + (1 - x_{\mathrm{bH5}})\phi_{\mathrm{D_2O}}(Q). \end{aligned} \tag{4.22}$$

The final inelasticity corrections for each of the samples are shown in figures 4-5 and 4-6.

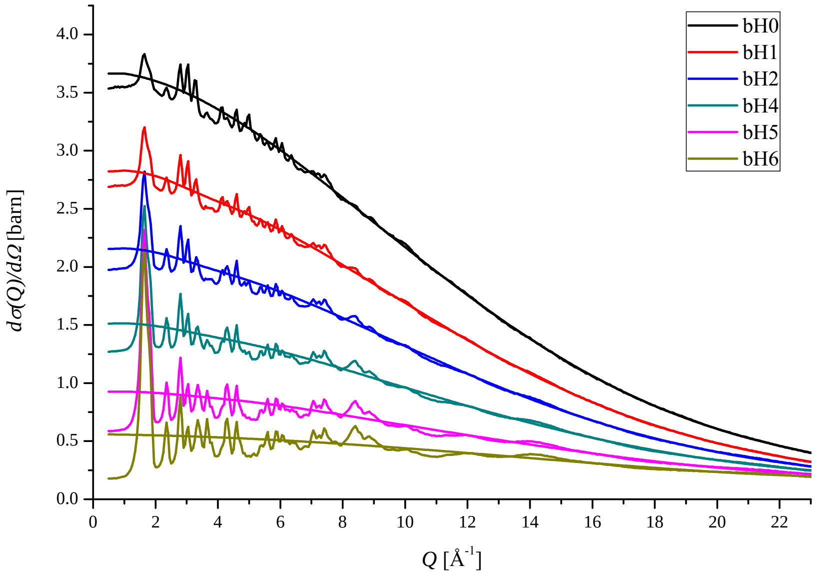

Figure 4-5: Differential scattering cross-sections $\frac{\mathrm{d}\sigma}{\mathrm{d}\Omega}(Q)$ for each of the samples of ice-Ih at 123 K as given by the solid curves with vertical error bars. The sample compositions are given in table 4.3. The smooth solid curves are the fitted inelasticity corrections for each dataset.

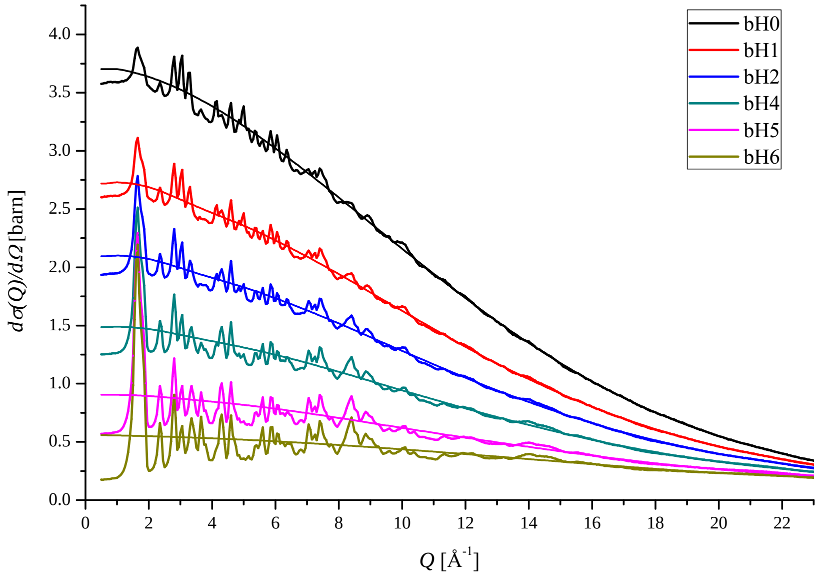

Figure 4-6: Differential scattering cross-sections $\frac{\mathrm{d}\sigma}{\mathrm{d}\Omega}(Q)$ for each of the samples of ice-Ih at 15 K as given by the solid curves with vertical error bars. The sample compositions are given in table 4.3. The smooth solid curves are the fitted inelasticity corrections for each dataset.

4.4.2 Total structure factors

Figure 4-7 shows the total structure factors $F(Q)$. The total pair-distribution functions $G(r)$, obtained by taking the Fourier transform of the $F(Q)$ functions, are given in figure 4-8. For the null water (bH0) sample, the isotopic H/D composition has been carefully balanced such that the hydrogen and deuterium scattering lengths cancel. Thus the bH0 total pair-distribution function ${}^{\mathrm{bH0}}G(r)$ gives the oxygen-oxygen distribution function $g_{\mathrm{OO}}(r)$ directly. The coordination numbers and peak positions for the first six O-O peaks are given in table 4.4.

Table 4.4: Positions r_{OO} and coordination numbers $\bar{n}_{\mathrm{O}}^{\mathrm{O}}$ for the peaks in the total pair-distribution function for the null water sample ${}^{\mathrm{bH0}}G(r)$ at 123 K and at 15 K. The values for r^{*}_{OO} are the positions in $r\,{}^{\mathrm{bH0}}G(r)$. In the case of the overlapping peaks 4 and 5, the coordination number was calculated by integrating over both peaks and thus is the sum of two individual coordination numbers.

	123 K				15 K		
	$\bar{n}_{\mathrm{O}}^{\mathrm{O}}$	$r_{\mathrm{OO}}/\text{Å}$	$r^{*}_{\mathrm{OO}}/\text{Å}$		$\bar{n}_{\mathrm{O}}^{\mathrm{O}}$	$r_{\mathrm{OO}}/\text{Å}$	$r^{*}_{\mathrm{OO}}/\text{Å}$
Peak				Peak			
1	3.98(3)	2.738(4)	2.744(4)	1	4.00(3)	2.735(4)	2.741(4)
2	13.15(3)	4.510(4)	4.516(4)	2	13.25(3)	4.498(4)	4.502(4)
3	10.03(3)	5.288(4)	5.294(4)	3	10.03(3)	5.263(4)	5.265(4)
4	23.07(4)	6.433(5)	6.435(5)	4	22.97(4)	6.384(5)	6.386(5)
5		6.942(4)	6.944(4)	5		6.908(4)	6.931(4)
6	18.44(5)	7.807(5)	7.808(5)	6	18.29(5)	7.777(5)	7.778(5)

The first well-defined real space peak in the other total pair-distribution functions is due to the intra-molecular oxygen-hydrogen correlations. The coordination number $\bar{n}_{\mathrm{O}}^{\mathrm{H}}$ and peak position r_{OH} for this feature, are given in table 4.5. This oxygen-hydrogen peak gives consistent results for the different isotopically enriched samples.

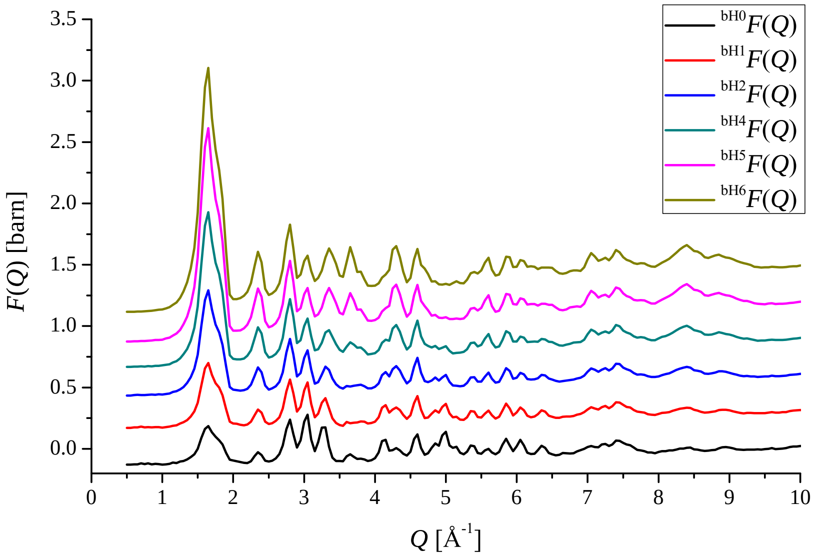

(a) 123 K

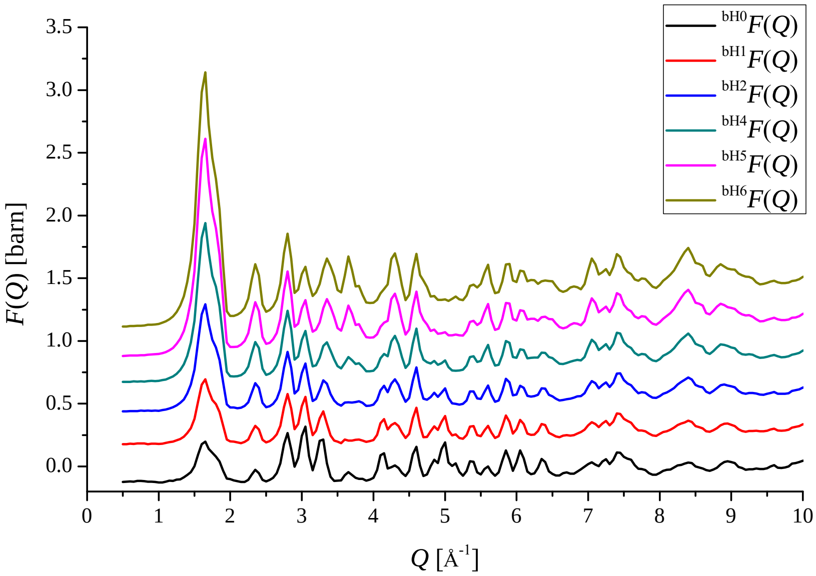

(b) 15 K

Figure 4-7: Total structure factors $F(Q)$ for ice-Ih at (a) 123 K and (b) 15 K. Note that the error bars are smaller than the line thickness. Each subsequent dataset has been offset by 0.3 barn for clarity of presentation. The datasets are referred to by the approximate hydrogen coherent scattering length, as given in table 4.3.

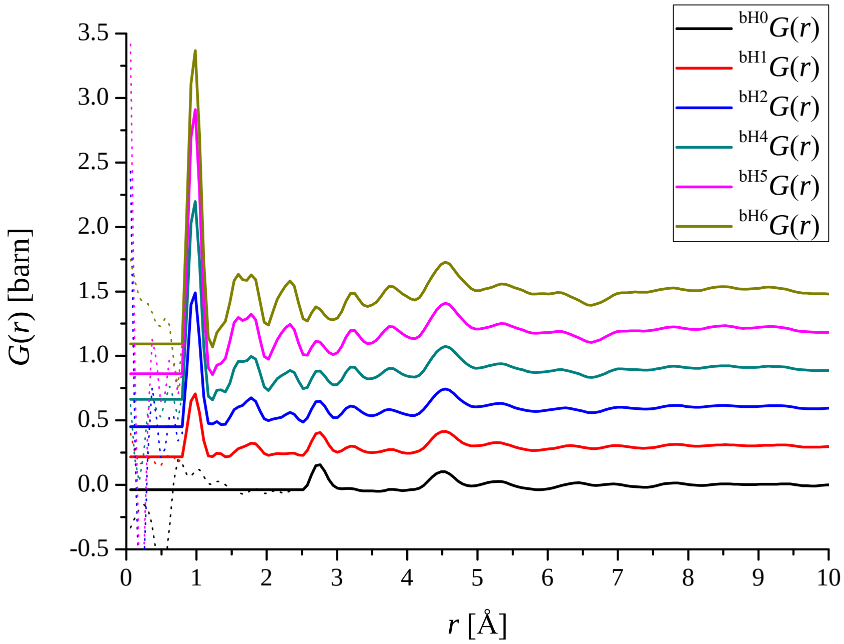

(a) 123 K

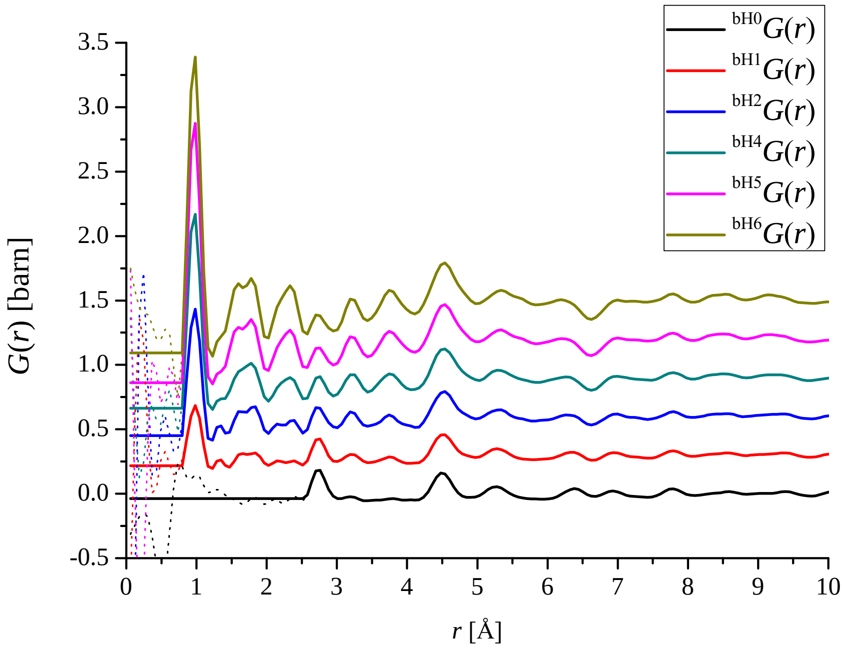

(b) 15 K

Figure 4-8: Total pair-distribution functions $G(r)$ for ice-Ih, at (a) 123 K and (b) 15 K. The solid lines are the Fourier transforms of the total structure factors given in figure 4-7, with the low-r oscillations (dashed lines) set to their theoretical $G(r \to 0) = 0$ limit. Curves are offset vertically for clarity of presentation.

Table 4.5: Positions r_{OH} and coordination numbers $\bar{n}_{\mathrm{O}}^{\mathrm{H}}$ from the first peak in the total pair-distribution functions $G(r)$. The values for r_{OH}^{*} are the positions in $rG(r)$. The samples are referred to by the approximate hydrogen coherent scattering length, as given in table 4.3.

	123 K			15 K		
	$\bar{n}_{\mathrm{O}}^{\mathrm{H}}$	$r_{\mathrm{OH}}/\mathrm{Å}$	$r_{\mathrm{OH}}^{*}/\mathrm{Å}$	$\bar{n}_{\mathrm{O}}^{\mathrm{H}}$	$r_{\mathrm{OH}}/\mathrm{Å}$	$r_{\mathrm{OH}}^{*}/\mathrm{Å}$
Sample						
bH1	2.03(2)	0.968(4)	0.974(4)	2.03(2)	0.980(4)	0.986(4)
bH2	2.01(2)	0.963(4)	0.969(4)	2.01(2)	0.974(4)	0.980(4)
bH4	2.02(2)	0.968(4)	0.974(4)	2.01(2)	0.965(4)	0.972(4)
bH5	2.03(2)	0.967(4)	0.973(4)	2.01(2)	0.966(4)	0.973(4)
bH6	2.02(2)	0.968(4)	0.974(4)	2.02(2)	0.968(4)	0.974(4)

4.4.3 First-order difference functions

Figure 4-9 shows the first-order difference functions $\Delta F_{\mathrm{no\ OO}}(Q)$ at 15 K and 123 K. It is possible to calculate 15 different first-order difference functions because six total structure factors have been measured. This is also true for the first-order difference functions $\Delta F_{\mathrm{no\ OH}}(Q)$ and $\Delta F_{\mathrm{no\ HH}}(Q)$ that are given in figures 4-10 and 4-11, respectively. Several of these samples do, however, have similar isotope compositions. When one of the weighting factors for $S_{\alpha\beta}(Q)$ in the difference function is < 0.03 barns it becomes difficult to obtain $\Delta F_{\mathrm{no\ OO}}(Q)$, $\Delta F_{\mathrm{no\ OH}}(Q)$ and $\Delta F_{\mathrm{no\ HH}}(Q)$. Therefore only the difference functions that have a large enough scattering length contrast (and thus weighting factors) have been plotted. Table 4.2 gives all of the weighting factors for each of the difference functions that have been plotted.

The $\Delta G_{\mathrm{no\ OO}}(r)$ functions for 15 K and 123 K are shown in figure 4-12. Each of these functions allows values for the intra-molecular O-H coordination number and peak position to be calculated, these provide a self-consistency check with those obtained from the total pair-distribution functions. The $\Delta G_{\mathrm{no\ HH}}(r)$ functions are plotted in figure 4-14 and allow the intra-molecular and first inter-molecular O-H coordination numbers and peak positions to be calculated. The $\Delta G_{\mathrm{no\ OH}}(r)$ functions are shown in figure 4-13 and give the intra-molecular H-H peak position and coordination number. Only the intra-molecular H-H peak can be evaluated from $\Delta G_{\mathrm{no\ OH}}(r)$ because there is overlap between $g_{\mathrm{HH}}(r)$ and $g_{\mathrm{OO}}(r)$ at larger r values.

Tables 4.6 and 4.7 give the coordination numbers and peak positions that are found from the first-order pair-distribution functions that are plotted in figures 4-12 – 4-14. The intra-molecular H-H peak in $\Delta G_{\mathrm{no\ OH}}(r)$ is asymmetric at both 15 K and 123 K.

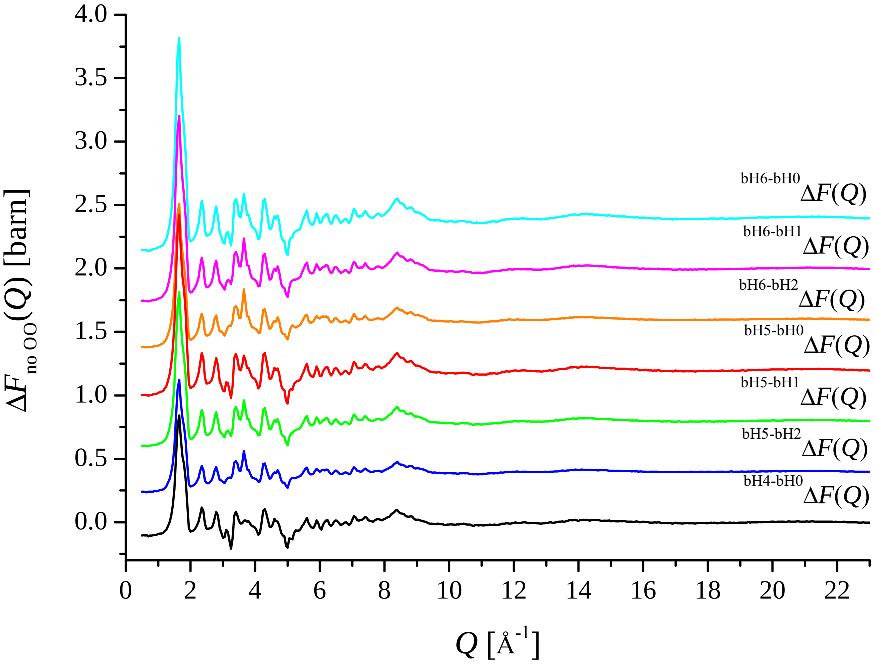

(a) 123 K

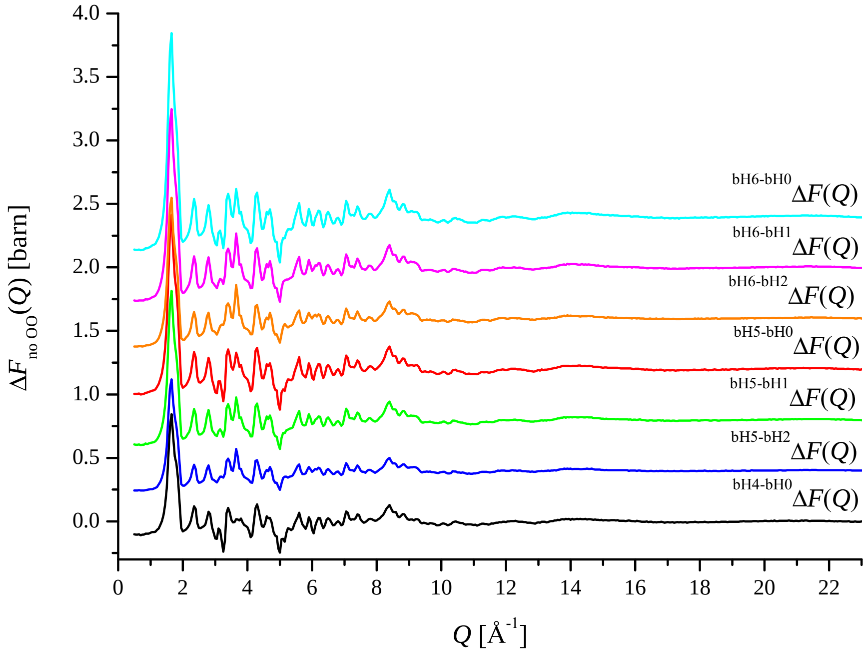

(b) 15 K

Figure 4-9: First-order difference functions $^{\text{bHY}-\text{bHX}}\Delta F_{\text{no OO}}(Q)$ at (a) 123 K and (b) 15 K, as defined by equation 4.13. The error bars are smaller than the line thickness. The curves are offset vertically for clarity of presentation.

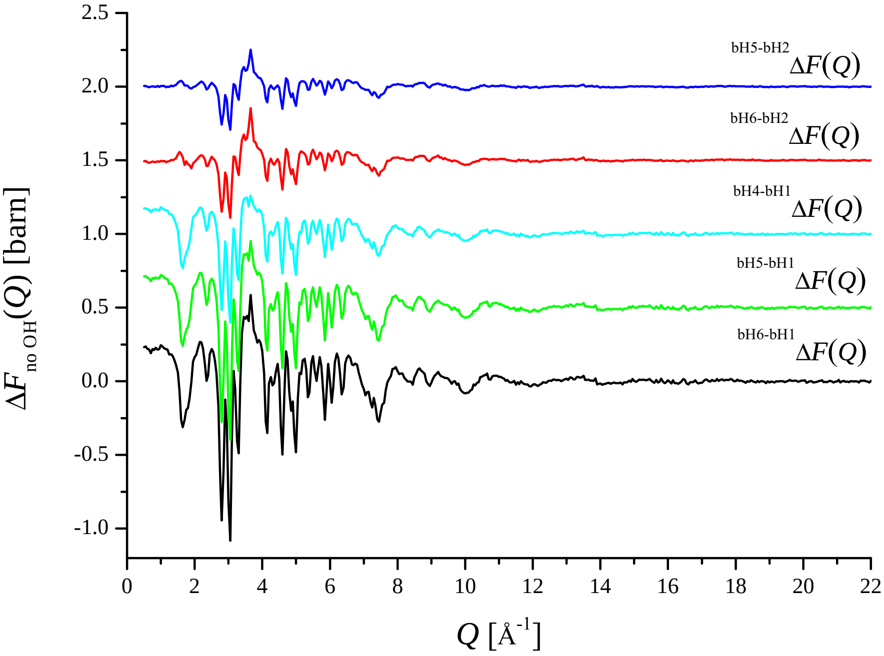

(a) 123 K

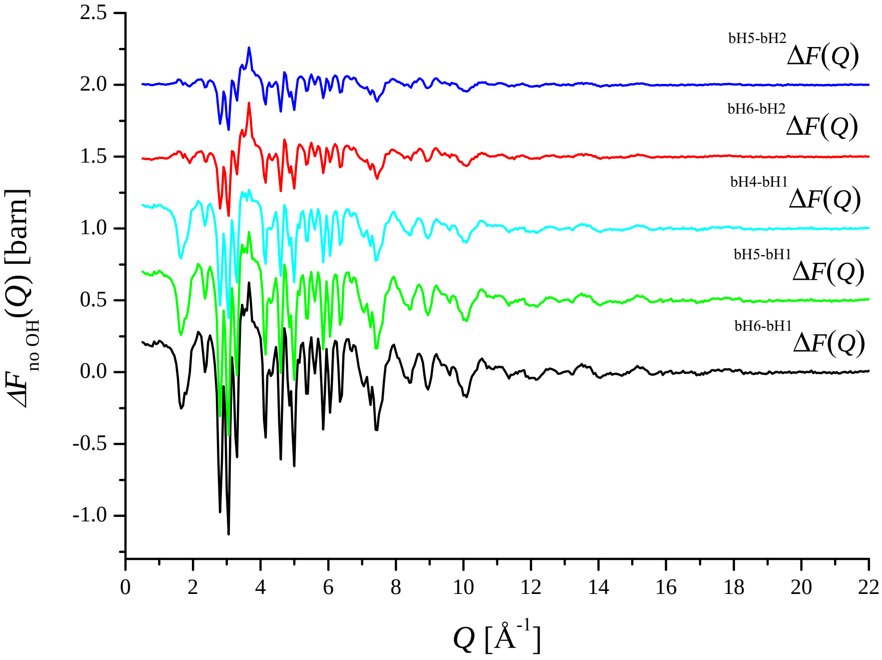

(b) 15 K

Figure 4-10: First-order difference functions $^{\mathrm{bHY-bHX}}\Delta F_{\mathrm{no\ OH}}(Q)$ at (a) 123 K and (b) 15 K, as defined by equation 4.15. The error bars are smaller than the line thickness. The curves are offset vertically for clarity of presentation.

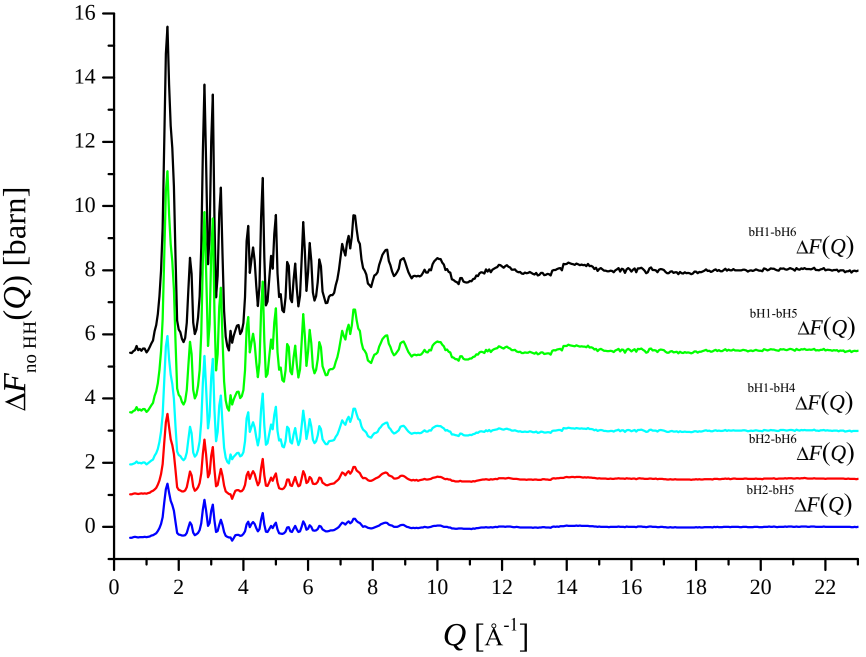

(a) 123 K

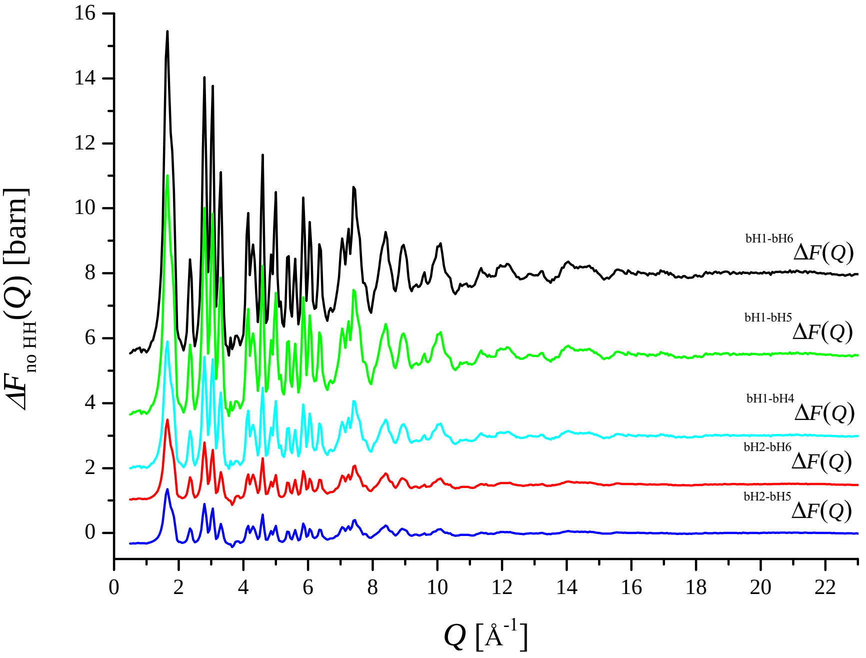

(b) 15 K

Figure 4-11: First-order difference functions $^{\text{bHX}-\text{bHY}}\Delta F_{\text{no HH}}(Q)$ at (a) 123 K and (b) 15 K, as defined by equation 4.14. The error bars are smaller than the line thickness. The curves are offset vertically for clarity of presentation.

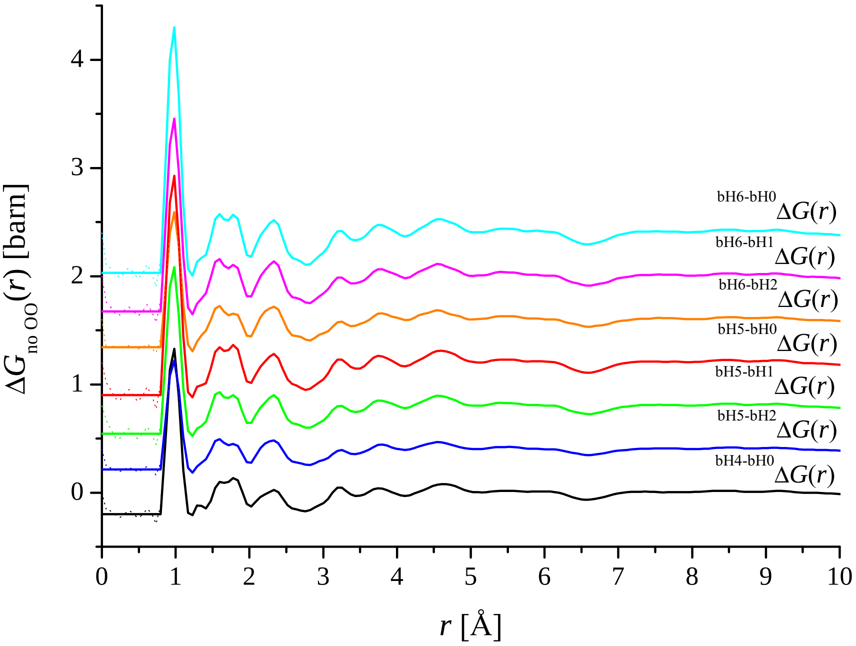

(a) 123 K

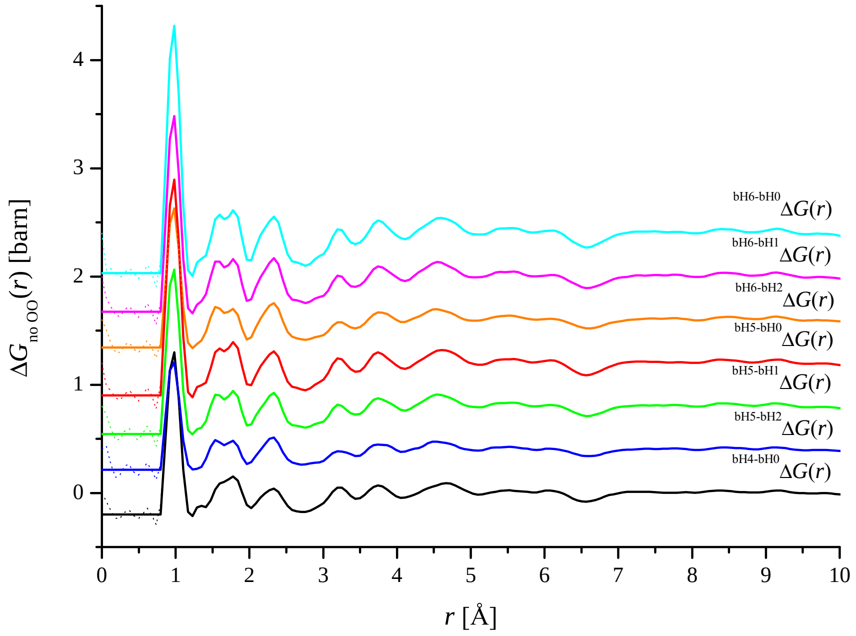

(b) 15 K

Figure 4-12: First-order difference pair-distribution functions $^{\text{bHY}-\text{bHX}}\Delta G_{\text{no OO}}(r)$ at (a) 123 K and (a) 15 K. The solid curves are obtained by Fourier transforming the first-order difference functions $^{\text{bHY}-\text{bHX}}\Delta F_{\text{no OO}}(Q)$ shown in figure 4-9. The low-r oscillations have been set to their theoretical $^{\text{bHY}-\text{bHX}}\Delta G_{\text{no OO}}(r \to 0)$ limit. The dotted lines show the extent of these unphysical oscillations. The curves are offset vertically for clarity of presentation.

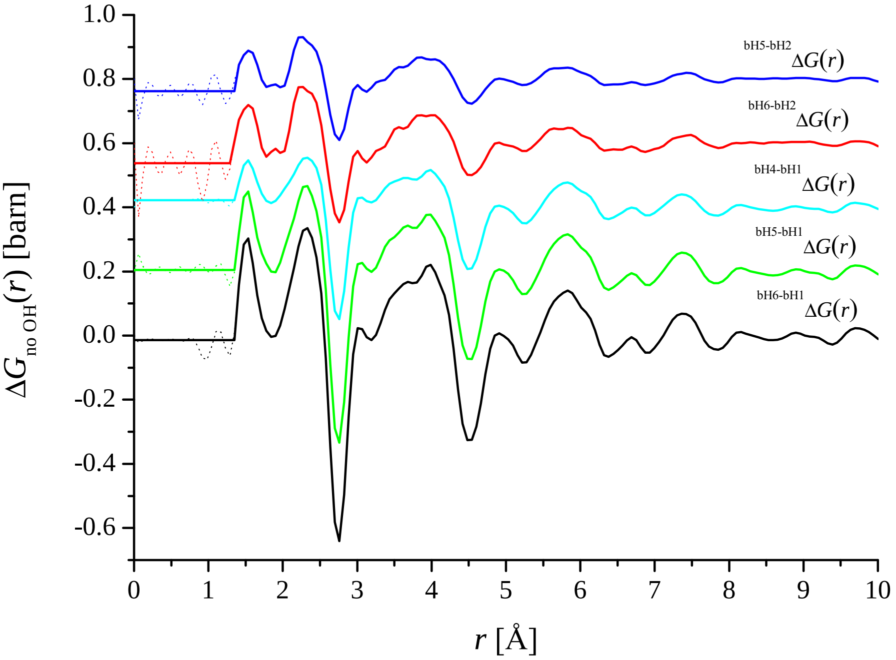

(a) 123 K

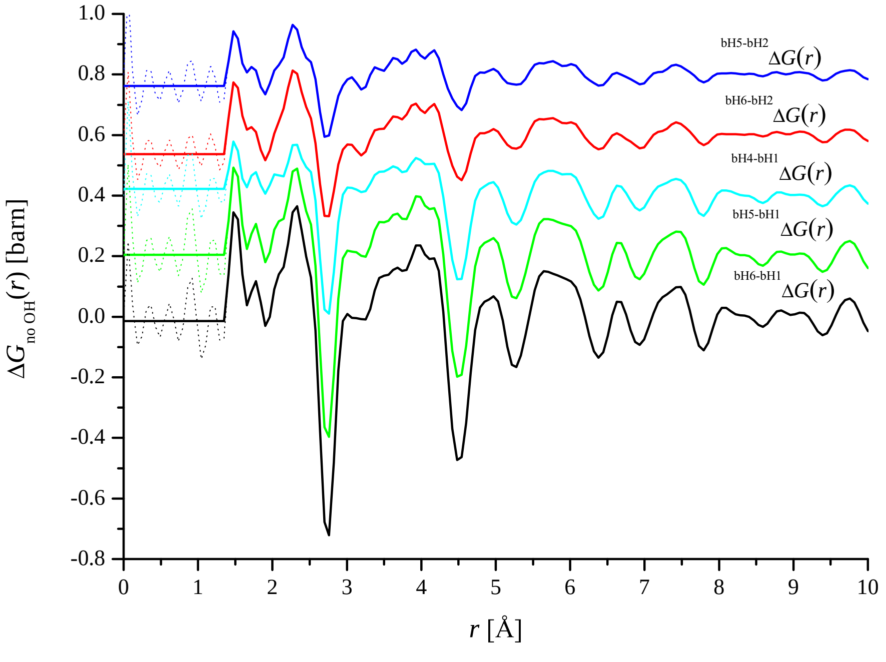

(b) 15 K

Figure 4-13: First-order difference pair-distribution functions $^{\mathrm{bHY-bHX}}\Delta G_{\mathrm{no\ OH}}(r)$ at (a) 123 K and (b) 15 K. The solid curves are obtained by Fourier transforming the first-order difference functions $^{\mathrm{bHY-bHX}}\Delta F_{\mathrm{no\ OH}}(Q)$ shown in figure 4-10. The low-r oscillations have been set to their theoretical $^{\mathrm{bHY-bHX}}\Delta G_{\mathrm{no\ OH}}(r \to 0)$ limit. The dotted lines show the extent of these unphysical oscillations. The curves are offset vertically for clarity of presentation.

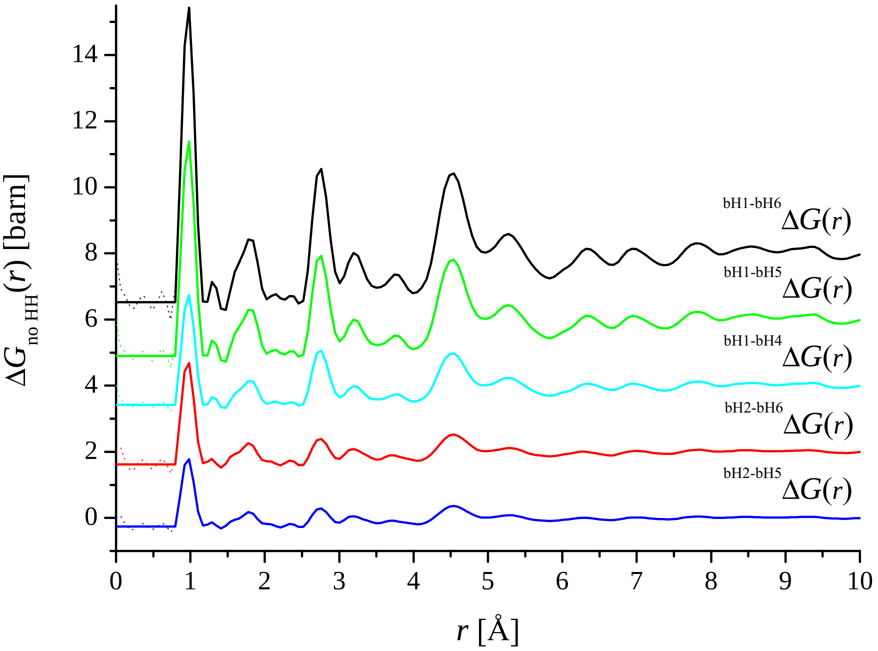

(a) 123 K

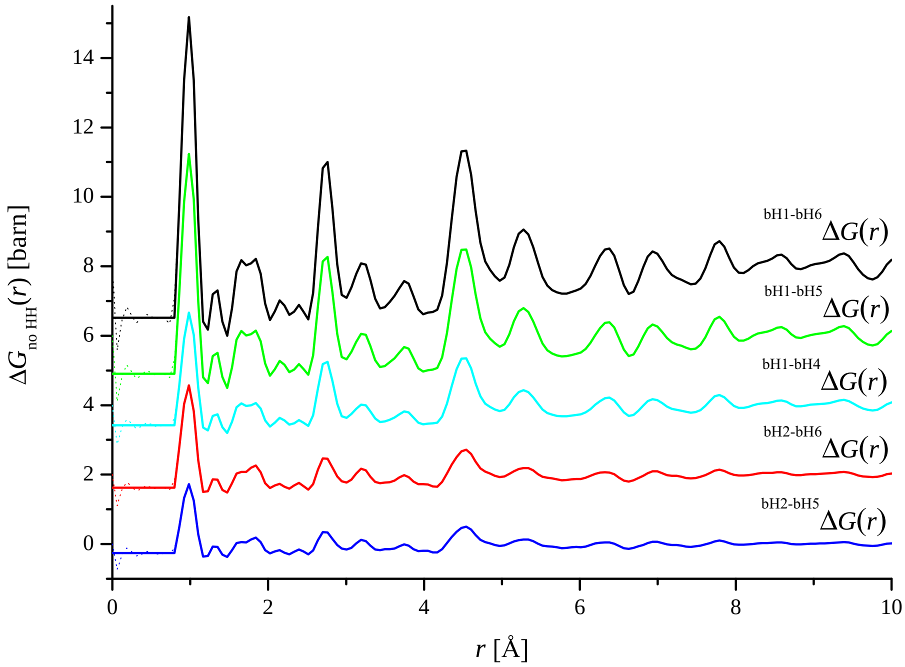

(b) 15 K

Figure 4-14: First-order difference pair-distribution functions ${}^{\text{bHX}-\text{bHY}}\Delta G_{\text{no HH}}(r)$ at (a) 123 K and (b) 15 K. The solid curves are obtained by Fourier transforming the first-order difference functions ${}^{\text{bHX}-\text{bHY}}\Delta F_{\text{no HH}}(Q)$ shown in figure 4-11. The low-r oscillations have been set to their theoretical ${}^{\text{bHX}-\text{bHY}}\Delta G_{\text{no HH}}(r \to 0)$ limit. The dotted lines show the extent of these unphysical oscillations. The curves are offset vertically for clarity of presentation.

Table 4.6: Peak positions $r_{\alpha\beta}$ and coordination numbers $\bar{n}_{\alpha}^{\beta}$ obtained from the first-order pair-distribution functions $\Delta G_{\text{no }\alpha\beta}(r)$ at 15 K plotted in figures 4-12 – 4-14. The triangular brackets $\langle\,\rangle$ indicate an average over the relevant difference functions. The weighted peak positions $\bar{r}_{\alpha\beta}$, as defined by equation 4.5, are also given. The values for $r^*_{\alpha\beta}$ and $\bar{r}^*_{\alpha\beta}$ are the corresponding peak positions in $r\Delta G_{\text{no }\alpha\beta}(r)$. The values from the intra-molecular peaks are labelled (1), and the values from the first inter-molecular peaks are labelled (2).

$\alpha\beta = \text{OH}$	$\left\langle \bar{n}_{\text{O}}^{\text{H}} \right\rangle (1)$	$\langle r_{\text{OH}} \rangle/\text{Å}$	$\langle \bar{r}_{\text{OH}} \rangle/\text{Å}$	$\langle r^*_{\text{OH}} \rangle/\text{Å}$	$\langle \bar{r}^*_{\text{OH}} \rangle/\text{Å}$
$\Delta G_{\text{no HH}}(r)$ (1)	2.015(17)	0.981(3)	0.981(3)	0.987(3)	0.983(3)
$\Delta G_{\text{no OO}}(r)$ (1)	2.031(22)	0.968(3)	0.973(1)	0.974(3)	0.978(1)
$\Delta G_{\text{no HH}}(r)$ (2)	2.044(19)	1.827(2)	1.769(2)	1.827(2)	1.754(3)

$\alpha\beta = \text{HH}$	$\left\langle \bar{n}_{\text{H}}^{\text{H}} \right\rangle (1)$	$\langle r_{\text{HH}} \rangle/\text{Å}$	$\langle \bar{r}_{\text{HH}} \rangle/\text{Å}$	$\langle r^*_{\text{HH}} \rangle/\text{Å}$	$\langle \bar{r}^*_{\text{HH}} \rangle/\text{Å}$
$\Delta G_{\text{no OH}}(r)$ (1)	1.007(14)	1.493(4)	1.559(6)	1.496(4)	1.568(6)

In the case of the 15 K difference functions shown in figure 4-13, it appears to be split into two peaks, with an overall coordination number of 1.007(14). This observation may, however, be partly due to low-r Fourier transform artefacts extending over the first peak.

The errors stated for the peak positions $r_{\alpha\beta}$ and coordination numbers $\bar{n}_{\alpha}^{\beta}$ given in tables 4.6 and 4.7 are the standard deviation from the average value given in triangular brackets $\langle\,\rangle$ i.e. the average over the relevant difference functions.

Table 4.7: Peak positions $r_{\alpha\beta}$ and coordination numbers $\bar{n}_{\alpha}^{\beta}$ obtained from the first-order pair-distribution functions $\Delta G_{\mathrm{no}\ \alpha\beta}(r)$ at 123 K plotted in figures 4-12 – 4-14. The triangular brackets $\langle\,\rangle$ indicate an average over the relevant difference functions. The weighted peak positions $\bar{r}_{\alpha\beta}$, as defined in equation 4.5 are also given. The values for $r^{*}_{\alpha\beta}$ and $\bar{r}^{*}_{\alpha\beta}$ are the same peak positions in $r\Delta G_{\mathrm{no}\ \alpha\beta}(r)$. The values from the intra-molecular peaks are labelled (1), and the values from the first inter-molecular peak are labelled (2).

$\alpha\beta = \mathrm{OH}$	$\left\langle \bar{n}_{\mathrm{O}}^{\mathrm{H}} \right\rangle(1)$	$\langle r_{\mathrm{OH}}\rangle/\text{Å}$	$\langle \bar{r}_{\mathrm{OH}}\rangle/\text{Å}$	$\langle r^{*}_{\mathrm{OH}}\rangle/\text{Å}$	$\langle \bar{r}^{*}_{\mathrm{OH}}\rangle/\text{Å}$
$\Delta G_{\mathrm{no\ HH}}(r)$ (1)	2.030(10)	0.967(4)	0.972(4)	0.973(4)	0.976(3)
$\Delta G_{\mathrm{no\ OO}}(r)$ (1)	2.024(43)	0.971(3)	0.974(3)	0.977(3)	0.980(3)
$\Delta G_{\mathrm{no\ HH}}(r)$ (2)	2.030(23)	1.799(10)	1.751(4)	1.801(10)	1.763(16)

$\alpha\beta = \mathrm{HH}$	$\left\langle \bar{n}_{\mathrm{H}}^{\mathrm{H}} \right\rangle(1)$	$\langle r_{\mathrm{HH}}\rangle/\text{Å}$	$\langle \bar{r}_{\mathrm{HH}}\rangle/\text{Å}$	$\langle r^{*}_{\mathrm{HH}}\rangle/\text{Å}$	$\langle \bar{r}^{*}_{\mathrm{HH}}\rangle/\text{Å}$
$\Delta G_{\mathrm{no\ OH}}(r)$ (1)	0.980(25)	1.528(13)	1.547(10)	1.536(14)	1.554(13)

4.4.4 Faber-Ziman partial structure factors

The partial structure factors obtained from a singular value decomposition (SVD) analysis of all six ice compositions are shown in figure 4-15, and the corresponding real space functions are given in figure 4-16. The coordination numbers and peak positions for both temperatures are given in table 4.8, along with values obtained from single crystal data for hydrogenated ice-Ih [59].

The intra-molecular and first inter-molecular peaks in $g_{\mathrm{OH}}(r)$ are readily distinguished from each other as the first peak is very sharp and is separated from the second. The intra-molecular coordination numbers $\bar{n}_{\mathrm{O}}^{\mathrm{H}}$ and peak positions r_{OH}, are consistent with intact water molecules. The first peak in $g_{\mathrm{HH}}(r)$ corresponds to the intra-molecular hydrogen-hydrogen distance in ice, and is well separated from the second peak. This allows the intra-molecular H-H correlations to be clearly distinguished from the inter-molecular H-H correlations. The intra-molecular H-H peak is asymmetric, and at 15 K there is a noticeable shoulder on its high-r side. This shoulder may be caused by Fourier transform artefacts extending over the first H-H peak, although the intra-molecular H-H peak for ice-Ih at 123 K is also asymmetric with a high-r tail.

The partial structure factors can also be calculated from any combination of three of the total structure factors. However, if the scattering length contrast is small, then the associated error will be large. In figure 4-17 the partial structure factors calculated from the SVD analysis are compared with two sets of partial structure factors calculated from three totals. Set A combines the total structure factors for the bH0, bH2 and bH5 samples, and set B combines the total structure factors for the bH1, bH4 and bH6 samples. The corresponding partial pair-distribution functions at 15 K and 123 K are shown in figure 4-18. The three sets of partial pair-distribution functions are the same within the experimental error indicating that all of the datasets are self-consistent e.g. the peak positions $r_{\alpha\beta}$ and coordination numbers $\bar{n}_{\alpha}^{\beta}$ are in agreement within the error.

Figure 4-19 compares the partial pair-distribution functions at 15 K and 123 K. The main difference between the two temperatures occurs for the oxygen-oxygen partial pair-distribution function, as there is a broadening of all of the O-O peaks with increasing temperature. The oxygen-hydrogen and hydrogen-hydrogen partial pair-distribution functions show comparatively little change with temperature.

The errors stated for the peak positions $r_{\alpha\beta}$ and coordination numbers $\bar{n}_{\alpha}^{\beta}$ given in tables 4.8 and 4.9 are the standard deviation from the average values, where the average peak positions and coordination numbers are the average over all three sets (SVD, Set A and Set B) of partial pair-distribution functions.

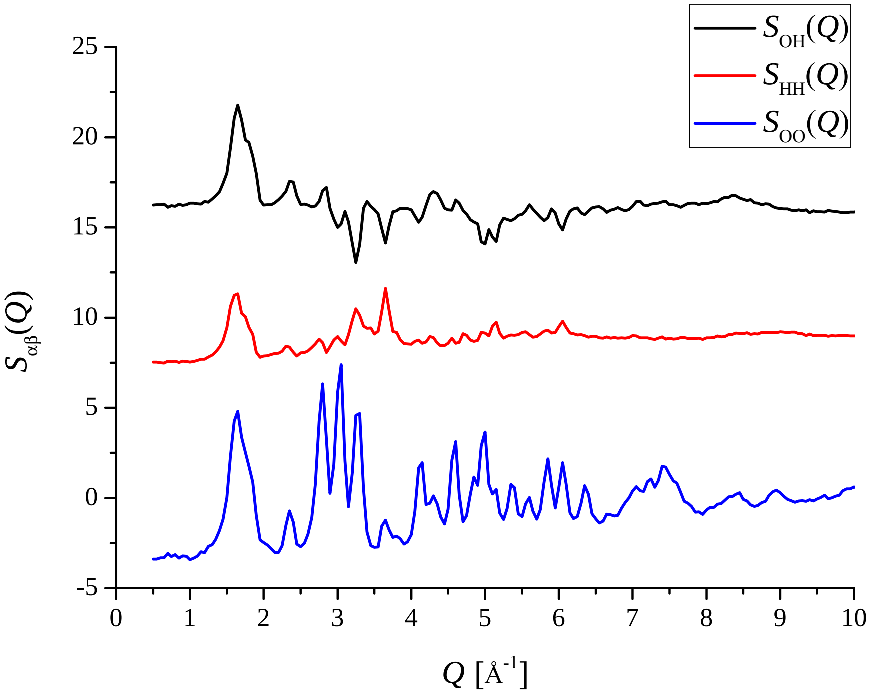

(a) 123 K

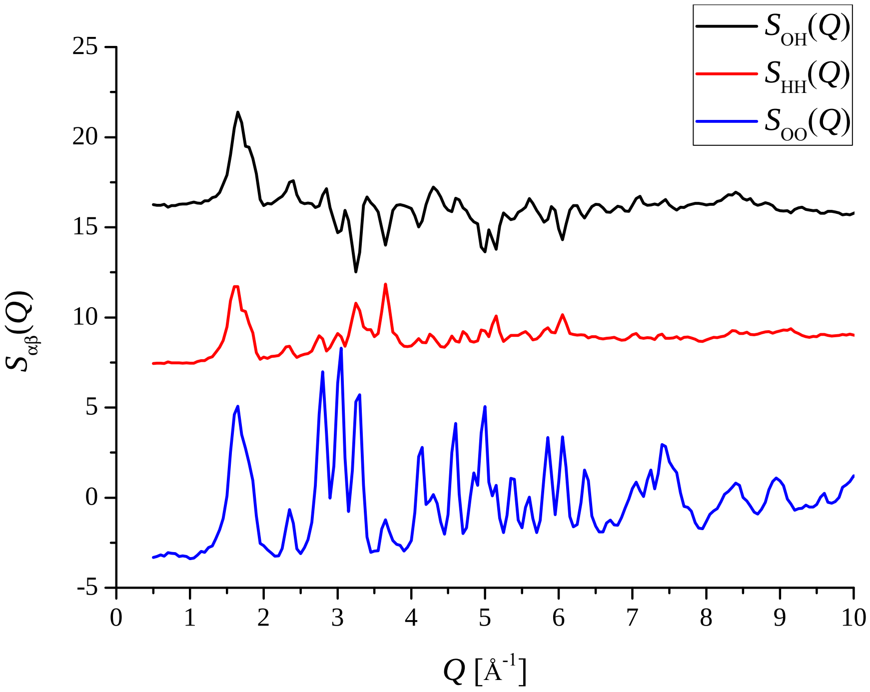

(b) 15 K

Figure 4-15: Faber-Ziman partial structure factors for ice-Ih at (a) 123 K and (b) 15 K obtained from the SVD analysis, offset vertically for clarity of presentation. The error bars are smaller than the thickness of a line. Note that the $S_{\mathrm{OH}}(Q)$ partial structure factor has some negative going peaks.

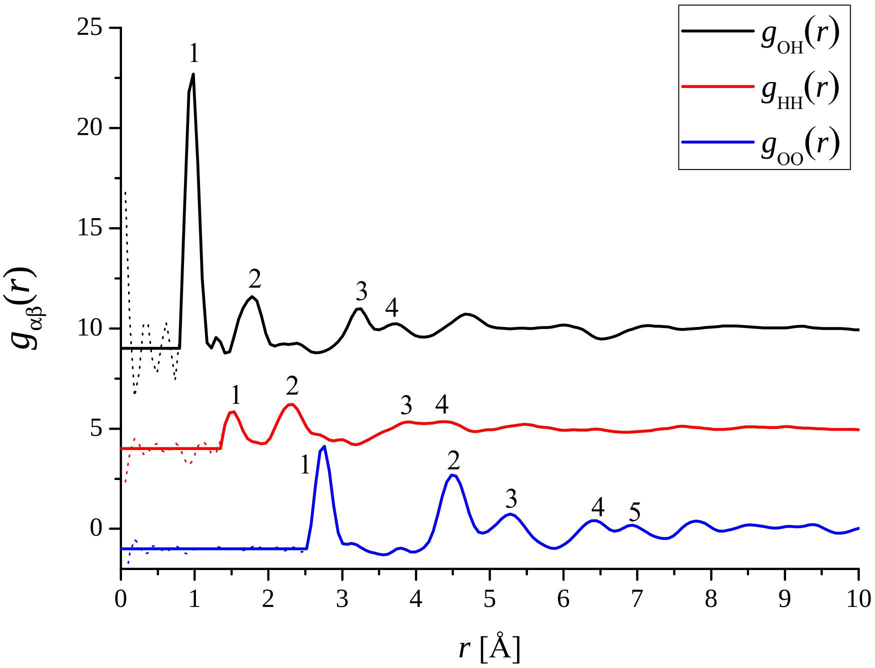

(a) 123 K

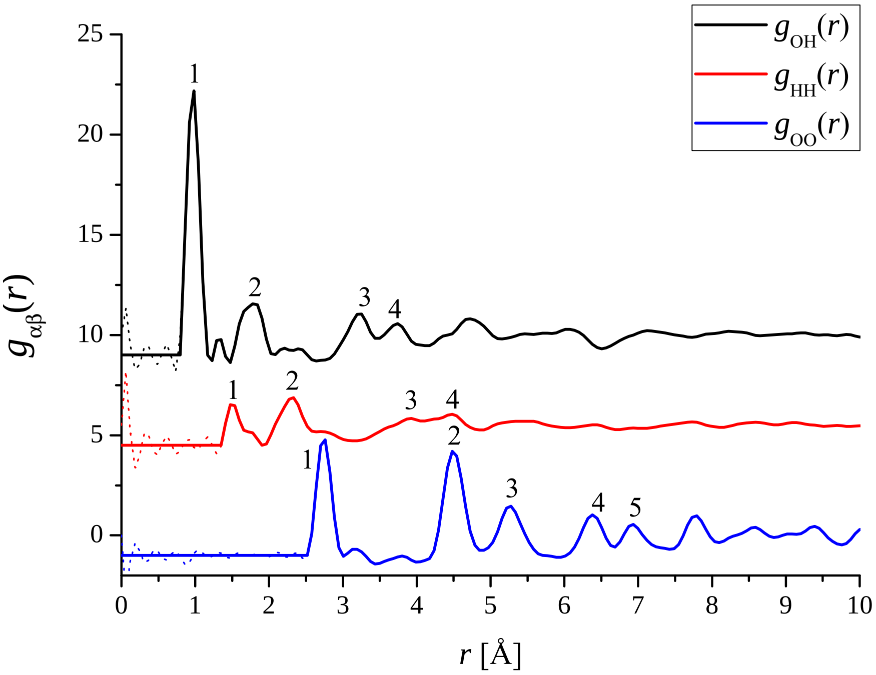

(b) 15 K

Figure 4-16: Faber-Ziman partial pair-distribution functions for ice-Ih at (a) 123 K and (b) 15 K. The data sets were obtained by Fourier transforming the Faber-Ziman partial structure factors $S_{\alpha\beta}(Q)$ shown in figure 4-15. The solid lines show these functions after the low-r oscillations (dotted lines) have been set to their theoretical $g_{\alpha\beta}(r \to 0) = 0$ limit. The labelled peak positions and coordination numbers are given in Table 4.8.

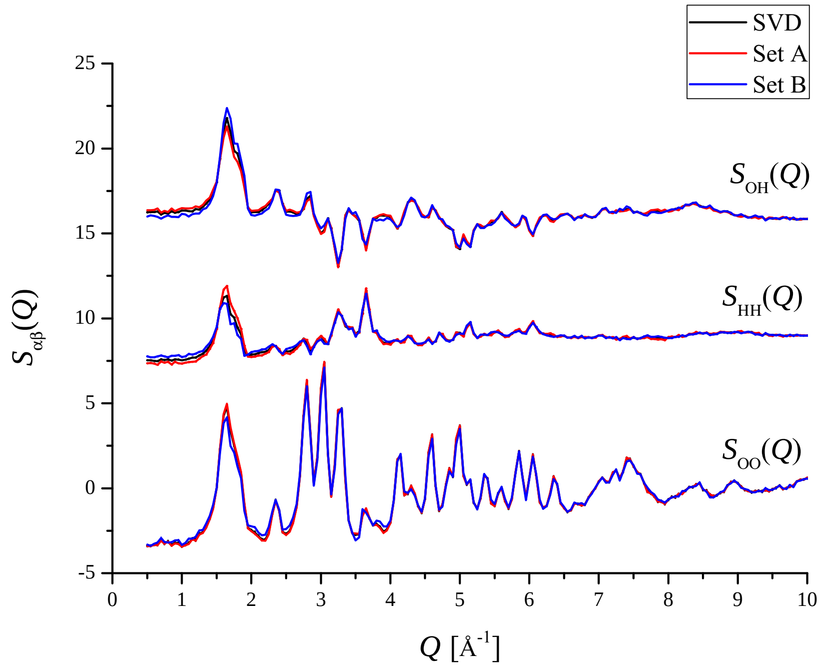

(a) 123 K

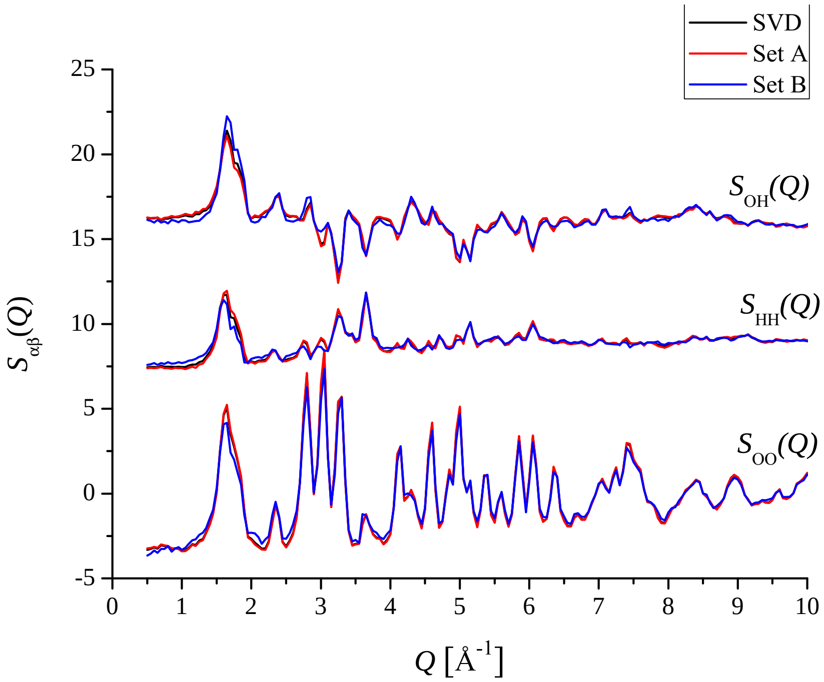

(b) 15 K

Figure 4-17: Faber-Ziman partial structure factors for ice-Ih at (a) 123 K and (b) 15 K calculated from the SVD analysis and from 2 sets of three total structure factors. Set A combines the total structure factors for bH0, bH2 and bH5, and set B combines the total structure factors for bH1, bH4 and bH6. The statistical errors are smaller than a line thickness and the datasets have been offset vertically for clarity of presentation.

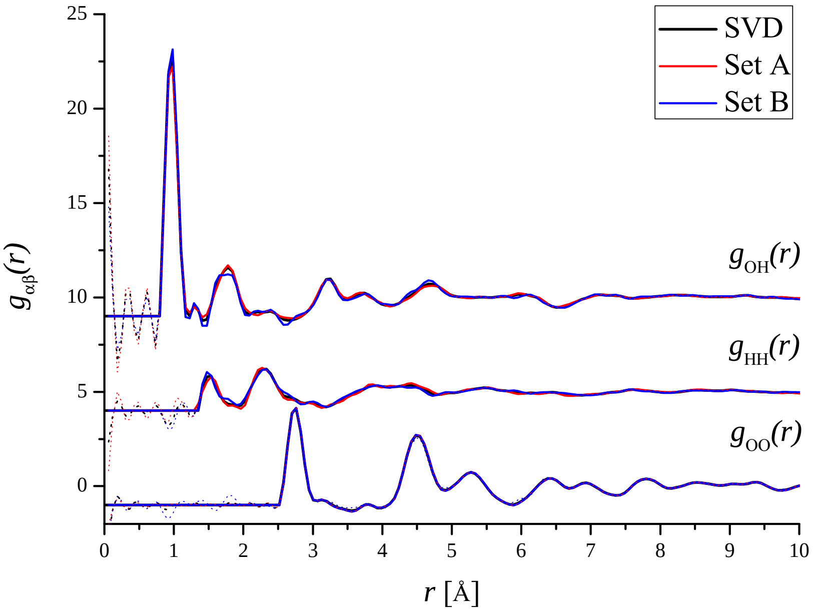

(a) 123 K

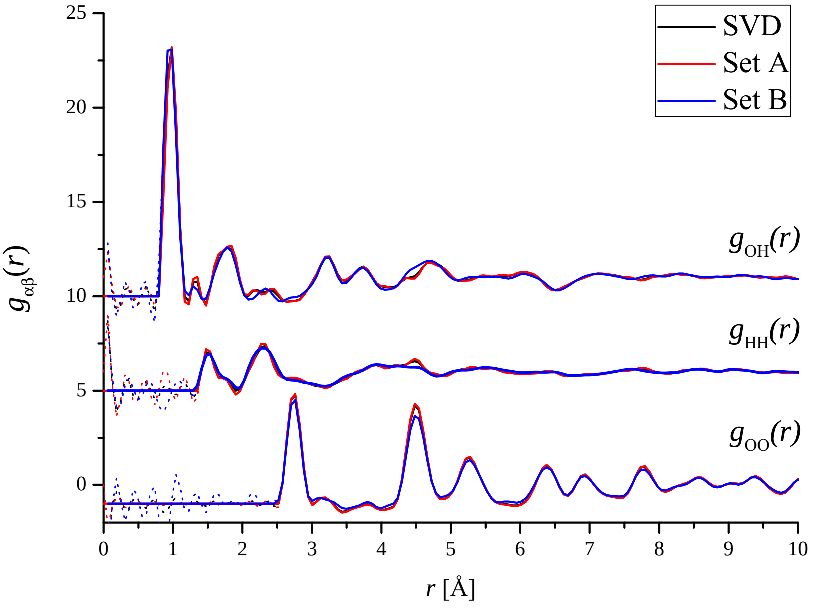

(b) 15 K

Figure 4-18: Faber-Ziman partial pair-distribution functions for ice-Ih at (a) 123 K and (b) 15 K calculated from the SVD analysis and from 2 sets of three total structure factors. The data sets were obtained by Fourier transforming the Faber-Ziman partial structure factors $S_{\alpha\beta}(Q)$ shown in figure 4-17 for sets A and B. The solid lines show these functions after the low-r oscillations (dotted lines) have been set to their theoretical $g_{\alpha\beta}(r \to 0) = 0$ limit. Set A combines the total structure factors for bH0, bH2 and bH5, and set B combines the total structure factors for bH1, bH4 and bH6. The datasets have been offset vertically for clarity of presentation.

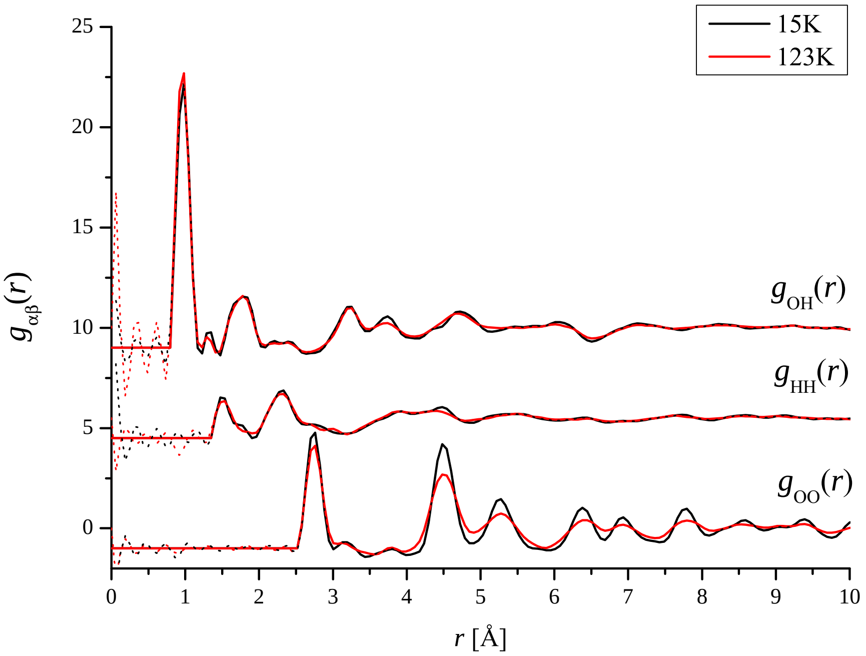

Figure 4-19: Faber-Ziman partial pair-distribution functions for ice-Ih at 15 K (black curves) and 123 K (red curves) calculated from the SVD analysis. The solid lines show the partials after the low-r oscillations (dotted lines) have been set to their theoretical $g_{\alpha\beta}(r \to 0) = 0$ limit. The datasets have been offset vertically for clarity of presentation.

Comparison with published crystallographic data

Figure 4-20 shows the Faber-Ziman partial pair-distribution functions, plotted as $r^2 g_{\alpha\beta}(r)$, against histograms of the interatomic distances calculated from single crystal data for hydrogenated ice-Ih [59]. The crystallographic data was obtained by taking the unit cell and atomic parameters stated in reference [59], and using the FullProf suite [60] to calculate the positions for all of the atoms using the standard symmetry operations for a hexagonal unit cell. These crystallographic results were checked using the ISAACS [61] suite of programs. The same atomic parameters [59] were used in ISAACS to build a supercell comprising 125 unit cells, from which the partial pair-distribution functions could be calculated out to 10 Å. The results obtained from FullProf and ISAACS were identical. As coordination numbers are calculated from the integral of $r^2 g_{\alpha\beta}(r)$ (equation 4.4), each of the figures provides an interesting comparison to single crystal data.

The peak positions given in table 4.8 can be used to calculate the intra-molecular and inter-molecular bond angles in ice-Ih by applying the cosine rule. These angles are given in tables 4.10 and 4.11. Different bond angles are obtained depending on whether weighted peak positions or maximum peak positions are used for $g_{\alpha\beta}(r)$ or $rg_{\alpha\beta}(r)$. The same bond angles have been calculated using the cosine rule for water and LDA ice using the peak positions given in reference [15], and these angles are given in tables 4.12 and 4.13 respectively. The O-O-O bond angle is difficult to calculated for water, because the second peak in $g_{\mathrm{OO}}(r)$ is ill-defined. Skinner *et al.* [62] obtained peak positions for the first and second O-O peaks in $g_{\mathrm{OO}}(r)$ for water by fitting a Gaussian curve locally around the peak maxima. They obtain peak positions of 2.80(2) Å and 4.50(2) Å at 300 K for the first and second peaks respectively, which gives a O-O-O bond angle of 107.6(5)° calculated using the cosine rule. Figure 4-21 represents the bond angles that are given in tables 4.10 – 4.13, providing a visual aid for the reader.

Table 4.9 gives the peak positions and coordination numbers found from the partial pair-distribution functions shown in figure4-18, which were calculated from Set A, which used the total structure factors for the bH0, bH2 and bH5 samples, or for set B, which used the total structure factors for the bH1, bH4 and bH6 samples. By comparing the values given in tables 4.8 and 4.9, it is found that the peak positions and coordination numbers from the SVD analysis agree with those from set A or set B within the experimental error.

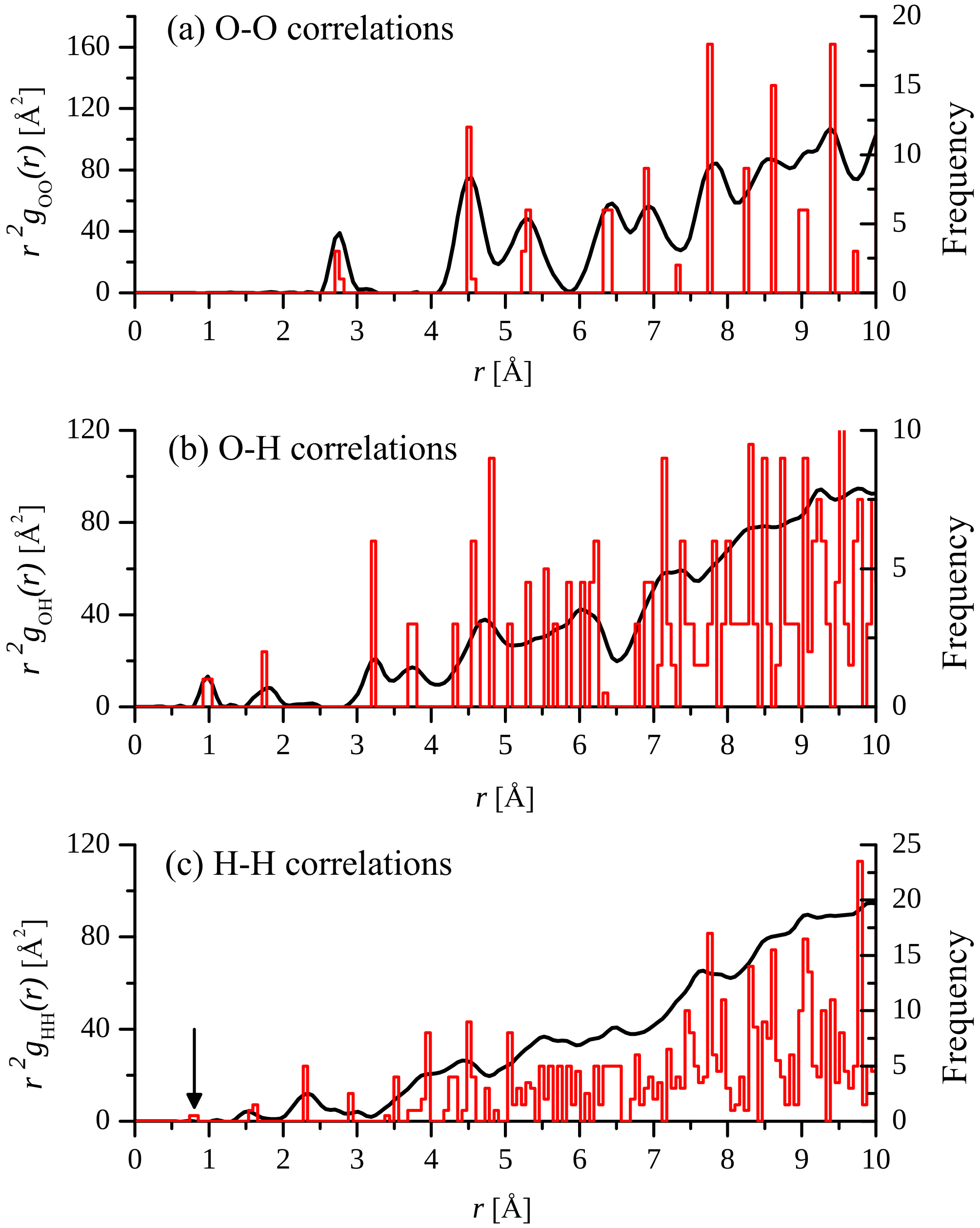

Figure 4-20: The black curves show the Faber-Ziman radial distribution functions $(r^2 g_{\alpha\beta}(r))$ at 123 K. Histograms of the crystallographic distances for a pure H_2O sample at 100 K [59] are shown in red. The latter were calculated from the published crystal structure using the FullProf analysis suite [60]. Note that the crystal structure assumes half occupancy of the hydrogen sites. Thus the peak indicated by a black arrow in (c) is not physical as it corresponds to the distance between 2 possible H sites in a hydrogen bond (see section 4.5).

Table 4.8: Bond distances $r_{\alpha\beta}$ and coordination numbers $\bar{n}_{\alpha}^{\beta}$ for ice-Ih at 123 K and 15 K from the $g_{\alpha\beta}(r)$ function calculated using the SVD method. The weighted peak positions in $g_{\alpha\beta}(r)$ ($\bar{r}_{\alpha\beta}$) are also given. The values for $r^*_{\alpha\beta}$ are the positions in $rg_{\alpha\beta}(r)$. In the case of two overlapping peaks (for example, peaks 4 and 5 in $g_{\mathrm{OO}}(r)$), the coordination number was calculated by integrating over both peaks and is thus the sum of two individual coordination numbers. The peaks are labelled in figure 4-16. The crystallographic distances and coordination numbers for a pure H_2O sample at 100 K are also given for comparison [59]. These were calculated from the published crystal structure using the FullProf analysis suite [60]. Note that the crystal structure assumes half occupancy of the hydrogen sites, and the distances given for the crystal are the average distances.

		PDF analysis at 123 K					PDF analysis at 15 K					Crystallography	
		$\bar{n}_{\alpha}^{\beta}$	$r_{\alpha\beta}$/Å	$r^*_{\alpha\beta}$/Å	$\bar{r}_{\alpha\beta}$/Å		$\bar{n}_{\alpha}^{\beta}$	$r_{\alpha\beta}$/Å	$r^*_{\alpha\beta}$/Å	$\bar{r}_{\alpha\beta}$/Å		$\bar{n}_{\alpha}^{\beta}$	$r_{\alpha\beta}$/Å
$\alpha\beta = \mathrm{OO}$													
	1	4.01(3)	2.740(3)	2.743(3)	2.763(2)	1	3.99(3)	2.740(2)	2.742(2)	2.746(4)	1	4.00(1)	2.75(2)
	2	13.04(4)	4.503(2)	4.508(2)	4.532(3)	2	13.09(10)	4.497(2)	4.500(2)	4.511(6)	2	13.00(1)	4.50(2)
	3	9.96(4)	5.275(4)	5.278(4)	5.267(3)	3	10.04(6)	5.262(3)	5.264(3)	5.240(20)	3	9.00(1)	5.28(2)
	4	22.77(30)	6.406(20)	6.408(20)	6.391(30)	4	22.96(20)	6.381(3)	6.382(3)	6.378(10)	4	12.00(1)	6.38(2)
	5		6.919(10)	6.920(10)	6.973(30)	5		6.923(3)	6.924(3)	6.969(10)	5	11.00(1)	6.90(2)
$\alpha\beta = \mathrm{OH}$													
	1	2.07(3)	0.961(3)	0.969(3)	0.967(2)	1	2.00(2)	0.965(12)	0.972(10)	0.970(6)	1	2.00(1)	0.98(2)
	2	2.02(3)	1.778(3)	1.789(7)	1.778(10)	2	2.07(2)	1.798(16)	1.806(15)	1.768(2)	2	2.00(1)	1.75(2)
	3	11.98(30)	3.224(6)	3.226(6)	3.224(10)	3	11.93(20)	2.223(6)	3.225(6)	3.211(8)	3	6.00(1)	3.22(2)
	4		3.709(20)	3.722(25)	3.718(10)	4		3.735(7)	3.737(7)	3.708(16)	4	6.00(1)	3.74(2)
$\alpha\beta = \mathrm{HH}$													
	1	1.01(3)	1.512(23)	1.515(24)	1.565(3)	1	1.03(4)	1.503(8)	1.505(9)	1.559(6)	1	1.25(4)	1.59(2)
	2	4.02(3)	2.295(21)	2.305(16)	2.321(8)	2	3.99(4)	2.305(6)	2.312(6)	2.298(16)	2	3.75(4)	2.50(2)
	3	21.10(40)	3.884(35)	3.887(36)	3.774(7)	3	21.50(40)	3.924(10)	3.927(11)	3.778(20)	3	8.75(4)	3.80(2)
	4		4.186(50)	4.401(20)	4.339(50)	4		4.478(10)	4.476(11)	4.406(10)	4	13.00(3)	4.46(2)

Table 4.9: Bond distances $r_{\alpha\beta}$ and coordination numbers $\bar{n}_{\alpha}^{\beta}$ for ice-Ih at 123 K and 15 K from the $g_{\alpha\beta}(r)$ function calculated from two different sets of total structure factors. Set A combines the total structure factors for bH0, bH2 and bH5, and set B combines the total structure factors for bH1, bH4 and bH6. In the case of two overlapping peaks (for example, peaks 4 and 5 in $g_{\mathrm{OO}}(r)$), the coordination number was calculated by integrating over both peaks and is thus the sum of two individual coordination numbers. The peaks are labelled in figure 4-16.

	Set A at 123 K			Set B at 123 K			Set A at 15 K			Set B at 15 K		
		$\bar{n}_{\alpha}^{\beta}$	$r_{\alpha\beta}$/Å		$\bar{n}_{\alpha}^{\beta}$	$r_{\alpha\beta}$/Å		$\bar{n}_{\alpha}^{\beta}$	$r_{\alpha\beta}$/Å		$\bar{n}_{\alpha}^{\beta}$	$r_{\alpha\beta}$/Å
$\alpha\beta = \mathrm{OO}$												
	1	4.00(3)	2.742(3)	1	3.99(3)	2.739(3)	1	3.98(3)	2.740(2)	1	4.03(3)	2.746(2)
	2	13.04(4)	4.503(2)	2	13.03(4)	4.504(2)	2	13.09(10)	4.497(2)	2	12.85(10)	4.500(2)
	3	9.96(4)	5.275(4)	3	9.97(4)	5.274(4)	3	10.04(6)	5.262(3)	3	10.02(6)	5.264(3)
	4	23.03(30)	6.406(20)	4	22.75(30)	6.405(20)	4	22.96(20)	6.381(3)	4	23.02(20)	6.382(3)
	5		6.919(10)	5		6.920(10)	5		6.923(3)	5		6.921(3)
$\alpha\beta = \mathrm{OH}$												
	1	2.07(3)	0.964(3)	1	2.03(3)	0.958(3)	1	2.00(2)	0.971(12)	1	2.01(2)	0.968(12)
	2	2.02(3)	1.775(3)	2	2.04(3)	1.779(3)	2	2.07(2)	1.797(16)	2	2.06(2)	1.810(16)
	3	12.31(30)	3.225(6)	3	11.96(30)	3.222(6)	3	11.88(20)	2.226(6)	3	12.03(20)	3.227(6)
	4		3.710(20)	4		3.711(20)	4		3.735(7)	4		3.730(7)
$\alpha\beta = \mathrm{HH}$												
	1	1.01(3)	1.536(23)	1	1.06(3)	1.489(23)	1	1.08(4)	1.499(8)	1	0.99(4)	1.497(8)
	2	4.00(3)	2.291(21)	2	3.98(3)	2.308(21)	2	3.98(4)	2.300(8)	2	4.01(4)	2.303(8)
	3	21.70(40)	3.854(35)	3	20.95(40)	3.916(35)	3	21.58(40)	3.919(10)	3	20.83(40)	3.935(10)
	4		4.402(50)	4		4.235(50)	4		4.483(10)	4		4.478(10)

Table 4.10: Bond angles in ice-Ih at 123 K. The angles were calculated (i) from the peak positions $r_{\alpha\beta}$ in $g_{\alpha\beta}(r)$, (ii) from the weighted peak positions $\bar{r}_{\alpha\beta}$ in $g_{\alpha\beta}(r)$, (iii) from the peak positions $r^*_{\alpha\beta}$ in $rg_{\alpha\beta}(r)$, and (iv) from the weighted peak positions $\bar{r}^*_{\alpha\beta}$ in $rg_{\alpha\beta}(r)$. In the notation used for the angles a dotted line ($\cdots$) represents a hydrogen bond. The O-H$\cdots$O angle from $\bar{r}_{\alpha\beta}$ cannot be calculated as the sum of the first and second $\bar{r}_{\mathrm{OH}}$ distances is less than the first $\bar{r}_{\mathrm{OO}}$ distance. This bond angle is therefore assumed to be linear with a value of 180.0°.

Bond angle	$r_{\alpha\beta}$	$\bar{r}_{\alpha\beta}$	$r^*_{\alpha\beta}$	$\bar{r}^*_{\alpha\beta}$
O-O-O	110.5(1.0)°	110.2(1.0)°	110.5(1.0)°	110.8(1.0)°
H-O-H	103.8(2.7)°	108.0(2.0)°	102.9(2.6)°	107.0(2.4)°
H-O$\cdots$H	110.2(1.6)°	110.9(1.1)°	109.5(1.1)°	111.5(1.1)°
O-H$\cdots$O	177.2(2.4)°	180.0(5.0)°	168.3(5.0)°	170.3(4.0)°

Table 4.11: Bond angles in ice-Ih at 15 K. The angles were calculated (i) from the peak positions $r_{\alpha\beta}$ in $g_{\alpha\beta}(r)$, (ii) from the weighted peak positions $\bar{r}_{\alpha\beta}$ in $g_{\alpha\beta}(r)$, (iii) from the peak positions $r^*_{\alpha\beta}$ in $rg_{\alpha\beta}(r)$, and (iv) from the weighted peak positions $\bar{r}^*_{\alpha\beta}$ in $rg_{\alpha\beta}(r)$. In the notation used for the angles a dotted line ($\cdots$) represents a hydrogen bond.

Bond angle	$r_{\alpha\beta}$	$\bar{r}_{\alpha\beta}$	$r^*_{\alpha\beta}$	$\bar{r}^*_{\alpha\beta}$
O-O-O	110.3(1.0)°	110.4(1.0)°	110.3(1.0)°	110.7(1.0)°
H-O-H	102.3(2.5)°	105.4(2.0)°	101.5(2.3)°	105.5(2.4)°
H-O$\cdots$H	109.3(1.9)°	110.7(0.9)°	108.9(1.9)°	111.3(1.0)°
O-H$\cdots$O	160.1(4.4)°	176.0(1.4)°	161.6(8.0)°	172.7(4.0)°

Table 4.12: Bond angles in water at 298 K [15]. The angles were calculated (i) from the peak positions $r_{\alpha\beta}$ in $g_{\alpha\beta}(r)$, (ii) from the weighted peak positions $\bar{r}_{\alpha\beta}$ in $g_{\alpha\beta}(r)$, (iii) from the peak positions $r^*_{\alpha\beta}$ in $rg_{\alpha\beta}(r)$, and (iv) from the weighted peak positions $\bar{r}^*_{\alpha\beta}$ in $rg_{\alpha\beta}(r)$. In the notation used for the angles a dotted line ($\cdots$) represents a hydrogen bond.

Bond angle	$r_{\alpha\beta}$	$\bar{r}_{\alpha\beta}$	$r^*_{\alpha\beta}$	$\bar{r}^*_{\alpha\beta}$
H-O-H	106.2(7)°	107.4(7)°	105.6(6)°	107.5(6)°
H-O$\cdots$H	114.8(2.0)°	115.9(2.0)°	115.9(2.0)°	115.3(2.0)°
O-H$\cdots$O	180.0(5.0)°	161.0(5.0)°	180.0(5.0)°	154.8(5.0)°

Table 4.13: Bond angles in LDA ice at 20 K [15]. The angles were calculated (i) from the peak positions $r_{\alpha\beta}$ in $g_{\alpha\beta}(r)$, and (ii) from the peak positions $r^*_{\alpha\beta}$ in $rg_{\alpha\beta}(r)$, (iii) from the peak positions $r^*_{\alpha\beta}$ in $rg_{\alpha\beta}(r)$, and (iv) from the weighted peak positions $\bar{r}^*_{\alpha\beta}$ in $rg_{\alpha\beta}(r)$. In the notation used for the angles a dotted line $(\cdots)$ represents a hydrogen bond.

Bond angle	$r_{\alpha\beta}$	$\bar{r}_{\alpha\beta}$	$r^*_{\alpha\beta}$	$\bar{r}^*_{\alpha\beta}$
O-O-O	108.2(1.9)°	1.08.9(1.9)°	109.0(1.9)°	109.6(1.9)°
H-O-H	108.2(2.1)°	107.0(2.1)°	109.1(2.9)°	108.5(2.1)°
H-O$\cdots$H	114.4(1.0)°	114.0(1.0)°	119.1(2.0)°	119.1(2.0)°
O-H$\cdots$O	180.0(2.5)°	180.0(2.5)°	180.0(2.5)°	170.8(3.0)°

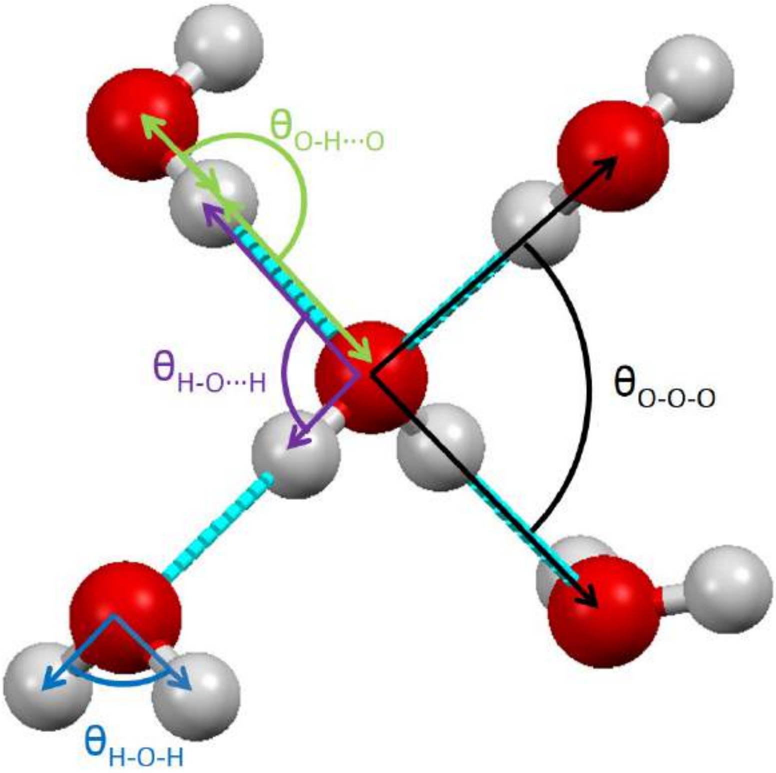

Figure 4-21: Diagram showing the bond angles in ice-Ih that were calculated using the cosine rule, as given in tables 4.10 and 4.11. Red spheres denote oxygen atoms, white spheres denote hydrogen atoms and the cyan dashed lines represent the hydrogen bonds.

4.4.5 Bhatia - Thornton partial structure factors

Figure 4-22 shows the Bhatia -Thornton partial structure factors for ice-Ih at 123 K and at 15 K. The Fourier transforms of these partial structure factors give the Bhatia-Thornton partial pair-distribution functions $g_{\alpha\beta}^{\mathrm{BT}}(r)$, as shown in figure 4-23. The first peak in the number-number partial pair-distribution function $g_{\mathrm{NN}}^{\mathrm{BT}}(r)$ corresponds to the intra-molecular oxygen-hydrogen bond, and has a peak position of 0.970(3) Å at 15 K and 0.979(3) Å at 123 K. This assignment is supported by the concentration-concentration partial pair-distribution function $g_{\mathrm{CC}}^{\mathrm{BT}}(r)$ which has a negative peak at the same position, confirming that this atomic correlation corresponds to bonds between unlike chemical species.

Once the Bhatia - Thornton structure factors have been calculated, the self consistency of the data can be verified. The partial structure factors must obey the relation:

$$S_{\mathrm{NN}}^{\mathrm{BT}}(Q) \cdot S_{\mathrm{CC}}^{\mathrm{BT}}(Q) \geq \left(S_{\mathrm{NC}}^{\mathrm{BT}}(Q) \right)^2 \tag{4.23}$$

which is equivalent to checking that the scattered intensity is non-negative at all scattering vectors. As shown in figure 4-24, this inequality is not fulfilled within the experimental uncertainty at low Q-values, due to problems in accurately correcting for stepping in the background at small scattering angles, as discussed in section 4.3.3. A small negative deviation in the $S_{\mathrm{CC}}^{\mathrm{BT}}(Q)$ function at low-Q, which results from a small error in correcting for the stepping, leads to a change in sign for the product $S_{\mathrm{NN}}^{\mathrm{BT}}(Q) \cdot S_{\mathrm{CC}}^{\mathrm{BT}}(Q)$. Here the inequality of equation 4.23 is not fulfilled at the lowest Q-values.

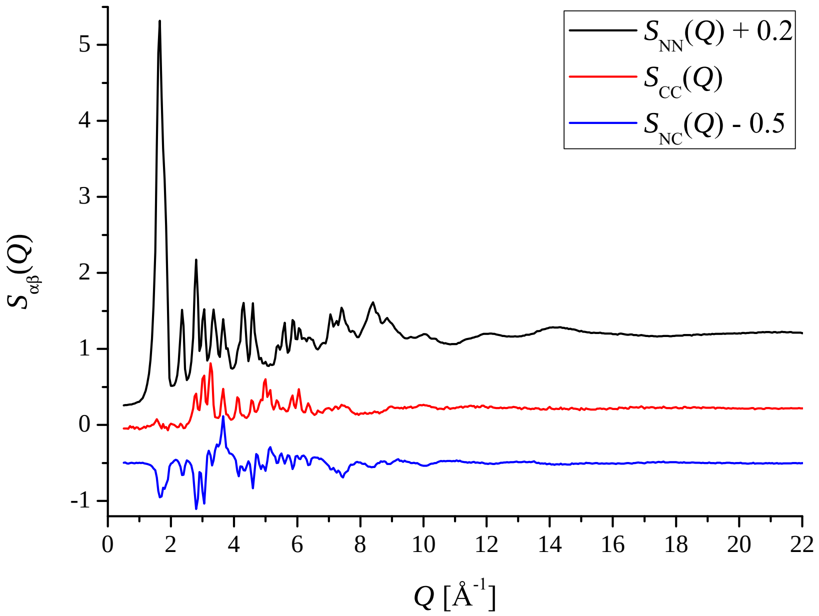

(a) 123 K

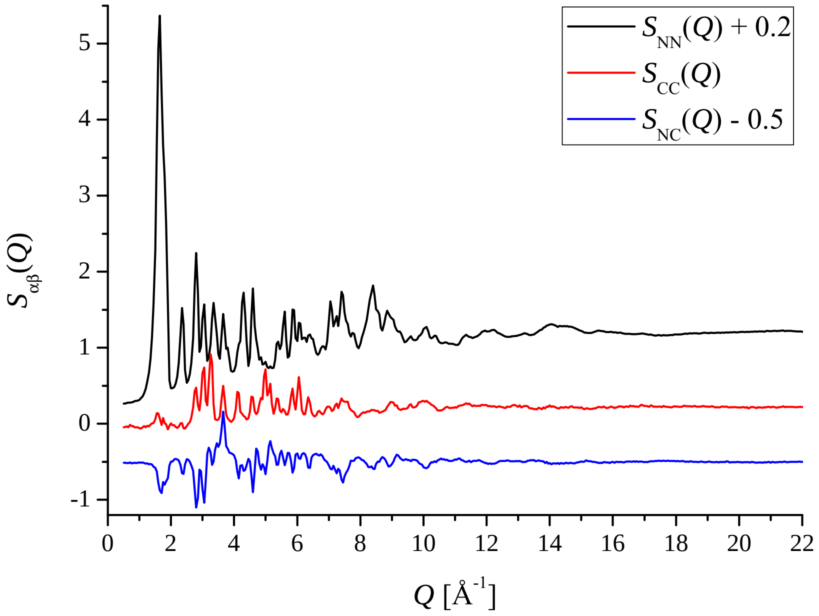

(b) 15 K

Figure 4-22: The Bhatia-Thornton partial structure factors for ice-Ih at (a) 123 K and (b) 15 K offset vertically for clarity of presentation. The vertical error bars are smaller than the line thickness.

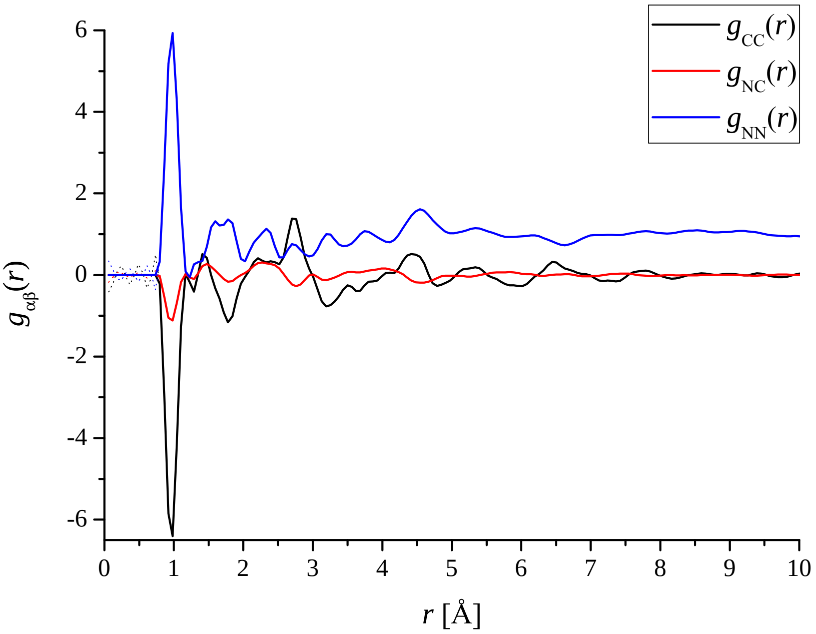

(a) 123 K

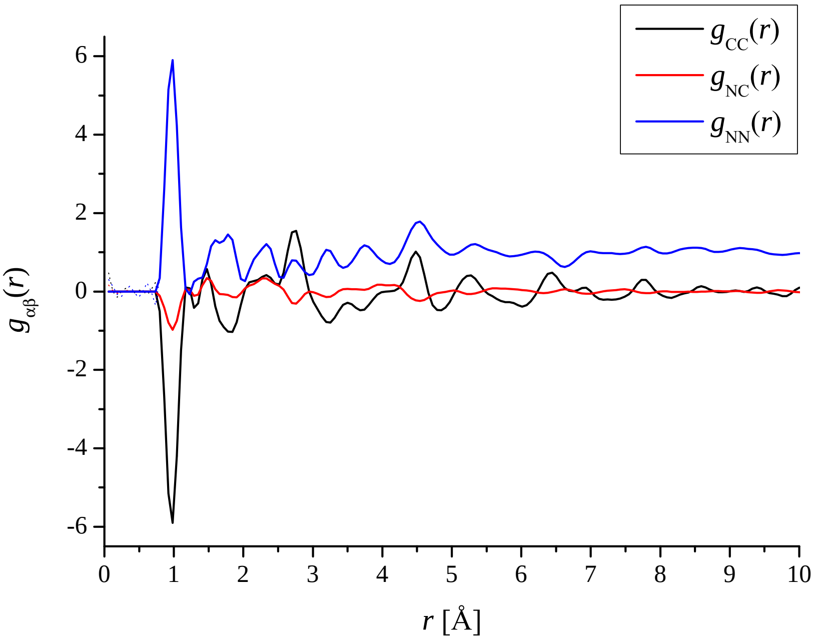

(b) 15 K

Figure 4-23: The Bhatia-Thornton partial pair-distribution functions for ice-Ih at (a) 123 K and (b) 15 K. The data sets were obtained by Fourier transforming the Faber-Ziman partial structure factors $S^{\mathrm{BT}}_{\alpha\beta}(Q)$ shown in figure 4-22. The solid lines show the functions after the low-r oscillations (dotted lines) have been set to their theoretical $g_{\alpha\beta}(r \to 0) = 0$ limit. The curves have been offset vertically for clarity of presentation.

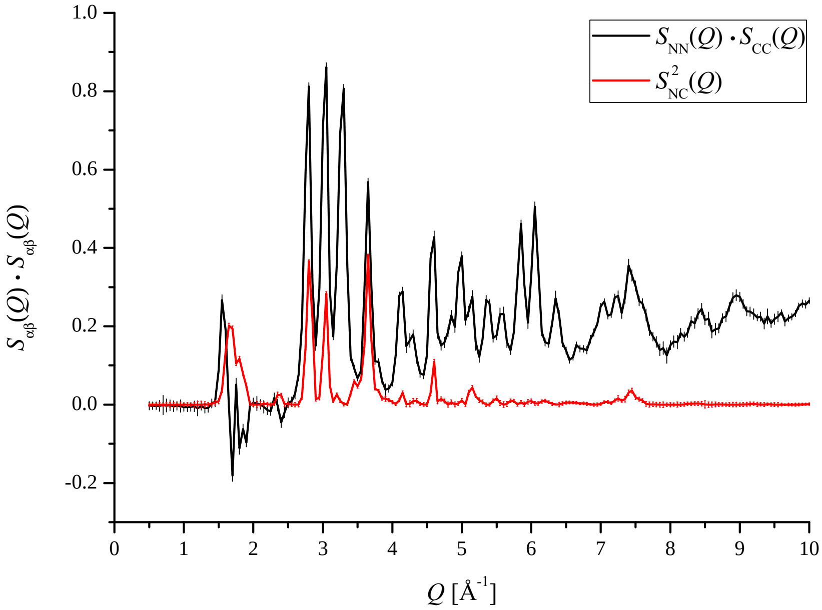

(a) 123 K

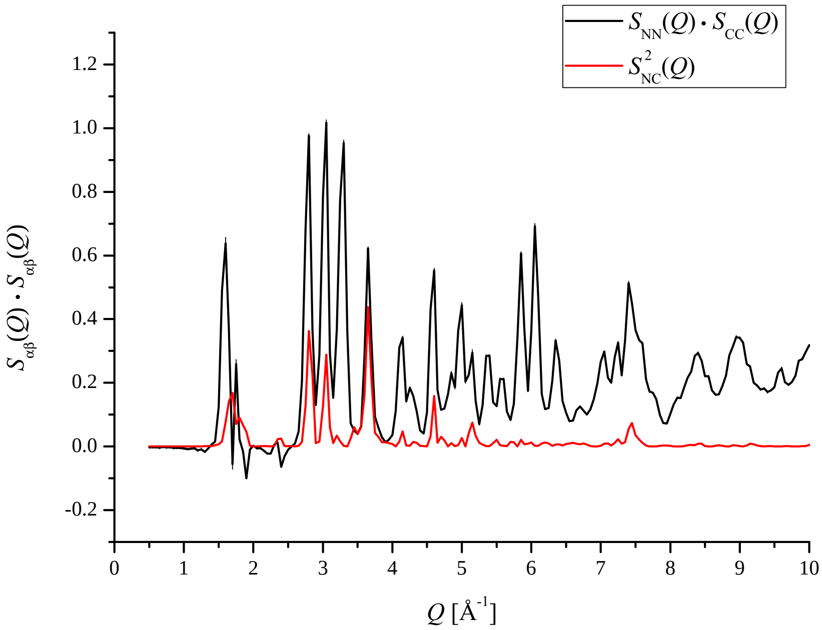

(b) 15 K

Figure 4-24: Self-consistency check using the Bhatia-Thornton partial structure factors for ice-Ih at (a) 123 K and (b) 15 K. The black curve shows the product of $S_{\mathrm{NN}}^{\mathrm{BT}}(Q)$ and $S_{\mathrm{CC}}^{\mathrm{BT}}(Q)$, and the red curve shows $(S_{\mathrm{NC}}^{\mathrm{BT}}(Q))^2$. The vertical error bars are smaller than the line thickness at most Q-values.

4.5 Discussion

The oxygen atoms in ice-Ih form the basic structure of the crystal lattice, and the time and space average positions of the oxygen atoms show translational periodicity, as expected for a crystal. As Kuhs and Lehmann showed [56], however, there exists a small component of oxygen disorder due to both thermal effects and static disorder. Figure 4-19 shows this in the broadening of the O-O peaks in the $g_{\mathrm{OO}}(r)$ functions at 123 K and 15 K. Recent measurements of the ice-Ih lattice parameters as a function of temperature [63] have shown that the c/a ratio remains constant with temperature, and thus the thermal expansion is isotropic. Therefore it is possible to take into account both the thermal effects and small amount of oxygen disorder in crystallographic experiments [12]. As a result the O-O peak positions and coordination numbers from the PDF analysis should be in agreement with those from crystallography, as given in table 4.8.

The values of the O-O coordination numbers are given in table 4.8. The first O-O peaks in both ${}^{\mathrm{bH0}}G(r)$ and $g_{\mathrm{OO}}(r)$ give a coordination number of 4 within the experimental error, which is consistent with a local tetrahedral structure for ice-Ih. The coordination number for the second O-O peak in both ${}^{\mathrm{bH0}}G(r)$ and $g_{\mathrm{OO}}(r)$ is 13, which is also consistent with crystallographic data where the 13th oxygen atom is located parallel to the c-axis in the opposite direction to the hydrogen bond. However as seen in table 4.8, the third O-O peak in ${}^{\mathrm{bH0}}G(r)$ or $g_{\mathrm{OO}}(r)$ gives a coordination number of 10.03(3) or 10.04(3), respectively, at both 15 K and 123 K, whereas the crystallographic data finds a coordination number of 9.00(1). The fourth and fifth peaks in $g_{\mathrm{OO}}(r)$ give a combined coordination number of 22.77(4) at 123 K and 22.96(4) at 15 K, which is closer to the expected value of 23 from crystallography, corresponding to 12 oxygen atoms in the fourth shell and 11 oxygen atoms in the fifth. The peak position and coordination numbers for the sixth peak and all subsequent peaks out to 10 Å can be calculated from the crystallographic data, and have been used in fits to the $D_{\mathrm{OO}}(r)$ functions that are shown in figure 4-25. All of the O-O peak positions in $rg_{\mathrm{OO}}(r)$ agree with the peak positions from crystallography within the error.

Figure 4-18 shows that the $g_{\mathrm{OO}}(r)$ functions calculated from the SVD analysis and from two sets of three total structure factors all agree within the experimental error. All of the $g_{\mathrm{OO}}(r)$ functions give self-consistent coordination numbers and peak positions as shown in tables 4.8 and 4.9, indicating that the third O-O peak having a coordination number of 10.04(3) is not simply an artefact of the singular value decomposition analysis.

Figure 4-25b shows the 15 K dataset for the oxygen-oxygen density correlation function $D_{\mathrm{OO}}(r)$, as defined previously in section 4.2. Each peak has been fitted with a Gaussian function (or several if required), such that the sum over the peaks

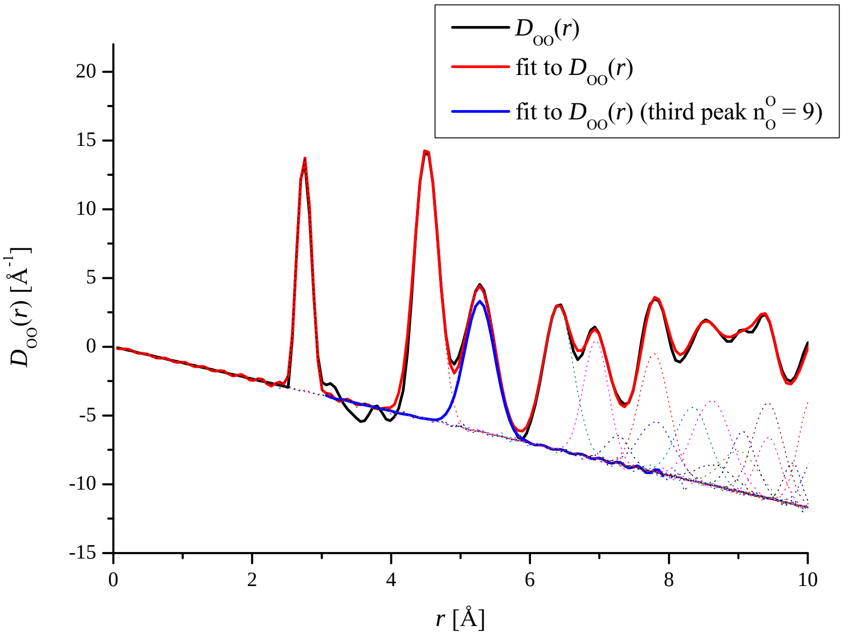

(a) 123 K

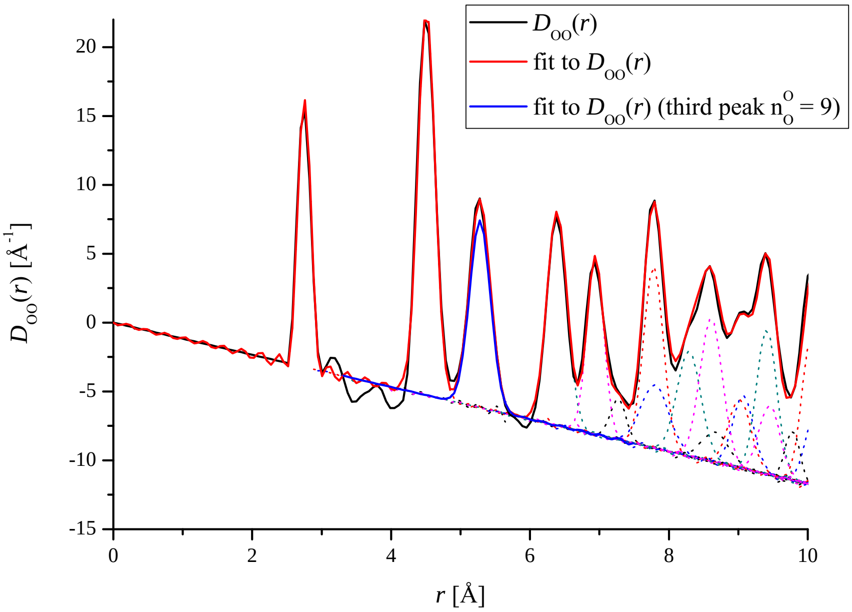

(b) 15 K

Figure 4-25: The density correlation function $D_{\mathrm{OO}}(r)$ as defined by equation 2.44 for ice-Ih at (a) 123 K and (b) 15 K. Each peak in $D_{\mathrm{OO}}(r)$ has been fitted with a Gaussian (or several Gaussians where appropriate), as shown by the dotted curves. The red curve corresponds to $\bar{n}_{\mathrm{O}}^{\mathrm{O}} = 10$ for the third peak, and the blue peak in (b) corresponds to $\bar{n}_{\mathrm{O}}^{\mathrm{O}} = 9$. $R_\chi = 0.102023$ at 123 K and $R_\chi = 0.114332$ at 15 K, where R_χ is defined in equation 2.46.

in $rg_{\mathrm{OO}}(r)$ matches the measured dataset. The coordination numbers and peak positions in $rg_{\mathrm{OO}}(r)$ for the fitted Gaussians have been taken from the same crystallographic data given in table 4.8, except for the third peak where $\bar{n}_{\mathrm{O}}^{\mathrm{O}} = 10$. The blue curve in the figure shows what the third peak would look like if the coordination number was set to $\bar{n}_{\mathrm{O}}^{\mathrm{O}} = 9$, as given by the crystallographic data. The same procedure was applied to the 123 K dataset and the results are shown in figure 4-25a, where the coordination number for the third peak is also $\bar{n}_{\mathrm{O}}^{\mathrm{O}} = 10$. The fit to this dataset is slightly worse, as can be seen in the overlap region between peaks, which suggests that the peaks in $D_{\mathrm{fit}}(r)$ are not Gaussian functions. Peaks 2 and 3 for the 123 K data appear to be asymmetric, as indicated by the data in table 4.8, where the weighted O-O peak positions $\bar{r}_{\mathrm{OO}}$ are larger than the peak maximum positions r_{OO}. Currently I cannot offer an explanation for this discrepancy in coordination number for the third O-O peak, as the coordination numbers for subsequent peaks (4, 5 and 6) in both ${}^{\mathrm{bH0}}G(r)$ and $g_{\mathrm{OO}}(r)$ do agree with the published data.

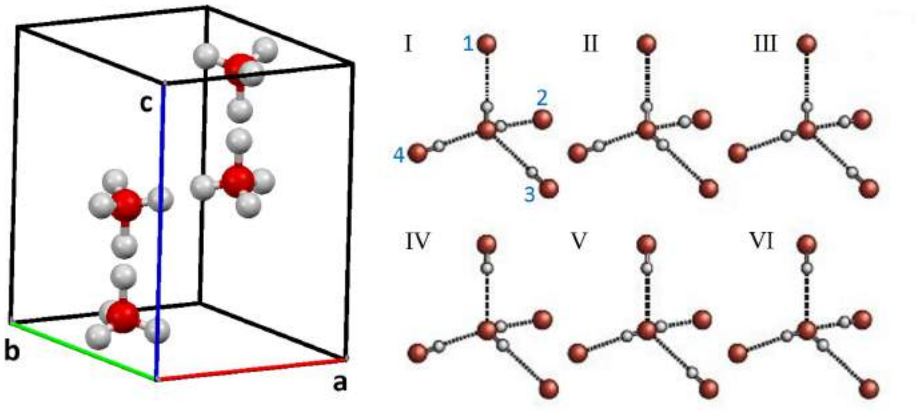

(a) (b)

Figure 4-26: (a) The average atomic positions within the hexagonal unit cell for ice-Ih assuming 50 % occupancy of the hydrogen sites (half-hydrogen model). The lattice parameters $a = b \neq c$. Red spheres denote oxygen atoms, and white spheres denote hydrogen atoms. The lattice parameters and unit cell volume are given by Röttger et al [63]. (b) The six possible configurations of the half hydrogen model allowed by the Bernal-Fowler rules, labelled I to VI in Roman numerals. Hydrogen bonds are shown by the broken curves.

The hexagonal unit cell for ice-Ih is shown in figure 4-26a which illustrates the time and space averaged local structure of the water molecules within ice-Ih. The crystallographic data assumes Pauling's half-hydrogen model and thus each of the hydrogen positions that are shown are only considered to be 50% occupied. Another method of thinking of the system is given in Figure 4-26b where six possible configurations of the local structure in ice-Ih are shown. Each configuration satisfies the Bernal-Fowler rules and is labelled I to VI in Roman numerals. in the case of I the central water molecule is oriented such that the hydrogen atoms associated with H are pointing in the direction of the oxygen atoms labelled 1 and 2, whereas the hydrogen bonds associated with O point in the direction of the oxygen atoms labelled 3 and 4. In the other five configurations II- VI, the central water molecule changes orientation such that the hydrogen bonds associated with the H of the central water molecule point to each of the other oxygen atoms (1-4) in turn.

Figure 4-20 compares histograms of the crystallographic data, given in table 4.8, with the radial pair-distribution functions. There is qualitatively good agreement between the two data sets. The only exception to this is the first bar in the H-H histogram (indicated by the black arrow) which is an artefact of the half hydrogen model, as it corresponds to the distance between two possible hydrogen sites within a single hydrogen bond. The Bernal-Fowler rules state that there is one (and only one) hydrogen atom located between two neighbouring oxygen atoms.

Table 4.8 compares the H-H peak positions and coordination numbers with those obtained from a crystallographic analysis. It is difficult to get reliable hydrogen positions from crystallographic data due to the disorder in ice-Ih, so here the peak positions and coordination numbers from the PDF analysis help to clarify the nature of the H-H correlations in ice-Ih. The intra-molecular H-H peak position of 1.512(23) Å at 123 K and 1.503(8) Å at 15 K from the PDF analysis are a lot shorter than the value of 1.59(2) Å that is found using crystallography, although they are in agreement with the value of 1.52(3) Å found for water at 298 K [15]. The reason for this can be seen in figure 4-16 which shows that the intra-molecular H-H peak is asymmetric with a large high-r tail. In this case the weighted peak positions $\bar{r}_{\mathrm{OH}}$ from table 4.8, are in better agreement with the crystallographic value. This asymmetry of the intra-molecular H-H peak is also seen in the first-difference functions in figure 4-13, and is reflected by the H-H peak positions in tables 4.7 and 4.6. Figure 4-19 shows that the asymmetry of the intra-molecular H-H peak occurs at both temperatures, and that its position and height does not change. Attempts to smooth out the low-r region of the $g_{\mathrm{HH}}(r)$ functions, by Fourier transforming a Harwell spline fit to the $S_{\mathrm{HH}}(Q)$ functions, did not remove the asymmetry of the first H-H peak but did smooth out the high-r shoulder of the H-H peak at 15 K suggesting that the peak asymmetry is not an artefact of the Fourier transformation process. The similarity of the $g_{\mathrm{HH}}(r)$ functions at 15 K and 123 K indicates that the proton disorder does not change appreciably with temperature.

The intra-molecular O-H peak positions calculated from the $g_{\mathrm{OH}}(r)$ functions of 0.961(3) Å at 123 K and 0.965(12) Å at 15 K (table 4.8), are considerably shorter than the value of 0.987(5) Å obtained from a combination of crystallographic, NMR and spectroscopic data [12]. Figure 4-19 compares the $g_{\mathrm{OH}}(r)$ functions at 123 K and 15 K, and shows that there is no change in peak position or height between the two temperatures. The intra-molecular O-H peak can also be obtained from the first difference functions $\Delta G_{\mathrm{no\ OO}}(r)$ and $\Delta G_{\mathrm{no\ HH}}(r)$, and their peak positions are summarised in tables 4.7 and 4.6.

To compare the the O-H correlations from $\Delta G_{\mathrm{no\ OO}}(r)$ and $\Delta G_{\mathrm{no\ HH}}(r)$ with $g_{\mathrm{OH}}(r)$, it is convenient to renormalise $\Delta G_{\mathrm{no\ OO}}(r)$ and $\Delta G_{\mathrm{no\ HH}}(r)$. Let us consider the difference function $\Delta G_{\mathrm{no\ HH}}(r)$ calculated from the total pair-distribution functions labelled ${}^{\mathrm{bHX}}G(r)$ and ${}^{\mathrm{bHY}}G(r)$. Then equation 4.18 can be rearranged to give the expression:

$$\begin{aligned}
{}^{\mathrm{bHX-bHY}}\Delta G'(r)_{\mathrm{no\ HH}} &= \frac{{}^{\mathrm{bHX-bHY}}\Delta G_{\mathrm{no\ HH}}(r) - {}^{\mathrm{bHX-bHY}}\,\Delta G_{\mathrm{no\ HH}}(r \to 0)}{2c_{\mathrm{O}}c_{\mathrm{H}}b_{\mathrm{O}}\left(\frac{b_{\mathrm{HY}}^2}{b_{\mathrm{HX}}} - b_{\mathrm{HY}}\right)} \\
&= g_{\mathrm{OH}}(r) + \frac{c_{\mathrm{O}}b_{\mathrm{O}}\left(\frac{b_{\mathrm{HY}}^2}{b_{\mathrm{HX}}^2} - 1\right)}{2c_{\mathrm{H}}\left(\frac{b_{\mathrm{HY}}^2}{b_{\mathrm{HX}}} - b_{\mathrm{HY}}\right)} g_{\mathrm{OO}}(r). \qquad (4.24)
\end{aligned}$$

These renormalised functions are shown in figure 4-27. A similar normalisation procedure can be applied to equation 4.16 that defines $\Delta G_{\mathrm{no\ OO}}(r)$ such that

$$\begin{aligned}
{}^{\mathrm{bHY-bHX}}\Delta G'(r)_{\mathrm{no\ OO}} &= \frac{{}^{\mathrm{bHY-bHX}}\Delta G_{\mathrm{no\ OO}}(r) - {}^{\mathrm{bHY-bHX}}\,\Delta G_{\mathrm{no\ OO}}(r \to 0)}{2c_{\mathrm{O}}c_{\mathrm{H}}b_{\mathrm{O}}(b_{\mathrm{HY}} - b_{\mathrm{HX}})} \\
&= g_{\mathrm{OH}}(r) + \frac{c_{\mathrm{H}}(b_{\mathrm{HY}}^2 - b_{\mathrm{HX}}^2)}{2c_{\mathrm{O}}b_{\mathrm{O}}(b_{\mathrm{HY}} - b_{\mathrm{HX}})} g_{\mathrm{HH}}(r), \qquad (4.25)
\end{aligned}$$

and the results are shown in figure 4-28. Figures 4-27 and 4-28 compare the first peaks in $g_{\mathrm{OH}}(r)$ thus obtained at 15 K. As discussed below, the peak position in $g_{\mathrm{OH}}(r)$ from the SVD analysis is at a shorter distance as compared to the first peak in $\Delta G'(r)_{\mathrm{no\ HH}}$, but agrees with the first peak in $\Delta G'(r)_{\mathrm{no\ OO}}$.

At 15 K there is a change in the first $\langle r_{\mathrm{OH}} \rangle$ peak position from 0.968(3) Å for $\Delta G_{\mathrm{no\ OO}}(r)$ to 0.981(3) Å for $\Delta G_{\mathrm{no\ HH}}(r)$. However at 123 K there is not a significant difference in $\langle r_{\mathrm{OH}} \rangle$ values, and the two difference functions give the same value of 0.967(4) Å within the experimental error. The change in the first O-H peak position between the $\Delta G_{\mathrm{no\ OO}}(r)$ and $g_{\mathrm{OH}}(r)$ functions and $\Delta G_{\mathrm{no\ HH}}(r)$ function may be due to the inelasticity corrections that are made to the data. It is possible that for the $\Delta G_{\mathrm{no\ HH}}(r)$ difference function at 15 K, there is better cancellation of the residual $P_{\mathrm{distinct}}(Q)$ scattering terms associated with the hydrogen. At higher temperatures the inelasticity terms do not cancel so well. According to Powles [64, 65] when interference

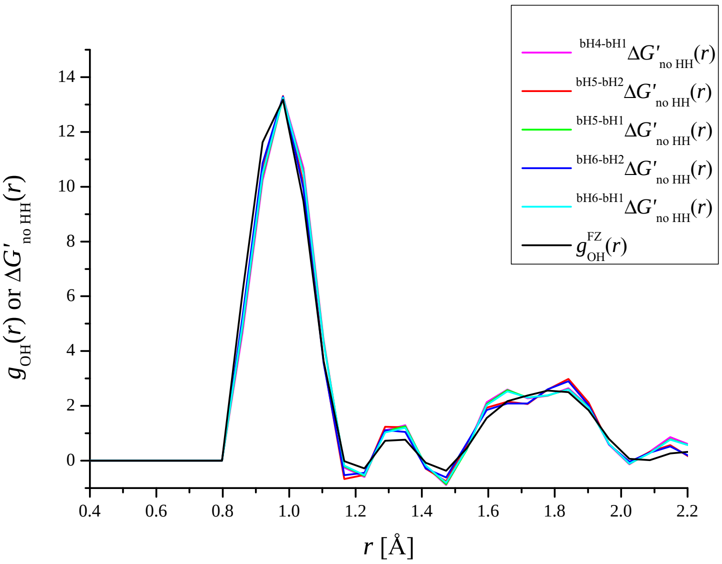

Figure 4-27: Normalised first-order difference pair-distribution functions ${}^{\text{bHX}-\text{bHY}}\Delta G'(r)_{\text{no HH}}$ compared with the SVD oxygen-hydrogen partial pair-correlation function $g_{\text{OH}}(r)$ at 15 K. The low-r oscillations have been set to their theoretical ${}^{\text{bHX}-\text{bHY}}\Delta G'(r \to 0)_{\text{no HH}}$ or $g_{\text{OH}}(r \to 0) = 0$ limit.

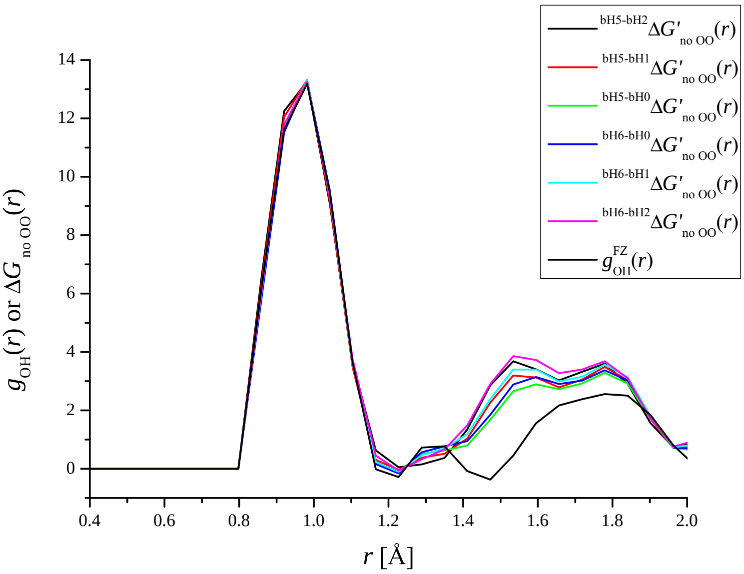

Figure 4-28: Normalised first-order difference pair-distribution functions ${}^{\text{bHX}-\text{bHY}}\Delta G'(r)_{\text{no OO}}$ compared with the SVD oxygen-hydrogen partial pair-correlation function $g_{\text{OH}}(r)$ at 15 K. The low-r oscillations have been set to their theoretical ${}^{\text{bHX}-\text{bHY}}\Delta G'(r \to 0)_{\text{no OO}}$ or $g_{\text{OH}}(r \to 0) = 0$ limit.

terms are taken into account in the inelasticity correction, the apparent r_{OD} distance in water increases by $\simeq$0.009 Å. A previous PDF study on deuterated ice [66] suggested that this correction may also be applicable to disordered ice-Ih. The $\langle r_{\mathrm{OH}} \rangle$ peak position of 0.981(3) Å from the $\Delta G_{\mathrm{no\ HH}}(r)$ difference function is likely to be the most accurate value from the PDF analysis. It also agrees within the experimental error with the intra-molecular O-H and O-D peak positions of 0.987(5) Å and 0.983(5) Å obtained from a combination of crystallographic, NMR and spectroscopic data [12].

The $\Delta G'(r)_{\mathrm{no\ HH}}$ function can also be used to compare the first inter-molecular O-H peak in $\Delta G_{\mathrm{no\ HH}}(r)$ with $g_{\mathrm{OH}}(r)$. This peak is very broad when compared to the intra-molecular O-H peak, and it is also asymmetric. This asymmetry can be seen in the difference between the r_{OH} and $\bar{r}_{\mathrm{OH}}$ peak positions given in tables 4.6 and 4.8. In figure 4-27 the inter-molecular O-H peak in several of the $\Delta G'(r)_{\mathrm{no\ HH}}$ difference functions appears to be a double peak, although this could be an artefact of the Fourier transform procedure. Nevertheless, all of the results are consistent with a range of inter-molecular hydrogen bond lengths. The $g_{\mathrm{OH}}(r)$ functions were also calculated by Fourier transforming a Harwell spline fit to the $S_{\mathrm{OH}}(Q)$ functions with and without a Lorch modification function, in order to reduce the effect of statistical noise. These procedures did not, however, alter the $g_{\mathrm{OH}}(r)$ functions, indicating that the asymmetry of the first inter-molecular O-H peak is not an artefact of the Fourier transformation procedure.

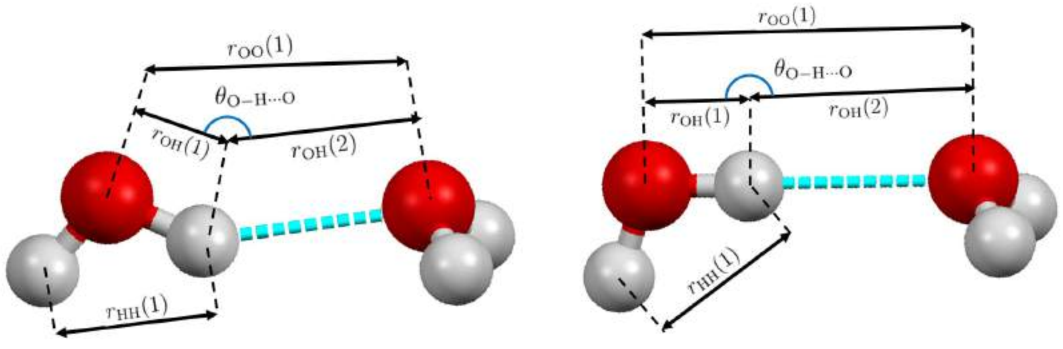

(a) Bent hydrogen bond geometry. (b) Linear hydrogen bond geometry.

Figure 4-29: Representation of bent and linear hydrogen bond geometries between two water molecules in ice-Ih. Red spheres represent oxygen atoms and white spheres represents hydrogen atoms. Intra-molecular and inter-molecular distances are shown by the black arrows, and the hydrogen bond is represented by a cyan dashed line.

Figure 4-29 shows the local geometry of the water molecules in ice-Ih for bent and linear hydrogen bonds. In the case of a linear hydrogen bond, the sum of the intra-molecular O-H and first inter-molecular O-H bond distances must be equal to the first

O-O bond distance, as seen in figure 4-29b. In the case where the hydrogen bond is bent (figure 4-29a), the sum of the intra-molecular and first inter-molecular O-H bond distances will be less than the first O-O bond distance.

There has been much debate about the angle of the hydrogen bond $\theta_{\mathrm{O-H\cdots O}}$ (see section 4.1) and whether it is linear or bent [12]. Nuclear quadrupole resonance experiments indicate a linear hydrogen bond, as they lead to a calculated inter-molecular O$\cdots$D distance of 1.80 Å [12, 67]. This value should be compared with the inter-molecular O$\cdots$D distance of 1.751(4) Å obtained from neutron crystallography [12], which suggests that the hydrogen bond is bent. The values from the PDF analysis are given in table 4.8 and show an O-H distance r_{OH} at 123 K of 1.778(3) Å and a O-H distance r_{OH} of 1.798(16) Å at 15 K.

The bond angles calculated using the cosine rule are given in tables 4.10 and 4.11. The results suggest that the hydrogen bond has an angle of 160.1(4.4)° at 15 K and 177.2(2.4)° at 123 K. A hydrogen bond angle of 162.4(2.0)° is calculated by using the cosine rule with the bond distances taken from neutron crystallography [12]. However if the longer O$\cdots$D distance from NQR [12, 67] experiments is used with the intra-molecular O-D and first O-O distances from crystallography, then the hydrogen bond angle is calculated to be 180.0°. The PDF analysis shows a distribution of bond lengths because the peaks in $g_{\alpha\beta}(r)$ have a finite width.

The O-O-O angle is calculated to be 110.5(1.0)° at 123 K and 110.3(1.0)° at 15 K using the r_{OO} distances taken from $g_{\mathrm{OO}}(r)$, which is larger than the value of 109.5° expected for perfect tetrahedra, suggesting a slight distortion of the tetrahedra. The values of the O-O-O bond angle calculated from $r_{\alpha\beta}$, $\bar{r}_{\alpha\beta}$, $r^*_{\alpha\beta}$ or $\bar{r}^*_{\alpha\beta}$ at 123 K and 15 K are all self-consistent giving the same value of 110.5(1.0)° within the random error.

The intra-molecular H-O-H bond angle of 103.8(2.7)° at 123 K and 102.3(2.5°) at 15 K using the $r_{\alpha\beta}$ peak positions, as given in tables 4.10 and 4.11 is smaller than the value of 104.5(4)° calculated for gaseous water vapour [12, 68, 69]. The H-OH bond angle of 104.5(4)° for gaseous water vapour was calculated from a thermal average value of instantaneous internuclear distances from gas electron diffraction, and this calculation is outlined in reference [68]. This result for the intra-molecular H-H and O-H distances that are too small due to an inability to fully correct for the inelasticity corrections [66]. The peak positions from crystallographic analysis [12] combined with spectroscopic and NMR data found an intra-molecular H-O-H angle of 107.3(1.6)° [50]. The H-O-H angle calculated from the intra-molecular weighted peak positions $\bar{r}_{\mathrm{OH}}$ and $\bar{r}_{\mathrm{HH}}$ is 108.0(2.0)° at 123 K and 105.5(2.4) at 15 K, which agrees with this result within the random error. As the intra-molecular H-H peak is asymmetric, the bond angle calculated from the weighted peak positions $\bar{r}_{\alpha\beta}$ may be a more representative measure of the H-O-H bond angle as this value takes into account the shape of the peak and therefore, the distribution of bond lengths.

The H-O$\cdots$H bond angle is calculated to be 110.2(1.6)° at 123 K and 109.3(1.9)° at 15 K using the $r_{\alpha\beta}$ peak positions. This bond angle will also be influenced by the intra-molecular O-H distance being too short due to an inability to fully correct for the inelasticity corrections. But the first inter-molecular O-H peak at 123 K and 15 K is asymmetric, and this asymmetry is more apparent at the lower temperature e.g. there is a difference between the weighted peak position $\bar{r}_{\mathrm{OH}}$ = 1.768(2) Å and the peak position r_{OH} =1.798(16) Å. This would suggest that for the H-O$\cdots$H bond angle the value calculated from the weighted peak positions $\bar{r}_{\alpha\beta}$ is better representation of the crystal structure, given that it takes into account the distribution of O-H distances.

4.5.1 Comparison with amorphous ice and water

Figure 4-30 shows a comparison between the Faber Ziman partial structure factors for ice-Ih at 15 K and the low density form of amorphous (LDA) ice at 20 K [15]. The atomic number of LDA ice (ρ = 0.094(2) Å^{-3}) is almost the same as that for ice-Ih (ρ = 0.09354(4) Å^{-3} at 15 K and ρ = 0.09346(4) Å^{-3} at 123 K). The LDA ice partial structure factors are very similar to those for ice-Ih, aside from a lack of Bragg peaks. Figure 4-31 shows the corresponding real space functions for ice-Ih and LDA ice, along with those for water (ρ = 0.100(1) Å^{-3} [15]). In H/D isotope substitution experiments the intra-molecular distances are always too short due to the inelasticity corrections [66]. This can be seen in figure 4-31 in the position of the first O-H peak for ice-Ih, LDA ice and water. All of these three datasets are from neutron diffraction with H/D substitution experiments. The O-H peak for water from an oxygen-18 isotope substitution experiment is longer at 0.990(5) Å. As discussed previously, in ice-Ih at 15 K there is a change in the first O-H peak position between the $\Delta G_{\mathrm{no\ OO}}(r)$ and $g_{\mathrm{OH}}(r)$ functions and the $\Delta G_{\mathrm{no\ HH}}(r)$ function. However, for ice-Ih at 123 K this difference in O-H peak positions does not occur. For water, from neutron diffraction with H/D substitution experiments at 298 K [15] there is also no change between the first r_{OH} peak position between the $\Delta G_{\mathrm{no\ OO}}(r)$ and $\Delta G_{\mathrm{no\ HH}}(r)$ difference functions. For LDA ice at 20 K, the $\Delta G_{\mathrm{no\ HH}}(r)$ difference function was ill-constrained, so it is not possible to know if the change in O-H peak position also occurs.

The real-space peaks in LDA ice are very similar to ice-Ih, and as these two solid phases have almost the same number density, the main difference between the two structures is the lack of translational periodicity for the oxygen atoms in LDA ice. This results in the broader peaks seen in the $g_{\mathrm{OO}}(r)$ function for LDA ice after about 4 Å. However, the intra-molecular H-H peaks for LDA ice and ice-Ih have the same peak position (r_{HH} = 1.6(1) Å for LDA ice [15]) and both are asymmetric. The intra-molecular O-H peak at 20 K in LDA ice is 0.96(2) Å which agrees with the value for ice-Ih as given in table 4.8.

There is a 7% increase in number density between ice-Ih and water reflecting the change in temperature and thus structure. The first inter-molecular O-O peak is shifted to higher-r and is much broader, and there is a lack of long range order. However the intra-molecular O-H peak position for water of 0.990(5) Å [70] is similar to the O-H peak position of 0.981(3) Å calculated from $\Delta G_{\text{no HH}}(r)$. The intra-molecular H-H peak in water shows the same asymmetry as observed for ice-Ih, and has a peak position of 1.52(2) Å which agrees with the peak position for Ice-Ih, as given in table 4.8, within the experimental error.

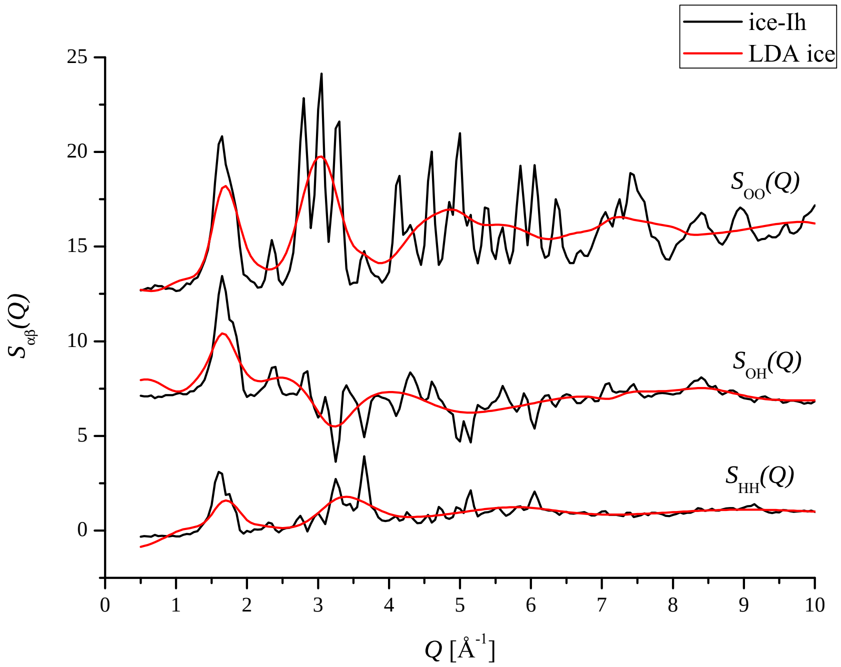

Figure 4-30: Comparison of the Faber-Ziman partial structure factors for ice-Ih at 15 K and low density amorphous ice (LDA) at 20 K. The datasets have been offset vertically for clarity of presentation.

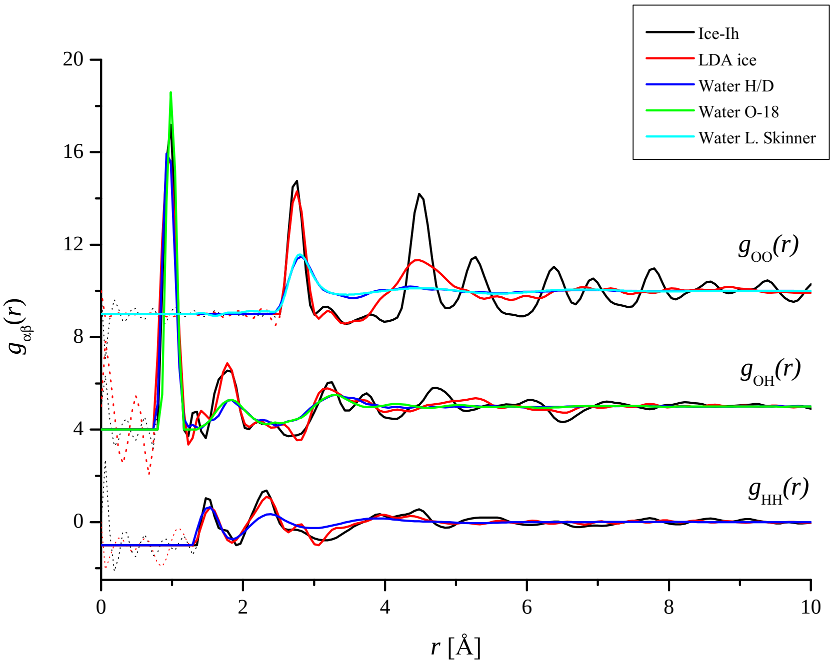

Figure 4-31: Comparison of the Faber-Ziman partial pair-distribution functions for ice-Ih at 15 K, low density amorphous ice (LDA) at 20 K, and water at 298 K from neutron diffraction with H/D substitution [15]. The O-H partial pair-distribution function for water from neutron diffraction with oxygen-18 substitution [70] is also shown, along with the oxygen-oxygen partial pair-distribution function from reference [71]. The datasets have been offset vertically for clarity of presentation.

4.6 Conclusion

The full set of partial structure factors have been measured for ice-Ih at 15 K and 123 K using the NDIS method. The first-order difference functions have also been calculated for both temperatures. The first inter-molecular O-H peak position and coordination number indicate that the water molecules in ice-Ih are hydrogen bonded to two others with a distribution of hydrogen bond lengths. The intra-molecular O-H distances of 1.778(3) Å and 1.798(16) Å at 123 K and 15 K respectively suggest that the hydrogen bond angle is bent with an angle of 160.1(4.4)° at 15 K and 177.2(2.4)° at 123 K. The intra-molecular O-H distances of 0.961(3) Å at 123 K and 0.965(12) Å at 15 K for the $g_{\mathrm{OH}}(r)$ function are considerably shorter than the published crystallographic value of 0.987(5) Å. This is probably due to residual inelasticity corrections, as the intra-molecular O-H peak position of 0.981(3) Å at 15 K from the $\Delta G_{\mathrm{no\ HH}}(r)$ difference function agrees with the crystallographic value within the random error. However this is not the case for the O-H peak position from the $\Delta G_{\mathrm{no\ HH}}(r)$ difference function at 123 K, or for the water data from the neutron diffraction with H/D substitution experiment presented in section 4.5.1 at 298 K.

The O-O correlations from the PDF analysis give peak positions and coordination numbers that are in agreement with those found for crystallographic data out to ∼10 Å, with the exception of the third peak where the PDF analysis gives $\bar{n}_{\mathrm{O}}^{\mathrm{O}} = 10$ as compared to the crystallographic value of $\bar{n}_{\mathrm{O}}^{\mathrm{O}} = 9$. The O-O-O angle is 110.5(1.0)° suggesting slightly distorted tetrahedra. The first H-H peak is asymmetric at both 15 K and 123 K indicating that the asymmetry is not due to thermal disorder and may be due to an intrinsic property of the water molecule in ice-Ih.

5. The structure of glassy GeSe_3 and GeSe_4

5.1 Introduction

GeSe_3 and GeSe_4 are in the $\mathrm{Ge}_x\mathrm{Se}_{1-x}$ $(0 \leq x \leq 1)$ network glass-forming system, which has often been the focus of interest as it is a major component in many materials having semiconducting, opto-electronic, infrared-optical, and acousto-optical applications [5, 6, 72–74]. The $\mathrm{Ge}_x\mathrm{Se}_{1-x}$ system also has a large glass-forming region covering the range $0 \leq x \leq 0.43$, where the connectivity and resultant network properties can be manipulated by altering the Ge:Se ratio. As a result the Ge-Se system is considered to be a prototypical network forming system, and investigations of this system aid in understanding the atomic-scale structural organisation of covalently bonded glassy materials.

On the basis of mean field constraint theory the network of $\mathrm{Ge}_x\mathrm{Se}_{1-x}$ is predicted to undergo the transition from an elastically floppy to a stressed rigid state with increasing Ge content [75]. This transition is predicted to occur at a single composition $x = 0.2$, where the network is rigid or isostatic. At this composition the mean number of Lagrangian bonding constraints per atom $\overline{N}_c$ is equal to the number of degrees of freedom per atom in three dimensions. The floppy phases are under-constrained ($\overline{N}_c < 3$), the stressed-rigid phases are over-constrained ($\overline{N}_c > 3$), and at the transition ($\overline{N}_c = 3$) the mean nearest-neighbour coordination number $\bar{n} = 2.4$ [76–78].

Recent spectroscopic and calorimetric measurements [79–81] have suggested that this transition actually extends over a small but finite range of compositions $0.20 \leq x \leq 0.26$, which corresponds to a so-called intermediate phase. Within this transition window it is thought that the network can self-organise, that is it can lower its free energy of formation by incorporating structural configurations that minimise the formation of over-constrained regions. This means that there are two transitions, and the floppy and stressed-rigid phases are separated by a range of compositions in which the network is rigid but stress free. In this intermediate phase, the non-reversing enthalpy of the glass-transition measured in temperature-modulated differential scanning calorimetry (MDSC) experiments is close to zero, which is indicative of a stress-free network [79, 80].

It is important to understand the structural arrangements that correspond to the intermediate phase. It is therefore desirable to measure the full set of partial structure factors, which describe the correlations between pairs of atoms on multiple length scales. These partial structure factors provide vital information that can be used to test the various structural models that have been proposed.

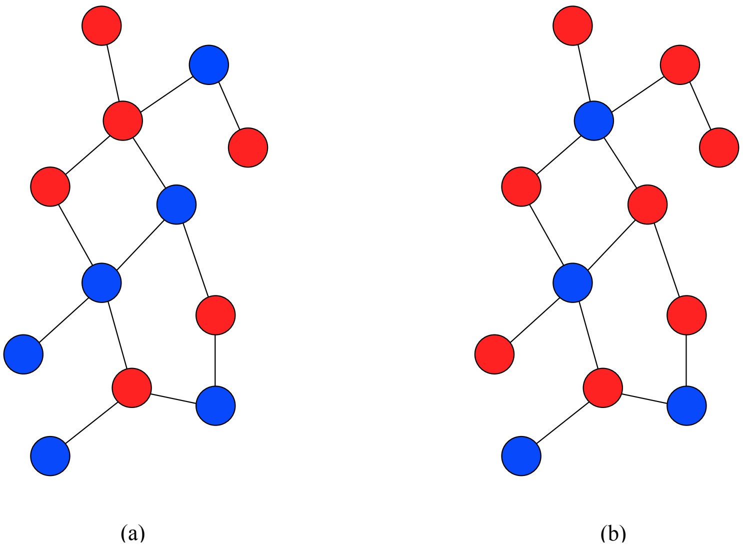

Figure 5-1: Schematic diagrams of (a) the random continuous network (RCN) and (b) the chemically ordered continuous random network (COCRN), where the blue and red circles represent the atoms of the two different chemical species, Ge and Se respectively.

In the case of $GeSe_4$ and $GeSe_3$, the simplest models correspond to a chemically ordered continuous random network (COCRN) [82], and to a random continuous network (RCN) [83, 84]. In the RCN there is no difference between the Ge-Ge, Se-Se and Ge-Se bond energies, or any other effects that would lead to preferential ordering. The distribution of bond types is purely statistical, as shown in the random distribution of (red) Se and (blue) Ge atoms in figure 5-1a. However, within the COCRN model heteropolar Ge-Se bonds are preferred, and homopolar Ge-Ge or Se-Se bonds are only allowed if the composition is Ge or Se-rich. Figure 5-1b shows this for a Se-rich composition, where the network consists of predominately Ge-Se bonds, with some Se-Se homopolar bonds.

For $GeSe_4$, the COCRN leads to a network composed of corner-sharing $GeSe_4$ tetrahedra connected by Se_2 dimers, where the fractions of Ge-Se-Ge, Se-Se-Se and Ge-Se-Se connections are 0%, 0% and 100%, respectively [75]. Departures from this model point to structural variability, which reflects the different structural conformations that allow for self-organisation in the intermediate phase. Note that for Se-rich compositions the COCRN model is sometimes referred to as the 'chain-crossing model'.

However, an alternative model has been proposed for $GeSe_4$ glass, called the bimodal phase percolation model, in which there is a microscopic phase separation into micro-domains of $GeSe_2$ and Se_n that prohibits the existence of Ge-Se-Se connections [85]. The experimental support for this model comes from ^{77}Se magic angle spinning (MAS) nuclear magnetic resonance (NMR) and Raman scattering experiments [85]. It has also found support from reverse Monte Carlo simulations of anomalous x-ray data corresponding to a maximum scattering vector $Q_{\max} < 10$ Å^{-1} [86]. The validity of the bimodal phase percolation model is hotly contested, as more recent ^{77}Se MAS NMR results contradict the previous findings [81], and recent first-principles molecular dynamics simulations do not support the absence of Ge-Se-Se connections [17, 87].

The work presented in this chapter makes use of the method of neutron diffraction with isotope substitution (NDIS) to measure the full set of partial structure factors for glassy $GeSe_3$ and $GeSe_4$. These results are compared to previous experimental work on the structure of glassy $GeSe_2$ [16], and to recent density functional based molecular dynamics simulations [17].

This chapter is organised as follows. The necessary theory for the neutron diffraction experiments is given in section 5.2. The experimental procedures for the work are given in section 5.3. The results are presented in section 5.4, followed by a discussion in section 5.5. Finally, the main conclusions are summarised in section 5.6.

5.2 Theory

As shown in Chapter 2, the total structure factor measured in a neutron diffraction experiment is given by

$$F(Q) = \sum_{\alpha=1}^{n} \sum_{\beta=1}^{n} c_\alpha c_\beta b_\alpha b_\beta \left[S_{\alpha\beta}(Q) - 1 \right], \tag{5.1}$$

where α and β denote the chemical species, n denotes the total number of chemical species, and c_α and b_α are the atomic fraction and bound coherent scattering length of atomic species α, respectively.

In the experiments on glassy $GeSe_3$ and $GeSe_4$, four total structure factors were measured corresponding to different isotopic compositions of Ge and/or Se. In this case, a singular value decomposition (SVD) analysis can be used to find the partial structure factors, making use of all available data. The glassy $GeSe_3$ samples $^{\mathrm{Nat}}\mathrm{Ge}^{\mathrm{Nat}}\mathrm{Se}_3$, $^{\mathrm{Nat}}\mathrm{Ge}^{\mathrm{Mix}}\mathrm{Se}_3$, $^{70}\mathrm{Ge}^{\mathrm{Nat}}\mathrm{Se}_3$ and $^{73}\mathrm{Ge}^{76}\mathrm{Se}_3$ and the glassy $GeSe_4$ samples $^{\mathrm{Nat}}\mathrm{Ge}^{\mathrm{Nat}}\mathrm{Se}_4$,

$^{\mathrm{Nat}}\mathrm{Ge}^{\mathrm{Mix}}\mathrm{Se}_4$, $^{70}\mathrm{Ge}^{\mathrm{Nat}}\mathrm{Se}_4$ and $^{73}\mathrm{Ge}^{76}\mathrm{Se}_4$ have measured total structure factors that are denoted by ${}^{\mathrm{Nat}}_{\mathrm{Nat}}F(Q)$, ${}^{\mathrm{Nat}}_{\mathrm{Mix}}F(Q)$, ${}^{70}_{\mathrm{Nat}}F(Q)$ and ${}^{73}_{76}F(Q)$, respectively. Here, Nat refers to the natural isotopic enrichment of either Ge or Se, and Mix refers to a 50.5:49.5 mixture by mass of ^{76}Se and $^{\mathrm{Nat}}$Se. The coherent neutron scattering lengths for these compositions are given in table 5.1. In the present work, the matrix equation to be solved is

Table 5.1: Table of the bound coherent scattering lengths for germanium b_{Ge} and selenium b_{Se} together with their mean value $\langle b \rangle$ for each of the isotopic compositions used for the diffraction experiments on GeSe$_3$ and GeSe$_4$. These values were calculated using the scattering lengths given by Sears [54] and the isotopic enrichment of the samples. Also given is the total scattering cross-section σ_T for neutrons at an incident wavelength λ.

Sample	b_{Ge}/fm	b_{Se}/fm	$\langle b \rangle$/fm	σ_T/barn ($\lambda = 0.4989(1)$Å)
$^{\mathrm{Nat}}\mathrm{Ge}^{\mathrm{Nat}}\mathrm{Se}_3$	8.185(20)	7.970(9)	8.024(12)	10.963(20)
$^{\mathrm{Nat}}\mathrm{Ge}^{\mathrm{Mix}}\mathrm{Se}_3$	8.185(20)	10.10(5)	9.624(13)	25.791(25)
$^{70}\mathrm{Ge}^{\mathrm{Nat}}\mathrm{Se}_3$	9.93(11)	7.970(9)	8.459(34)	11.968(57)
$^{73}\mathrm{Ge}^{76}\mathrm{Se}_3$	5.15(5)	12.19(10)	10.438(45)	40.160(83)
Sample	b_{Ge}/fm	b_{Se}/fm	$\langle b \rangle$/fm	σ_T/barn ($\lambda = 0.4990(1)$Å)
$^{\mathrm{Nat}}\mathrm{Ge}^{\mathrm{Nat}}\mathrm{Se}_4$	8.185(20)	7.970(9)	8.013(11)	11.079(18)
$^{\mathrm{Nat}}\mathrm{Ge}^{\mathrm{Mix}}\mathrm{Se}_4$	8.185(20)	10.10(5)	9.719(12)	26.839(23)
$^{70}\mathrm{Ge}^{\mathrm{Nat}}\mathrm{Se}_4$	9.93(11)	7.970(9)	8.361(29)	11.884(48)
$^{73}\mathrm{Ge}^{76}\mathrm{Se}_4$	5.15(5)	12.19(10)	10.789(45)	42.243(87)

$$\begin{pmatrix} {}^{\mathrm{Nat}}_{\mathrm{Nat}}F(Q) \\ {}^{\mathrm{Nat}}_{\mathrm{Mix}}F(Q) \\ {}^{70}_{\mathrm{Nat}}F(Q) \\ {}^{73}_{76}F(Q) \end{pmatrix} = \mathbf{A} \cdot \begin{pmatrix} S_{\mathrm{GeGe}}(Q) - 1 \\ S_{\mathrm{SeSe}}(Q) - 1 \\ S_{\mathrm{GeSe}}(Q) - 1 \end{pmatrix}, \tag{5.2}$$

where the matrix of weighting factors $\mathbf{A}$ is given by

$$\mathbf{A} = \begin{pmatrix} c_{\mathrm{Ge}}^2 b_{^{\mathrm{Nat}}\mathrm{Ge}}^2 & c_{\mathrm{Se}}^2 b_{^{\mathrm{Nat}}\mathrm{Se}}^2 & 2c_{\mathrm{Ge}}c_{\mathrm{Se}} b_{^{\mathrm{Nat}}\mathrm{Ge}} b_{^{\mathrm{Nat}}\mathrm{Se}} \\ c_{\mathrm{Ge}}^2 b_{^{\mathrm{Nat}}\mathrm{Ge}}^2 & c_{\mathrm{Se}}^2 b_{^{\mathrm{Mix}}\mathrm{Se}}^2 & 2c_{\mathrm{Ge}}c_{\mathrm{Se}} b_{^{\mathrm{Nat}}\mathrm{Ge}} b_{^{\mathrm{Mix}}\mathrm{Se}} \\ c_{\mathrm{Ge}}^2 b_{^{70}\mathrm{Ge}}^2 & c_{\mathrm{Se}}^2 b_{^{\mathrm{Nat}}\mathrm{Se}}^2 & 2c_{\mathrm{Ge}}c_{\mathrm{Se}} b_{^{70}\mathrm{Ge}} b_{^{\mathrm{Nat}}\mathrm{Se}} \\ c_{\mathrm{Ge}}^2 b_{^{73}\mathrm{Ge}}^2 & c_{\mathrm{Se}}^2 b_{^{76}\mathrm{Se}}^2 & 2c_{\mathrm{Ge}}c_{\mathrm{Se}} b_{^{73}\mathrm{Ge}} b_{^{76}\mathrm{Se}} \end{pmatrix}. \tag{5.3}$$

In the case of $\mathrm{GeSe_3}$, the numerical values of the matrix elements for the pseudo-inverse of $\mathbf{A}$ are given by

$$\frac{\mathbf{A}^{-1}}{\mathrm{barn}^{-1}} = \begin{pmatrix} -15.7999 & -85.2797 & 76.1240 & 32.7685 \\ -1.3906 & -4.7627 & 3.1862 & 3.6984 \\ 5.8508 & 23.0017 & -16.5963 & -11.1993 \end{pmatrix}. \tag{5.4}$$

In the case of $\mathrm{GeSe_4}$, the numerical values of the matrix elements for the pseudo-inverse of $\mathbf{A}$ are given by

$$\frac{\mathbf{A}^{-1}}{\mathrm{barn}^{-1}} = \begin{pmatrix} -24.6874 & -133.2495 & 118.9438 & 51.2008 \\ -1.2222 & -4.1860 & 2.8004 & 3.2506 \\ 6.8564 & 26.9551 & -19.4489 & -13.1243 \end{pmatrix}. \tag{5.5}$$

A singular value decomposition (SVD) analysis can also be used to calculate the Bhatia-Thornton partial structure factors using all four of the measured total structure factors. In this case, the matrix equation that must be solved is

$$\begin{pmatrix} {}^{\mathrm{Nat}}_{\mathrm{Nat}}F(Q) \\ {}^{\mathrm{Nat}}_{\mathrm{Mix}}F(Q) \\ {}^{70}_{\mathrm{Nat}}F(Q) \\ {}^{73}_{76}F(Q) \end{pmatrix} = \mathbf{B} \cdot \begin{pmatrix} S^{\mathrm{BT}}_{\mathrm{NN}}(Q) - 1 \\ \dfrac{S^{\mathrm{BT}}_{\mathrm{CC}}(Q)}{c_{\mathrm{Ge}}c_{\mathrm{Se}}} - 1 \\ S^{\mathrm{BT}}_{\mathrm{NC}}(Q) \end{pmatrix}, \tag{5.6}$$

where the matrix of weighting factor coefficients is given by

$$\mathbf{B} = \begin{pmatrix} \langle {}^{\mathrm{Nat}}_{\mathrm{Nat}}b \rangle^2 & c_{\mathrm{Ge}}c_{\mathrm{Se}}\left(b_{{}^{\mathrm{Nat}}\mathrm{Ge}} - b_{{}^{\mathrm{Nat}}\mathrm{Se}}\right)^2 & 2\langle {}^{\mathrm{Nat}}_{\mathrm{Nat}}b \rangle \left(b_{{}^{\mathrm{Nat}}\mathrm{Ge}} - b_{{}^{\mathrm{Nat}}\mathrm{Se}}\right) \\ \langle {}^{\mathrm{Nat}}_{\mathrm{Mix}}b \rangle^2 & c_{\mathrm{Ge}}c_{\mathrm{Se}}\left(b_{{}^{\mathrm{Nat}}\mathrm{Ge}} - b_{{}^{\mathrm{Mix}}\mathrm{Se}}\right)^2 & 2\langle {}^{\mathrm{Nat}}_{\mathrm{Mix}}b \rangle \left(b_{{}^{\mathrm{Nat}}\mathrm{Ge}} - b_{{}^{\mathrm{Mix}}\mathrm{Se}}\right) \\ \langle {}^{70}_{\mathrm{Nat}}b \rangle^2 & c_{\mathrm{Ge}}c_{\mathrm{Se}}\left(b_{{}^{70}\mathrm{Ge}} - b_{{}^{\mathrm{Nat}}\mathrm{Se}}\right)^2 & 2\langle {}^{70}_{\mathrm{Nat}}b \rangle \left(b_{{}^{70}\mathrm{Ge}} - b_{{}^{\mathrm{Nat}}\mathrm{Se}}\right) \\ \langle {}^{73}_{76}b \rangle^2 & c_{{}^{73}\mathrm{Ge}}c_{\mathrm{Se}}\left(b_{{}^{73}\mathrm{Ge}} - b_{{}^{76}\mathrm{Se}}\right)^2 & 2\langle {}^{73}_{76}b \rangle \left(b_{{}^{73}\mathrm{Ge}} - b_{{}^{76}\mathrm{Se}}\right) \end{pmatrix}, \tag{5.7}$$

and

$$\begin{aligned} \langle {}^{\mathrm{Nat}}_{\mathrm{Nat}}b \rangle &= c_{\mathrm{Ge}}b_{{}^{\mathrm{Nat}}\mathrm{Ge}} + c_{\mathrm{Se}}b_{{}^{\mathrm{Nat}}\mathrm{Se}} \\ \langle {}^{\mathrm{Nat}}_{\mathrm{Mix}}b \rangle &= c_{\mathrm{Ge}}b_{{}^{\mathrm{Nat}}\mathrm{Ge}} + c_{\mathrm{Se}}b_{{}^{\mathrm{Mix}}\mathrm{Se}} \\ \langle {}^{70}_{\mathrm{Nat}}b \rangle &= c_{\mathrm{Ge}}b_{{}^{70}\mathrm{Ge}} + c_{\mathrm{Se}}b_{{}^{\mathrm{Nat}}\mathrm{Se}} \\ \langle {}^{73}_{76}b \rangle &= c_{\mathrm{Ge}}b_{{}^{73}\mathrm{Ge}} + c_{\mathrm{Se}}b_{{}^{76}\mathrm{Se}}. \end{aligned} \tag{5.8}$$

In the case of $GeSe_3$, the numerical values of the matrix elements for the pseudo-inverse of $\mathbf{B}$ are given by

$$\frac{\mathbf{B}^{-1}}{\mathrm{barn}^{-1}} = \begin{pmatrix} 0.42435 & 0.61659 & 0.32636 & -0.07138 \\ -5.41729 & -25.50862 & 21.09432 & 11.03733 \\ 3.44691 & -1.17131 & 1.56434 & -0.03401 \end{pmatrix}. \tag{5.9}$$

In the case of $GeSe_4$, the numerical values of the matrix elements for the pseudo-inverse of $\mathbf{B}$ are given by

$$\frac{\mathbf{B}^{-1}}{\mathrm{barn}^{-1}} = \begin{pmatrix} 0.42436 & 0.61660 & 0.32636 & -0.07138 \\ -6.33961 & -30.61534 & 25.70272 & 12.91199 \\ 0.02466 & -1.14047 & 1.58066 & -0.03758 \end{pmatrix}. \tag{5.10}$$

Site specific structural information can also be obtained by measuring first-order difference functions. In these functions, one of the pair correlation functions is eliminated, thus reducing the overall complexity of correlations associated with a single diffraction pattern. It is possible to choose the pair-correlation function to be removed. For example, consider the total structure factors ${}^{\mathrm{X}}_{\mathrm{Y}}F(Q)$ and ${}^{\mathrm{X}'}_{\mathrm{Y}'}F(Q)$ for two samples ${}^{\mathrm{X}}\mathrm{Ge}{}^{\mathrm{Y}}\mathrm{Se}_3$ and ${}^{\mathrm{X}'}\mathrm{Ge}{}^{\mathrm{Y}'}\mathrm{Se}_3$. Then the difference function

$$\begin{aligned} {}^{\mathrm{X,Y-X',Y'}}\Delta F_{\mathrm{no\ GeGe}}(Q) &= {}^{\mathrm{X}}_{\mathrm{Y}}F(Q) - \frac{b^2_{{}^{\mathrm{X}}\mathrm{Ge}}}{b^2_{{}^{\mathrm{X}'}\mathrm{Ge}}}\,{}^{\mathrm{X}'}_{\mathrm{Y}'}F(Q) \\ &= c^2_{\mathrm{Se}}\left(b^2_{{}^{\mathrm{Y}}\mathrm{Se}} - \frac{b^2_{{}^{\mathrm{X}}\mathrm{Ge}}}{b^2_{{}^{\mathrm{X}'}\mathrm{Ge}}}b^2_{{}^{\mathrm{Y}'}\mathrm{Se}}\right)\left[S_{\mathrm{SeSe}}(Q)-1\right] \\ &+ 2c_{\mathrm{Ge}}c_{\mathrm{Se}}\left(b_{{}^{\mathrm{X}}\mathrm{Ge}}b_{{}^{\mathrm{Y}}\mathrm{Se}} - \frac{b^2_{{}^{\mathrm{X}}\mathrm{Ge}}}{b^2_{{}^{\mathrm{X}'}\mathrm{Ge}}}b_{{}^{\mathrm{X}'}\mathrm{Ge}}b_{{}^{\mathrm{Y}'}\mathrm{Se}}\right)\left[S_{\mathrm{GeSe}}(Q)-1\right], \end{aligned} \tag{5.11}$$

removes the Ge-Ge correlations. Alternatively the difference function

$$\begin{aligned}
{}^{\mathrm{X',Y'-X,Y}}\Delta F_{\mathrm{no\ SeSe}}(Q) &= {}^{\mathrm{X'}}_{\mathrm{Y'}}F(Q) - \frac{b^2_{\mathrm{Y'Se}}}{b^2_{\mathrm{YSe}}}\,{}^{\mathrm{X}}_{\mathrm{Y}}F(Q) \\
&= c^2_{\mathrm{Ge}}\left(b^2_{\mathrm{X'Ge}} - \frac{b^2_{\mathrm{Y'Se}}}{b^2_{\mathrm{YSe}}}b^2_{\mathrm{XGe}}\right)\big[S_{\mathrm{GeGe}}(Q)-1\big] \\
&+ 2c_{\mathrm{Ge}}c_{\mathrm{Se}}\left(b_{\mathrm{X'Ge}}b_{\mathrm{Y'Se}} - \frac{b^2_{\mathrm{Y'Se}}}{b^2_{\mathrm{YSe}}}b_{\mathrm{XGe}}b_{\mathrm{YSe}}\right)\big[S_{\mathrm{GeSe}}(Q)-1\big]\,,
\end{aligned} \tag{5.12}$$

removes the Se-Se correlations. Similarly the Ge-Se correlations can be removed by constructing the difference function

$$\begin{aligned}
{}^{\mathrm{X,Y-X',Y'}}\Delta F_{\mathrm{no\ GeSe}}(Q) &= {}^{\mathrm{X}}_{\mathrm{Y}}F(Q) - \frac{b_{\mathrm{XGe}}b_{\mathrm{YSe}}}{b_{\mathrm{X'Ge}}b_{\mathrm{Y'Se}}}\,{}^{\mathrm{X'}}_{\mathrm{Y'}}F(Q) \\
&= c^2_{\mathrm{Se}}\left(b^2_{\mathrm{YSe}} - \frac{b_{\mathrm{XGe}}b_{\mathrm{YSe}}}{b_{\mathrm{X'Ge}}b_{\mathrm{Y'Se}}}b^2_{\mathrm{Y'Se}}\right)\big[S_{\mathrm{SeSe}}(Q)-1\big] \\
&+ c^2_{\mathrm{Ge}}\left(b^2_{\mathrm{XGe}} - \frac{b_{\mathrm{XGe}}b_{\mathrm{YSe}}}{b_{\mathrm{X'Ge}}b_{\mathrm{Y'Se}}}b^2_{\mathrm{X'Ge}}\right)\big[S_{\mathrm{GeGe}}(Q)-1\big]\,.
\end{aligned} \tag{5.13}$$

The weighting factors for the difference functions are given in tables 5.2 and 5.3 for $\mathrm{GeSe_3}$ and $\mathrm{GeSe_4}$, respectively. The corresponding real space information can be obtained via Fourier transformation, e.g for ${}^{\mathrm{X,Y-X',Y'}}\Delta F_{\mathrm{no\ GeGe}}(Q)$

$$\begin{aligned}
{}^{\mathrm{X,Y-X',Y'}}\Delta G_{\mathrm{no\ GeGe}}(r) &= \frac{1}{2\pi^2 r\rho}\int_0^\infty Q\ {}^{\mathrm{X,Y-X',Y'}}\Delta F_{\mathrm{no\ GeGe}}(Q)\sin(Qr)\,\mathrm{d}Q \\
&= {}^{\mathrm{X}}_{\mathrm{Y}}G(r) - \frac{b^2_{\mathrm{XGe}}}{b^2_{\mathrm{X'Ge}}}\,{}^{\mathrm{X'}}_{\mathrm{Y'}}G(r) \\
&= c^2_{\mathrm{Se}}\left(b^2_{\mathrm{YSe}} - \frac{b^2_{\mathrm{XGe}}}{b^2_{\mathrm{X'Ge}}}b^2_{\mathrm{Y'Se}}\right)g_{\mathrm{SeSe}}(r) \\
&+ 2c_{\mathrm{Ge}}c_{\mathrm{Se}}\left(b_{\mathrm{XGe}}b_{\mathrm{YSe}} - \frac{b^2_{\mathrm{XGe}}}{b^2_{\mathrm{X'Ge}}}b_{\mathrm{X'Ge}}b_{\mathrm{Y'Se}}\right)g_{\mathrm{GeSe}}(r) \\
&+{}^{\mathrm{X,Y-X',Y'}}\,\Delta G_{\mathrm{no\ GeGe}}(r\to 0),
\end{aligned} \tag{5.14}$$

where the low-r limit is given by

$$
\begin{aligned}
{}^{\mathrm{X,Y-X',Y'}}\Delta G_{\mathrm{no\ GeGe}}(r \to 0) = {} & -c_{\mathrm{Se}}^{2}\left(b^{2}_{\mathrm{Y_{Se}}} - \frac{b^{2}_{\mathrm{X_{Ge}}}}{b^{2}_{\mathrm{X'_{Ge}}}}b^{2}_{\mathrm{Y'_{Se}}}\right) \\
& - 2c_{\mathrm{Ge}}c_{\mathrm{Se}}\left(b_{\mathrm{X_{Ge}}}b_{\mathrm{Y_{Se}}} - \frac{b^{2}_{\mathrm{X_{Ge}}}}{b^{2}_{\mathrm{X'_{Ge}}}}b_{\mathrm{X'_{Ge}}}b_{\mathrm{Y'_{Se}}}\right). \qquad (5.15)
\end{aligned}
$$

Table 5.2: The weighting factors for the $S_{\alpha\beta}(Q)$ functions in units of barns (10^{-28} m^2) for the GeSe$_3$ first-order difference functions as defined by equations 5.11 to 5.13. The numerical values take into account the isotopic enrichments of the samples used in the experiment.

$\Delta F_{\mathrm{no}\ \alpha\beta}(Q)$	${}^{\mathrm{X}}_{\mathrm{Y}}F(Q)$	${}^{\mathrm{X'}}_{\mathrm{Y'}}F(Q)$	$S_{\mathrm{GeGe}}(Q)$(barn)	$S_{\mathrm{SeSe}}(Q)$(barn)	$S_{\mathrm{GeSe}}(Q)$(barn)
${}^{\mathrm{X,Y-X',Y'}}\Delta F_{\mathrm{no\ GeGe}}(Q)$	${}^{73}_{76}F(Q)$	${}^{70}_{\mathrm{Nat}}F(Q)$	0.0000(6)	0.7397(4)	0.1556(5)
	${}^{73}_{76}F(Q)$	${}^{\mathrm{Nat}}_{\mathrm{Mix}}F(Q)$	0.0000(6)	0.6084(4)	0.1127(5)
	${}^{73}_{76}F(Q)$	${}^{\mathrm{Nat}}_{\mathrm{Nat}}F(Q)$	0.0000(6)	0.6944(4)	0.1386(5)
	${}^{\mathrm{Nat}}_{\mathrm{Mix}}F(Q)$	${}^{70}_{\mathrm{Nat}}F(Q)$	0.0000(6)	0.3311(4)	0.1083(5)
	${}^{\mathrm{Nat}}_{\mathrm{Mix}}F(Q)$	${}^{\mathrm{Nat}}_{\mathrm{Nat}}F(Q)$	0.0000(6)	0.2167(4)	0.0654(5)
	${}^{\mathrm{Nat}}_{\mathrm{Nat}}F(Q)$	${}^{70}_{\mathrm{Nat}}F(Q)$	0.0000(6)	0.1143(4)	0.0429(5)
${}^{\mathrm{X',Y'-X,Y}}\Delta F_{\mathrm{no\ SeSe}}(Q)$	${}^{73}_{76}F(Q)$	${}^{70}_{\mathrm{Nat}}F(Q)$	0.0544(3)	0.0000(1)	0.1959(4)
	${}^{73}_{76}F(Q)$	${}^{\mathrm{Nat}}_{\mathrm{Mix}}F(Q)$	0.0304(3)	0.0000(1)	0.1482(4)
	${}^{73}_{76}F(Q)$	${}^{\mathrm{Nat}}_{\mathrm{Nat}}F(Q)$	0.0347(3)	0.0000(1)	0.1439(4)
	${}^{\mathrm{Nat}}_{\mathrm{Mix}}F(Q)$	${}^{70}_{\mathrm{Nat}}F(Q)$	0.0355(3)	0.0000(1)	0.1036(4)
	${}^{\mathrm{Nat}}_{\mathrm{Mix}}F(Q)$	${}^{\mathrm{Nat}}_{\mathrm{Nat}}F(Q)$	0.0158(3)	0.0000(1)	0.0516(4)
	${}^{\mathrm{Nat}}_{\mathrm{Nat}}F(Q)$	${}^{70}_{\mathrm{Nat}}F(Q)$	0.0197(3)	0.0000(1)	0.0520(4)
${}^{\mathrm{X,Y-X',Y'}}\Delta F_{\mathrm{no\ GeSe}}(Q)$	${}^{73}_{76}F(Q)$	${}^{70}_{\mathrm{Nat}}F(Q)$	-0.0323(8)	0.5523(4)	0.0000(3)
	${}^{73}_{76}F(Q)$	${}^{\mathrm{Nat}}_{\mathrm{Mix}}F(Q)$	-0.0152(8)	0.3998(4)	0.0000(3)
	${}^{73}_{76}F(Q)$	${}^{\mathrm{Nat}}_{\mathrm{Nat}}F(Q)$	-0.0237(8)	0.4918(4)	0.0000(3)
	${}^{\mathrm{Nat}}_{\mathrm{Mix}}F(Q)$	${}^{70}_{\mathrm{Nat}}F(Q)$	-0.0224(8)	0.2006(4)	0.0000(3)
	${}^{\mathrm{Nat}}_{\mathrm{Mix}}F(Q)$	${}^{\mathrm{Nat}}_{\mathrm{Nat}}F(Q)$	-0.0112(8)	0.1211(4)	0.0000(3)
	${}^{\mathrm{Nat}}_{\mathrm{Nat}}F(Q)$	${}^{70}_{\mathrm{Nat}}F(Q)$	-0.0089(8)	0.0627(4)	0.0000(3)

Table 5.3: The weighting factors for the $S_{\alpha\beta}(Q)$ functions in units of barns (10^{-28} m^2) for the GeSe$_4$ first-order difference functions as defined by equations 5.11 to 5.13. The numerical values take into account the isotopic enrichments of the samples used in the experiment.

$\Delta F_{\text{no }\alpha\beta}(Q)$	${}^{\text{X}}_{\text{Y}}F(Q)$	${}^{\text{X}'}_{\text{Y}'}F(Q)$	$S_{\text{GeGe}}(Q)$(barn)	$S_{\text{SeSe}}(Q)$(barn)	$S_{\text{GeSe}}(Q)$(barn)
${}^{\text{X,Y}-\text{X}',\text{Y}'}\Delta F_{\text{no GeGe}}(Q)$	${}^{73}_{76}F(Q)$	${}^{70}_{\text{Nat}}F(Q)$	0.0000(8)	0.8417(5)	0.1329(7)
	${}^{73}_{76}F(Q)$	${}^{\text{Nat}}_{\text{Mix}}F(Q)$	0.0000(8)	0.6923(5)	0.0962(7)
	${}^{73}_{76}F(Q)$	${}^{\text{Nat}}_{\text{Nat}}F(Q)$	0.0000(8)	0.7901(5)	0.1183(7)
	${}^{\text{Nat}}_{\text{Mix}}F(Q)$	${}^{70}_{\text{Nat}}F(Q)$	0.0000(8)	0.3767(5)	0.0925(7)
	${}^{\text{Nat}}_{\text{Mix}}F(Q)$	${}^{\text{Nat}}_{\text{Nat}}F(Q)$	0.0000(8)	0.2466(5)	0.0558(7)
	${}^{\text{Nat}}_{\text{Nat}}F(Q)$	${}^{70}_{\text{Nat}}F(Q)$	0.0000(8)	0.1301(5)	0.0366(7)
${}^{\text{X}',\text{Y}'-\text{X,Y}}\Delta F_{\text{no SeSe}}(Q)$	${}^{73}_{76}F(Q)$	${}^{70}_{\text{Nat}}F(Q)$	0.0349(5)	0.0000(2)	0.1672(8)
	${}^{73}_{76}F(Q)$	${}^{\text{Nat}}_{\text{Mix}}F(Q)$	0.0195(5)	0.0000(2)	0.1265(8)
	${}^{73}_{76}F(Q)$	${}^{\text{Nat}}_{\text{Nat}}F(Q)$	0.0223(5)	0.0000(2)	0.1228(8)
	${}^{\text{Nat}}_{\text{Mix}}F(Q)$	${}^{70}_{\text{Nat}}F(Q)$	0.0227(5)	0.0000(2)	0.0885(8)
	${}^{\text{Nat}}_{\text{Mix}}F(Q)$	${}^{\text{Nat}}_{\text{Nat}}F(Q)$	0.0101(5)	0.0000(2)	0.0441(8)
	${}^{\text{Nat}}_{\text{Nat}}F(Q)$	${}^{70}_{\text{Nat}}F(Q)$	0.0126(5)	0.0000(2)	0.0444(8)
${}^{\text{X,Y}-\text{X}',\text{Y}'}\Delta F_{\text{no GeSe}}(Q)$	${}^{73}_{76}F(Q)$	${}^{70}_{\text{Nat}}F(Q)$	-0.0207(10)	0.6284(6)	0.0000(5)
	${}^{73}_{76}F(Q)$	${}^{\text{Nat}}_{\text{Mix}}F(Q)$	-0.0097(10)	0.4549(6)	0.0000(5)
	${}^{73}_{76}F(Q)$	${}^{\text{Nat}}_{\text{Nat}}F(Q)$	-0.0152(10)	0.5597(6)	0.0000(5)
	${}^{\text{Nat}}_{\text{Mix}}F(Q)$	${}^{70}_{\text{Nat}}F(Q)$	-0.0144(10)	0.2282(6)	0.0000(5)
	${}^{\text{Nat}}_{\text{Mix}}F(Q)$	${}^{\text{Nat}}_{\text{Nat}}F(Q)$	-0.0072(10)	0.1378(6)	0.0000(5)
	${}^{\text{Nat}}_{\text{Nat}}F(Q)$	${}^{70}_{\text{Nat}}F(Q)$	-0.0057(10)	0.0713(6)	0.0000(5)

5.3 Experiment

5.3.1 Sample preparation

The glassy $GeSe_3$ and $GeSe_4$ samples were prepared at the University of Bath in the liquids and amorphous materials laboratory. The silica ampoules (5 mm inner diameter, 1 mm wall thickness) used for the samples were etched with concentrated (48 % wt) hydrofluoric acid and rinsed with acetone, and then dried under vacuum at 800 ℃ for 2 hours.

The $GeSe_4$ samples were measured in the first part of the neutron diffraction experiment, and were prepared using the required stoichiometric ratio of germanium and selenium powders. Germanium was then added to the $GeSe_4$ samples, to create $GeSe_3$ samples with the same isotopic composition. The $GeSe_3$ samples were then measured in the second part of the neutron diffraction experiment.

The elements used in the samples were: germanium of natural isotopic abundance (^{Nat}Ge, 99.999 % purity from Alfa Aesar), isotopically enriched ^{70}Ge (^{70}Ge 95.30 %, ^{72}Ge 4.10 %, ^{76}Ge 0.51 %, ^{74}Ge 0.05 % and ^{73}Ge 0.04 % enrichment from Isoflex USA) or ^{73}Ge (^{73}Ge 95.60 %, ^{72}Ge 2.34 %, ^{74}Ge 2.03 %, ^{70}Ge 0.025 % and ^{76}Ge 0.0005 % enrichment from Isoflex USA), with selenium of natural isotopic abundance (^{Nat}Se 99.999+ % purity from Sigma Aldrich), isotopically enriched ^{76}Se (^{76}Se 99.8 % and ^{77}Se 0.20 % enrichment from Isoflex USA) or a 50.5:49.5 mixture by mass of ^{Nat}Se and ^{76}Se (referred to as ^{Mix}Se).

To obtain glassy samples, it was necessary to purify the germanium isotopes to remove any germanium oxide impurities. The germanium isotopes were placed into a glass crucible inside a reduction furnace. The crucible has a glass frit with a pore size of 3 μm to allow gas flow through the sample. The reduction furnace was flushed through with argon gas for $\sim$ 1 min to remove any air, then the gas flow was switched to hydrogen. The temperature of the furnace was ramped up to 600 ℃ at 4 ℃/min, and the isotopes were reduced under hydrogen gas flow for 48 hours. The temperature of the furnace was then ramped down at 1 ℃/min to room temperature and the gas flow switched back to argon. Once cooled the isotopes were removed and stored inside of an argon-filled glove-box prior to the sample preparation. This procedure gave a yield of 83%, and it is worth noting that the colour of the isotopes changed from black to metallic grey. Infra-red spectroscopy was used to confirm that all of the Ge-O impurities had been removed in the reduction, as shown in figure 5-2.

The ampoules loaded with the desired stoichiometric ratio of germanium and selenium were evacuated to $\approx 10^{-5}$ Torr and sealed, and were then placed into a rocking furnace. The furnaces have a rocking rate of 0.57 rpm with a maximum rocking angle of 30 degrees from the horizontal. The furnace was heated to 975 ℃ at 1 ℃/min,

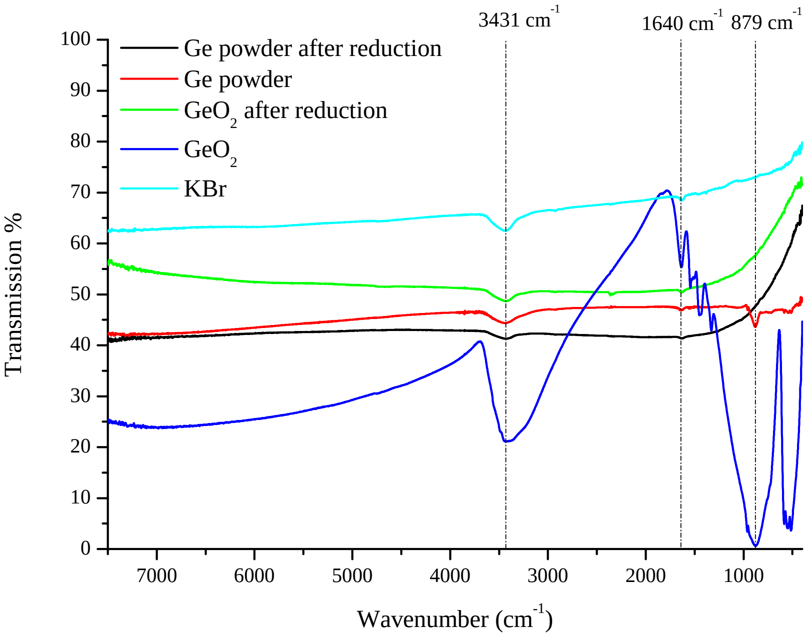

Figure 5-2: Infra-red transmission spectra for GeO_2 powder and Ge powder before and after the reduction procedure. Notice the lack of the Ge-O absorption band at 879 cm^{-1} for the reduced samples [88]. The absorption bands at 1640 cm^{-1} and 3431 cm^{-1} are due to the presence of water in the KBr used as a matrix for the samples [89].

dwelling at the melting and boiling points of Se (221 ℃ and 685 ℃, respectively) and the melting point of Ge (938 ℃) for 4 hours each. Once at 975 ℃, the samples were rocked for 48 hours, before being placed vertically and left for 4 hours (52 hours in total). The temperature was then ramped down at 1 ℃/min to 655 ℃ and left for 5 hours to equilibrate, before being quenched by dropping into an ice-water mixture. The glasses separated cleanly from the silica ampoules and were fully amorphous, which is consistent with negligible oxygen contamination. Infra-red spectroscopy was used to determine that there is no contamination from oxygen or hydrogen in the $^{\mathrm{Nat}}\mathrm{Ge}^{\mathrm{Nat}}\mathrm{Se}_3$ and $^{\mathrm{Nat}}\mathrm{Ge}^{\mathrm{Nat}}\mathrm{Se}_4$ samples as shown in figure 5-3. Temperature modulated differential scanning calorimetry (MDSC) measurements indicated the presence of a single glass transition temperature of 249.9(3.0) ℃ for all of the isotopically enriched $GeSe_3$ samples, as shown in figure 5-4 for the sample having the natural isotopic abundance. MDSC measurements also indicated the presence of a single glass transition temperature for $GeSe_4$ of 190.3(3.0) ℃ as shown in figure 5-5 for the sample having the natural isotopic abundance, which indicated that the glasses were not phase separated.

The mass densities of both $GeSe_3$ and $GeSe_4$ were measured, using a helium pycnometer, to be 4.309(3) g/cm^3 and 4.334(4) g/cm^3, respectively. The values stated are

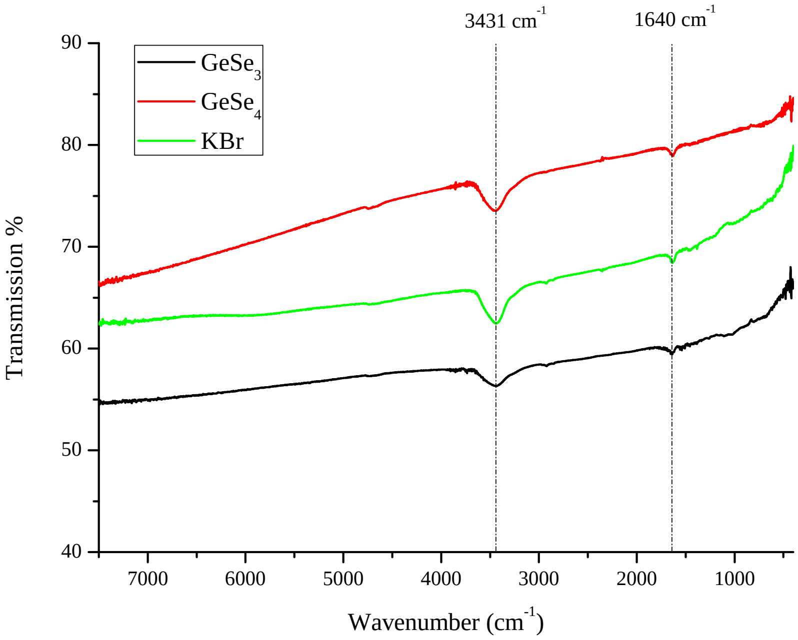

Figure 5-3: Infra-red transmission spectra for the KBr powder and for the $^{\mathrm{Nat}}\mathrm{Ge}^{\mathrm{Nat}}\mathrm{Se}_3$ and $^{\mathrm{Nat}}\mathrm{Ge}^{\mathrm{Nat}}\mathrm{Se}_4$ samples. The absorption bands at 1640 cm^{-1} and 3431 cm^{-1} are due to the presence of water in the KBr used as a matrix for the samples [89].

the average over several measurements, where the error given is the standard deviation of the measurements. The mass densities correspond to atomic number densities for GeSe$_3$ and GeSe$_4$ of 0.03353(2) Å^{-3} and 0.03359(3) Å^{-3}, respectively.

5.3.2 Neutron diffraction experiment

Both parts of the neutron diffraction experiment were carried out on the D4c diffractometer at the Institut Laue-Langevin, with part 1 in May of 2013 and part 2 in July of 2013. The GeSe$_3$ and GeSe$_4$ samples were loaded into a 5 mm diameter vanadium can (inner diameter = 4.8 mm, wall thickness = 0.1 mm) inside the argon filled glove-box at the D4c diffractometer. Loading the samples inside the glove-box prevents any contamination of the samples which could lead to long-term ageing, and ensured that the GeSe$_4$ samples were kept clean so they could be made into GeSe$_3$.

Diffraction patterns were measured for the samples inside the vanadium can, the empty vanadium can, the empty belljar, a 6.08 mm diameter vanadium rod for normalisation purposes, and a slab of $^{10}\mathrm{B}_4\mathrm{C}$ to account for the effect of the sample's attenuation on the background signal at low scattering angles. The data analysis followed the procedure outlined in chapter 3.

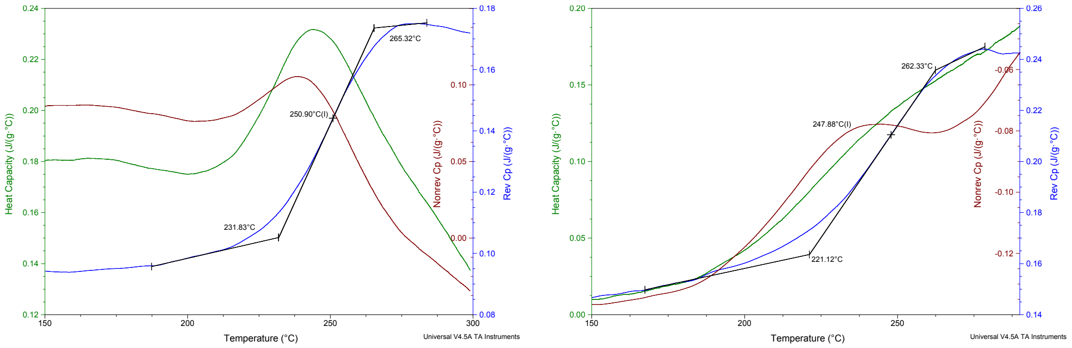

(a) Up scan (b) Down scan

Figure 5-4: Temperature-modulated differential scanning calorimetry measurement for the $^{\mathrm{Nat}}$Ge$^{\mathrm{Nat}}$Se$_3$ sample. The reversible heat capacity (solid blue curve) gives the glass transition temperature. The scan rate was 3 ℃/min with a modulation of 1 ℃ every 100 s.

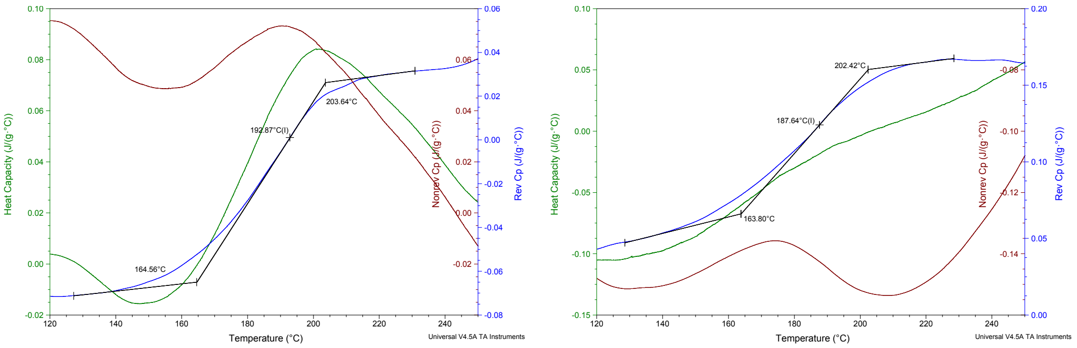

(a) Up scan (b) Down scan

Figure 5-5: Temperature-modulated differential scanning calorimetry measurement for the $^{\mathrm{Nat}}$Ge$^{\mathrm{Nat}}$Se$_4$ sample. The reversible heat capacity (solid blue curve) gives the glass transition temperature. The scan rate was 3 ℃/min with a modulation of 1 ℃ every 100 s.

5.4 Results

5.4.1 Total structure factors

GeSe$_3$

The slope corrected measured total structure factors $F(Q)$ for glassy GeSe$_3$ are shown in figure 5-6 and the total pair-distribution functions $G(r)$ are shown in figure 5-7. To correct for any residual slope on the total structure factors, the first few data-points in $G(r)$ were set to the $G(r \to 0)$ limit, and the resultant functions were then back Fourier transformed into reciprocal space. These slope corrected total structure factors were used to calculate the first-order difference functions and partial structure factors presented in this chapter. In the total pair-distribution functions there is some ringing around the first peak that originates from truncation of the reciprocal space functions due to D4c's limited Q-range. Hence in the data analysis procedure, the oscillation before the first peak in $G(r)$ was not set to the $G(r \to 0)$ limit, to aid in correctly normalising the data.

As the bound coherent scattering lengths for Ge ($b_{^{\mathrm{Nat}}\mathrm{Ge}} = 8.185(20)$ fm) and Se ($b_{^{\mathrm{Nat}}\mathrm{Se}} = 7.970(9)$ fm) are very similar, the $^{\mathrm{Nat}}$Ge$^{\mathrm{Nat}}$Se$_3$ composition is almost identical to the Bhatia-Thornton number-number partial structure factor $S_{\mathrm{NN}}^{\mathrm{BT}}(Q)$. Therefore, the $^{\mathrm{Nat}}$Ge$^{\mathrm{Nat}}$Se$_3$ total pair-distribution function can be used to calculate the mean nearest-neighbour coordination number, which should be $\bar{n} = 2.5$ according to the '8-N' rule. The coordination number obtained from the RDFgenie fit to the first peak in the $^{\mathrm{Nat}}$Ge$^{\mathrm{Nat}}$Se$_3$ $D(r)$ function, (see figure 5-8) is $\bar{n} = 2.52(2)$ which agrees with the predicted value within the error.

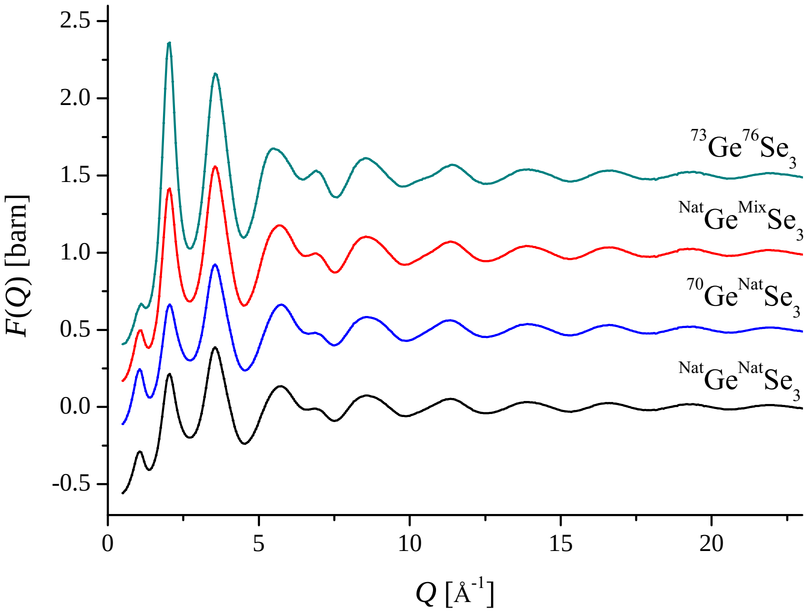

Figure 5-6: Total structure factors $F(Q)$ measured for the four glassy $GeSe_3$ isotopic compositions. Note that the error bars are smaller than the line thickness. Each subsequent dataset has been offset vertically by 0.5 barn for clarity of presentation.

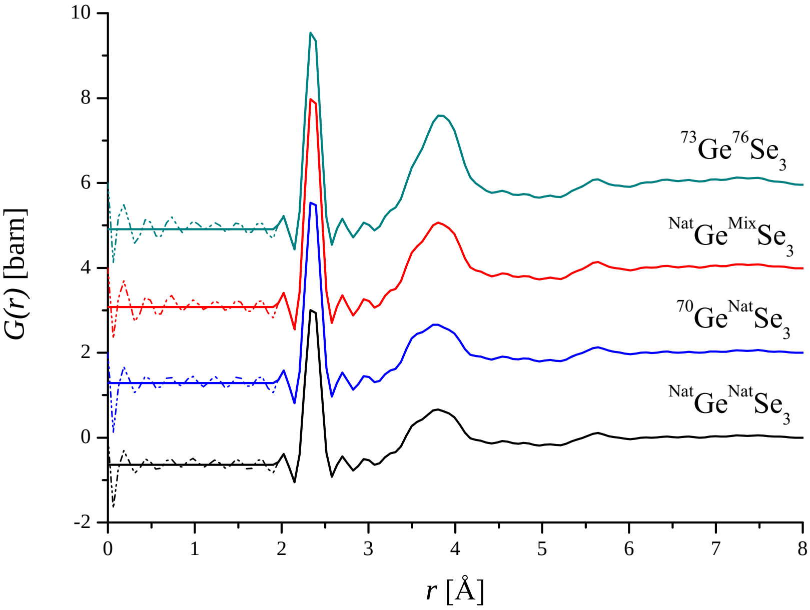

Figure 5-7: Total pair-distribution functions $G(r)$ for the four glassy GeSe$_3$ isotopic compositions. The solid lines are the Fourier transforms of the total structure factors given in figure 5-6, with the low-r oscillations (dashed lines) set to their theoretical $G(r \to 0)$ limit. The curves are offset vertically for clarity of presentation.

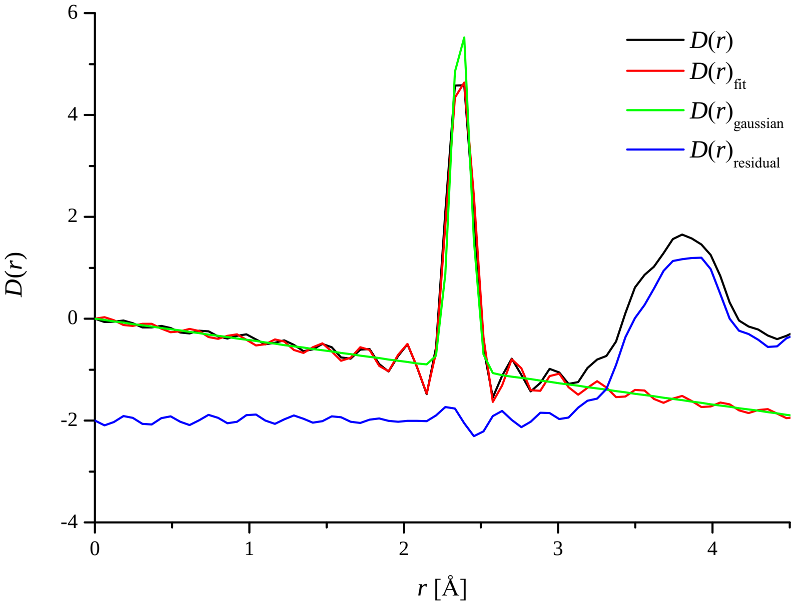

Figure 5-8: The first peak in the measured $D(r)$ function for glassy $^{\text{Nat}}\text{Ge}^{\text{Nat}}\text{Se}_3$ (solid black curve), fitted with a Gaussian convoluted with a sinc function using RDFgenie (solid red curve). The resulting fitted Gaussian in $D(r)$ is given by the solid green curve, and the residual is the solid blue curve. The fit has an R_χ goodness-of-fit parameter of 0.076.

$GeSe_4$

The slope corrected measured total structure factors $F(Q)$ and the total pair-distribution functions $G(r)$ for glassy $GeSe_4$ are shown in figures 5-9 and 5-10, respectively. These data sets were obtained using the same procedures as for $GeSe_3$. Therefore not all of the oscillations before the first peak in $G(r)$ were set to the $G(r \to 0)$ limit: one was left to aid in the normalisation of the data.

Since $b_{^{\mathrm{Nat}}\mathrm{Ge}} \simeq b_{^{\mathrm{Nat}}\mathrm{Se}}$, the $^{\mathrm{Nat}}\mathrm{Ge}^{\mathrm{Nat}}\mathrm{Se}_4$ total pair-distribution function is almost identical to the Bhatia-Thornton number-number pair-distribution function, and can be used to calculate the mean nearest-neighbour coordination number, which should be $\bar{n} = 2.4$ according to the '8-N' rule. The coordination number obtained from the RDFgenie fit to the first peak in the $^{\mathrm{Nat}}\mathrm{Ge}^{\mathrm{Nat}}\mathrm{Se}_4$ $D(r)$ function (see figure 5-11) is $\bar{n} = 2.43(2)$, which agrees with the predicted value within the error.

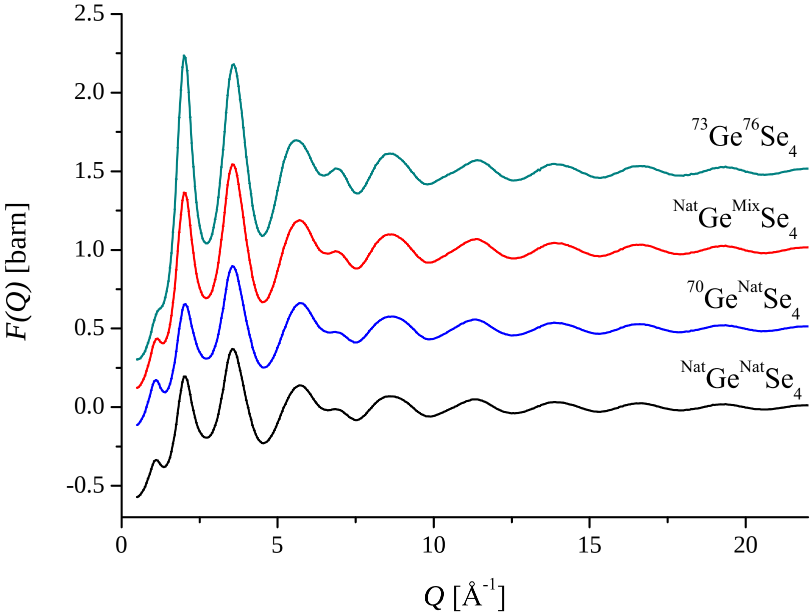

Figure 5-9: Total structure factors $F(Q)$ measured for the four glassy $GeSe_4$ isotopic compositions. Note that the error bars are smaller than the line thickness. Each subsequent dataset has been offset vertically by 0.5 barn for clarity of presentation.

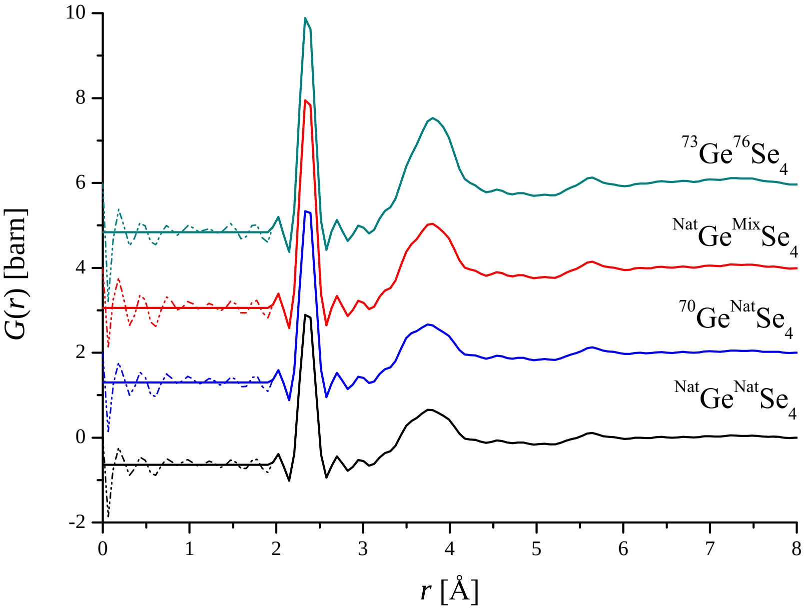

Figure 5-10: Total pair-distribution functions $G(r)$ for the four glassy GeSe$_4$ isotopic compositions. The solid lines are the Fourier transforms of the total structure factors given in figure 5-9, with the low-r oscillations (dashed lines) set to their theoretical $G(r \to 0)$ limit. The curves are offset vertically for clarity of presentation.

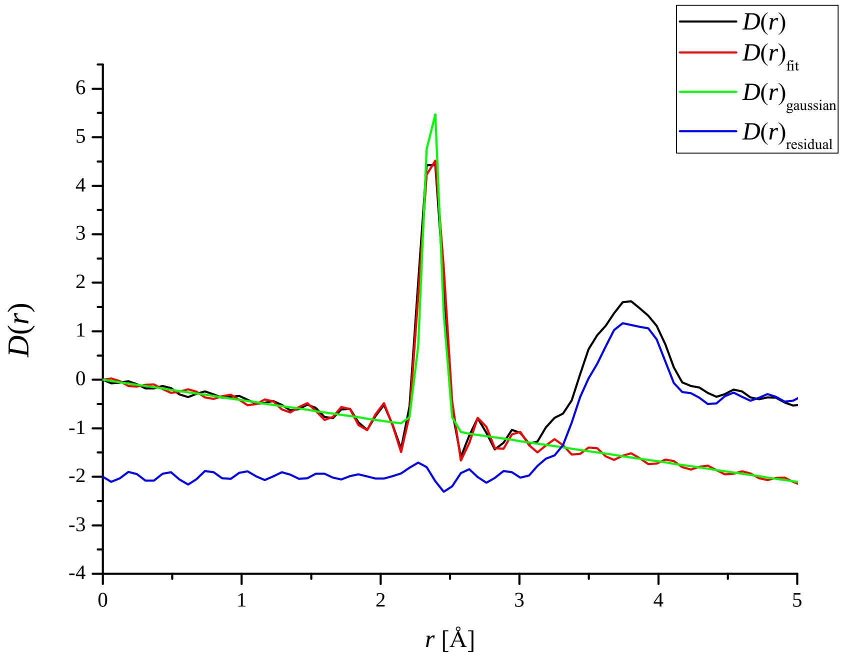

Figure 5-11: The first peak in the measured $D(r)$ function for glassy $^{\mathrm{Nat}}\mathrm{Ge}^{\mathrm{Nat}}\mathrm{Se}_4$ (solid black curve), fitted with a Gaussian convoluted with a sinc function using RDFgenie (solid red curve). The resulting fitted Gaussian in $D(r)$ is given by the solid green curve, and the residual is the solid blue curve. The fit has an R_χ goodness-of-fit parameter of 0.077.

5.4.2 First-order difference functions

GeSe$_3$

The six weighted difference functions that can be calculated from the four total structure factors are plotted in figures 5-12 – 5-17, in both reciprocal and real space. A summary of the corresponding bond distances and coordination numbers is given in table 5.4.

The bond distances and coordination numbers were obtained from the measured $\Delta G_{\text{no GeSe}}(r)$ and $\Delta G_{\text{no SeSe}}(r)$ difference functions (i) by integrating over the first peak in $\Delta G(r)$ (see table 5.4) or (ii) by fitting a Gaussian function to the first peak in $\Delta D(r)$ using the RDFgenie program (see table 5.5). In both of these procedures it was assumed that there are no Ge-Ge homopolar bonds under the first peak, so that it was possible to obtain the Ge-Se and Se-Se coordination numbers from the $\Delta G_{\text{no SeSe}}(r)$ and $\Delta G_{\text{no GeSe}}(r)$ difference functions, respectively. This assumption is consistent with the GeSe$_3$ stoichiometry which places it on the Se-rich side of the Ge$_x$Se$_{1-x}$ system. The first peak in $\Delta G_{\text{no GeGe}}(r)$ has contributions from the Ge-Se and Se-Se partial pair-distribution functions. The bond distances and coordination numbers were obtained by fitting two Gaussians to the first peak in $\Delta D(r)$ using the RDFgenie program (Figure 5-18), and the results are given in table 5.5. The coordination numbers are consistent with those found for the $\Delta G_{\text{no SeSe}}(r)$ and $\Delta G_{\text{no GeSe}}(r)$ difference functions.

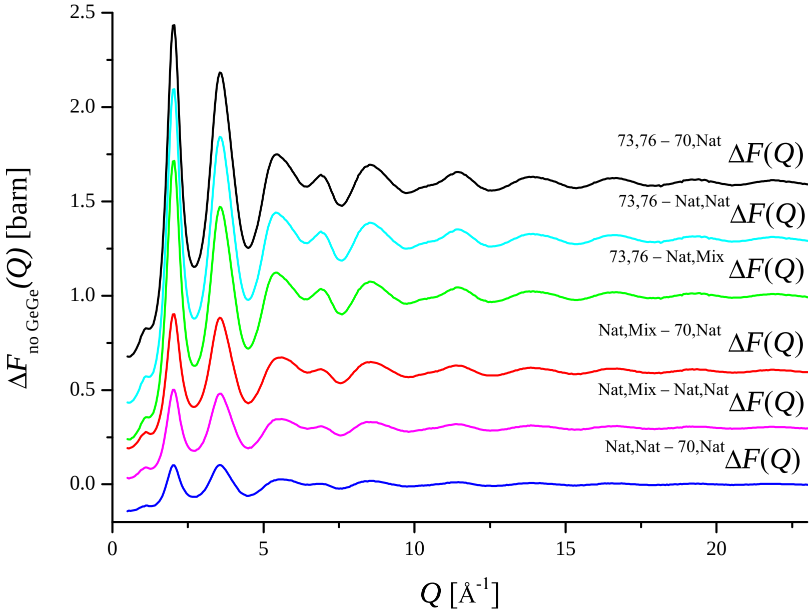

Figure 5-12: The measured first-order difference functions $\Delta F_{\text{no GeGe}}(Q)$ for glassy $GeSe_3$, as defined by equation 5.11. The error bars are smaller than the line thickness. The curves are offset vertically for clarity of presentation.

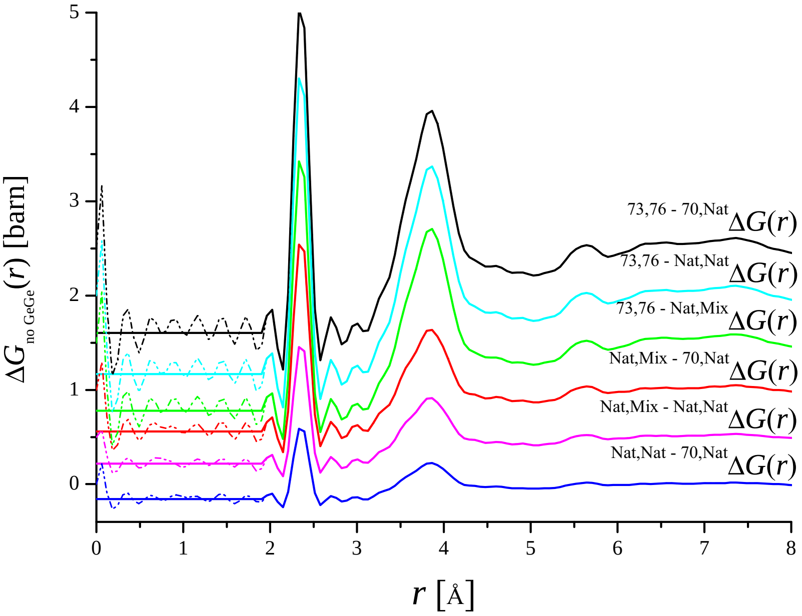

Figure 5-13: The first-order difference pair-distribution functions $\Delta G_{\text{no GeGe}}(r)$ for glassy GeSe$_3$. The solid curves are obtained by Fourier transforming the first-order difference functions $\Delta F_{\text{no GeGe}}(Q)$ shown in figure 5-12. The low-r oscillations have been set to their theoretical $\Delta G_{\text{no GeGe}}(r \to 0)$ limit. The dotted lines show the extent of these unphysical oscillations. The curves are offset vertically for clarity of presentation.

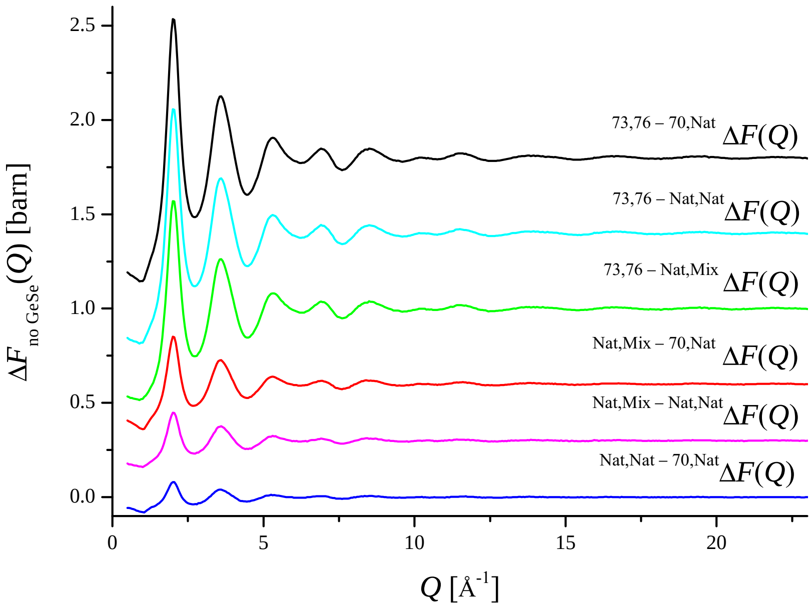

Figure 5-14: The measured first-order difference functions $\Delta F_{\text{no GeSe}}(Q)$ for glassy GeSe$_3$, as defined by equation 5.13. The error bars are smaller than the line thickness. The curves are offset vertically for clarity of presentation.

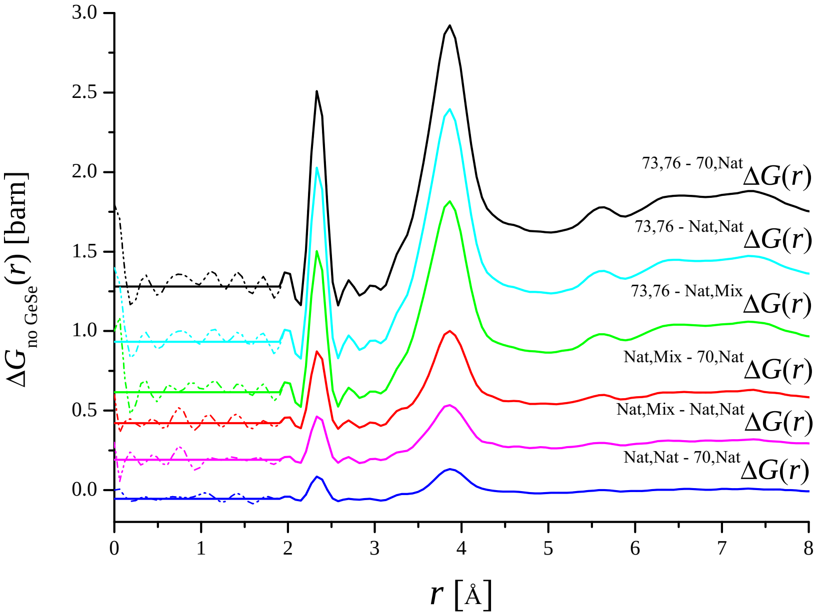

Figure 5-15: The first-order difference pair-distribution functions $\Delta G_{\text{no GeSe}}(r)$ for glassy GeSe_3. The solid curves are obtained by Fourier transforming the first-order difference functions $\Delta F_{\text{no GeSe}}(Q)$ shown in figure 5-14. The low-r oscillations have been set to their theoretical $\Delta G_{\text{no GeSe}}(r \to 0)$ limit. The dotted lines show the extent of these unphysical oscillations. The curves are offset vertically for clarity of presentation.

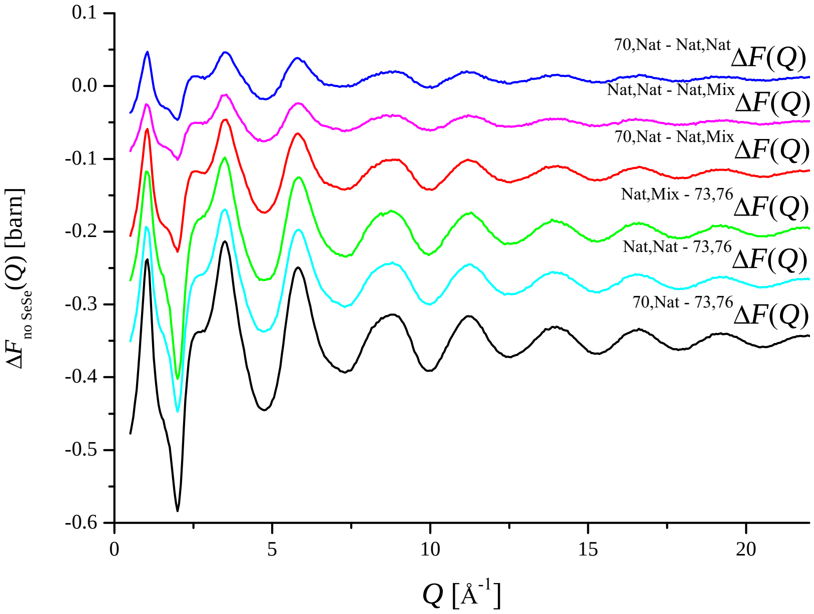

Figure 5-16: The measured first-order difference functions $\Delta F_{\text{no SeSe}}(Q)$ for glassy GeSe$_3$, as defined by equation 5.12. The error bars are smaller than the line thickness. The curves are offset vertically for clarity of presentation

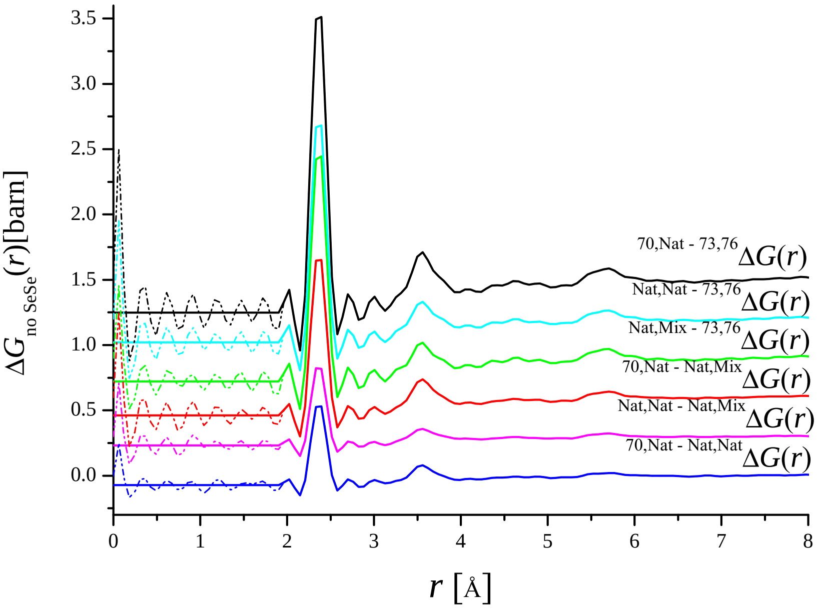

Figure 5-17: The first-order difference pair-distribution functions $\Delta G_{\text{no SeSe}}(r)$ for glassy GeSe$_3$. The solid curves are obtained by Fourier transforming the first-order difference functions $\Delta F_{\text{no SeSe}}(Q)$ shown in figure 5-16. The low-r oscillations have been set to their theoretical $\Delta G_{\text{no SeSe}}(r \to 0)$ limit. The dotted lines show the extent of these unphysical oscillations. The curves are offset vertically for clarity of presentation.

Table 5.4: Bond distances $r_{\alpha\beta}$ and coordination numbers $\bar{n}_{\alpha}^{\beta}$ obtained for the first-order difference functions $\Delta G_{\mathrm{no}\ \alpha\beta}(r)$ for glassy GeSe$_3$. The latter were obtained by integrating over the range given in the table for the functions shown in figures 5-15 and 5-17.

$\Delta G_{\mathrm{no\ GeSe}}(r)$	$\bar{n}_{\mathrm{Se}}^{\mathrm{Se}}$	r_{SeSe}/Å	range/Å
$^{73,76-70,\mathrm{Nat}}\Delta G(r)$	0.76(2)	2.35(2)	2.148-2.516
$^{73,76-\mathrm{Nat},\mathrm{Nat}}\Delta G(r)$	0.76(2)	2.35(2)	2.148-2.516
$^{73,76-\mathrm{Nat},\mathrm{Mix}}\Delta G(r)$	0.75(2)	2.34(2)	2.148-2.516
$^{\mathrm{Nat},\mathrm{Mix}-70,\mathrm{Nat}}\Delta G(r)$	0.78(2)	2.35(2)	2.148-2.516
$^{\mathrm{Nat},\mathrm{Mix}-\mathrm{Nat},\mathrm{Nat}}\Delta G(r)$	0.81(2)	2.35(2)	2.148-2.516
$^{\mathrm{Nat},\mathrm{Nat}-70,\mathrm{Nat}}\Delta G(r)$	0.75(2)	2.34(2)	2.148-2.516
$\Delta G_{\mathrm{no\ SeSe}}(r)$	$\bar{n}_{\mathrm{Ge}}^{\mathrm{Se}}$	r_{GeSe}/Å	range /Å
$^{70,\mathrm{Nat}-73,76}\Delta G(r)$	4.15(2)	2.36(2)	2.148-2.516
$^{\mathrm{Nat},\mathrm{Nat}-73,76}\Delta G(r)$	4.14(2)	2.36(2)	2.148-2.516
$^{\mathrm{Nat},\mathrm{Mix}-73,76}\Delta G(r)$	4.18(2)	2.36(2)	2.148-2.516
$^{70,\mathrm{Nat}-\mathrm{Nat},\mathrm{Mix}}\Delta G(r)$	4.13(2)	2.36(2)	2.148-2.516
$^{\mathrm{Nat},\mathrm{Nat}-\mathrm{Nat},\mathrm{Mix}}\Delta G(r)$	4.08(2)	2.36(2)	2.148-2.516
$^{70,\mathrm{Nat}-\mathrm{Nat},\mathrm{Nat}}\Delta G(r)$	4.18(2)	2.36(2)	2.148-2.516

Table 5.5: Bond distances $r_{\alpha\beta}$ and coordination numbers $\bar{n}_{\alpha}^{\beta}$ from the RDFgenie fits to the measured first order difference functions for glassy GeSe$_3$ with $Q_{\mathrm{max}} = 23$ Å^{-1}. The R_{χ} goodness-of-fit parameter is defined in equation 2.46.

$\Delta G_{\mathrm{no\ GeSe}}(r)$	$\bar{n}_{\mathrm{Se}}^{\mathrm{Se}}$	r_{SeSe}/Å	$\bar{n}_{\mathrm{Ge}}^{\mathrm{Se}}$	r_{GeSe}/Å	R_{χ}
${}^{73,76-70,\mathrm{Nat}}\Delta G(r)$	0.72(2)	2.35(2)	-	-	0.048
${}^{73,76-\mathrm{Nat},\mathrm{Nat}}\Delta G(r)$	0.71(2)	2.35(2)	-	-	0.049
${}^{73,76-\mathrm{Nat},\mathrm{Mix}}\Delta G(r)$	0.71(2)	2.35(2)	-	-	0.049
${}^{\mathrm{Nat},\mathrm{Mix}-70,\mathrm{Nat}}\Delta G(r)$	0.72(2)	2.35(2)	-	-	0.060
${}^{\mathrm{Nat},\mathrm{Nat}-\mathrm{Nat},\mathrm{Mix}}\Delta G(r)$	0.77(2)	2.35(2)	-	-	0.063
${}^{\mathrm{Nat},\mathrm{Nat}-70,\mathrm{Nat}}\Delta G(r)$	0.71(2)	2.35(2)	-	-	0.150
$\Delta G_{\mathrm{no\ SeSe}}(r)$	$\bar{n}_{\mathrm{Se}}^{\mathrm{Se}}$	r_{SeSe}/Å	$\bar{n}_{\mathrm{Ge}}^{\mathrm{Se}}$	r_{GeSe}/Å	R_{χ}
${}^{70,\mathrm{Nat}-73,76}\Delta G(r)$	-	-	4.02(2)	2.37(2)	0.055
${}^{\mathrm{Nat},\mathrm{Nat}-73,76}\Delta G(r)$	-	-	3.99(2)	2.37(2)	0.053
${}^{\mathrm{Nat},\mathrm{Mix}-73,76}\Delta G(r)$	-	-	4.00(2)	2.37(2)	0.051
${}^{70,\mathrm{Nat}-\mathrm{Nat},\mathrm{Mix}}\Delta G(r)$	-	-	3.99(2)	2.37(2)	0.059
${}^{\mathrm{Nat},\mathrm{Nat}-\mathrm{Nat},\mathrm{Mix}}\Delta G(r)$	-	-	3.96(2)	2.37(2)	0.063
${}^{70,\mathrm{Nat}-\mathrm{Nat},\mathrm{Nat}}\Delta G(r)$	-	-	4.00(2)	2.37(2)	0.071
$\Delta G_{\mathrm{no\ GeGe}}(r)$	$\bar{n}_{\mathrm{Se}}^{\mathrm{Se}}$	r_{SeSe}/Å	$\bar{n}_{\mathrm{Ge}}^{\mathrm{Se}}$	r_{GeSe}/Å	R_{χ}
${}^{73,76-70,\mathrm{Nat}}\Delta G(r)$	0.72(2)	2.35(2)	4.02(2)	2.37(2)	0.065
${}^{73,76-\mathrm{Nat},\mathrm{Nat}}\Delta G(r)$	0.71(2)	2.35(2)	3.99(2)	2.37(2)	0.051
${}^{73,76-\mathrm{Nat},\mathrm{Mix}}\Delta G(r)$	0.71(2)	2.35(2)	4.00(2)	2.37(2)	0.050
${}^{\mathrm{Nat},\mathrm{Mix}-70,\mathrm{Nat}}\Delta G(r)$	0.72(2)	2.35(2)	3.99(2)	2.37(2)	0.065
${}^{\mathrm{Nat},\mathrm{Nat}-\mathrm{Nat},\mathrm{Mix}}\Delta G(r)$	0.77(2)	2.35(2)	3.96(2)	2.37(2)	0.048
${}^{\mathrm{Nat},\mathrm{Nat}-70,\mathrm{Nat}}\Delta G(r)$	0.71(2)	2.35(2)	4.00(2)	2.37(2)	0.053

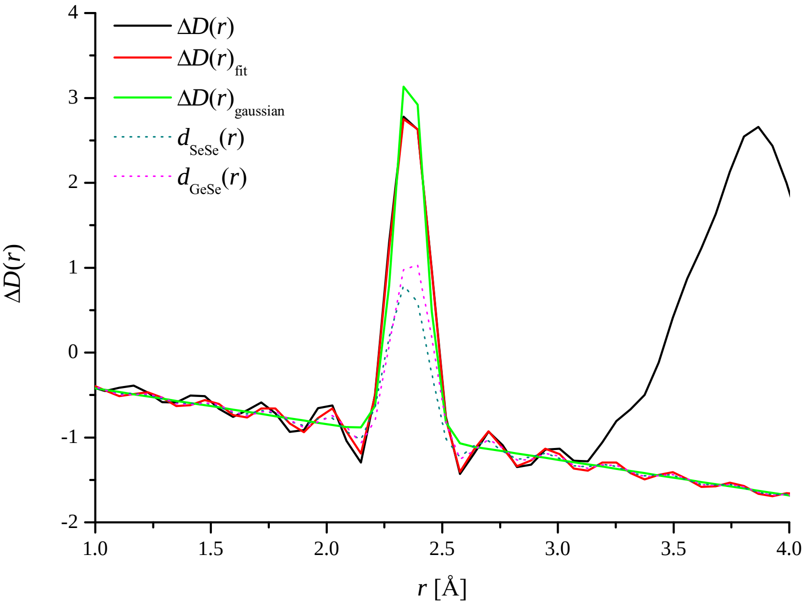

Figure 5-18: The first peak in the measured ${}^{73,76-70,\mathrm{Nat}}\Delta D(r)$ function for glassy GeSe$_3$ (solid black curve), fitted with two Gaussians convoluted with a sinc function using RDFgenie (solid red curve). The sum of the fitted Gaussians is given by the solid green curve. The dark green and magenta broken curves shown the contributions from $d_{\mathrm{SeSe}}(r)$ and $d_{\mathrm{GeSe}}(r)$, respectively. The fit has an R_χ goodness-of-fit parameter of 0.065.

$GeSe_4$

There are six weighted difference functions that can be calculated from the four total structure factors. Figures 5-19 – 5-24 shows these difference functions in both reciprocal and real space. A summary of the corresponding bond distances and coordination numbers is given in table 5.6.

The bond distances and coordination numbers were obtained from the measured $\Delta G_{\text{no GeSe}}(r)$ and $\Delta G_{\text{no SeSe}}(r)$ difference functions (i) by integrating over the first peak in $\Delta G(r)$ (see table 5.6) or (ii) by fitting a Gaussian function to the first peak in $\Delta D(r)$ using the RDFgenie program (see table 5.7). In both of these procedures it was assumed that there are no Ge-Ge homopolar bonds under the first peak, then it is possible to obtain Ge-Se and Se-Se coordination numbers from the $\Delta G_{\text{no SeSe}}(r)$ and $\Delta G_{\text{no GeSe}}(r)$ difference functions, respectively. This assumption is consistent with the $GeSe_4$ stoichiometry which places it on the Se-rich side of the Ge_xSe_{1-x}system. The first peak in $\Delta G_{\text{no GeGe}}(r)$ has contributions from the Ge-Se and Se-Se partial pair-distribution functions. The bond distances and coordination numbers were obtained by fitting two Gaussians to the first peak in $\Delta D(r)$ using the RDFgenie program (Figure 5-25), and the results are given in table 5.7. The coordination numbers are consistent with those found for the $\Delta G_{\text{no SeSe}}(r)$ and $\Delta G_{\text{no GeSe}}(r)$ difference functions.

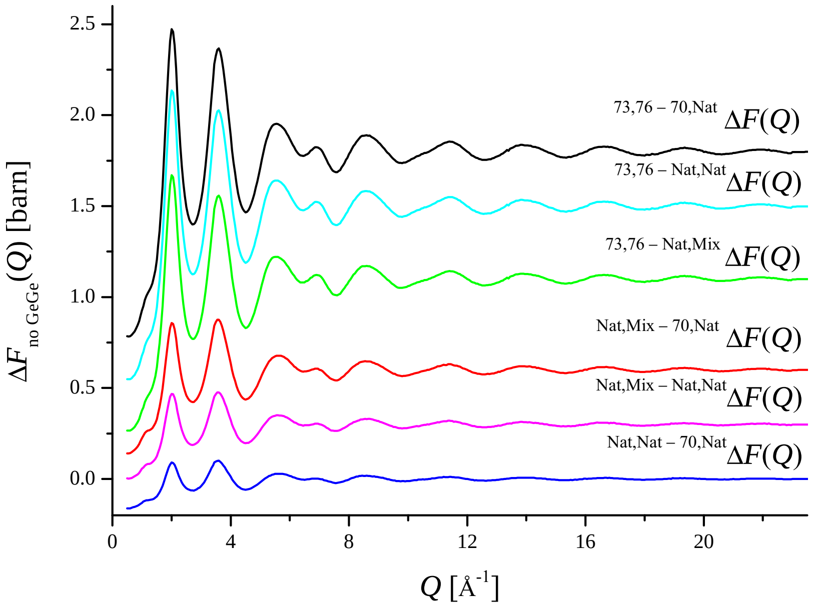

Figure 5-19: The measured first-order difference functions $\Delta F_{\text{no GeGe}}(Q)$ for glassy $GeSe_4$, as defined by equation 5.11. The error bars are smaller than the line thickness. The curves are offset vertically for clarity of presentation.

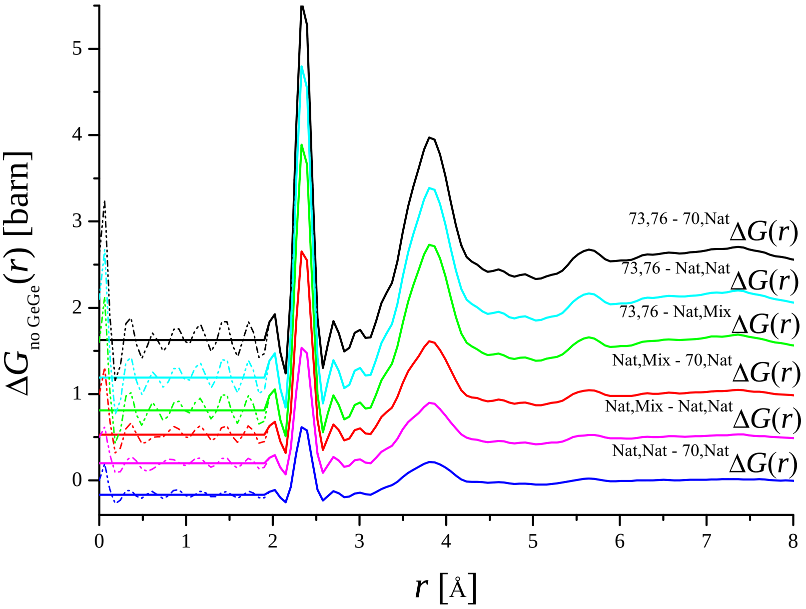

Figure 5-20: The first-order difference pair-distribution functions $\Delta G_{\text{no GeGe}}(r)$ for glassy GeSe$_4$. The solid curves are obtained by Fourier transforming the first-order difference functions $\Delta F_{\text{no GeGe}}(Q)$ shown in figure 5-19. The low-r oscillations have been set to their theoretical $\Delta G_{\text{no GeGe}}(r \to 0)$ limit. The dotted lines show the extent of these unphysical oscillations. The curves are offset vertically for clarity of presentation.

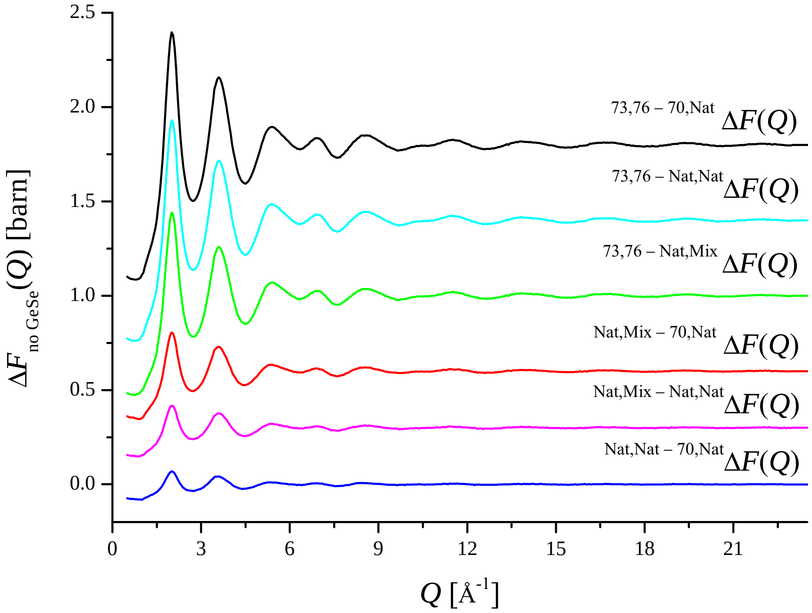

Figure 5-21: The measured first-order difference functions $\Delta F_{\text{no GeSe}}(Q)$ for glassy $GeSe_4$, as defined by equation 5.13. The error bars are smaller than the line thickness. The curves are offset vertically for clarity of presentation.

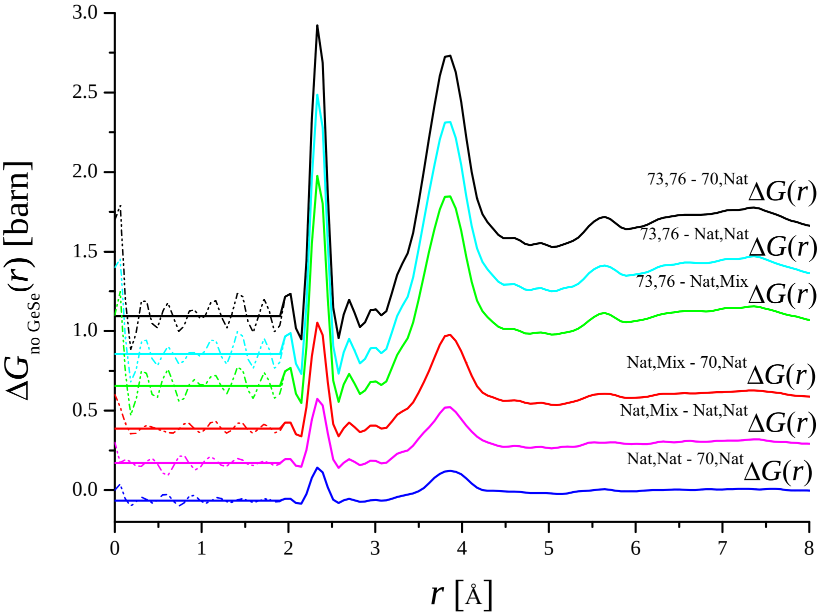

Figure 5-22: The first-order difference pair-distribution functions $\Delta G_{\text{no GeSe}}(r)$ for glassy GeSe_4. The solid curves are obtained by Fourier transforming the first-order difference functions $\Delta F_{\text{no GeSe}}(Q)$ shown in figure 5-21. The low-r oscillations have been set to their theoretical $\Delta G_{\text{no GeSe}}(r \to 0)$ limit. The dotted lines show the extent of these unphysical oscillations. The curves are offset vertically for clarity of presentation.

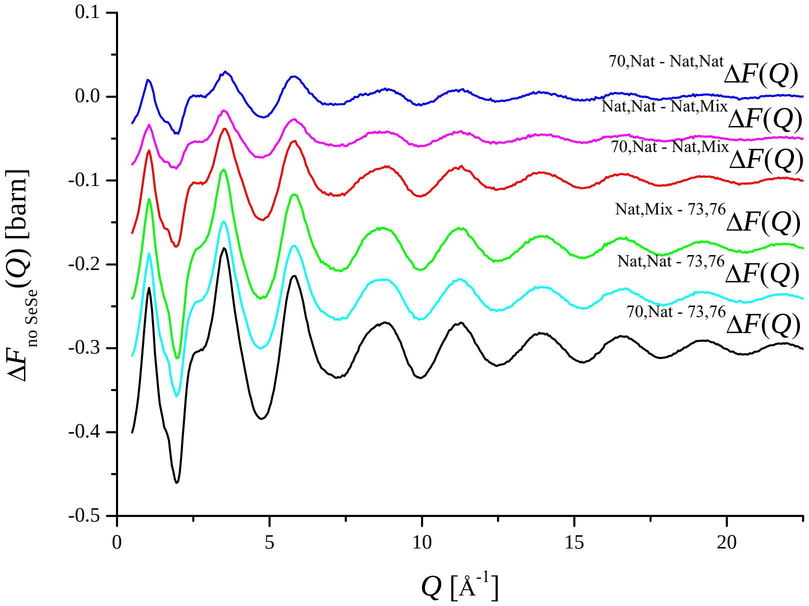

Figure 5-23: The measured first-order difference functions $\Delta F_{\text{no SeSe}}(Q)$ for glassy GeSe_4, as defined by equation 5.12. The error bars are smaller than the line thickness. The curves are offset vertically for clarity of presentation.

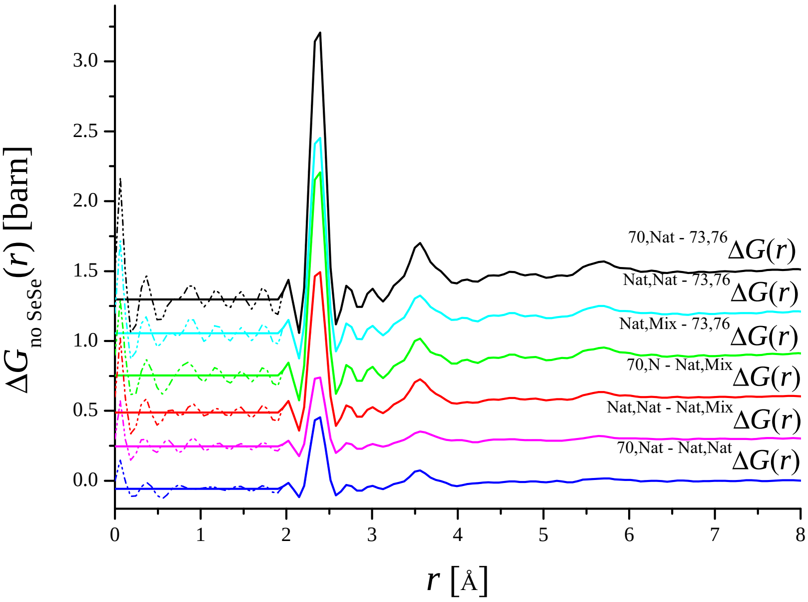

Figure 5-24: The first-order difference pair-distribution functions $\Delta G_{\text{no SeSe}}(r)$ for glassy GeSe$_4$. The solid curves are obtained by Fourier transforming the first-order difference functions $\Delta F_{\text{no SeSe}}(Q)$ shown in figure 5-23. The low-r oscillations have been set to their theoretical $\Delta G_{\text{no SeSe}}(r \to 0)$ limit. The dotted lines show the extent of these unphysical oscillations. The curves are offset vertically for clarity of presentation.

Table 5.6: Bond distances $r_{\alpha\beta}$ and coordination numbers $\bar{n}_{\alpha}^{\beta}$ for the measured first-order difference functions $\Delta G_{\text{no }\alpha\beta}(r)$ for glassy GeSe$_4$. The latter were obtained by integrating over the range given in the table for the functions shown in figures 5-22 and 5-24.

$\Delta G_{\text{no GeSe}}(r)$	$\bar{n}_{\text{Se}}^{\text{Se}}$	r_{SeSe}/Å	range/Å
$^{73,76-70,\text{Nat}}\Delta G(r)$	1.06(2)	2.35(2)	2.148-2.516
$^{73,76-\text{Nat},\text{Nat}}\Delta G(r)$	1.06(2)	2.35(2)	2.148-2.516
$^{73,76-\text{Nat},\text{Mix}}\Delta G(r)$	1.05(2)	2.34(2)	2.148-2.516
$^{\text{Nat},\text{Mix}-70,\text{Nat}}\Delta G(r)$	1.08(2)	2.35(2)	2.148-2.516
$^{\text{Nat},\text{Mix}-\text{Nat},\text{Nat}}\Delta G(r)$	1.11(2)	2.35(2)	2.148-2.516
$^{\text{Nat},\text{Nat}-70,\text{Nat}}\Delta G(r)$	1.04(2)	2.35(2)	2.148-2.516
$\Delta G_{\text{no SeSe}}(r)$	$\bar{n}_{\text{Ge}}^{\text{Se}}$	r_{GeSe}/Å	range /Å
$^{70,\text{Nat}-73,76}\Delta G(r)$	4.29(2)	2.37(2)	2.148-2.516
$^{\text{Nat},\text{Nat}-73,76}\Delta G(r)$	4.29(2)	2.37(2)	2.148-2.516
$^{\text{Nat},\text{Mix}-73,76}\Delta G(r)$	4.33(2)	2.36(2)	2.148-2.516
$^{70,\text{Nat}-\text{Nat},\text{Mix}}\Delta G(r)$	4.26(2)	2.37(2)	2.148-2.516
$^{\text{Nat},\text{Nat}-\text{Nat},\text{Mix}}\Delta G(r)$	4.20(2)	2.37(2)	2.148-2.516
$^{70,\text{Nat}-\text{Nat},\text{Nat}}\Delta G(r)$	4.32(2)	2.37(2)	2.148-2.516

Table 5.7: Bond distances $r_{\alpha\beta}$ and coordination numbers $\bar{n}_{\alpha}^{\beta}$ from the RDFgenie fits to the measured first order difference functions for glassy GeSe$_4$ with $Q_{\text{max}} = 23$ Å^{-1}. The R_χ goodness-of-fit parameter is defined in equation 2.46.

$\Delta G_{\text{no GeSe}}(r)$	$\bar{n}_{\text{Se}}^{\text{Se}}$	r_{SeSe}/Å	$\bar{n}_{\text{Ge}}^{\text{Se}}$	r_{GeSe}/Å	R_χ
${}^{73,76-70,\text{Nat}}\Delta G(r)$	1.01(2)	2.35(2)	-	-	0.052
${}^{73,76-\text{Nat},\text{Nat}}\Delta G(r)$	0.99(2)	2.35(2)	-	-	0.049
${}^{73,76-\text{Nat},\text{Mix}}\Delta G(r)$	1.00(2)	2.35(2)	-	-	0.048
${}^{\text{Nat},\text{Mix}-70,\text{Nat}}\Delta G(r)$	1.05(2)	2.35(2)	-	-	0.034
${}^{\text{Nat},\text{Nat}-\text{Nat},\text{Mix}}\Delta G(r)$	1.08(2)	2.35(2)	-	-	0.045
${}^{\text{Nat},\text{Nat}-70,\text{Nat}}\Delta G(r)$	1.03(2)	2.35(2)	-	-	0.045
$\Delta G_{\text{no SeSe}}(r)$	$\bar{n}_{\text{Se}}^{\text{Se}}$	r_{SeSe}/Å	$\bar{n}_{\text{Ge}}^{\text{Se}}$	r_{GeSe}/Å	R_χ
${}^{70,\text{Nat}-73,76}\Delta G(r)$	-	-	4.11(2)	2.37(2)	0.064
${}^{\text{Nat},\text{Nat}-73,76}\Delta G(r)$	-	-	4.07(2)	2.37(2)	0.053
${}^{\text{Nat},\text{Mix}-73,76}\Delta G(r)$	-	-	4.17(2)	2.37(2)	0.050
${}^{70,\text{Nat}-\text{Nat},\text{Mix}}\Delta G(r)$	-	-	4.02(2)	2.37(2)	0.024
${}^{\text{Nat},\text{Nat}-\text{Nat},\text{Mix}}\Delta G(r)$	-	-	4.08(2)	2.37(2)	0.065
${}^{70,\text{Nat}-\text{Nat},\text{Nat}}\Delta G(r)$	-	-	4.08(2)	2.37(2)	0.057
$\Delta G_{\text{no GeGe}}(r)$	$\bar{n}_{\text{Se}}^{\text{Se}}$	r_{SeSe}/Å	$\bar{n}_{\text{Ge}}^{\text{Se}}$	r_{GeSe}/Å	R_χ
${}^{73,76-70,\text{Nat}}\Delta G(r)$	1.01(2)	2.35(2)	4.11(2)	2.37(2)	0.067
${}^{73,76-\text{Nat},\text{Nat}}\Delta G(r)$	1.05(2)	2.35(2)	4.02(2)	2.37(2)	0.061
${}^{73,76-\text{Nat},\text{Mix}}\Delta G(r)$	1.00(2)	2.35(2)	4.17(2)	2.37(2)	0.048
${}^{\text{Nat},\text{Mix}-70,\text{Nat}}\Delta G(r)$	1.03(2)	2.35(2)	4.08(2)	2.37(2)	0.061
${}^{\text{Nat},\text{Nat}-\text{Nat},\text{Mix}}\Delta G(r)$	0.99(2)	2.35(2)	4.07(2)	2.37(2)	0.044
${}^{\text{Nat},\text{Nat}-70,\text{Nat}}\Delta G(r)$	1.08(2)	2.35(2)	4.08(2)	2.37(2)	0.045

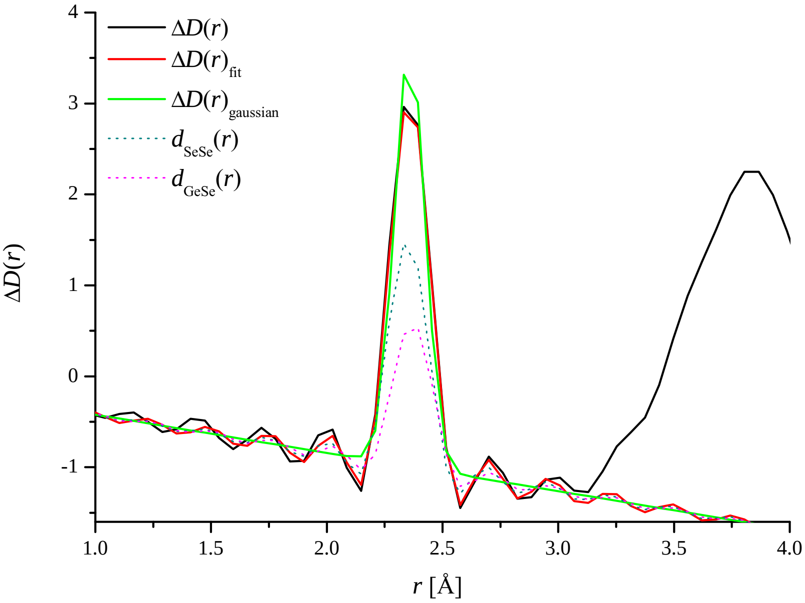

Figure 5-25: The first peak in the measured $^{73,76-70,\mathrm{Nat}}\Delta D(r)$ function for glassy GeSe$_4$ (solid black curve), fitted with two Gaussians convoluted with a sinc function using RDFgenie (solid red curve). The sum of the fitted Gaussians is given by the solid green curve. The dark green and magenta broken curves shown the contributions from $d_{\mathrm{SeSe}}(r)$ and $d_{\mathrm{GeSe}}(r)$, respectively. The fit has an R_χ goodness-of-fit parameter of 0.067.

5.4.3 Faber-Ziman partial structure factors

$\mathbf{GeSe_3}$

As four total structure factors were measured for $GeSe_3$ the solution for the Faber-Ziman partial structure factors is over-constrained and can be found from a singular value decomposition (SVD) analysis. The partial structure factors calculated from the ${}^{\mathrm{Nat}}_{\mathrm{Mix}}F(Q)$, ${}^{70}_{\mathrm{Nat}}F(Q)$ and ${}^{73}_{76}F(Q)$ total structure factors are labelled as set A, whilst the partial structure factors calculated from the ${}^{\mathrm{Nat}}_{\mathrm{Nat}}F(Q)$, ${}^{70}_{\mathrm{Nat}}F(Q)$ and ${}^{73}_{76}F(Q)$ total structure factors are labelled as set B. The reciprocal and real space data sets obtained from the SVD analysis are shown in figures 5-26 and 5-27, respectively.

As mentioned in chapter 2, the determinant of a square matrix $|A|$ normalised by dividing each row i by $\sum_{\alpha}\sum_{\beta} c_{\alpha}c_{\beta}b_{\alpha,i}b_{\beta,i}$ can be used as a measure of the conditioning of the matrix. If the determinant of the normalised matrix is small compared with ±1, the system is ill-conditioned [27]. For the set A partial structure factors $|A| = 0.0066$, and for the set B partial structure factors $|A| = 0.0048$, indicating that set A is better conditioned. The relative conditioning of the matrix gives an indication of how sensitive the partial structure factors are to uncertainties $\delta F(Q)$ in the total structure factors $F(Q)$.

An alternative measure of the conditioning of a matrix $\mathbf{A}$ is to calculate the two-norm condition number of the matrix, sometimes known as the Turing number [27, 28]. The two-norm condition number is given by $\kappa_2 = \sigma_1/\sigma_n$, where σ_1 and σ_n are the largest and smallest singular values of matrix $\mathbf{A}$, respectively. Thus $\kappa_2 \geq 1$, and values near unity indicate a well conditioned matrix [27, 28]. Often the two-norm condition number κ_2' of the normalised matrix $\mathbf{A}'$ is quoted, where the ith row of matrix $\mathbf{A}$ is divided by $\sum_{\alpha}\sum_{\beta} c_{\alpha}c_{\beta}b_{\alpha,i}b_{\beta,i}$ [28]. The normalised two-norm condition number for the SVD partial structure factors is $\kappa_2' = 144$, which compares to $\kappa_2' = 133$ for the Set A partial structure factors and $\kappa_2' = 190$ for the Set B partial structure factors. Hence, the conditioning of the SVD and Set A matrices is similar, (i.e. and that the inclusion of the ${}^{\mathrm{Nat}}_{\mathrm{Nat}}F(Q)$ total structure factor in the SVD does not improve the conditioning of the matrix.) whereas the Set B matrix is less well conditioned. As $b_{^{\mathrm{Nat}}\mathrm{Ge}} \simeq b_{^{\mathrm{Nat}}\mathrm{Se}}$ it follows that $S^{\mathrm{BT}}_{\mathrm{NN}}(Q) = {}^{\mathrm{Nat}}_{\mathrm{Nat}}F(Q)/\langle b\rangle^2$ (see section 5.4.1), and the measured structure factor does not contain information on the chemical ordering of the system.

Figures 5-28 and 5-29 show a closer comparison of the partial pair-correlation functions obtained from the three best constrained methods of calculating the real and reciprocal space partials. The bond distances and coordination numbers for the peaks in the $g_{\alpha\beta}(r)$ functions are given in table 5-29. The reciprocal space differences functions obtained from SVD, set A and set B are shown in figure 5-28. The best constrained partial structure factor is $S_{\mathrm{SeSe}}(Q)$ and the data sets obtained from the different methods are all in excellent agreement. The $S_{\mathrm{GeSe}}(Q)$ functions obtained from the different methods are also consistent, except for the low-Q values. The $S_{\mathrm{GeGe}}(Q)$ partial structure factor is the most difficult to obtain, which leads to the largest discrepancies between the (i) set B and (ii) SVD and set A results. The relative conditioning of the partial structure factors can be inferred from the magnitude of the weighting factors given in equation 5.4.

The $g_{\mathrm{SeSe}}(r)$ functions shown in figure 5.8, obtained from the different methods are all in excellent agreement. The $g_{\mathrm{GeSe}}(r)$ functions obtained from the SVD, set A and set B are also consistent, except for the height of the Ge-Se peak for the set B data set and a discrepancy at $\simeq 4$ Å. The $g_{\mathrm{GeGe}}(r)$ functions found from SVD and set A agree very well (Figure 5.8). However, set B shows a sharper peak at ~ 3 Å, and less of a high-r tail on the main Ge-Ge peak at 3.58(2) Å. It is likely that the discrepancies originate from the relatively poor conditioning of the Set B results compared to the Set A and the SVD results. Note that the difference in shape of the second Ge-Ge peak leads to the different integration ranges given in table 5.8.

The first peaks in $d_{\mathrm{GeSe}}(r)$ and $d_{\mathrm{SeSe}}(r)$ for the SVD, set A and set B results were fitted to a Gaussian convoluted with a sinc function using RDFgenie. The results for the SVD data sets are shown in figures 5-30 and 5-31. The bond distances and coordination numbers obtained from these RDFgenie fits are given in table 5.9, and agree with the values found from the first-order difference functions that are given in table 5.5.

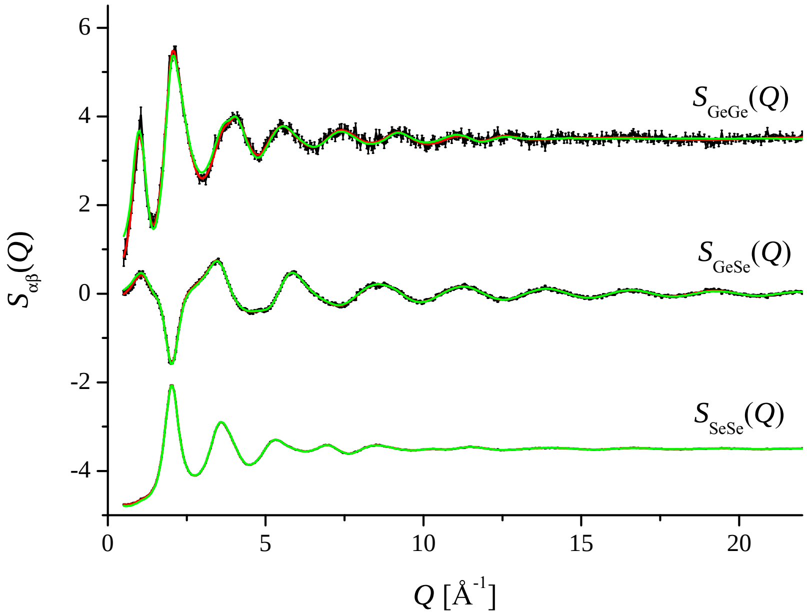

Figure 5-26: Faber-Ziman partial structure factors for glassy $GeSe_3$ obtained from the SVD analysis, offset vertically for clarity of presentation. The data sets (solid black curves) with vertical error bars are shown along with the back Fourier transforms of the corresponding unsmoothed $g_{\alpha\beta}(r)$ functions shown in figure 5-27 (solid red curves) and the Harwell spline fits (solid green curves).

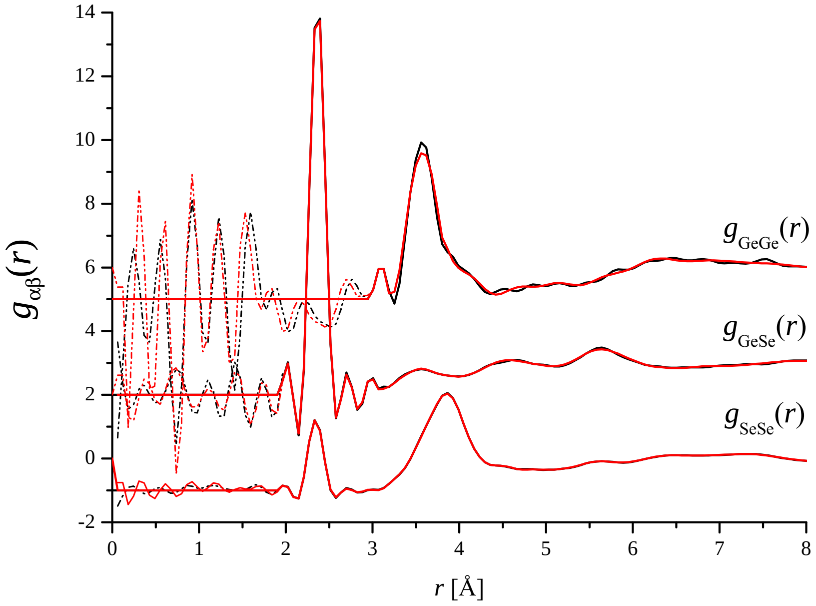

Figure 5-27: Partial pair-distribution functions for glassy $GeSe_3$ obtained from the SVD analysis. The black curves were obtained by Fourier transforming the Faber-Ziman partial structure factors $S_{\alpha\beta}(Q)$ shown in figure 5-26. The red curves were obtained by Fourier transforming the Harwell spline fits to the Faber-Ziman partial structure factors shown in figure 5-26. The solid lines show these functions after the low-r oscillations (dotted lines) have been set to their theoretical $g_{\alpha\beta}(r \to 0) = 0$ limit.

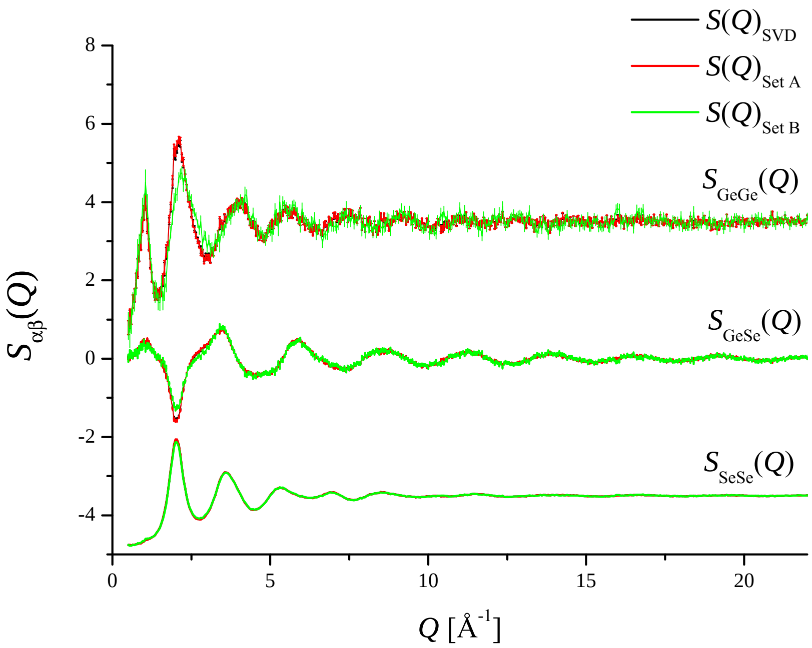

Figure 5-28: Faber-Ziman partial structure factors $S_{\alpha\beta}(Q)$ for glassy GeSe$_3$ calculated from the SVD analysis and from 2 sets of three total structure factors. Set A combines the total structure factors for $^{\mathrm{Nat}}\mathrm{Ge}^{\mathrm{Mix}}\mathrm{Se}_3$, $^{70}\mathrm{Ge}^{\mathrm{Nat}}\mathrm{Se}_3$ and $^{73}\mathrm{Ge}^{76}\mathrm{Se}_3$. Set B combines the total structure factors for $^{\mathrm{Nat}}\mathrm{Ge}^{\mathrm{Nat}}\mathrm{Se}_3$, $^{70}\mathrm{Ge}^{\mathrm{Nat}}\mathrm{Se}_3$ and $^{73}\mathrm{Ge}^{76}\mathrm{Se}_3$. The datasets have been offset vertically for clarity of presentation. Note that the black curves for $S_{\alpha\beta}(Q)_{\mathrm{SVD}}$ lie underneath the red curves for $S_{\alpha\beta}(Q)_{\mathrm{Set\,A}}$.

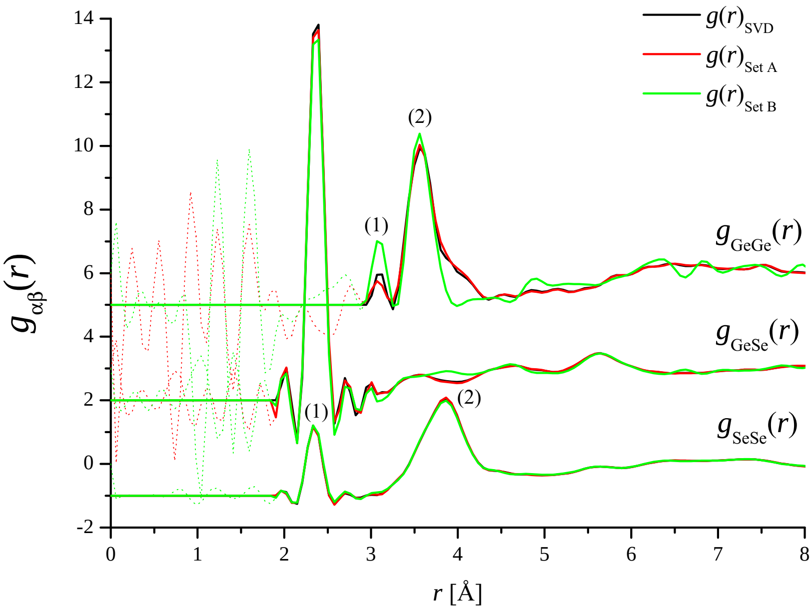

Figure 5-29: Partial pair-distribution functions for glassy $GeSe_3$ calculated from the SVD analysis and from 2 sets of three total structure factors. The data sets were obtained by Fourier transforming the Faber-Ziman partial structure factors $S_{\alpha\beta}(Q)$ shown in figure 5-28 for sets A and B. The solid lines show these functions after the low-r oscillations (dotted lines) have been set to their theoretical $g_{\alpha\beta}(r \to 0) = 0$ limit. Set A combines the total structure factors for $^{\mathrm{Nat}}\mathrm{Ge}^{\mathrm{Mix}}\mathrm{Se}_3$, $^{70}\mathrm{Ge}^{\mathrm{Nat}}\mathrm{Se}_3$ and $^{73}\mathrm{Ge}^{76}\mathrm{Se}_3$. Set B combines the total structure factors for $^{\mathrm{Nat}}\mathrm{Ge}^{\mathrm{Nat}}\mathrm{Se}_3$, $^{70}\mathrm{Ge}^{\mathrm{Nat}}\mathrm{Se}_3$ and $^{73}\mathrm{Ge}^{76}\mathrm{Se}_3$. The datasets have been offset vertically for clarity of presentation. Note that the black curves for $g_{\alpha\beta}(r)_{\mathrm{SVD}}$ lie underneath the red curves for $g_{\alpha\beta}(r)_{\mathrm{Set\,A}}$. The numbered peaks in the $g_{\mathrm{GeGe}}(r)$ and $g_{\mathrm{SeSe}}(r)$ functions correspond to the bond distances and coordination numbers given in table 5.8.

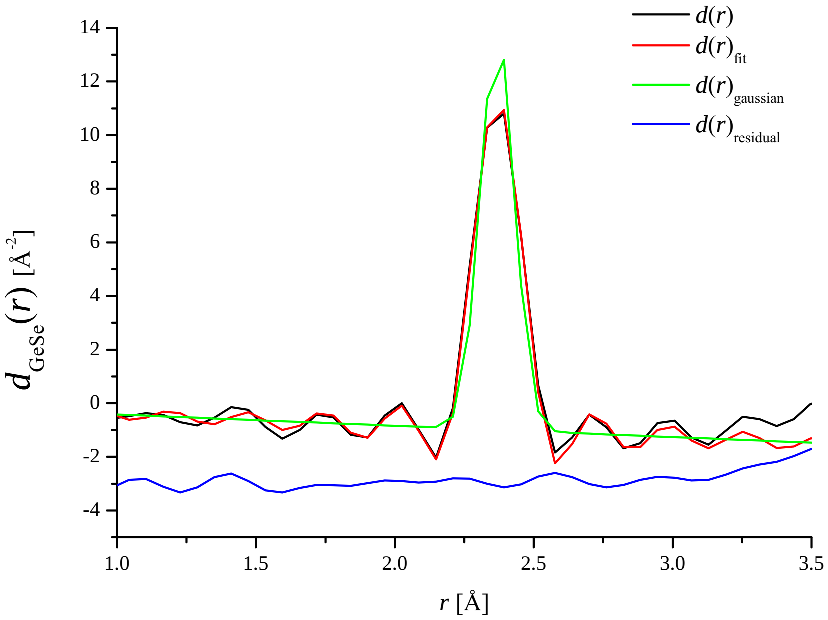

Figure 5-30: The first peak in the SVD generated $d_{\text{GeSe}}(r)$ function for glassy GeSe$_3$ (solid black curve), fitted with a Gaussian convoluted with a sinc function using RDF-genie (solid red curve). The resulting fitted Gaussian in $d_{\text{GeSe}}(r)$ is given by the solid green curve, and the residual is given by the solid blue curve.

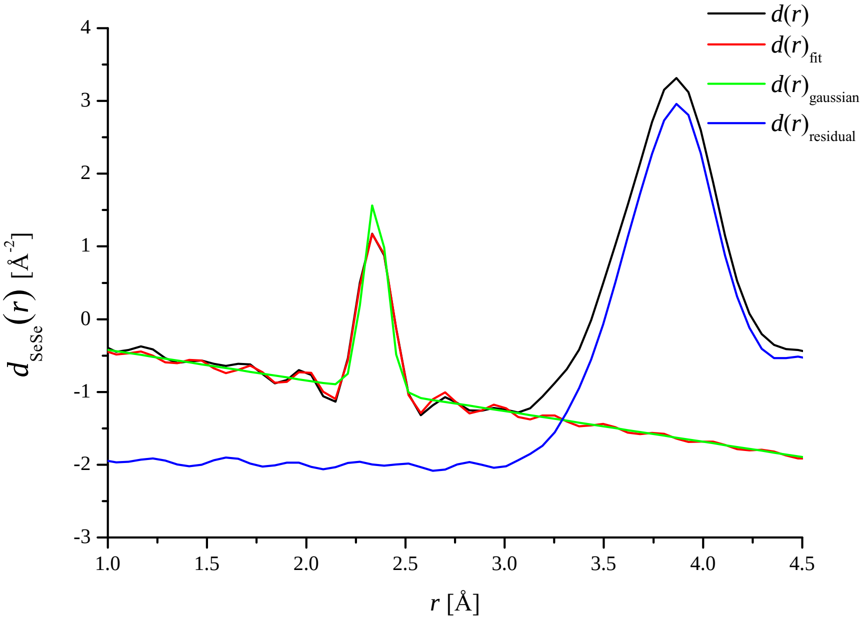

Figure 5-31: The first peak in the SVD generated $d_{\text{SeSe}}(r)$ function for glassy GeSe$_3$ (solid black curve), fitted with a Gaussian convoluted with a sinc function using RDF-genie (solid red curve). The resulting fitted Gaussian in $d_{\text{SeSe}}(r)$ is given by the solid green curve, and the residual is given by the solid blue curve.

Table 5.8: Bond distances $r_{\alpha\beta}$ and coordination numbers $\bar{n}_{\alpha}^{\beta}$ from the partial pair-distribution functions for glassy $GeSe_3$. The latter were obtained by integrating over the range given in the table for the functions shown in figure 5-29. Set A combines the total structure factors for ${}^{Nat}Ge^{Mix}Se_3$, ${}^{70}Ge^{Nat}Se_3$ and ${}^{73}Ge^{76}Se_3$. Set B combines the total structure factors for ${}^{Nat}Ge^{Nat}Se_3$, ${}^{70}Ge^{Nat}Se_3$ and ${}^{73}Ge^{76}Se_3$.

$g_{\mathrm{GeGe}}(r)$	$\bar{n}_{\mathrm{Ge}}^{\mathrm{Ge}}$ (1)	r_{GeGe} (1) /Å	range/ Å	$\bar{n}_{\mathrm{Ge}}^{\mathrm{Ge}}$ (2)	r_{GeGe} (2) /Å	range/ Å
SVD	0.08(3)	2.94(3)	2.945 - 3.129	3.08(3)	3.58(2)	3.191 - 4.357
Set A	0.17(3)	3.02(3)	2.700 - 3.129	3.17(3)	3.59(2)	3.191 - 4.357
Set B	0.36(3)	3.07(3)	2.884 - 3.191	2.15(3)	3.59(3)	3.252 - 3.866
$g_{\mathrm{SeSe}}(r)$	$\bar{n}_{\mathrm{Se}}^{\mathrm{Se}}$ (1)	r_{SeSe} (1) /Å	range/ Å	$\bar{n}_{\mathrm{Se}}^{\mathrm{Se}}$ (2)	r_{SeSe} (2) /Å	range/ Å
SVD	0.74(2)	2.34(2)	2.148 - 2.516	9.22(3)	3.85(3)	2.945 - 4.357
Set A	0.73(2)	2.34(2)	2.148 - 2.516	9.24(3)	3.86(3)	3.068 - 4.357
Set B	0.78(2)	2.35(2)	2.148 - 2.516	9.12(3)	3.85(3)	2.945 - 4.357
$g_{\mathrm{GeSe}}(r)$	$\bar{n}_{\mathrm{Ge}}^{\mathrm{Se}}$	r_{GeSe}/Å	range/ Å			
SVD	4.24(2)	2.37(2)	2.148 - 2.516			
Set A	4.22(2)	2.37(2)	2.148 - 2.516			
Set B	4.09(2)	2.36(2)	2.148 - 2.516			

Table 5.9: Bond distances and coordination numbers from the RDFgenie fits to the first peak in the SVD generated $d_{\alpha\beta}(r)$ functions for glassy GeSe$_3$, as shown in figures 5-30 and 5-31 with $Q_{\max} = 23$ Å^{-1}. The R_χ goodness-of-fit parameter is defined in equation 2.46. Set A combines the total structure factors for $^{\mathrm{Nat}}$Ge$^{\mathrm{Mix}}$Se$_3$, ^{70}Ge$^{\mathrm{Nat}}$Se$_3$ and ^{73}Ge^{76}Se$_3$. Set B combines the total structure factors for $^{\mathrm{Nat}}$Ge$^{\mathrm{Nat}}$Se$_3$, ^{70}Ge$^{\mathrm{Nat}}$Se$_3$ and ^{73}Ge^{76}Se$_3$.

$g(r)$	$\bar{n}_{\mathrm{Ge}}^{\mathrm{Se}}$	r_{GeSe}/Å	R_χ	$\bar{n}_{\mathrm{Se}}^{\mathrm{Se}}$	r_{SeSe}/Å	R_χ
$g(r)_{\mathrm{SVD}}$	3.99(2)	2.37(2)	0.048	0.70(2)	2.35(2)	0.047
$g(r)_{\mathrm{Set\,A}}$	4.04(2)	2.37(2)	0.050	0.72(2)	2.35(2)	0.060
$g(r)_{\mathrm{Set\,B}}$	3.95(2)	2.37(2)	0.095	0.74(2)	2.35(2)	0.122

GeSe$_4$

The Faber-Ziman partial structure factors for GeSe$_4$ can be calculated by using any set of three total structure factors, or by using all four in a singular value decomposition (SVD). However, some of these sets of partials are better conditioned than others, and for simplicity only the three best constrained data sets will be presented. The partial structure factors that are calculated from the ${}^{\mathrm{Nat}}_{\mathrm{Mix}}F(Q)$, ${}^{70}_{\mathrm{Nat}}F(Q)$ and ${}^{73}_{76}F(Q)$ total structure factors are labelled as set A, while the partial structure factors calculated from the ${}^{\mathrm{Nat}}_{\mathrm{Nat}}F(Q)$, ${}^{70}_{\mathrm{Nat}}F(Q)$ and ${}^{73}_{76}F(Q)$ total structure factors are labelled as set B. Figures 5-32 and 5-33 show the reciprocal and real space data sets obtained from the SVD analysis, respectively.

As mentioned in chapter 2, the determinant of a square matrix $|A|$ normalised by dividing each row i by $\sum_{\alpha}\sum_{\beta} c_{\alpha}c_{\beta}b_{\alpha,i}b_{\beta,i}$ can be used as a measure of the conditioning of the matrix. If the determinant of the normalised matrix is small compared with ±1, the system is ill-conditioned [27]. For the set A partial structure factors $|A| = 0.0033$, and for the set B partial structure factors $|A| = 0.0025$, indicating that set A is better conditioned.

An alternative measure of the conditioning of a matrix $\mathbf{A}$ is to calculate the two-norm condition number of the matrix, sometimes known as the Turing number [27, 28]. The two-norm condition number is given by $\kappa_2 = \sigma_1/\sigma_n$, where σ_1 and σ_n are the largest and smallest singular values of matrix $\mathbf{A}$, respectively. Thus $\kappa_2 \geq 1$, and values near unity indicate a well conditioned matrix [27, 28]. Often the two-norm condition number κ_2' of the normalised matrix $\mathbf{A}'$ is quoted, where the ith row of matrix $\mathbf{A}$ is divided by $\sum_{\alpha}\sum_{\beta} c_{\alpha}c_{\beta}b_{\alpha,i}b_{\beta,i}$ [28]. The normalised two-norm condition number for the SVD partial structure factors is $\kappa_2' = 236$, which compares to $\kappa_2' = 221$ for the Set A partial structure factors and $\kappa_2' = 307$ for the Set B partial structure factors. Here, the conditioning of the SVD and Set A matrices is similar, (i.e. and that the inclusion of the ${}^{\mathrm{Nat}}_{\mathrm{Nat}}F(Q)$ total structure factor in the SVD does not improve the conditioning of the matrix.) whereas the Set B matrix is less well conditioned. As $b_{\mathrm{^{Nat}Ge}} \simeq b_{\mathrm{^{Nat}Se}}$ it follows that $S_{\mathrm{NN}}^{\mathrm{BT}}(Q) = {}^{\mathrm{Nat}}_{\mathrm{Nat}}F(Q)/\langle b\rangle^2$ (see section 5.4.1), and the measured structure factor does not contain information on the chemical ordering of the system. system.

Figures 5-34 and 5-35 show a closer comparison of the partial pair-correlation functions obtained from the three best constrained methods of calculating the real and reciprocal space partials. The bond distances and coordination numbers for the peaks in the $g_{\alpha\beta}(r)$ functions are given in table 5.10. The reciprocal space functions obtained for the SVD, set A and set B are shown in figure 5-34. The best constrained partial structure factor is $S_{\mathrm{SeSe}}(Q)$ and the data sets obtained from the different methods are all in excellent agreement. The $S_{\mathrm{GeSe}}(Q)$ functions obtained from the different methods are also consistent, except from the low-Q values. The $S_{\mathrm{GeGe}}(Q)$ partial structure factor is the most difficult to obtain, which leads to the largest discrepancies between the (i) set B and (ii) SVD and set A results. The relative conditioning of the partial structure factors can be inferred from the magnitude of the weighting factors given in matrix 5.4.

The $g_{\mathrm{SeSe}}(r)$ functions shown in figure 5-35, obtained from the different methods are all in excellent agreement. The $g_{\mathrm{GeSe}}(r)$ functions obtained from the SVD, set A and set B are also consistent, except for the height of the Ge-Se peak for the set B data set and a discrepancy at $\simeq 4$ Å. The $g_{\mathrm{GeGe}}(r)$ functions found from SVD and set A agree very well (figure 5-35). However, set B shows a sharper main Ge-Ge peak at 3.58(3) Å, and less of a high-r tail on this peak. It is likely that these discrepancies originate from the relatively poor conditioning of the Set B results compared to the Set A and the SVD results. Note that the difference in shape of the main Ge-Ge peak leads to the different integration ranges given in table 5.10.

The first peaks in $d_{\mathrm{GeSe}}(r)$ and $d_{\mathrm{SeSe}}(r)$ for the SVD, set A and set B results were fitted to a Gaussian convoluted with a sinc function using RDFgenie. The results for the SVD data sets are shown in figures 5-36 and 5-37. The bond distances and coordination numbers obtained from these RDFgenie fits are given in table 5.11, and agree with the values found from the first-order difference functions that are given in table 5.7.

Table 5.10: Bond distances $r_{\alpha\beta}$ and coordination numbers $\bar{n}_{\alpha}^{\beta}$ from the partial pair-distribution functions for glassy GeSe$_4$. The latter were obtained by integrating over the range given in the table for the functions shown in figure 5-35. Set A combines the total structure factors for $^{\mathrm{Nat}}\mathrm{Ge}^{\mathrm{Mix}}\mathrm{Se}_4$, $^{70}\mathrm{Ge}^{\mathrm{Nat}}\mathrm{Se}_4$ and $^{73}\mathrm{Ge}^{76}\mathrm{Se}_4$. Set B combines the total structure factors for $^{\mathrm{Nat}}\mathrm{Ge}^{\mathrm{Nat}}\mathrm{Se}_4$, $^{70}\mathrm{Ge}^{\mathrm{Nat}}\mathrm{Se}_4$ and $^{73}\mathrm{Ge}^{76}\mathrm{Se}_4$.

$g(r)$	$\bar{n}_{\mathrm{Ge}}^{\mathrm{Ge}}$ (1)	r_{GeGe} (1) /Å	range /Å	$\bar{n}_{\mathrm{Ge}}^{\mathrm{Se}}$	r_{GeSe} /Å	range /Å
$g(r)_{\mathrm{SVD}}$	2.51(2)	3.58(3)	3.068 - 3.927	4.41(2)	2.37(2)	2.148 - 2.516
$g(r)_{\mathrm{Set\,A}}$	2.55(2)	3.60(3)	3.068 - 3.927	4.48(2)	2.37(2)	2.148 - 2.516
$g(r)_{\mathrm{Set\,B}}$	2.25(2)	3.53(3)	2.945 - 3.804	4.23(2)	2.36(2)	2.148 - 2.516
$g(r)$	$\bar{n}_{\mathrm{Se}}^{\mathrm{Se}}$ (1)	r_{SeSe} (1) /Å	range/ Å	$\bar{n}_{\mathrm{Se}}^{\mathrm{Se}}$ (2)	r_{SeSe} (2) /Å	range /Å
$g(r)_{\mathrm{SVD}}$	1.04(2)	2.35(2)	2.148 - 2.516	9.10(3)	3.83(3)	3.007 - 4.418
$g(r)_{\mathrm{Set\,A}}$	1.04(2)	2.35(2)	2.148 - 2.516	9.10(3)	3.82(3)	3.007 - 4.418
$g(r)_{\mathrm{Set\,B}}$	1.07(2)	2.35(2)	2.148 - 2.516	9.02(3)	3.82(3)	3.007 - 4.418

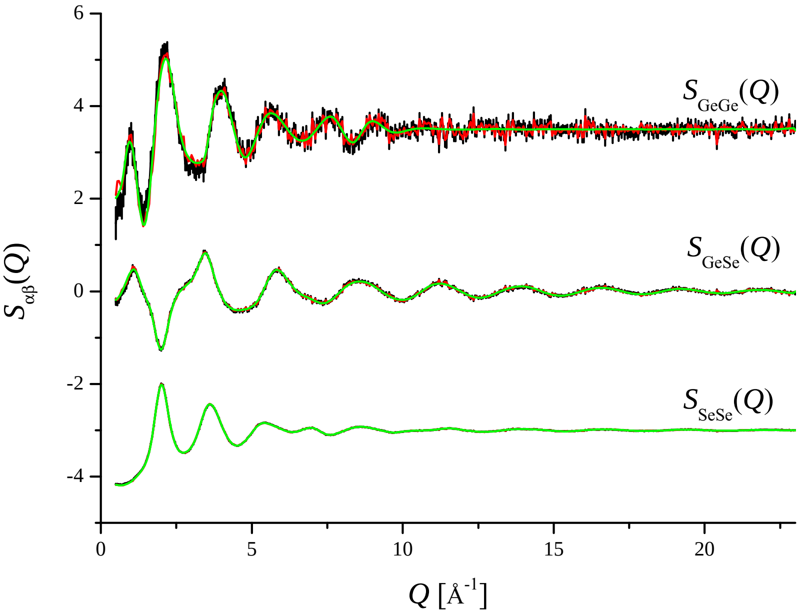

Figure 5-32: Faber-Ziman partial structure factors for glassy $GeSe_4$ obtained from the SVD analysis, offset vertically for clarity of presentation. The data sets (solid black curves) with vertical error bars are shown along with the back Fourier transforms of the corresponding unsmoothed $g_{\alpha\beta}(r)$ functions shown in figure 5-33 (solid red curves) and the Harwell spline fits (solid green curves).

Table 5.11: Bond distances and coordination numbers from the RDFgenie fits to the first peak in the SVD generated $d_{\alpha\beta}(r)$ functions for glassy $GeSe_4$, as shown in figures 5-36 and 5-37 with $Q_{\max} = 23$ Å^{-1}. The R_χ goodness-of-fit parameter is defined in equation 2.46. Set A combines the total structure factors for $^{\mathrm{Nat}}\mathrm{Ge}^{\mathrm{Mix}}\mathrm{Se}_4$, $^{70}\mathrm{Ge}^{\mathrm{Nat}}\mathrm{Se}_4$ and $^{73}\mathrm{Ge}^{76}\mathrm{Se}_4$. Set B combines the total structure factors for $^{\mathrm{Nat}}\mathrm{Ge}^{\mathrm{Nat}}\mathrm{Se}_4$, $^{70}\mathrm{Ge}^{\mathrm{Nat}}\mathrm{Se}_4$ and $^{73}\mathrm{Ge}^{76}\mathrm{Se}_4$.

$g(r)$	$\bar{n}_{\mathrm{Ge}}^{\mathrm{Se}}$	r_{GeSe}/Å	R_χ	$\bar{n}_{\mathrm{Se}}^{\mathrm{Se}}$	r_{SeSe}/Å	R_χ
$g(r)_{\mathrm{SVD}}$	4.09(2)	2.37(2)	0.062	1.00(2)	2.35(2)	0.044
$g(r)_{\mathrm{Set\,A}}$	4.12(2)	2.37(2)	0.085	1.00(2)	2.35(2)	0.042
$g(r)_{\mathrm{Set\,B}}$	4.00(2)	2.37(2)	0.068	1.00(2)	2.35(2)	0.047

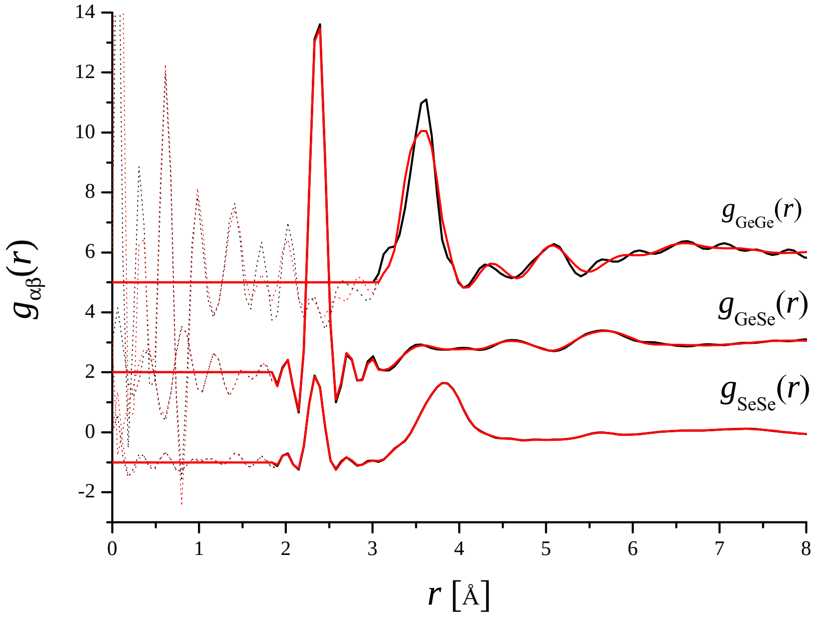

Figure 5-33: Partial pair-distribution functions for glassy $GeSe_4$ obtained from the SVD analysis. The black curves were obtained by Fourier transforming the Faber-Ziman partial structure factors $S_{\alpha\beta}(Q)$ shown in figure 5-32. The solid red curves were obtained by Fourier transforming the Harwell spline fits to the Faber-Ziman partial structure factors shown in figure 5-32. The solid lines show these functions after the low-r oscillations (dotted lines) have been set to their theoretical $g_{\alpha\beta}(r \to 0) = 0$ limit.

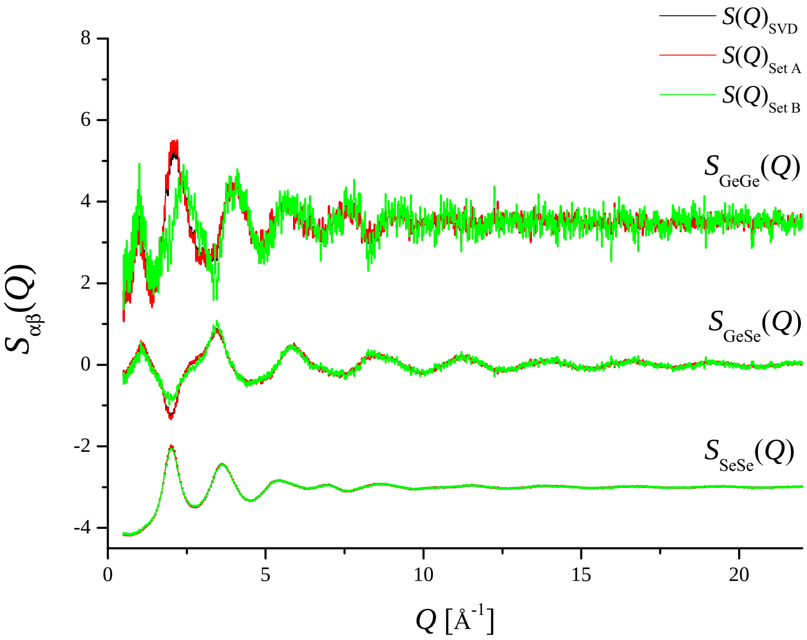

Figure 5-34: Faber-Ziman partial structure factors $S_{\alpha\beta}(Q)$ for glassy GeSe$_4$ calculated from the SVD analysis and from 2 sets of three total structure factors. Set A combines the total structure factors for $^{\mathrm{Nat}}$Ge$^{\mathrm{Mix}}$Se$_4$, ^{70}Ge$^{\mathrm{Nat}}$Se$_4$ and ^{73}Ge^{76}Se$_4$. Set B combines the total structure factors for $^{\mathrm{Nat}}$Ge$^{\mathrm{Nat}}$Se$_4$, ^{70}Ge$^{\mathrm{Nat}}$Se$_4$ and ^{73}Ge^{76}Se$_4$. The datasets have been offset vertically for clarity of presentation. Note that the black curves for $S_{\alpha\beta}(Q)_{\mathrm{SVD}}$ lie underneath the red curves for $S_{\alpha\beta}(Q)_{\mathrm{Set\,A}}$.

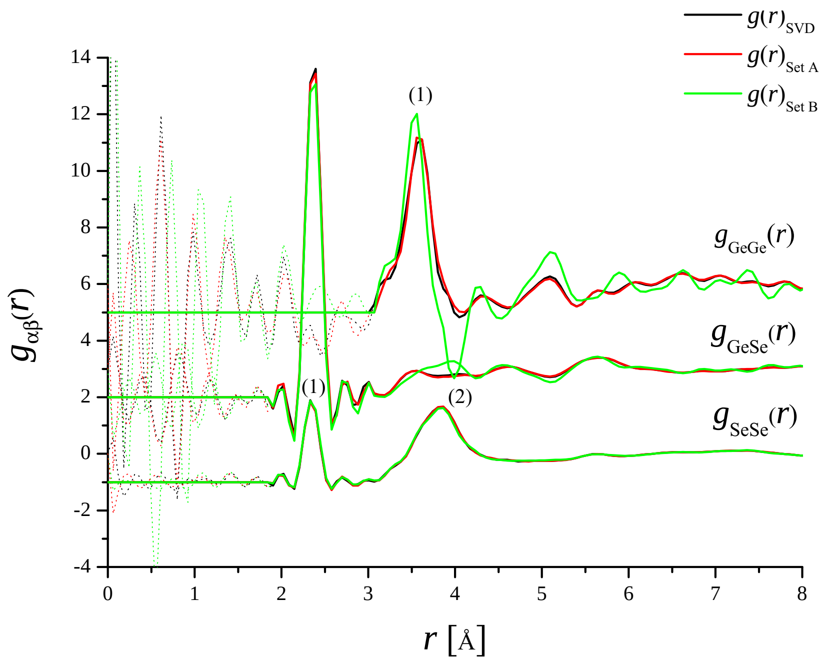

Figure 5-35: Partial pair-distribution functions for glassy GeSe$_4$ calculated from the SVD analysis and from 2 sets of three total structure factors. The data sets were obtained by Fourier transforming the Faber-Ziman partial structure factors $S_{\alpha\beta}(Q)$ shown in figure 5-34 for sets A and B. The solid lines show these functions after the low-r oscillations (dotted lines) have been set to their theoretical $g_{\alpha\beta}(r \to 0) = 0$ limit. Set A combines the total structure factors for $^{\rm Nat}$Ge$^{\rm Mix}$Se$_4$, ^{70}Ge$^{\rm Nat}$Se$_4$ and ^{73}Ge^{76}Se$_4$. Set B combines the total structure factors for $^{\rm Nat}$Ge$^{\rm Nat}$Se$_4$, ^{70}Ge$^{\rm Nat}$Se$_4$ and ^{73}Ge^{76}Se$_4$. The datasets have been offset vertically for clarity of presentation. Note that the black curves for $g_{\alpha\beta}(r)_{\rm SVD}$ lie underneath the red curves for $g_{\alpha\beta}(r)_{\rm Set\,A}$. The numbered peaks in the $g_{\rm GeGe}(r)$ and $g_{\rm SeSe}(r)$ functions correspond to the bond distances and coordination numbers given in table 5.10.

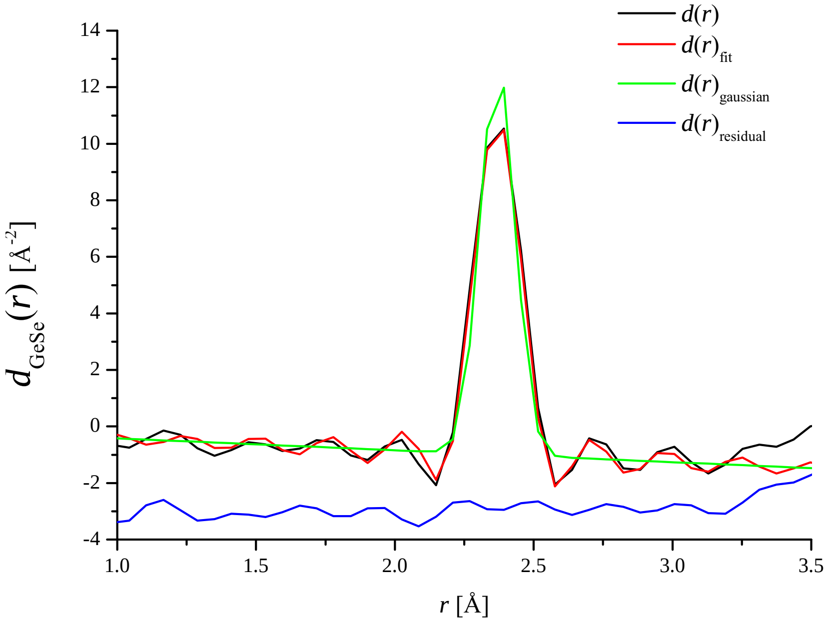

Figure 5-36: The first peak in the SVD generated $d_{\mathrm{GeSe}}(r)$ function for glassy GeSe$_4$ (solid black curve), fitted with a Gaussian convoluted with a sinc function using RDF-genie (solid red curve). The resulting fitted Gaussian in $d_{\mathrm{GeSe}}(r)$ is given by the solid green curve, and the residual is given by the solid blue curve.

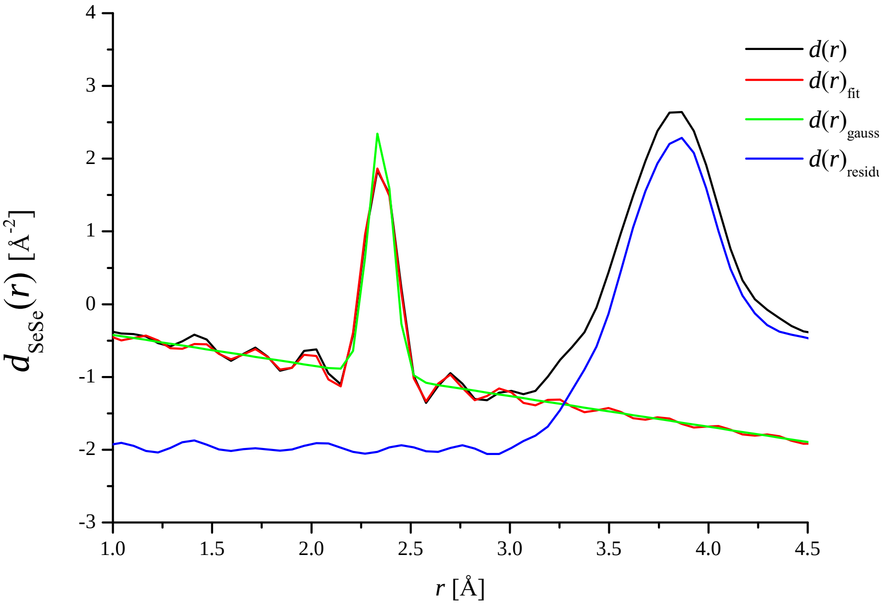

Figure 5-37: The first peak in the SVD generated $d_{\mathrm{SeSe}}(r)$ function for glassy GeSe_4 (solid black curve), fitted with a Gaussian convoluted with a sinc function using RDF-genie (solid red curve). The resulting fitted Gaussian in $d_{\mathrm{SeSe}}(r)$ is given by the solid green curve, and the residual is given by the solid blue curve.

5.4.4 Bhatia - Thornton partial structure factors

$GeSe_3$

The $S_{\alpha\beta}^{\mathrm{BT}}(Q)$ functions are shown in figure 5-38 and the $g_{\alpha\beta}^{\mathrm{BT}}(r)$ functions are shown in figure 5-39. Once the Bhatia - Thornton structure factors have been calculated, the self consistency of the data can be tested. The partial structure factors should obey the relation [13]:

$$S_{\mathrm{NN}}^{\mathrm{BT}}(Q) \cdot S_{\mathrm{CC}}^{\mathrm{BT}}(Q) \geq \left[S_{\mathrm{NC}}^{\mathrm{BT}}(Q)\right]^2 \tag{5.16}$$

which is equivalent to checking that the measured intensity is non-negative at all scattering vectors. As shown in figure 5-40, this inequality is fulfilled within the experimental uncertainty at all Q-values.

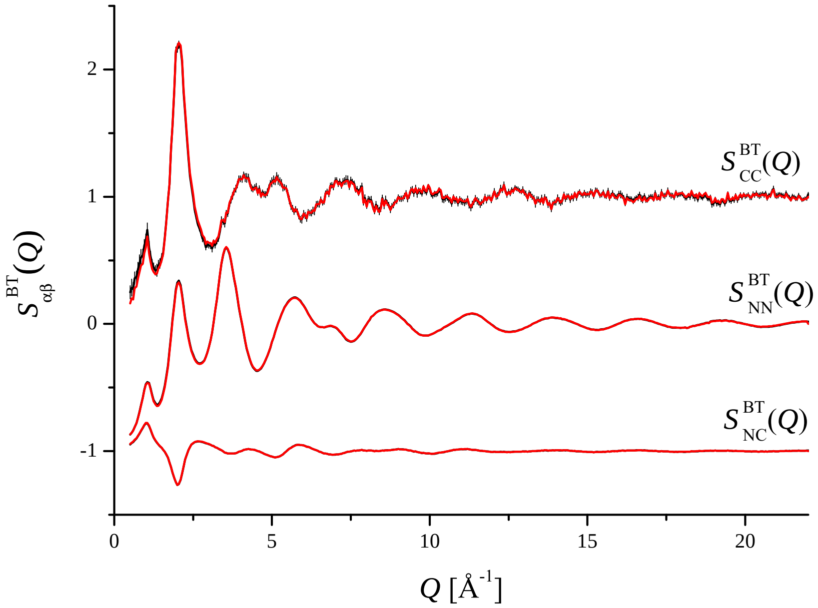

Figure 5-38: Bhatia - Thornton partial structure factors $S_{\alpha\beta}^{\mathrm{BT}}(Q)$ for glassy $GeSe_3$ obtained from the SVD analysis, offset vertically for clarity of presentation. The data sets (solid black curves) with vertical error bars are shown along with the back Fourier transforms of the corresponding $g_{\alpha\beta}^{\mathrm{BT}}(r)$ functions shown in figure 5-39 (solid red curves).

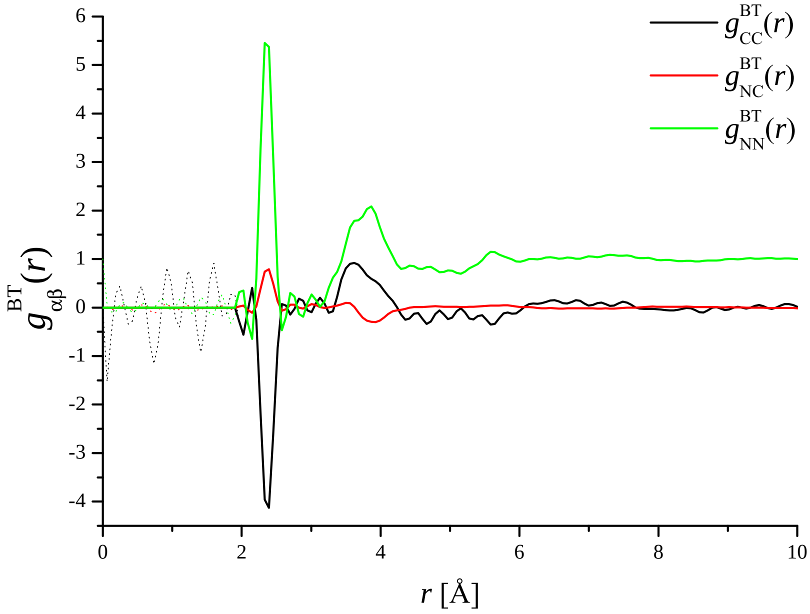

Figure 5-39: Bhatia - Thornton partial pair-distribution functions $g^{\mathrm{BT}}_{\alpha\beta}(r)$ for glassy GeSe$_3$, obtained from the SVD analysis by Fourier transforming the Bhatia - Thornton partial structure factors $S^{\mathrm{BT}}_{\alpha\beta}(Q)$ shown in figure 5-38. The solid curves show these functions after the low-r oscillations (dotted lines) have been set to their theoretical $g^{\mathrm{BT}}_{\alpha\beta}(r \to 0) = 0$ limit.

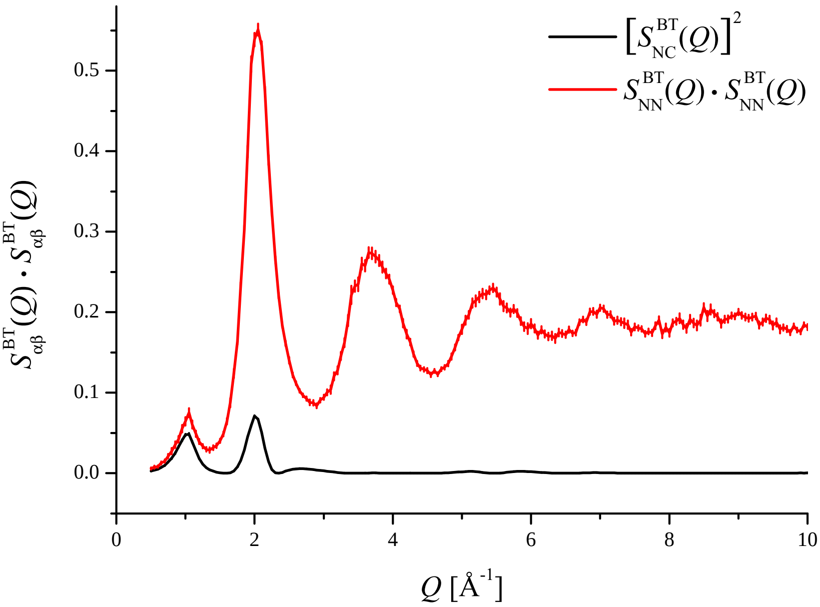

Figure 5-40: Self-consistency check on the data sets measured for glassy $GeSe_3$ using the Bhatia-Thornton partial structure factors obtained from the SVD analysis. The solid red curve shows the product of $S_{\mathrm{NN}}^{\mathrm{BT}}(Q)$ and $S_{\mathrm{CC}}^{\mathrm{BT}}(Q)$, and the solid black curve shows $[S_{\mathrm{NC}}^{\mathrm{BT}}(Q)]^2$. The vertical error bars are smaller than the line thickness at some Q-values.

GeSe_4

The $S^{\mathrm{BT}}_{\alpha\beta}(Q)$ functions are shown in figure 5-41 and the $g^{\mathrm{BT}}_{\alpha\beta}(r)$ functions are shown in figure 5-42. The self consistency of the GeSe_4 partial structure factors can be tested by using equation 5.16, and as shown in figure 5-43, this inequality is fulfilled within the experimental uncertainty at all Q-values [13].

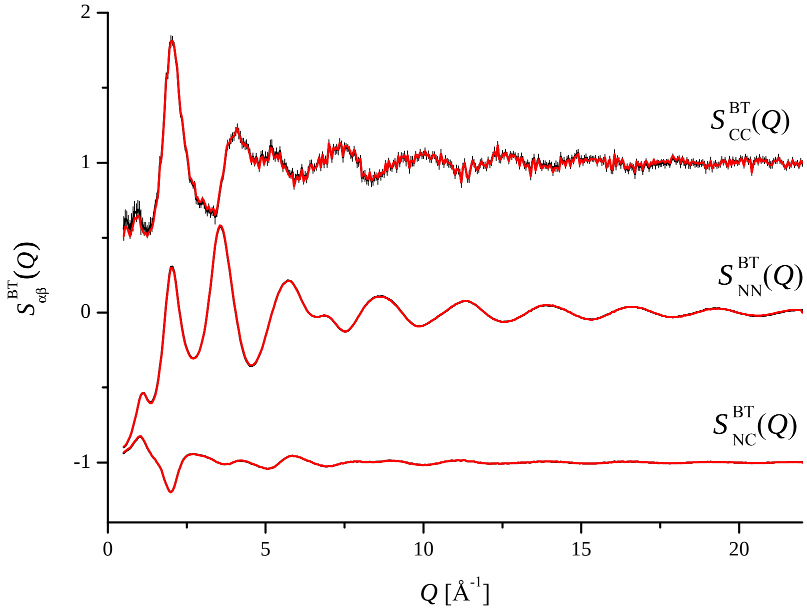

Figure 5-41: Bhatia - Thornton partial structure factors $S^{\mathrm{BT}}_{\alpha\beta}(Q)$ for glassy GeSe_4 obtained from the SVD analysis, offset vertically for clarity of presentation. The data sets (solid black curves) with vertical error bars are shown along with the back Fourier transforms of the corresponding $g^{\mathrm{BT}}_{\alpha\beta}(r)$ functions shown in figure 5-42 (solid red curves).

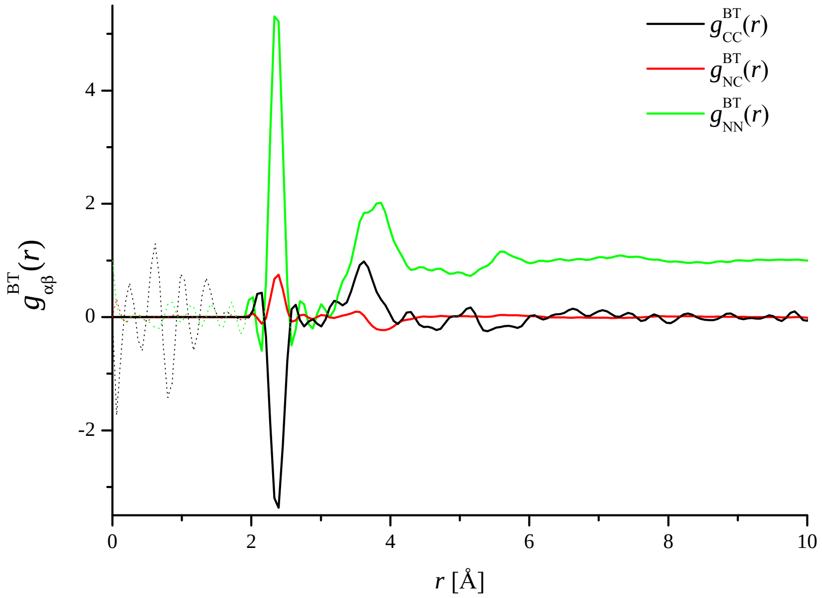

Figure 5-42: Bhatia - Thornton partial pair-distribution functions $g^{\mathrm{BT}}_{\alpha\beta}(r)$ for glassy GeSe_4, obtained from the SVD analysis by Fourier transforming the Bhatia - Thornton partial structure factors $S^{\mathrm{BT}}_{\alpha\beta}(Q)$ shown in figure 5-41. The solid lines show these functions after the low-r oscillations (dotted lines) have been set to their theoretical $g^{\mathrm{BT}}_{\alpha\beta}(r \to 0) = 0$ limit.

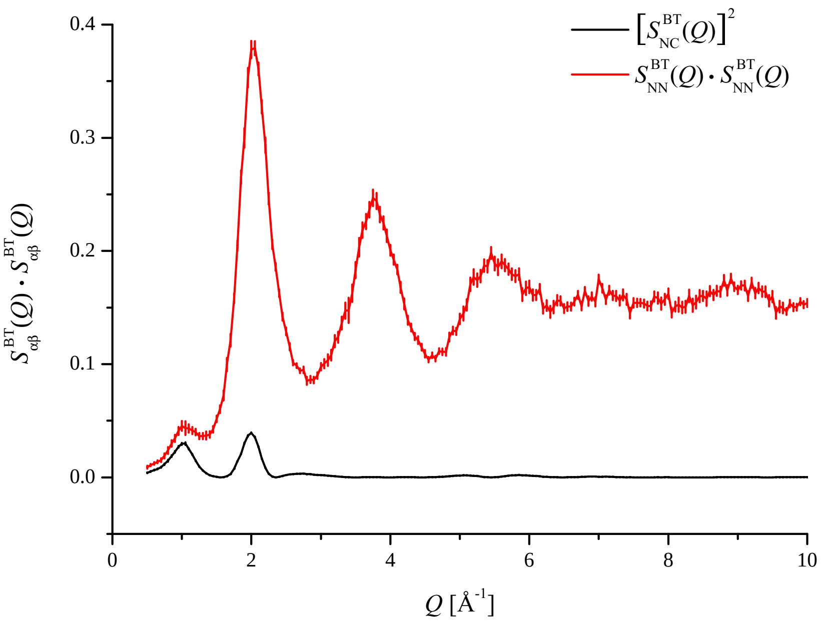

Figure 5-43: Self-consistency check on the data sets measured for glassy $GeSe_4$ using the Bhatia-Thornton partial structure factors obtained from the SVD analysis. The solid red curve shows the product of $S^{BT}_{NN}(Q)$ and $S^{BT}_{CC}(Q)$, and the solid black curve shows $[S^{BT}_{NC}(Q)]^2$. The vertical error bars are smaller than the line thickness at some Q-values.

5.5 Discussion

The final set of Faber-Ziman partial structure factors for $GeSe_3$ and $GeSe_4$ are given in figures 5-44 and 5-46, and the corresponding set of partial pair distribution functions are shown in figures 5-45 and 5-47, respectively.

The first peak in the $g_{\mathrm{SeSe}}(r)$ functions was taken from the fitted Gaussian from RDFgenie (figures 5-31 and 5-37), the second peak was obtained by Fourier transforming the spline fitted $S_{\mathrm{SeSe}}(Q)$ function, and the higher-r data was obtained by Fourier transforming the spline fitted $S_{\mathrm{GeSe}}(Q)$ function after a Lorch function had been applied.

The first peak in the $g_{\mathrm{GeSe}}(r)$ functions was obtained from the fitted Gaussian from RDFgenie (figures 5-30 and 5-36), and the higher-r data was obtained by Fourier transforming the spline fitted $S_{\mathrm{GeSe}}(Q)$ function after a Lorch function had been applied.

The low-r region of the $g_{\mathrm{GeGe}}(r)$ functions was obtained by Fourier transforming the un-smoothed $S_{\mathrm{GeGe}}(Q)$ function, and the data after the main Ge-Ge peak at 3.58(2) Å was obtained by Fourier transforming the spline fitted $S_{\mathrm{GeGe}}(Q)$ function after a Lorch function had been applied.

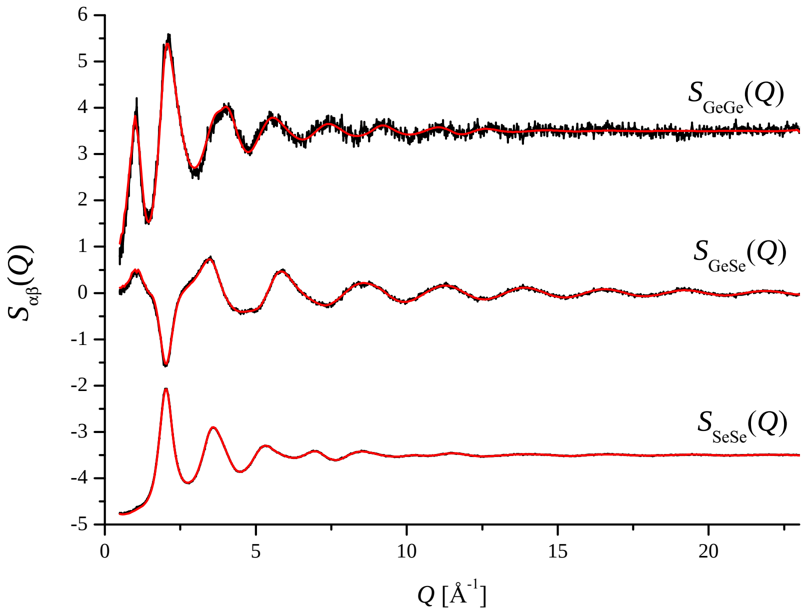

Figure 5-44: Faber-Ziman partial structure factors for glassy $GeSe_3$ obtained from the SVD analysis, offset vertically for clarity of presentation. The data sets (solid black curves) with vertical error bars are shown along with the back Fourier transforms of the corresponding smoothed $g_{\alpha\beta}(r)$ functions shown in figure 5-45 (solid red curves).

Figures 5-44 and 5-46 show that the back Fourier transforms of the smoothed $g_{\alpha\beta}(r)$

functions agree with the measured $S_{\alpha\beta}(Q)$ functions, within the experimental error. The coordination numbers and peak positions measured for $GeSe_3$ and $GeSe_4$ from the first-order difference functions (tables 5.5 and 5.7) and Faber-Ziman partial pair-correlation functions (tables 5.9 and 5.11) are all self-consistent within the random error. The final peak positions and coordination numbers are summarised in tables 5.12 and 5.13, respectively.

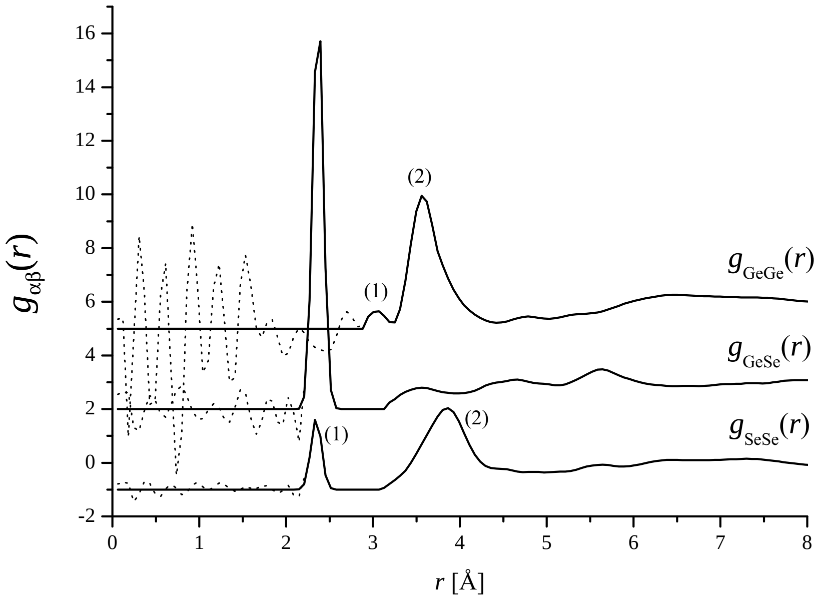

Figure 5-45: Partial pair-distribution functions for glassy $GeSe_3$ obtained from the SVD analysis. The solid curves were obtained by using the procedures described in the text and have been set to the $g_{\alpha\beta}(r \to 0) = 0$ limit, the distance of closest approach between two atoms. The low-r oscillations (dotted curves) correspond to the Fourier transform of the measured $S_{\alpha\beta}(Q)$ datasets, given in figure 5-44. The numbered peaks in the $g_{\mathrm{GeGe}}(r)$ and $g_{\mathrm{SeSe}}(r)$ functions correspond to the bond distances and coordination numbers given in table 5.12.

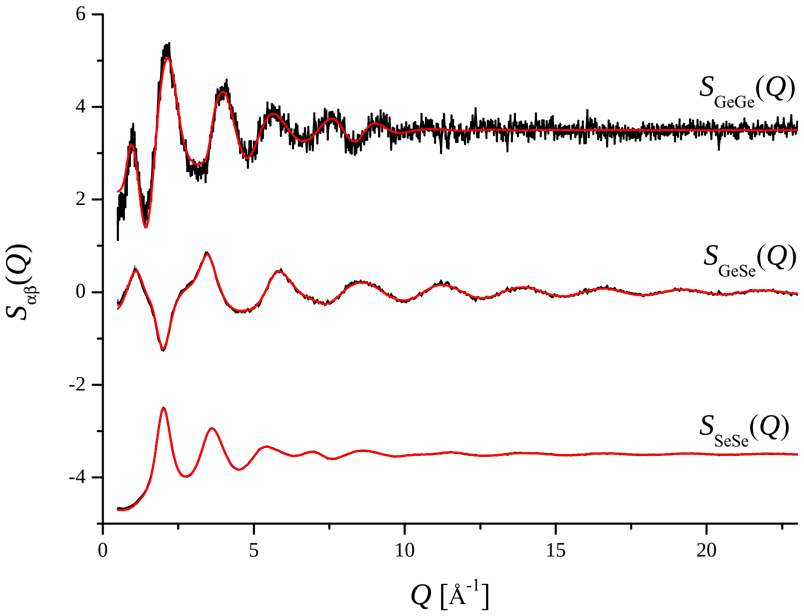

Figure 5-46: Faber-Ziman partial structure factors for glassy $GeSe_4$ obtained from the SVD analysis, offset vertically for clarity of presentation. The data sets (solid black curves) with vertical error bars are shown along with the back Fourier transforms of the corresponding smoothed $g_{\alpha\beta}(r)$ functions shown in figure 5-47 (solid red curves).

Table 5.12: Bond distances $r_{\alpha\beta}$ and coordination numbers $\bar{n}_{\alpha}^{\beta}$ from the partial pair-distribution functions shown in figure 5-45 for glassy $GeSe_3$.

$g_{\mathrm{GeGe}}(r)$	$\bar{n}_{\mathrm{Ge}}^{\mathrm{Ge}}$ (1)	r_{GeGe} (1) /Å	$\bar{n}_{\mathrm{Ge}}^{\mathrm{Ge}}$ (2)	r_{GeGe} (2) /Å
SVD	0.08(3)	2.94(3)	3.08(3)	3.58(2)
Set A	0.17(3)	3.02(3)	3.17(3)	3.59(2)
Set B	0.36(3)	3.07(3)	2.15(3)	3.59(3)
$g_{\mathrm{SeSe}}(r)$	$\bar{n}_{\mathrm{Se}}^{\mathrm{Se}}$ (1)	r_{SeSe} (1) /Å	$\bar{n}_{\mathrm{Se}}^{\mathrm{Se}}$ (2)	r_{SeSe} (2) /Å
SVD	0.70(2)	2.35(2)	9.22(3)	3.85(3)
Set A	0.72(2)	2.35(2)	9.24(3)	3.86(3)
Set B	0.74(2)	2.35(2)	9.12(3)	3.85(3)
$g_{\mathrm{GeSe}}(r)$	$\bar{n}_{\mathrm{Ge}}^{\mathrm{Se}}$	r_{GeSe}/Å		
SVD	3.99(2)	2.37(2)		
Set A	4.04(2)	2.37(2)		
Set B	3.95(2)	2.37(2)		

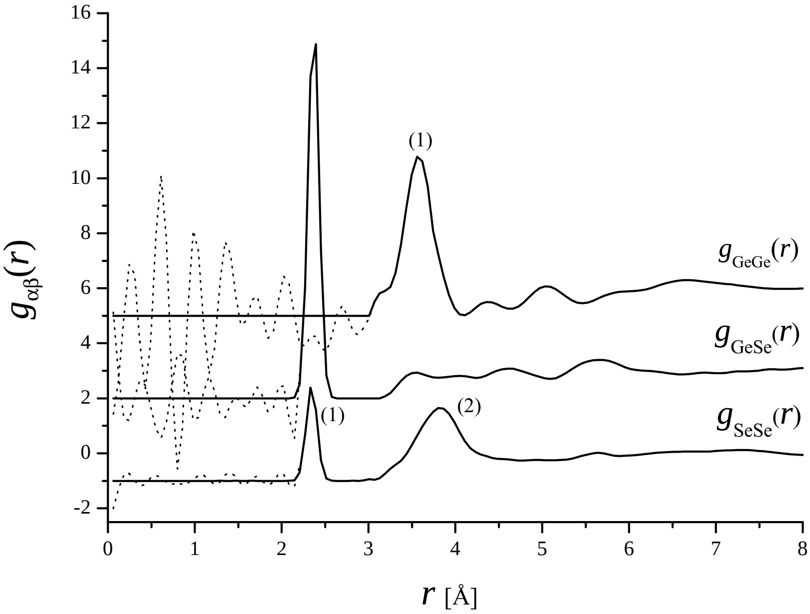

Figure 5-47: Partial pair-distribution functions for glassy GeSe$_4$ obtained from the SVD analysis. The solid curves were obtained by using the procedures described in the text and have been set to the $g_{\alpha\beta}(r \to 0) = 0$ limit, the distance of closest approach between two atoms. The low-r oscillations (dotted curves) correspond to the Fourier transform of the measured $S_{\alpha\beta}(Q)$ datasets, given in figure 5-46. The numbered peaks in the $g_{\text{GeGe}}(r)$ and $g_{\text{SeSe}}(r)$ functions correspond to the bond distances and coordination numbers given in table 5.13.

Table 5.13: Bond distances $r_{\alpha\beta}$ and coordination numbers $\bar{n}_{\alpha}^{\beta}$ from the partial pair-distribution functions shown in figure 5-47 for glassy GeSe$_4$.

$g(r)$	$\bar{n}_{\text{Ge}}^{\text{Ge}}$ (1)	r_{GeGe} (1) /Å	$\bar{n}_{\text{Ge}}^{\text{Se}}$	r_{GeSe} /Å
SVD	2.51(2)	3.58(3)	4.09(2)	2.37(2)
Set A	2.55(2)	3.60(3)	4.12(2)	2.37(2)
Set B	2.25(2)	3.53(3)	4.00(2)	2.37(2)
$g(r)$	$\bar{n}_{\text{Se}}^{\text{Se}}$ (1)	r_{SeSe} (1) /Å	$\bar{n}_{\text{Se}}^{\text{Se}}$ (2)	r_{SeSe} (2) /Å
SVD	1.00(2)	2.35(2)	9.10(3)	3.83(3)
Set A	1.00(2)	2.35(2)	9.10(3)	3.82(3)
Set B	1.00(2)	2.35(2)	9.02(3)	3.82(3)

5.5.1 Network models

The total pair-distribution functions for ${}^{\mathrm{Nat}}\mathrm{Ge}^{\mathrm{Nat}}\mathrm{Se}_3$ and ${}^{\mathrm{Nat}}\mathrm{Ge}^{\mathrm{Nat}}\mathrm{Se}_4$ given in figures 5-7 and 5-10 show that the mean nearest-neighbour coordination numbers are $\bar{n} = 2.52(2)$ and $\bar{n} = 2.43(2)$, respectively, which is consistent with the '8-N' rule for 4-fold coordinated Ge atoms and 2-fold coordinated Se atoms.

The measured coordination numbers given in tables 5.12 and 5.13 are compared with those obtained for the chemically ordered continuous random network (COCRN) and for the random continuous network (RCN) in tables 5.14 and 5.15, respectively.

Table 5.14: Nearest neighbour coordination numbers for different Ge-Se compositions calculated from the chemically ordered continuous random network (COCRN) model [1].

Composition	$\bar{n}_{\mathrm{Ge}}^{\mathrm{Se}}$	$\bar{n}_{\mathrm{Se}}^{\mathrm{Ge}}$	$\bar{n}_{\mathrm{Se}}^{\mathrm{Se}}$	$\bar{n}_{\mathrm{Ge}}^{\mathrm{Ge}}$
GeSe_4	4	1	1	0
GeSe_3	4	4/3 = 1.3333	2/3 = 0.6667	0
GeSe_2	4	2	0	0
$\mathrm{GeSe}_{1.5}$	3	2	0	1

Table 5.15: Nearest neighbour coordination numbers for different Ge-Se compositions calculated from the random continuous network (RCN) model. [1]

Composition	$\bar{n}_{\mathrm{Ge}}^{\mathrm{Se}}$	$\bar{n}_{\mathrm{Se}}^{\mathrm{Ge}}$	$\bar{n}_{\mathrm{Se}}^{\mathrm{Se}}$	$\bar{n}_{\mathrm{Ge}}^{\mathrm{Ge}}$
$\mathrm{Ge}_x\mathrm{Se}_{(1-x)}$	$4(1-x)/(1+x)$	$4x/(1+x)$	$2(1-x)/(1+x)$	$8x/(1+x)$
GeSe_4 (x=0.2)	8/3=2.6667	2/3=0.6667	4/3=1.3333	4/3=1.3333
GeSe_3 (x=0.25)	2.4	0.8	1.2	1.6
GeSe_2 (x=1/3)	2	1	1	2
$\mathrm{GeSe}_{1.5}$ (x=2/3)	0.8	1.6	2.5	3.2

Glassy GeSe_3 has a Ge-Se coordination number of 3.99(2), as given in table 5.12, indicating that the Ge-atoms are 4-fold coordinated by Se atoms. The second peak in $g_{\mathrm{SeSe}}(r)$ at 3.85(3) Å, which corresponds to a coordination number of $\bar{n}_{\mathrm{Se}}^{\mathrm{Se}} = 9.22(3)$, gives a ratio of Ge-Se:Se-Se distances of 0.615(5), close to the value of $\sqrt{3/8} = 0.612$ expected for perfect tetrahedra. The first peak in $g_{\mathrm{SeSe}}(r)$ gives a bond distance of 2.34(2) Å, which corresponds to a coordination number of 0.70(2). Figure 5-45 shows that there is no indication of Ge-Ge homopolar bonds, that would occur at 2.42(2) Å [16]. All of the measured coordination numbers for GeSe_3 are consistent with those expected from the COCRN model, indicating that $GeSe_3$ forms a predominately chemically ordered network. The $g_{\mathrm{GeGe}}(r)$ function in figure 5-45 also shows that there are some edge-sharing (ES) configurations, with a peak at 2.94(3) Å just before the main corner-sharing (CS) peak at 3.58(2) Å. A schematic of these different configurations is given in figure 5-48, where edge sharing configurations are shown in (d) and corner sharing configurations are shown in (c).

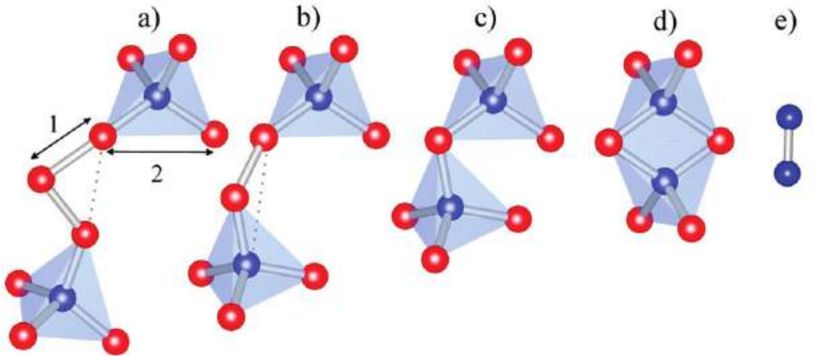

Figure 5-48: Schematic diagrams of the connection types reported to occur in Ge_xSe_{1-x} glasses. Blue spheres are Ge-atoms and red spheres are Se-atoms. (a) $GeSe_4$ tetrahedra separated by two Se atoms, where the short homopolar Se-Se distance is labelled 1 and the longer intra-tetrahedral Se-Se distance is labelled 2. (b) $GeSe_4$ tetrahedra linked by a single Se-Se homopolar bond. (c) $GeSe_4$ tetrahedra in a corner sharing (CS) configuration. (d) Edge-sharing (ES) tetrahedra. (e) A Ge-Ge homopolar bond. Reproduced from figure 1b in Skinner et al [90].

For glassy $GeSe_4$, the Ge-Se coordination number of 4.09(2), given in table 5.13, shows that the Ge-atoms are also 4-fold coordinated by Se atoms. The second peak in $g_{\mathrm{SeSe}}(r)$ at 3.85(3) Å, which corresponds to a coordination number $\bar{n}_{\mathrm{Se}}^{\mathrm{Se}} = 9.22(3)$, gives a ratio of Ge-Se:Se-Se distances of 0.618(5), close to the value expected for a tetrahedral arrangement. In $GeSe_4$, the Se-Se coordination number for homopolar bonds is 1.00(2). In figure 5-47 there is no indication of Ge-Ge homopolar bonds that would occur at 2.42(2) Å [16]. However, there is a low-r shoulder at 3.18(2) Å on the main CS peak at 3.85(3) Å, which may originate from the Ge-Ge distance in edge-sharing tetrahedra. The coordination numbers for $GeSe_4$ match those calculated using the COCRN model, which suggests that the $GeSe_4$ glass is also predominately chemically ordered.

The bond distances in tables 5.12 and 5.13 can be used to estimate bond angles for the $GeSe_3$ and $GeSe_4$ glasses. For example, the Ge-Se bond distance combined with the Se-Se intra-tetrahedral distance allows the Se-Ge-Se bond angle to be calculated using the cosine rule. The Se-Ge-Se bond angle is 108.6(1.0)° for $GeSe_3$ and 107.8(1.0)° for $GeSe_4$, values that are close to the ideal tetrahedral angle of 109.5°. In the high-temperature crystalline structure of $GeSe_2$ [91], a range of Se-Ge-Se bond angles are found from 99.0° – 115.9°. In the case of ES tetrahedra, the Ge-Se-Ge bond angle can be calculated using the Ge-Se bond distance and the Ge-Ge ES distance. For $GeSe_3$, the ES Ge-Ge distance is 2.94(3) Å which gives a Ge-Se-Ge bond angle of 76.6(1.0)°. For $GeSe_4$, the position of the ES shoulder at 3.18(2) Å gives a Ge-Se-Ge bond angle of 84.3(1.0)°. In the high-temperature crystalline structure of $GeSe_2$ [91], a range of Ge-Se-Ge bond angles is given from 80.2° – 100.1°.

Raman spectroscopy experiments indicate that edge-sharing Ge-Ge configurations occur in both $GeSe_3$ and $GeSe_4$ [81, 85, 92]. For example, Lucas *et al.* [85] suggest that $GeSe_3$, $GeSe_4$ and $GeSe_9$ all have ES configurations [85], where the ratio of corner sharing to edge sharing intensities in the Raman spectra is 4.43 for $GeSe_3$ and 5.53 for $GeSe_4$ [85], *i.e.* ES units are less prevalent in $GeSe_4$ as compared to $GeSe_3$, but are still present. This suggests that the low-r shoulder at 3.18(2) Å on the main CS peak in $g_{\mathrm{GeGe}}(r)$ function for $GeSe_4$ is not a Fourier transform artefact, and does represent a small amount of ES configurations. In the high-temperature crystalline structure of $GeSe_2$, the ES Ge-Ge bond distance is 3.049 Å [91], which is close to the value of 3.02(2) Å found for glassy $GeSe_2$ [16]. In glassy $GeSe_3$ the ES Ge-Ge peak is at a distance of 2.94(3) Å, whereas the shoulder on the CS Ge-Ge peak in $GeSe_4$ is at a somewhat longer distance of 3.18(2) Å.

As discussed in section 5.1, structural indications for the existence of the intermediate phase would manifest themselves in deviations from the COCRN model, reflecting structural variability in the network. Figure 5-48 shows the different connection types that have been reported to exist in Ge-Se glasses [90]. Whilst Ge-Ge homopolar bonds could not be detected in either $GeSe_3$ or $GeSe_4$, it is possible that configurations (a) – (d) do exist in both glasses. For example, in $GeSe_3$ there is an ES Ge-Ge peak, which corresponds to configuration (d) in figure 5-48, with a coordination number of 0.08(3). The main CS Ge-Ge peak at 3.83(3) Å suggests that configuration (c) is also present, and the existence of Se-Se homopolar bonds indicates that configuration (b) is also present in the network structure. It is likely that there is a distribution of inter-tetrahedral Ge-Se_n-Ge connections, where n is an integer ≥ 1. However, as it is difficult to obtain the exact proportions of each configuration from a PDF analysis, it is necessary to look at simulations of these materials that accurately reproduce the measured data sets.

Finally the proportion of Ge atoms involved in CS and ES tetrahedral structures is shown in table 5.16 [16]. For the glass, an estimate of the number of Ge atoms in CS tetrahedra can be obtained by assuming that the total number of Ge atoms $N_{\mathrm{Ge}} = N_{\mathrm{Ge,ES}} + N_{\mathrm{Ge,CS}} + N_{\mathrm{Ge,homo}}$, where $N_{\mathrm{Ge,ES}}$ is the number of Ge atoms in ES tetrahedra, $N_{\mathrm{Ge,CS}}$ is the number of Ge atoms in CS tetrahedra, and $N_{\mathrm{Ge,homo}}$ is the number of Ge atoms in homopolar bonds [93]. Assuming there are no extended chains of ES tetrahedra then $\bar{n}_{\mathrm{Ge}}^{\mathrm{Ge}} = N_{\mathrm{Ge,ES}}/N_{\mathrm{Ge}}$, and if homopolar bonds form only in pairs then $\bar{n}_{\mathrm{Ge}}^{\mathrm{Ge}} = N_{\mathrm{Ge,homo}}/N_{\mathrm{Ge}}$. Hence, we can assume that $N_{\mathrm{Ge,CS}}/N_{\mathrm{Ge}} = 1-N_{\mathrm{Ge,ES}}/N_{\mathrm{Ge}}-N_{\mathrm{Ge,homo}}/N_{\mathrm{Ge}}$ [93]. For GeSe$_3$, $N_{\mathrm{Ge,homo}} = 0$ such that $N_{\mathrm{Ge,CS}}/N_{\mathrm{Ge}} = 1-N_{\mathrm{Ge,ES}}/N_{\mathrm{Ge}}$.

Table 5.16: Description of the Ge centred correlations in GeSe$_3$ in terms of the fraction of Ge atoms involved in edge-sharing (ES) or corner-sharing (CS) structural motifs.

$g(r)$	$\frac{N_{\mathrm{Ge}}(\mathrm{ES})}{N_{\mathrm{Ge}}}$ (%)	$\frac{N_{\mathrm{Ge}}(\mathrm{CS})}{N_{\mathrm{Ge}}}$ (%)	$\frac{N_{\mathrm{Ge}}(\mathrm{ES})}{N_{\mathrm{Ge}}(\mathrm{CS})}$ (%)
$g(r)_{\mathrm{SVD}}$	8(5)	92(5)	8.7
$g(r)_{\mathrm{Set\,A}}$	17(5)	83(5)	20.5
$g(r)_{\mathrm{Set\,B}}$	36(5)	63(5)	57.1

For GeSe$_4$, if the low-r shoulder on the main Ge-Ge peak corresponds to a small number of ES Ge-atoms, then configuration (d) exists in the glass structure. The main structural configurations will be (a), (b) and (c), although it is difficult to ascertain from pair-distribution functions the exact proportion of each. Overall, the proportions of each configuration must balance to give a homopolar Se-Se coordination number of $\bar{n}_{\mathrm{Se}}^{\mathrm{Se}} = 1.00(2)$. The $g_{\mathrm{GeGe}}(r)$ function also shows peaks at 4.30(3) Å and 5.05(3) Å that correspond to the longer Ge-Ge distances associated with intermediate range ordering.

5.5.2 Comparison with GeSe$_2$

The full set of partial pair-distribution functions for GeSe$_2$ has been measured on D4B by Ingrid Petri [16] with an incident neutron wavelength of 0.7046 Å. In figures 5-49 - 5-51 these data sets are compared to the results obtained from the present work on GeSe$_3$ and GeSe$_4$. The GeSe$_3$ and GeSe$_4$ data sets in these figures were obtained as described at the beginning of section 5.5, except that the reciprocal space functions were truncated at $Q_{\mathrm{max}} = 16$ Å^{-1} to be consistent with the D4B GeSe$_2$ data sets.

The first three peaks in $g_{\mathrm{GeGe}}(r)$ for GeSe$_2$ are at 2.42(2), 3.02(2) and 3.57(2) Å and correspond to Ge-Ge homopolar bonds, ES Ge-Ge and CS Ge-Ge configurations, respectively [16]. In GeSe$_3$, Ge-Ge homopolar bonds are no longer found, but a small number of ES Ge-Ge configurations occur giving a coordination number of $\bar{n}_{\mathrm{Ge}}^{\mathrm{Ge}} = 0.08(3)$, as compared to $\bar{n}_{\mathrm{Ge}}^{\mathrm{Ge}} = 0.34(5)$ for GeSe$_2$ [16]. In GeSe$_4$, homopolar Ge-Ge bonds could not be detected, and the Ge atoms are typically surrounded by four Se atoms. For all three compositions the Ge-Ge CS peak position is the same within the random error, at 3.57(2), 3.58(2) and 3.58(2) Å for GeSe$_2$, GeSe$_3$ and GeSe$_4$, respectively. However, with increasing Se content the CS Ge-Ge coordination number decreases from 3.2(2) in GeSe$_2$ to 3.08(3) in GeSe$_3$ to 2.51(2) in GeSe$_4$, despite the

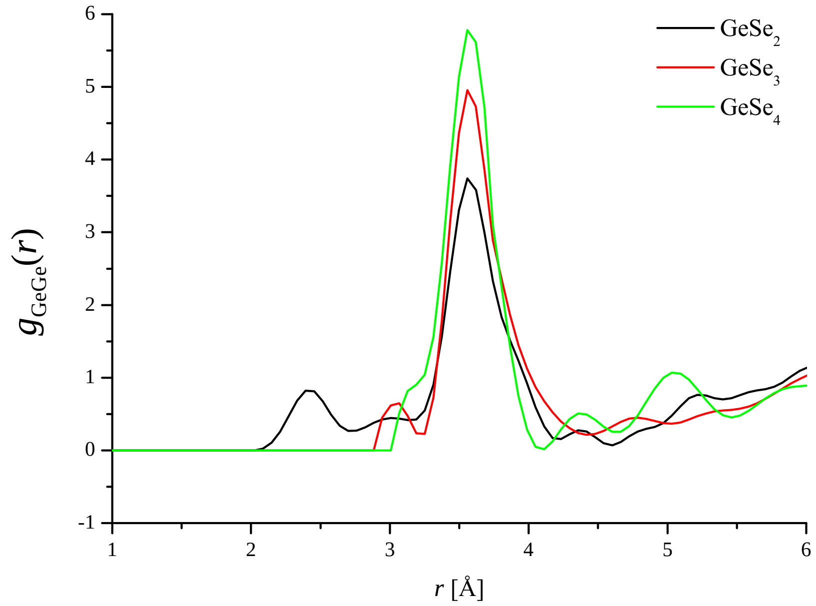

Figure 5-49: The Ge-Ge partial pair-distribution functions $g_{\mathrm{GeGe}}(r)$ for GeSe$_3$ (solid red curve) and GeSe$_4$ (solid green curve) obtained from the SVD analysis, compared with Ingrid Petri's GeSe$_2$ data (solid black curve) [16]. The data sets were obtained by truncating the reciprocal space data at the same maximum Q-value, $Q_{\mathrm{max}} = 16$ Å^{-1}. The solid lines show the functions after the low-r oscillations have been set to their theoretical $g_{\alpha\beta}(r \to 0) = 0$ limit.

sharpening of the peak seen in figure 5-49.

Figure 5-50 shows that the $g_{\mathrm{GeSe}}(r)$ functions for GeSe$_2$, GeSe$_3$ and GeSe$_4$ are very similar. The Ge-Se peak position is the same within the error at 2.36(2), 2.37(2) and 2.37(2) Å for GeSe$_2$, GeSe$_3$ and GeSe$_4$, respectively. Although the first peak height in the $g_{\mathrm{GeSe}}(r)$ functions is similar, there is a change in $\bar{n}_{\mathrm{Ge}}^{\mathrm{Se}}$ from 3.7(1) in GeSe$_2$ to 3.99(2) in GeSe$_3$ to 4.09(2) in GeSe$_4$.

For all three compositions the peak position for Se-Se homopolar bonds, seen in figure 5-51, is the same within the error at 2.32(2) Å for GeSe$_2$, 2.34(2) Å for GeSe$_3$ and 2.35(2) Å for GeSe$_4$. As expected, the coordination number for Se-Se homopolar bonds increases with Se-composition, from 0.20(5) in GeSe$_2$ to 0.70(2) in GeSe$_3$ and to 1.00(2) in GeSe$_4$. The second Se-Se peak position moves to lower-r with increasing Se-content, and is 3.89(2) Å for GeSe$_2$, 3.85(3) Å for GeSe$_3$, and 3.83(3) Å for GeSe$_4$. This shift can be seen in figure 5-51 where the second Se-Se peak is asymmetric and leans towards the high-r side. As the Se-content increases, the second peak height decreases as the peak broadens. This leads to a small reduction in the coordination number, with $\bar{n}_{\mathrm{Se}}^{\mathrm{Se}} = 9.3(2)$ for GeSe$_2$, $\bar{n}_{\mathrm{Se}}^{\mathrm{Se}} = 9.22(3)$ for GeSe$_3$ and $\bar{n}_{\mathrm{Se}}^{\mathrm{Se}} = 9.10(3)$ for

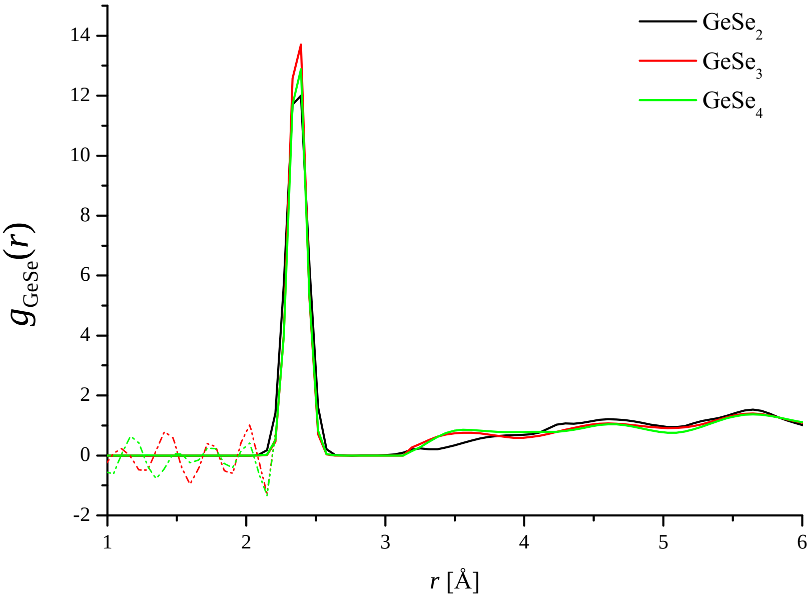

Figure 5-50: The Ge-Se partial pair-distribution functions $g_{\mathrm{GeSe}}(r)$ for $\mathrm{GeSe_3}$ (solid red curve) and $\mathrm{GeSe_4}$ (solid green curve) obtained from the SVD analysis, compared with Ingrid Petri's $\mathrm{GeSe_2}$ data (solid black curve) [16]. The data sets were obtained by truncating the reciprocal space data at the same maximum Q-value, $Q_{\mathrm{max}} = 16$ Å^{-1}. The solid lines show the functions after the low-r oscillations (dotted lines) have been set to their theoretical $g_{\alpha\beta}(r \to 0) = 0$ limit.

$\mathrm{GeSe_4}$.

Overall, these results show that whilst $\mathrm{GeSe_3}$ and $\mathrm{GeSe_4}$ are chemically ordered continuous random network glasses, the intrinsic chemical order of glassy $\mathrm{GeSe_2}$ is broken by the existence of Ge-Ge and Se-Se homopolar bonds, where 25(5)% of the Ge atoms and 20(5)% of the Se atoms are involved in these homopolar bonds [16].

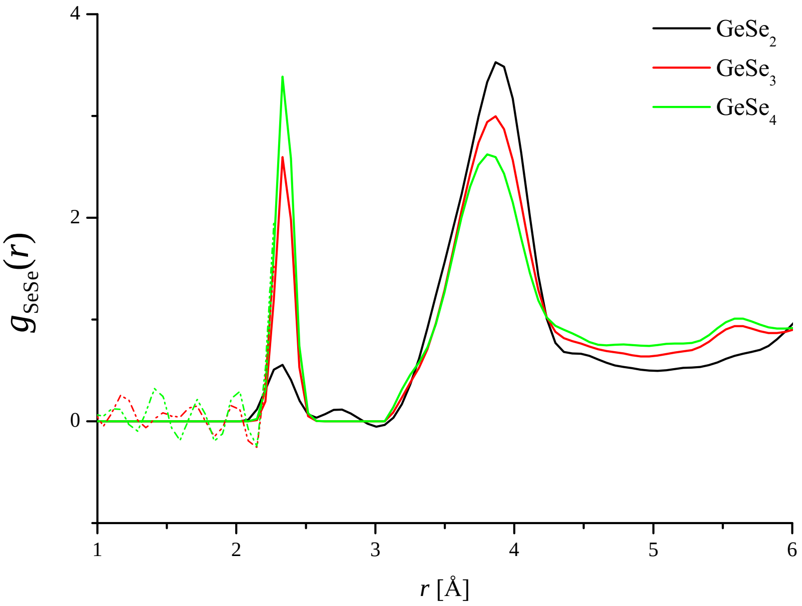

Figure 5-51: The Se-Se partial pair-distribution functions $g_{\mathrm{SeSe}}(r)$ for GeSe$_3$ (solid red curve) and GeSe$_4$ (solid green curve) obtained from the SVD analysis, compared with Ingrid Petri's GeSe$_2$ data (solid black curve) [16]. The data sets were obtained by truncating the reciprocal space data at the same maximum Q-value, $Q_{\max} = 16$ Å^{-1}. The solid lines show the functions after the low-r oscillations (dotted lines) have been set to their theoretical $g_{\alpha\beta}(r \to 0) = 0$ limit.

5.5.3 Comparison with simulations

In figures 5-52 – 5-57, the results from the density functional based molecular dynamics simulations by Micoulaut *et al* [17] and Bouzid *et al* [18, 19] are compared with the measured partial pair-correlation functions for GeSe$_2$ [16], GeSe$_3$ and GeSe$_4$. The simulations were performed using the Car-Parrinello method within the NVT ensemble with $N = 120$ atoms [17, 18] or $N = 480$ atoms [19] in a periodically repeated cubic cell. The electronic structure was described using density functional theory (DFT) within the generalised gradient approximation (GGA) using the Becke-Lee-Yang-Parr (BLYP) functional to describe the electron exchange and correlation parts of the total energy [17–19]. The box sizes used in the simulations allowed the experimental density of the glasses to be reproduced with pressures that do not exceed 0.5 GPa for the work by Micoulaut *et al* [17] and 0.15 GPa for the work by Bouzid *et al* [18, 19]. In both sets of simulations the system was randomized at 2000 K for 25 ps to loose the memory of the initial configuration. Micoulaut *et al* [17] performed additional runs of 25 ps at temperatures of 1373 K and 1050 K, before selecting four configurations to quench to the glassy state. Statistical averages were performed at 300 K on these four configurations for 84 ps. Bouzid *et al* [18, 19], quenched the system in steps of 500 K each lasting 25 ps, with the last step bringing the simulation temperature to 300 K. Statistical averages were performed over the simulations for 10 ps at 300 K for both $N = 120$ atoms and $N = 480$ atoms simulations.

A comparison between the measured ($S(Q)^{\text{exp}}$) and simulated ($S(Q)^{\text{sim}}$) reciprocal space functions were quantified using

$$\chi^2 = \sum_{i=1}^{N} \frac{\left[S(Q)_i^{\text{exp}} - S(Q)_i^{\text{sim}}\right]^2}{\sigma_{\text{exp},i}^2} \tag{5.17}$$

after the simulated data sets had been re-binned to have the same Q-binning as the experimental data sets, and $\sigma_{\text{exp},i}$ is the experimental error for data point i. The χ^2 values were used to compare the relative fits between the simulated and experimental datasets.

For the $S_{\text{SeSe}}(Q)$ functions (figure 5-52) the simulations accurately reproduce the main features seen in the measured data sets, although for GeSe_2 the height of the first peak is not reproduced in the simulations by Micoulaut *et al* [17].

For the $S_{\text{GeSe}}(Q)$ functions (figure 5-53) the simulations also reproduce the main features seen by experiment. For GeSe_2 and GeSe_4 the simulations by Micoulaut *et al* [17] give χ^2 values of 2.48 and 0.38, respectively, although for GeSe_3 there are some discrepancies at low-Q that result in a larger χ^2 value of 23.82. For GeSe_2, the simulations by Bouzid *et al* [18, 19], give χ^2 values that are comparable to those found for the simulations by Micoulaut *et al* [17]. For GeSe_4, the N=120 atom simulations by Bouzid *et al* [18] result in better agreement with experiment than the previous work by Micoulaut *et al* [17], resulting in a smaller χ^2 value of 0.22.

For the $S_{\text{GeGe}}(Q)$ functions (figure 5-54) the agreement between simulation and experiment is poorer than for $S_{\text{GeSe}}(Q)$ and $S_{\text{SeSe}}(Q)$. For example, the molecular dynamics simulations for GeSe_2, GeSe_3 and GeSe_4 give more structure than experiment at medium-Q values (4 - 10 Å^{-1}). The simulations do, however, reproduce an FSDP in the measured $S_{\text{GeGe}}(Q)$ functions, which is associated with intermediate range order [94–96], although its position and height is not accurately reproduced. For GeSe_2, the simulations by Bouzid *et al* [18] with $N = 120$ atoms are the least accurate, giving a χ^2 value of 931.5 , whereas the simulations by Micoulaut *et al* [17] give a χ^2 value of 2.09. For GeSe_4, all of the simulations give comparable χ^2 values: $\chi^2 = 4.80$ for Micoulaut *et al* [17], $\chi^2 = 4.23$ for the $N = 120$ atom simulation by Bouzid *et al* [18] and $\chi^2 = 5.61$ for the $N = 480$ atom simulation by Bouzid *et al* [19]. It is interesting to note that increasing the number of atoms in the simulation box does not improve the agreement

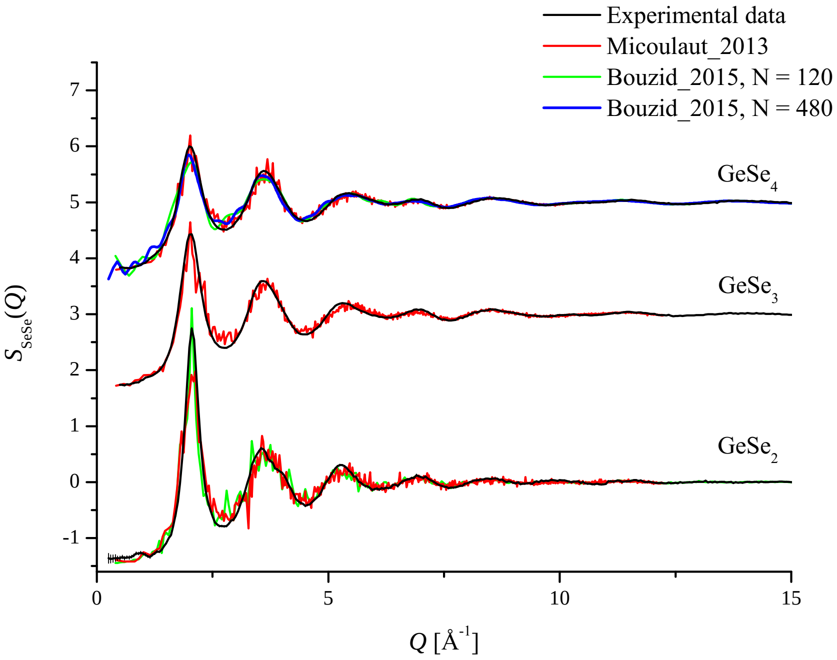

Figure 5-52: The Se-Se partial structure factors for GeSe$_2$, GeSe$_3$ and GeSe$_4$ offset vertically for clarity of presentation. The data sets from the first principles molecular dynamics simulations from Micoulaut *et al* (solid red curves) [17] and Bouzid *et al* (solid green curves) [18, 19] are compared with the data sets from experiment (solid black curves). A comparison between experiment and simulations is given by the χ^2 parameter. For GeSe$_2$, $\chi^2 = 6.07$ for the simulations from Micoulaut *et al* and $\chi^2 = 0.63$ for the simulations from Bouzid *et al.* For GeSe$_3$, $\chi^2 = 0.09$ for the simulations from Micoulaut *et al.* For GeSe$_4$, $\chi^2 = 0.64$ for the simulations from Micoulaut *et al* [17], whereas $\chi^2 = 0.13$ for the $N = 120$ atom and $\chi^2 = 20.56$ for the $N = 480$ atom simulations from Bouzid *et al* [18, 19].

between simulation and experiment.

Figures 5-55 compares the molecular dynamics simulations for $g_{\text{SeSe}}(r)$ to the measured real space data sets. For GeSe$_3$ and GeSe$_4$, both the coordination number (0.70(2) and 1.00(2)) and peak position (2.35(2) Å) for Se-Se homopolar bonds are well reproduced in the molecular dynamics simulations by Micoulaut *et al* [17]. However, the simulations underestimate the height of the main Se-Se peak at 3.58(3) Å, producing a peak that is broader and shifted to larger r. The molecular dynamics simulations by Bouzid *et al* [18, 19] reproduce the width of the main Se-Se peak for GeSe$_2$ and GeSe$_4$, but also underestimate the height of this feature. The height of the homopolar bond Se-Se peak at 2.35(2) Å in the $N = 120$ simulations is larger than found from experiment, whereas the height of this feature in the $N = 480$ simulations is smaller than found from experiment.

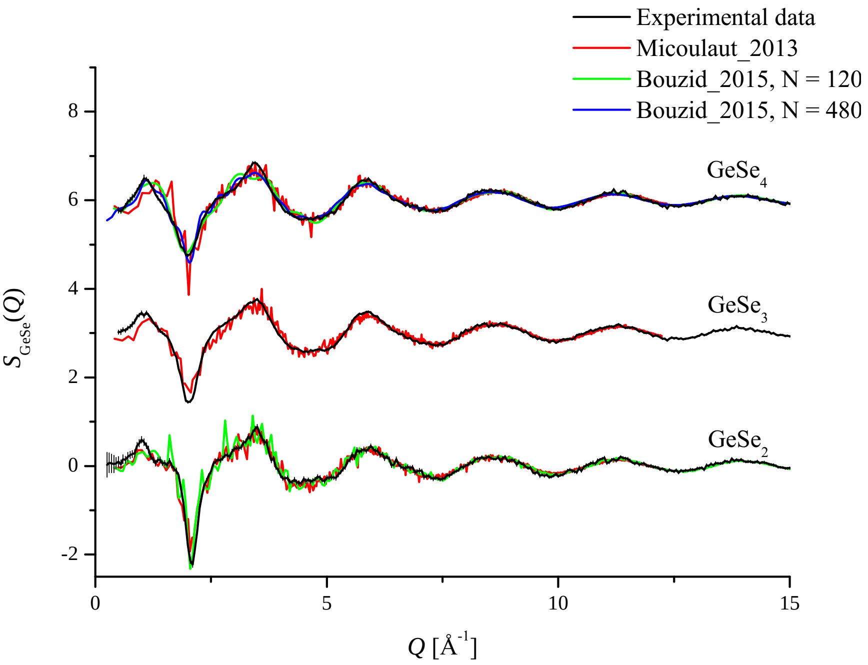

Figure 5-53: The Ge-Se partial structure factors for GeSe$_2$, GeSe$_3$ and GeSe$_4$ offset vertically for clarity of presentation. The data sets from the first principles molecular dynamics simulations from Micoulaut *et al* (solid red curves) [17] and Bouzid *et al* (solid green curves) [18, 19] are compared with the data sets from experiment (solid black curves). A comparison between experiment and simulations is given by the χ^2 parameter. For GeSe$_2$, $\chi^2 = 2.48$ for the simulations from Micoulaut *et al* and $\chi^2 = 5.39$ for the simulations from Bouzid *et al*. For GeSe$_3$, $\chi^2 = 23.82$ for the simulations from Micoulaut *et al* [17]. For GeSe$_4$, $\chi^2 = 0.38$ for the simulations from Micoulaut *et al* [17], whereas $\chi^2 = 0.22$ for the $N = 120$ atom and $\chi^2 = 0.41$ for $N = 480$ atom simulations from Bouzid *et al* [18, 19].

Figure 5-56 compares the molecular dynamics simulations for $g_{\mathrm{GeSe}}(r)$ to the measured real space functions. For all three materials, the molecular dynamics simulations by Micoulaut *et al* [17] reproduce the main features in the measured $g_{\mathrm{GeSe}}(r)$ functions, and exactly match the first Ge-Se peak position of 2.37(2) Å. The first peak heights are accurately reproduced for GeSe$_2$ and GeSe$_3$, but the peak height for GeSe$_4$ is overestimated. The simulations by Bouzid *et al* [18, 19] for GeSe$_2$ and GeSe$_4$ give comparable results to those found by Micoulaut *et al* [17]. The $\bar{n}_{\mathrm{Ge}}^{\mathrm{Se}}$ coordination numbers calculated from the simulated $g_{\mathrm{GeSe}}(r)$ functions are 3.55, 3.87 and 3.92 for GeSe$_2$, GeSe$_3$ and GeSe$_4$, respectively [17]. The values are all smaller than found from experiment (tables 5.12 and 5.13). The high-r experimental data is reproduced by both sets of simulations.

Figure 5-57 compares the molecular dynamics simulations for $g_{\mathrm{GeGe}}(r)$ to the mea-

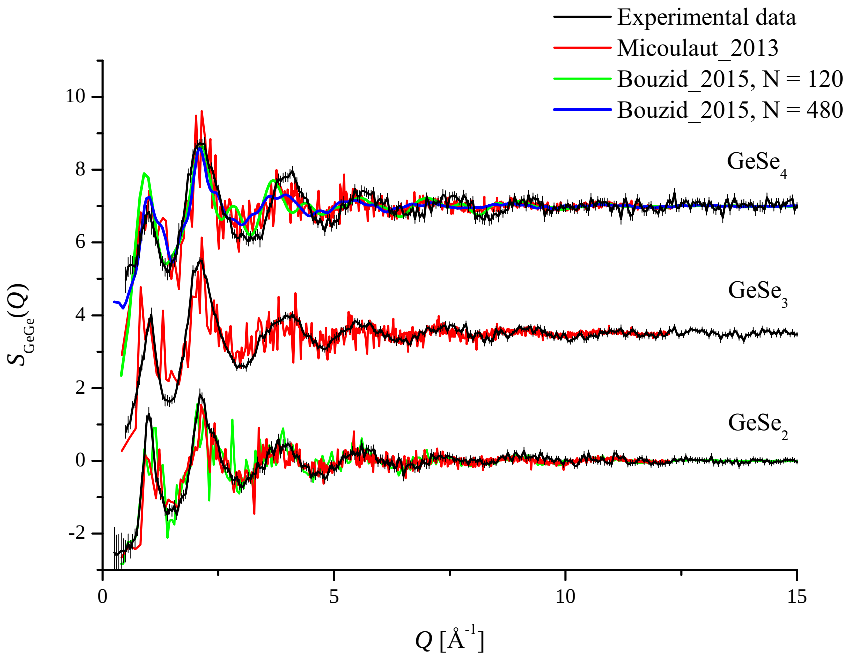

Figure 5-54: The Ge-Ge partial structure factors for GeSe$_2$, GeSe$_3$ and GeSe$_4$ offset vertically for clarity of presentation. The data sets from the first principles molecular dynamics simulations of Micoulaut *et al* (solid red curves) [17] and Bouzid *et al* (solid green curves) [18, 19] are compared to those obtained from experiment (solid black curves). A comparison between the simulations and experiment is given by the χ^2 parameter. For GeSe$_2$, $\chi^2 = 2.09$ for the simulations from Micoulaut *et al* and $\chi^2 = 931.5$ for the simulations from Bouzid *et al.* For GeSe$_3$, $\chi^2 = 1.79$ for the simulations from Micoulaut *et al.* For GeSe$_4$, $\chi^2 = 4.80$ for the simulations from Micoulaut *et al* [17], whereas $\chi^2 = 4.23$ for the $N = 120$ atom and $\chi^2 = 5.61$ for the $N = 480$ atom simulations from Bouzid *et al* [18, 19].

sured real-space functions. In accordance with the reciprocal space comparison given in figure 5-54, there are discrepancies between simulation and experiment for GeSe$_2$, GeSe$_3$ and GeSe$_4$. For GeSe$_3$, the simulations predict the existence of Ge-Ge homopolar bonds although these bonds could not be found from experiment. For GeSe$_4$, the $N = 120$ atom simulation by Bouzid *et al* [18] does not find Ge-Ge homopolar bonds, but the $N = 480$ atom simulation by Bouzid *et al* [19] does find these features i.e. there are discernible size effects between the $N = 120$ and $N = 480$ atom simulations that affect the nearest neighbour structural motifs. For GeSe$_2$, the breadth of the Ge-Ge homopolar bond peak in the measured $g_{\mathrm{GeGe}}(r)$ function is larger than the peak found from simulation.

For GeSe$_3$, the simulations predicted an ES Ge-Ge peak at 2.42 Å [17], which is seen at 2.94(3) Å in the experimental data. For GeSe$_4$, both sets of $N = 120$

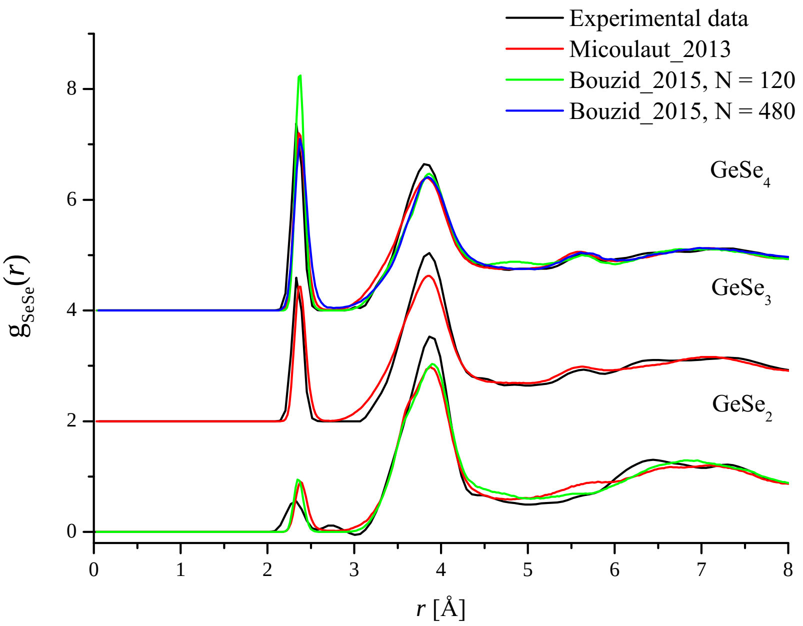

Figure 5-55: The Se-Se partial pair-distribution functions for $GeSe_2$, $GeSe_3$ and $GeSe_4$ offset vertically for clarity of presentation. The data sets from the first principles molecular dynamics simulations of Micoulaut *et al* (solid red curves) [17] and Bouzid *et al* (solid green curves) [18, 19] are compared with those obtained from experiment (solid black curves).

atom simulations show an ES Ge-Ge peak at 3.01 Å [19], which is not reproduced by experiment. However, for the measured $g_{\mathrm{GeGe}}(r)$ function there is a shoulder on the low-r side of the main CS Ge-Ge peak at 3.18(2) Å that may account for the existence of a small number of ES Ge-Ge configurations. For $GeSe_2$, the measured ES Ge-Ge peak position of 3.02 Å is reproduced by the simulations, although the measured peak is broader.

For all three compositions, the molecular dynamics simulations underestimate the height of the main CS Ge-Ge peak. However, the simulations by Bouzid *et al* which correspond to a lower residual pressure, are the closest to reproducing this peak height for $GeSe_2$ and $GeSe_4$. For $GeSe_2$ and $GeSe_4$, the CS Ge-Ge peak positions from the simulations are 3.68 Å and 3.65 Å [17], respectively, slightly larger than the values of 3.57(2) Å and 3.58(2) Å found experimentally. For $GeSe_3$, the CS Ge-Ge peak position of 3.59 Å from the simulations [17] agrees with the measured value of 3.58(2) Å within the error.

Overall, the results from both sets of molecular dynamics simulations for $GeSe_3$ and $GeSe_4$ produce glassy networks that are more disordered than found from experiment. Further refinements of these simulations is therefore required, and the experimental

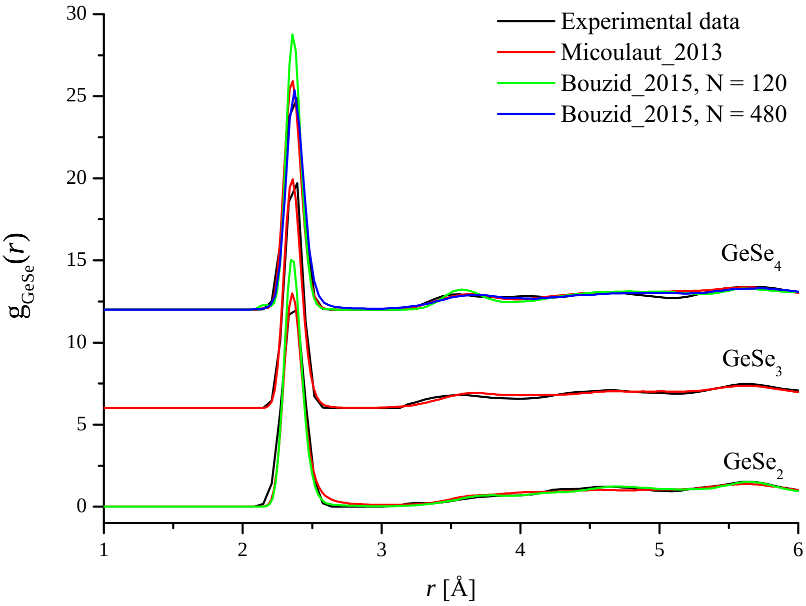

Figure 5-56: The Ge-Se partial pair-distribution functions for GeSe$_2$, GeSe$_3$ and GeSe$_4$ offset vertically for clarity of presentation. The data sets from the first principles molecular dynamics simulations of Micoulaut *et al* (solid red curves) [17] and Bouzid *et al* (solid green curves) [18, 19] are compared with those obtained from experiment (solid black curves).

data presented in this chapter provides an ability to test the results from these revised simulations. The latter will provide complementary information on the glass structure, such as the proportions of the different configurations shown in figure 5-48, which will further an understanding of the intermediate phase in these materials.

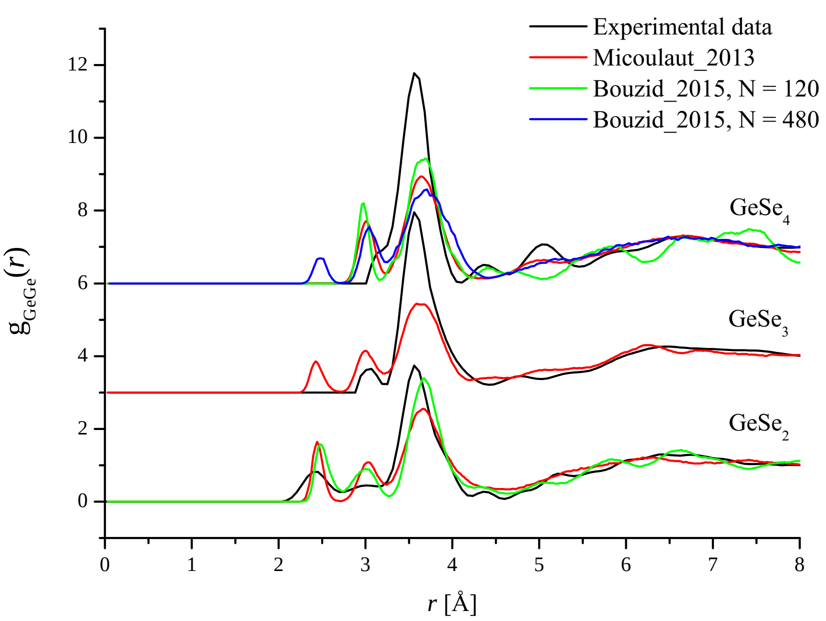

Figure 5-57: The Ge-Ge partial pair-distribution functions for $GeSe_2$, $GeSe_3$ and $GeSe_4$ offset vertically for clarity of presentation. The data sets from the first principles molecular dynamics simulations of Micoulaut *et al* (solid red curves) [17] and Bouzid *et al* (solid green curves) [18, 19] are compared with those obtained from experiment (solid black curves).

5.6 Conclusion

The full set of partial structure factors have been measured for both glassy $GeSe_3$ and $GeSe_4$ using the NDIS method. First-order difference functions have also been measured for both glasses, and the resulting peak positions and coordination number are consistent with those obtained from the partial structure factors. The measured coordination numbers for both $GeSe_3$ and $GeSe_4$ are consistent with a chemically ordered continuous random network (COCRN) model [1].

Further complementary information could be obtained via simulations of the glasses, providing additional information on *e.g.* the proportions of different structural configurations. However the current molecular dynamics simulations of glassy $GeSe_3$ and $GeSe_4$ [17–19] do not accurately reproduce all of the features in the measured pair-distribution functions.

A comparison of glassy $GeSe_3$ and $GeSe_4$ with previous measurements on glassy $GeSe_2$ [16] provides insight into the compositional dependence of the chemical ordering. $GeSe_3$ and $GeSe_4$ are more chemically ordered glasses as compared to $GeSe_2$, where the intrinsic chemical order is broken by the existence of Ge-Ge and Se-Se homopolar bonds, involving 25(5)% of the Ge atoms and 20(5)% of the Se atoms [16].

6. Coordination environment of Cl^- in a 5 molal aqueous solution of NaCl under pressure

6.1 Introduction

The NaCl – H_2O system under high temperature and/or high pressure conditions represents one of the most important geological fluids for understanding processes such as the metamorphism of rock, the sequestration of CO_2 by solubility trapping in deep aquifers, enhanced oil recovery, mass transfer within the Earth's crust via hydrothermal transport, and the generation of magma at the margins of convergent tectonic plates [97–105]. The development of models to describe the properties of geological fluids, and their interaction with a host rock, is still in it infancy.

There are several thermodynamic models that account for mineral-fluid interactions, which mainly occur through dissolution and crystallization processes [106, 107]. Whilst the Debye-Huckel theory [108] and the Pitzer model [107] work well for moderately concentrated solutions, extending these models to the highly concentrated solutions that are of interest for low-temperature metamorphism or CO_2 sequestration exceeds their reasonable limits of application, i.e. their predictions are associated with considerable uncertainty [109–111]. The problem stems from the fact that these models are poorly constrained, there being a lack of clear and quantitative experimental results on the speciation of concentrated fluids under high pressure and temperature conditions e.g. for the NaCl – H_2O system which is the principal component of most geological fluids. As shown in figure 6-1, the dielectric constant of water depends strongly on temperature and pressure, such that ion-pairing in an aqueous solution also depends on the thermodynamic conditions as well as the concentration of the solution [112]. For the NaCl – H_2O system the relative abundance of species such as dissociated Na^+ and Cl^- ions, associated neutral dimers of $NaCl^0$, and polynuclear clusters such as Na_2Cl^+ is not well understood [106, 111]. Therefore, a prerequisite for developing realistic microscopic and thermodynamic models of geological fluids is a detailed knowledge about their structure and speciation under high pressure and temperature conditions. A detailed knowledge of the atomic structure is also required for understanding the dynamics.

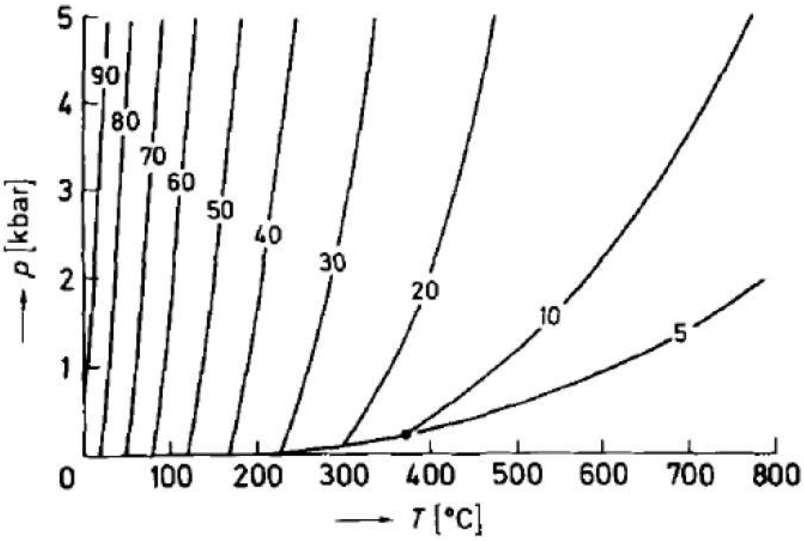

Figure 6-1: Variation of the dielectric constant of water with temperature and pressure [113]. The solid circle at 374°C and 0.22 kbar denotes the critical point of water.

The work presented in this chapter makes use of neutron diffraction with isotope substitution (NDIS) to measure the Cl^- coordination environment in a 5 molal NaCl – D_2O solution under high temperature and high pressure conditions. The solution concentration was chosen because it corresponds to a large mole fraction of Cl, which is necessary for a NDIS experiment on ionic solutions. Heavy water was chosen to avoid the large incoherent scattering associated with light hydrogen. Changes to the structure are predicted to manifest themselves by changes to the Cl-D and Cl-O bond lengths and coordination numbers. The structural information can be used to inform molecular dynamics simulations of the NaCl – H_2O system under high temperature and/or high pressure conditions [114–116].

This chapter is organised as follows. The essential theory for the neutron diffraction experiment is discussed in section 6.2. The experimental procedures for the work are presented in section 6.3. The experimental results are given in section 6.4, and are discussed in section 6.5. Lastly the conclusions are presented in section 6.6, along with some ideas for further work.

6.2 Theory

As discussed in Chapter 2, in a diffraction experiment the total structure factor

$$F(Q) = \sum_{\alpha=1}^{n} \sum_{\beta=1}^{n} c_\alpha c_\beta b_\alpha b_\beta \left[S_{\alpha\beta}(Q) - 1\right] \tag{6.1}$$

is measured, where α and β denote the chemical species, n is the total number of different chemical species, and c_α and b_α are the atomic fraction and bound coherent scattering length of atomic species α, respectively. The corresponding real space information is represented by the total pair-distribution function

$$\begin{aligned} G(r) &= \frac{1}{2\pi^2 r\rho} \int_0^\infty Q M(Q) F(Q) \sin(Qr)\, \mathrm{d}Q \\ &= \sum_{\alpha=1}^{n} \sum_{\beta=1}^{n} c_\alpha c_\beta b_\alpha b_\beta \left[g_{\alpha\beta}(r) - 1\right], \end{aligned} \tag{6.2}$$

where ρ is the atomic number density of the sample, $g_{\alpha\beta}(r)$ is a partial pair-distribution function, and $M(Q)$ is a modification function defined by $M(Q) = 1$ for $Q \leq Q_{\mathrm{max}}$, $M(Q) = 0$ for $Q > Q_{\mathrm{max}}$. The latter is included because a diffractometer can only measure over a limited Q-range up to some maximum value Q_{max}. The low-r limit is given by

$$G(r \to 0) = -\sum_{\alpha=1}^{n} \sum_{\beta=1}^{n} c_\alpha c_\beta b_\alpha b_\beta. \tag{6.3}$$

To produce smoother real space functions a Lorch modification function is occasionally used, where

$$M(Q) = \sin\left(\frac{\pi Q}{Q_{\mathrm{max}}}\right) \tag{6.4}$$

for $Q \leq Q_{\mathrm{max}}$ and $M(Q) = 0$ for $Q > Q_{\mathrm{max}}$.

If a peak in $g_{\alpha\beta}(r)$ is asymmetric it can be useful to find the weighted peak position

$$\bar{r}_{\alpha\beta} = \frac{\int_{r_{\mathrm{min}}}^{r_{\mathrm{max}}} r g_{\alpha\beta}(r)\, \mathrm{d}r}{\int_{r_{\mathrm{min}}}^{r_{\mathrm{max}}} g_{\alpha\beta}(r)\, \mathrm{d}r} \tag{6.5}$$

where the integration range over the peak is defined by the limits r_{min} and r_{max}.

For a four component system such as a NaCl – D_2O solution, the method of NDIS can be used to reduce the overall complexity of correlations associated with a single diffraction pattern. Let two solutions be prepared that are identical in every aspect, except that one contains the isotope ^{35}Cl and the other a 50:50 mixture of ^{35}Cl and ^{37}Cl

Table 6.1: The atomic fraction c_α of elements in the sample, along with the bound coherent scattering lengths b_α [54] and the average coherent scattering length $\langle b \rangle$ for the sample, taking into account the isotopic enrichments of the isotopes.

Sample	c_{Na}	c_{Cl}	c_{D}	c_{O}	b_{Na} /fm	b_{Cl} /fm	b_{D} /fm	b_{O} /fm	$\langle b \rangle$ /fm
$\mathrm{Na^{35}Cl-D_2O}$	0.0313(1)	0.0313(1)	0.6249(1)	0.3125(1)	3.63(2)	11.65(2)	6.671(4)	5.803(4)	6.454(3)
$\mathrm{Na^{Mix}Cl-D_2O}$	0.0313(1)	0.0313(1)	0.6249(1)	0.3125(1)	3.63(2)	7.365(5)	6.671(4)	5.803(4)	6.319(3)

which will be denoted by ${}^{\mathrm{Mix}}\mathrm{Cl}$. Let the associated total structure factors be represented by ${}^{\mathrm{Na}^{35}\mathrm{Cl}}F(Q)$ and ${}^{\mathrm{Na}^{\mathrm{Mix}}\mathrm{Cl}}F(Q)$, respectively. Then the first order difference function

$$\begin{aligned}\Delta F_{\mathrm{Cl}}(Q) &= {}^{\mathrm{Na}^{35}\mathrm{Cl}}F(Q) - {}^{\mathrm{Na}^{\mathrm{Mix}}\mathrm{Cl}}F(Q) \\ &= 2c_{\mathrm{Cl}}c_{\mathrm{D}}b_{\mathrm{D}}\left(b_{^{35}\mathrm{Cl}} - b_{^{\mathrm{Mix}}\mathrm{Cl}}\right)\left[S_{\mathrm{ClD}}(Q) - 1\right] \\ &+ 2c_{\mathrm{Cl}}c_{\mathrm{O}}b_{\mathrm{O}}\left(b_{^{35}\mathrm{Cl}} - b_{^{\mathrm{Mix}}\mathrm{Cl}}\right)\left[S_{\mathrm{ClO}}(Q) - 1\right] \\ &+ 2c_{\mathrm{Cl}}c_{\mathrm{Na}}b_{\mathrm{Na}}\left(b_{^{35}\mathrm{Cl}} - b_{^{\mathrm{Mix}}\mathrm{Cl}}\right)\left[S_{\mathrm{ClNa}}(Q) - 1\right] \\ &+ c_{\mathrm{Cl}}^2\left(b_{^{35}\mathrm{Cl}}^2 - b_{^{\mathrm{Mix}}\mathrm{Cl}}^2\right)\left[S_{\mathrm{ClCl}}(Q) - 1\right], \end{aligned} \tag{6.6}$$

eliminates those pair-correlations not associated with Cl. Importantly, $\Delta F_{\mathrm{Cl}}(Q)$ also eliminates the large inelastic scattering associated with D_2O [117]. The corresponding real space function is given by

$$\begin{aligned}\Delta G_{\mathrm{Cl}}(r) &= \frac{1}{2\pi^2 r\rho}\int_0^\infty Q\Delta F_{\mathrm{Cl}}(Q)\sin(Qr)\,\mathrm{d}Q \\ &= {}^{\mathrm{Na}^{35}\mathrm{Cl}}G(r) - {}^{\mathrm{Na}^{\mathrm{Mix}}\mathrm{Cl}}G(r) \\ &= 2c_{\mathrm{Cl}}c_{\mathrm{D}}b_{\mathrm{D}}\left(b_{^{35}\mathrm{Cl}} - b_{^{\mathrm{Mix}}\mathrm{Cl}}\right)\left[g_{\mathrm{ClD}}(r) - 1\right] \\ &+ 2c_{\mathrm{Cl}}c_{\mathrm{O}}b_{\mathrm{O}}\left(b_{^{35}\mathrm{Cl}} - b_{^{\mathrm{Mix}}\mathrm{Cl}}\right)\left[g_{\mathrm{ClO}}(r) - 1\right] \\ &+ 2c_{\mathrm{Cl}}c_{\mathrm{Na}}b_{\mathrm{Na}}\left(b_{^{35}\mathrm{Cl}} - b_{^{\mathrm{Mix}}\mathrm{Cl}}\right)\left[g_{\mathrm{ClNa}}(r) - 1\right] \\ &+ c_{\mathrm{Cl}}^2\left(b_{^{35}\mathrm{Cl}}^2 - b_{^{\mathrm{Mix}}\mathrm{Cl}}^2\right)\left[g_{\mathrm{ClCl}}(r) - 1\right], \end{aligned} \tag{6.7}$$

where the low-r limit is given by

$$\begin{aligned}\Delta G_{\mathrm{Cl}}(r \to 0) = -\Big\{ & 2c_{\mathrm{Cl}}c_{\mathrm{D}}b_{\mathrm{D}}\left(b_{^{35}\mathrm{Cl}} - b_{^{\mathrm{Mix}}\mathrm{Cl}}\right) + 2c_{\mathrm{Cl}}c_{\mathrm{O}}b_{\mathrm{O}}\left(b_{^{35}\mathrm{Cl}} - b_{^{\mathrm{Mix}}\mathrm{Cl}}\right) \\ & + 2c_{\mathrm{Cl}}c_{\mathrm{Na}}b_{\mathrm{Na}}\left(b_{^{35}\mathrm{Cl}} - b_{^{\mathrm{Mix}}\mathrm{Cl}}\right) + c_{\mathrm{Cl}}^2\left(b_{^{35}\mathrm{Cl}}^2 - b_{^{\mathrm{Mix}}\mathrm{Cl}}^2\right)\Big\}. \end{aligned} \tag{6.8}$$

The atomic fraction and bound coherent scattering lengths for the samples used in the experiment are given in table 6.1, and the corresponding weighting coefficients are given in table 6.2.

The first-order difference functions can also be calculated from the measured intensities $I(\theta)$ for the two samples instead of the total structure factors $F(Q)$. Following

Table 6.2: The weighting factors in units of millibarns (1 barn = 10^{-28} m^2) for the first order difference function defined by equation 6.6. The numerical values take into account the isotopic enrichment of the samples used in the experiment.

Coefficients	Weighting factor /millibarns
$2c_{\mathrm{Cl}}c_{\mathrm{D}}b_{\mathrm{D}}\left(b_{^{35}\mathrm{Cl}} - b_{^{\mathrm{Mix}}\mathrm{Cl}}\right)$	11.16(71)
$2c_{\mathrm{Cl}}c_{\mathrm{O}}b_{\mathrm{O}}\left(b_{^{35}\mathrm{Cl}} - b_{^{\mathrm{Mix}}\mathrm{Cl}}\right)$	4.86(31)
$2c_{\mathrm{Cl}}c_{\mathrm{Na}}b_{\mathrm{Na}}\left(b_{^{35}\mathrm{Cl}} - b_{^{\mathrm{Mix}}\mathrm{Cl}}\right)$	0.15(2)
$c_{\mathrm{Cl}}^2\left(b_{^{35}\mathrm{Cl}}^2 - b_{^{\mathrm{Mix}}\mathrm{Cl}}^2\right)$	0.79(7)

section 3.5, equation 3.7 can be rewritten as

$$\begin{aligned} I_{\mathrm{Cl}}^{\mathrm{E}'}(\theta) &= \left[I_{^{35}\mathrm{Cl}}^{\mathrm{E}}(\theta) - I_{\mathrm{B}}^{\mathrm{E}}(\theta)\right] - \left[I_{^{\mathrm{Mix}}\mathrm{Cl}}^{\mathrm{E}}(\theta) - I_{\mathrm{B}}^{\mathrm{E}}(\theta)\right] \\ &= I_{^{35}\mathrm{Cl}}^{\mathrm{E}}(\theta) - I_{^{\mathrm{Mix}}\mathrm{Cl}}^{\mathrm{E}}(\theta) \end{aligned} \tag{6.9}$$

where $I_{^{35}\mathrm{Cl}}^{\mathrm{E}}(\theta)$ and $I_{^{\mathrm{Mix}}\mathrm{Cl}}^{\mathrm{E}}(\theta)$ are the measured intensities for the Na^{35}Cl – D_2O and Na$^{\mathrm{Mix}}$Cl – D_2O solutions, respectively. Here, contributions to the measured intensities from the background and container will cancel as they are the same for both samples. The intensity $I_{\mathrm{Cl}}^{\mathrm{E}'}(\theta)$ can then be corrected for beam attenuation in the sample, such that the difference between the differential scattering cross-section for the samples is given by

$$\begin{aligned} \left.\frac{\mathrm{d}\sigma}{\mathrm{d}\Omega}\right|_{^{35}\mathrm{Cl}-^{\mathrm{Mix}}\mathrm{Cl}} &= \left.\frac{\mathrm{d}\sigma}{\mathrm{d}\Omega}\right|_{^{35}\mathrm{Cl}} - \left.\frac{\mathrm{d}\sigma}{\mathrm{d}\Omega}\right|_{^{\mathrm{Mix}}\mathrm{Cl}} \\ &= \frac{1}{N_{\mathrm{S}}A_{\mathrm{S,SC}}(\theta)}\left[\frac{I_{^{35}\mathrm{Cl}}^{\mathrm{E}}(\theta) - I_{^{\mathrm{Mix}}\mathrm{Cl}}^{\mathrm{E}}(\theta)}{a(\theta)}\right] \\ &= \Delta F_{\mathrm{Cl}}(Q) + \frac{\Delta\sigma_{\mathrm{S}}}{4\pi}, \end{aligned} \tag{6.10}$$

where it is assumed that the attenuation coefficients $A_{\mathrm{S,SC}}(\theta)$ are the same for both solutions, and the difference between the scattering cross-sections $\Delta\sigma_{\mathrm{S}}$ is defined in equation 3.6. Hence, $\Delta F_{\mathrm{Cl}}(Q)$ can be obtained.

The main advantage to this method of producing first-order difference functions is that the Q-dependent scattering associated with the Ti-Zr gasket used to contain the sample cancels out more accurately. The inelasticity slope associated with the D_2O in the samples also cancels exactly, and there is no need for a further empirical slope correction. In practice, it was found that this method gave the most reliable $\Delta F_{\mathrm{Cl}}(Q)$ functions, and it is the results from this method that will be presented in this chapter.

6.2.1 Units of Concentration

In this chapter many different methods of expressing concentration are used [118]. These are listed below:-

$$\textbf{Molality} = \frac{\text{number of moles of solute}}{\text{1 kg of solvent}} \tag{6.11}$$

$$\textbf{Mole fraction} = \frac{\text{number of moles of solute}}{\text{number of moles of solute + number of moles of solvent}} \tag{6.12}$$

$$\textbf{Weight\%} = \frac{\text{mass of solute}}{\text{mass of solution}} \times 100 \tag{6.13}$$

$$\textbf{Normality} = \frac{\text{equivalents of solute}}{\text{litre of solution}} \tag{6.14}$$

The equivalent of solute, sometimes known as the molar equivalent, can be defined as the amount of substance that will react with or supply one mole of hydrogen ions H^+ in an acid-base reaction.

6.3 Experiment

The 5 molal aqueous $NaCl - D_2O$ solutions were made from D_2O (99.9% D from Sigma Aldrich), $Na^{35}Cl$ (99 % isotopic enrichment from Sigma-Aldrich) and $Na^{Mix}Cl$ which contains a 50/50 mixture of ^{37}Cl and ^{35}Cl.

Table 6.3: The total scattering cross-section σ_T at an incident neutron wavelength of 0.4971(8) Å for each isotopically enriched sample. The measured mass density ρ_{mass} and number density ρ are also given for each sample at 25°C and 1 bar.

	$Na^{35}Cl - D_2O$	$Na^{Mix}Cl - D_2O$
molality	5.002(3)	4.999(3)
σ_T [barn]	4.691(4)	4.181(4)
ρ_{mass} [g/cm^3]	1.273(3)	1.280(3)
ρ [Å^{-3}]	0.09500(20)	0.09517(20)

6.3.1 Purification of chlorine isotopes

The isotopically enriched NaCl salts were previously used to study the structure of molten NaCl [15] where the molten salts reacted with their silica containers due to the presence of impurities. Thus, before the isotopes could be reused to produce aqueous solutions, it was necessary to remove these impurities. The apparatus that was used is shown in figure 6-2, which consists of a vacuum line and two flasks that can be sealed off from the vacuum line by Young's taps. A two step procedure was used to purify the chlorine isotopes.

In the first step, the left hand flask (figure 6-2) was filled with the dirty salt and left overnight under high vacuum ($\sim 10^{-5}$ Torr) to ensure the salt was dry. The magnetic stirrer was left stirring to move the salt around the flask. The dried NaCl salt was reacted with concentrated (98 wt %) sulphuric acid to produce hydrochloric acid (HCl) and sodium hydrogen sulphate ($NaHSO_4$), as given by

$$\mathrm{NaCl} + \mathrm{H_2SO_4} \rightarrow \mathrm{NaHSO_4} + \mathrm{HCl}. \tag{6.15}$$

To begin the reaction, the tap between the vacuum pump and the vacuum line was closed and the finger on the right hand flask was covered with a liquid nitrogen dewar to create a cold trap for the HCl. The concentrated sulphuric acid was dripped very slowly onto the NaCl, where it started fizzing and bubbling, whilst the solution was stirred vigorously. Gaseous HCl was produced and the isotopically enriched HCl was captured in the cold trap. Sulphuric acid was added slowly until the reaction ceased, there was no more bubbling and the solution was clear. Using an external magnet the magnetic stirrer was moved around the inside of the left hand side flask to make sure any salt stuck to the sides was reacted with the sulphuric acid.

Once the reaction was complete, the right hand flask was sealed off and detached from the vacuum line, ensuring that the cold trap remained within the liquid nitrogen. Distilled water was added to the main body of the right hand side flask and the cold finger was removed from the liquid nitrogen. The frozen HCl in the cold finger was allowed to slowly warm up and dissolve in the water whilst the water was stirred vigorously. It was important not to allow the HCl to warm up too quickly as the volume of the HCl in its gaseous state was larger than the volume of the sealed flask, and there was therefore a risk that the flask could explode from the increased pressure. Once all of the HCl had dissolved into the water, the first stage of the purification was complete.

In the second stage of the purification process, the enriched HCl solution was neutralised using a 0.5 N solution of NaOH, where the reaction is given by

$$\mathrm{HCl} + \mathrm{NaOH} \rightarrow \mathrm{NaCl} + \mathrm{H_2O}. \tag{6.16}$$

A titration set-up was used to measure the amount of NaOH added to the solution. In this case the base (NaOH) was filled into a burette and added drop-by-drop to the

(a) (b)

Figure 6-2: Photographs of the chlorine purification apparatus. (a) Two flasks attached to the vacuum line. The left hand flask was used to react the salt with concentrated sulphuric acid. The right hand flask is where the isotopically enriched HCl gas was first captured using a nitrogen trap, and then dissolved into distilled water. (b) A. Zeidler holds the right hand flask, as the isotopically enriched HCl dissolves into the water, whilst being stirred vigorously.

HCl solution. A meter was used to measure the pH of the solution throughout the titration. It was important not to add an excess of NaOH, as the resulting neutralised solution would be dried to form the clean NaCl salt. Therefore NaOH was added until the neutral point was almost reached, and the solution had a pH $\simeq 6$. Figure 6-3 shows the calibration curve for the titration of the purified HCl solution.

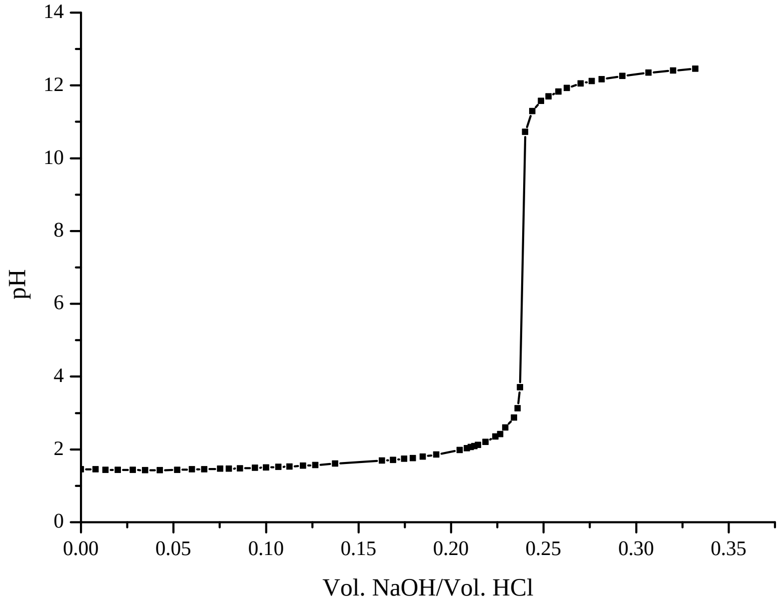

Figure 6-3: Calibration curve for the titration of a test HCl solution with 0.5 N NaOH.

Finally the neutralised NaCl solutions were dried in an oven set to 80°C, a temperature that was chosen so that a solution would not boil and splash out of its beaker. The dried NaCl was washed into nalgene bottles, and dried further in the oven at 80°C for approximately 4 weeks.

6.3.2 Neutron diffraction experiment

The neutron diffraction experiment was carried out on the D4c diffractometer at the Institut Laue Langevin using a VX5 version of the Paris-Edinburgh press with an incident wavelength of 0.4971(8) Å.

The sample was loaded into hemispherical Ti-Zr gaskets by pipetting 30 μL of solution into each half of the gasket. The high surface tension of the solution allowed for one half of the gasket to be flipped over and placed on-top of the other half. The excess sample was wiped away, and the two halves placed onto the lower anvil of the PE press, along with the outer toroid. This procedure ensured that no bubbles were present, which would alter the response of the sample and gasket assembly to the applied pressure. The top anvil of the press, complete with its cartridge heater and cooling ring, was then manoeuvred into position without disturbing the sample within the encapsulated gaskets resting on the lower anvil. The electrical wires for the cartridge heater then were threaded through the backing seat, before the grub screws were tightened to hold the upper anvil in place. A nominal oil pressure of 70 bar was then applied to the system to seal the encapsulated gaskets, prior to the belljar being evacuated by the vacuum system. The lower anvil was also equipped with a cartridge heater and cooling ring.

The gaskets used for the $\mathrm{Na}^{35}\mathrm{Cl}$ – $\mathrm{D_2O}$ and $\mathrm{Na}^{\mathrm{Mix}}\mathrm{Cl}$ – $\mathrm{D_2O}$ solutions were as similar as possible: they were machined from the same billet of metal and had the same mass, volume and dimensions. However, the orientation of the gasket with respect to the incident neutron beam has a significant effect on the resulting diffraction pattern. Therefore, although the two gaskets were as identical as possible, they showed slightly different structure at low-Q values. As the pressure increases the Q-dependent structure of the gaskets decreases, resulting in a more homogeneous material.

Measurements were made for the sample contained within its encapsulated Ti-Zr gasket at 150°C with an applied oil pressure of 70 bar, 198 bar, 407 bar, 500 bar and 600 bar. At pressures greater than 600 bar, the NaCl–$\mathrm{D_2O}$ solution began to crystallise i.e. Bragg peaks appeared in the measured diffraction patterns. Measurements were also made for: an empty uncompressed Ti-Zr encapsulated gasket, eight encapsulated Ti-Zr gaskets that had been recovered from different pressures with the sample removed, three empty anvil measurements with different anvil spacings, and large, small and medium vanadium pellets within toroidal Ti-Zr gaskets for normalisation purposes.

6.3.3 Pressure at the sample position

Figure 6-4 shows the calibration curve used to convert the applied oil pressure to the pressure at the sample position. This calibration curve was obtained from previous work on the pressure dependence of water at 150°C using the same VX5 variant of the Paris-Edinburgh large-volume press and encapsulated Ti-Zr gaskets [119]. The upper calibration point was provided by the pressure of 3.38 GPa at which $\mathrm{D_2O}$ crystallises at 150°C [120] and corresponds to an applied oil pressure of 600 bar. The lower end of the calibration curve was obtained from diffraction measurements on $\mathrm{D_2O}$ at pressures up to 2 kbar using a Ti-Zr pressure cell, where the applied pressure is known. By plotting the position of the principal peak Q_{PP} in $F(Q)$ versus pressure it was possible to find the lowest pressure corresponding to the Q_{PP} position measured for $\mathrm{D_2O}$ obtained using the PE press. Given that the highest and lowest pressure points were then known, a linear fit was used to estimate the intermediate pressure points. The resulting fit is shown in figure 6-4.

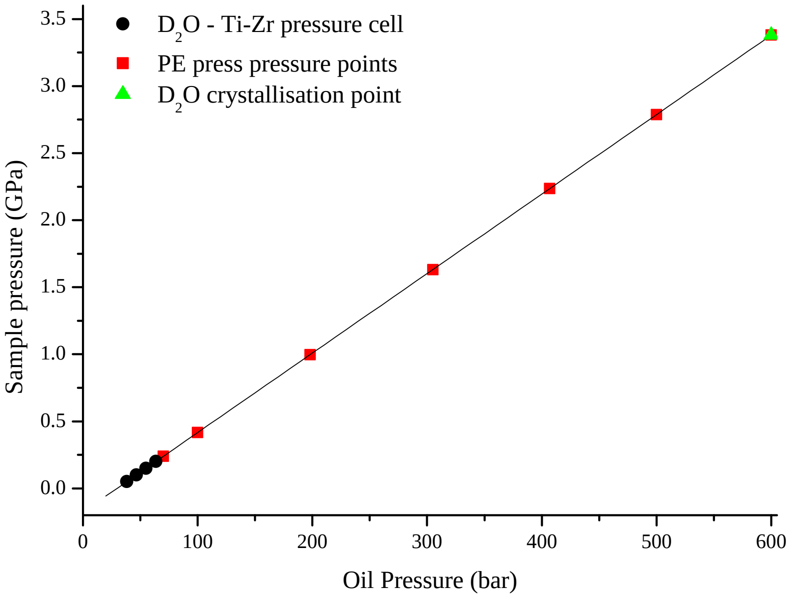

Figure 6-4: Pressure calibration curve for the VX5 variant of the Paris-Edinburgh large-volume press for use with Ti-Zr encapsulated gaskets and aqueous solutions. The linear fit is given by $P_{\mathrm{sample}}(\mathrm{GPa}) = -0.1761(1) + 0.00592(2)\ P_{\mathrm{oil}}(\mathrm{bar})$ (solid black line). The black circles are the pressure points obtained from the Ti-Zr cell D_2O data, and the green triangle is the pressure at which D_2O crystallises at 150°C [120]. The red squares are the pressures at which diffraction measurements were made for the NaCl – D_2O solutions.

6.3.4 Density of NaCl solutions under pressure

The pressure dependence of the number density for the aqueous NaCl solutions is required for the analysis of the neutron diffraction data. There is no experimental data for the density of 5 molal NaCl – D_2O solutions under high pressures comparable to those achieved with a Paris-Edinburgh press.

First, the data for D_2O was used to plot the principal peak position Q_{pp} versus number density [121] for pressures ranging from ambient to 3.38 GPa (see in figure 6-5) and it was found that this plot was approximately linear. Then the principal peak position versus number density measured for a 5 molal NaCl – D_2O solution in a Ti-Zr pressure cell experiment on D4c was extrapolated to higher densities using the same rate of change of principal peak position with density as for D_2O. The densities for the 5 molal NaCl – D_2O solutions measured in the Ti-Zr pressure cell were taken from Potter and Brown [122].

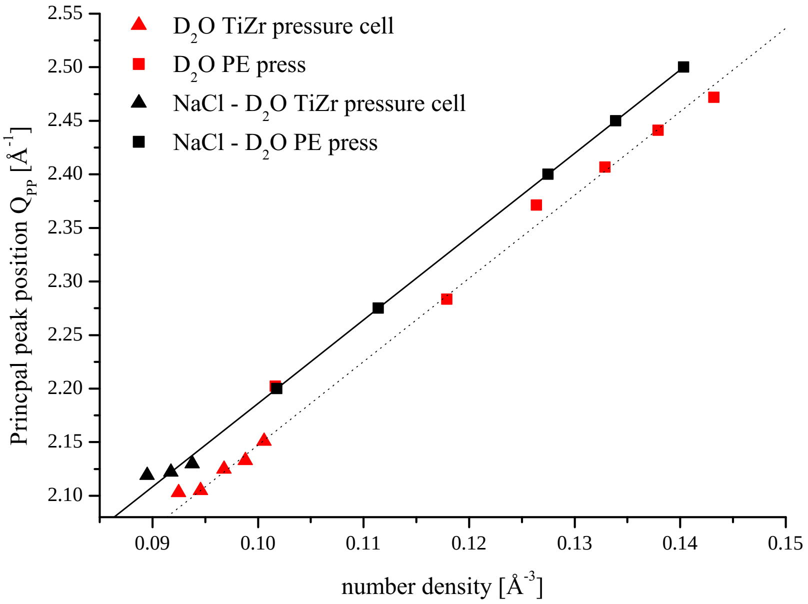

Figure 6-5: Principal peak position vs number density for D_2O and for a 5 molal NaCl – D_2O solution. The red and black upwards triangles are the data points from Ti-Zr pressure cell experiments on D_2O and NaCl – D_2O, respectively. The red and black squares are the data points from Paris-Edinburgh press experiments on D_2O and NaCl – D_2O, respectively. The black line shows a linear extrapolation of the NaCl – D_2O Ti-Zr pressure cell data points to higher densities using the same gradient as for the D_2O dataset (dotted line).

Table 6.4 shows the number densities as a function of pressure up to 3.38 GPa along the trajectory used in this and other experiments on 5 molal NaCl–D_2O solutions and D_2O [119]. The ratio of ρ/ρ_0, where ρ_0 =0.09536 Å^{-3}, shows that as the temperature is increased to 150 °C the number density is reduced by $\simeq$ 7%. At 150 °C and 0.2 GPa the number density is roughly the same as under ambient conditions. After 0.2 GPa the number density increases with pressure such that $\rho/\rho_0 = 1.47$ at 3.38 GPa.

Table 6.4: Pressure and temperature dependence of the number density ρ for a 5 molal NaCl – D_2O solution, along with the ratio ρ/ρ_0, where ρ_0 is the number density at 0.00001 GPa and 25 °C. An asterix indicates a number density that has been obtained by using the method discussed in section 6.3.4. The other number densities were obtained from Potter and Brown [122].

Pressure /GPa	Temperature /°C	ρ /Å^{-3}	ρ/ρ_0
0.00001	25	0.09536	1.00000
0.01	25	0.09567	1.00325
0.01	50	0.09468	0.99287
0.01	100	0.09233	0.96823
0.01	150	0.08951	0.93865
0.05	150	0.09175	0.96214
0.10	150	0.09377	0.98333
0.20	150	0.09669	1.01395
0.24	150	0.10177*	1.06722
1.00	150	0.11141*	1.16831
2.24	150	0.12748*	1.33683
2.79	150	0.13390*	1.40415
3.38	150	0.14033*	1.47158

6.4 Results

6.4.1 Total structure factors

The slope corrected measured total structure factors $F(Q)$ for the 5 molal $\mathrm{Na}^{35}\mathrm{Cl}$ – $\mathrm{D_2O}$ and 5 molal $\mathrm{Na}^{\mathrm{Mix}}\mathrm{Cl}$ – $\mathrm{D_2O}$ solutions at pressures up to 3.38 GPa are plotted in figures 6-6 and 6-7, respectively. The slope, which arises from inelasticity effects, was corrected for by fitting a 5th order polynomial to $Q\frac{\mathrm{d}\sigma}{\mathrm{d}\Omega}(Q)$, as described in chapter 4. The corresponding $G(r)$ functions are shown in figures 6-8 and 6-9 for the 5 molal $\mathrm{Na}^{35}\mathrm{Cl}$ – $\mathrm{D_2O}$ and 5 molal $\mathrm{Na}^{\mathrm{Mix}}\mathrm{Cl}$ – $\mathrm{D_2O}$ solutions, respectively. The O - D bond distance and coordination number did not change with pressure, as indicated by the data given in table 6.5.

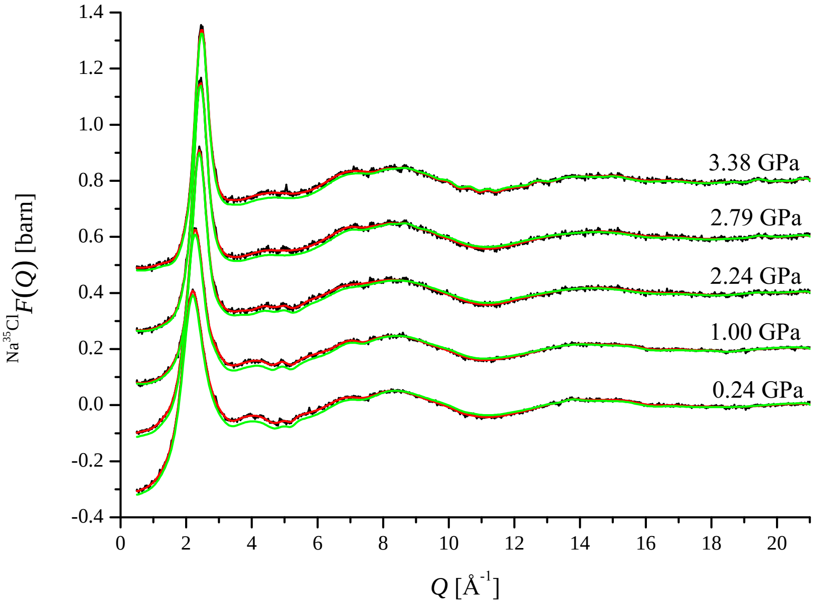

Figure 6-6: The pressure dependence of the total structure factor $^{\mathrm{Na^{35}Cl}}F(Q)$ for a 5 molal $\mathrm{Na}^{35}\mathrm{Cl}$ – $\mathrm{D_2O}$ solution. The solid black curves are the measured datasets, and the solid green curves are the back Fourier transforms of the $^{\mathrm{Na^{35}Cl}}G(r)$ functions shown by the solid curves in figure 6-8. The solid red curves are Harwell spline fits to the measured datasets. The curves are offset vertically for clarity of presentation.

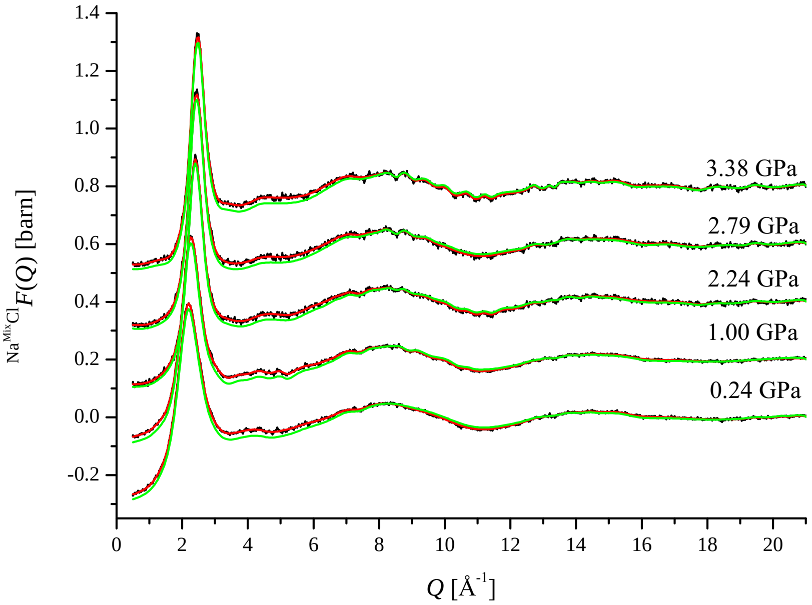

Figure 6-7: The pressure dependence of the total structure factor $^{\mathrm{Na^{Mix}Cl}}F(Q)$ for a 5 molal $\mathrm{Na^{Mix}Cl}$ – D_2O solution. The solid black curves are the measured datasets, and the solid green curves are the back Fourier transforms of the $^{\mathrm{Na^{Mix}Cl}}G(r)$ functions shown by the solid curves in figure 6-9. The solid red curves are Harwell spline fits to the measured datasets. The curves are offset vertically for clarity of presentation.

Table 6.5: The pressure dependence of the oxygen - deuterium bond distance r_{OD} and coordination number $\bar{n}_{\mathrm{O}}^{\mathrm{D}}$ as obtained from the first peak in the measured $G(r)$ function, for a 5 molal solution of $\mathrm{Na^{35}Cl}$ – D_2O and $\mathrm{Na^{35}Cl}$ – D_2O, shown in figures 6-8 and 6-9, respectively.

	Pressure /GPa	$\bar{n}_{\mathrm{O}}^{\mathrm{D}}$	r_{OD} /Å
$\mathrm{Na^{35}Cl}$	0.24(5)	2.04(3)	0.95(2)
	1.00(5)	1.97(3)	0.96(2)
	2.24(5)	2.02(3)	0.95(2)
	2.79(5)	2.06(3)	0.95(2)
	3.38(5)	2.02(3)	0.95(2)
$\mathrm{Na^{Mix}Cl}$	0.24(5)	1.97(3)	0.95(2)
	1.00(5)	1.96(3)	0.95(2)
	2.24(5)	2.01(3)	0.96(2)
	2.79(5)	2.04(3)	0.96(2)
	3.38(5)	2.00(3)	0.95(2)

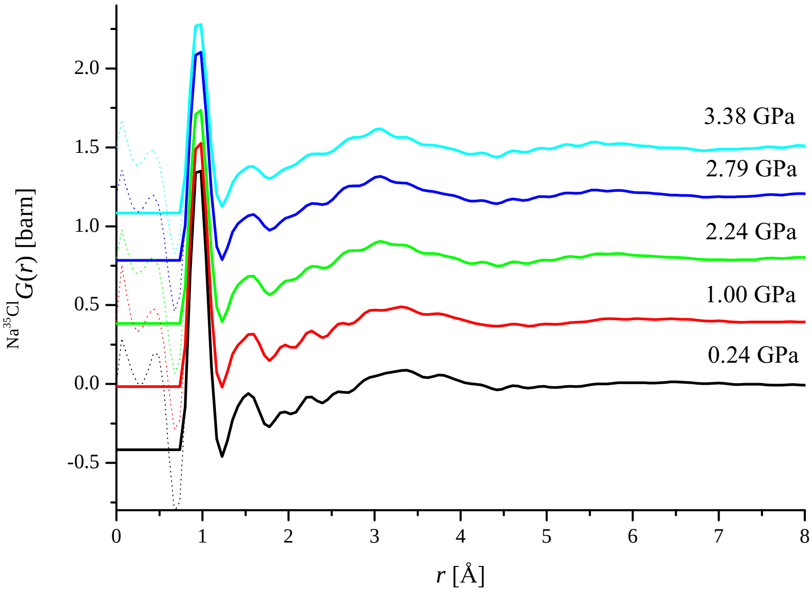

Figure 6-8: The pressure dependence of the total pair-distribution function $^{\mathrm{Na}^{35}\mathrm{Cl}}G(r)$ for a 5 molal $\mathrm{Na}^{35}\mathrm{Cl} - \mathrm{D_2O}$ solution. The solid lines were obtained by Fourier transforming the total structure factors $^{\mathrm{Na}^{35}\mathrm{Cl}}F(Q)$ given in figure 6-6, after the low-r oscillations (dashed lines) are set to their theoretical $G(r \to 0)$ limit. The curves are offset vertically for clarity of presentation.

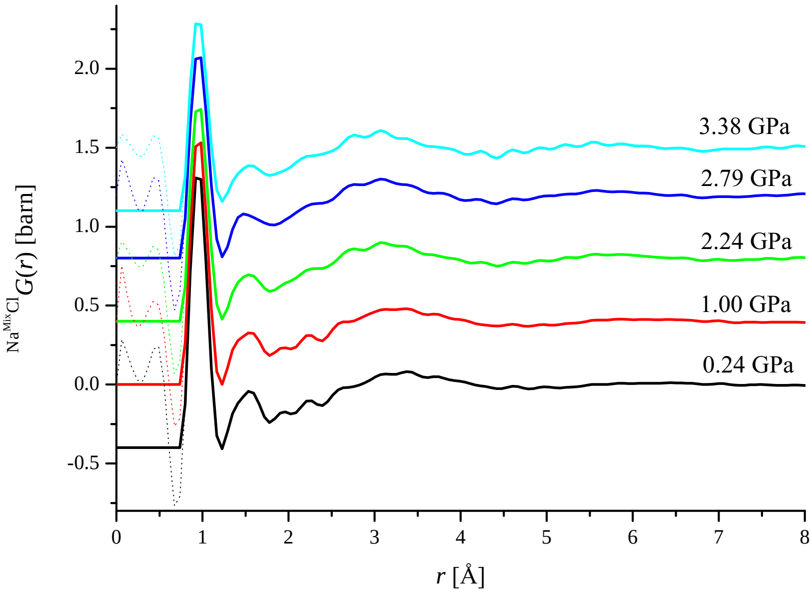

Figure 6-9: The pressure dependence of the total pair-distribution function $^{\text{Na}^{\text{Mix}}\text{Cl}}G(r)$ for a 5 molal $\text{Na}^{\text{Mix}}\text{Cl} - \text{D}_2\text{O}$ solution. The solid lines were obtained by Fourier transforming the total structure factors $^{\text{Na}^{\text{Mix}}\text{Cl}}F(Q)$ given in figure 6-6, after the low-r oscillations (dashed lines) are set to their theoretical $G(r \to 0)$ limit. The curves are offset vertically for clarity of presentation.

6.4.2 First-order difference functions

Figure 6-10 shows the first-order difference functions $\Delta F_{\mathrm{Cl}}(Q)$ for a 5 molal NaCl – D_2O solution solution under pressure. These first-order difference functions were obtained by taking the difference of the two measured intensities $I(\theta)$, as described in section 6.2. The corresponding real space first-order difference functions $\Delta G_{\mathrm{Cl}}(r)$ are shown in figure 6-11 and were obtained by using a Lorch modification function with $Q_{\mathrm{max}} = 21$ Å^{-1}. Table 6.6 gives the Cl - D coordination number and peak position as obtained from the first peak in the $\Delta G_{\mathrm{Cl}}(r)$ functions. Figures 6-12 and 6-13 show the effect on $\Delta G_{\mathrm{Cl}}(r)$ of truncating the $\Delta F_{\mathrm{Cl}}(Q)$ functions at $Q_{\mathrm{max}} = 18$ Å^{-1} and at $Q_{\mathrm{max}} = 12$ Å^{-1} with a Lorch modification function, respectively. Tables 6.7 and 6.8 give the Cl - D coordination number and peak position as obtained from the first peak in the $\Delta G_{\mathrm{Cl}}(r)$ functions shown in figures 6-12 and 6-13, respectively.

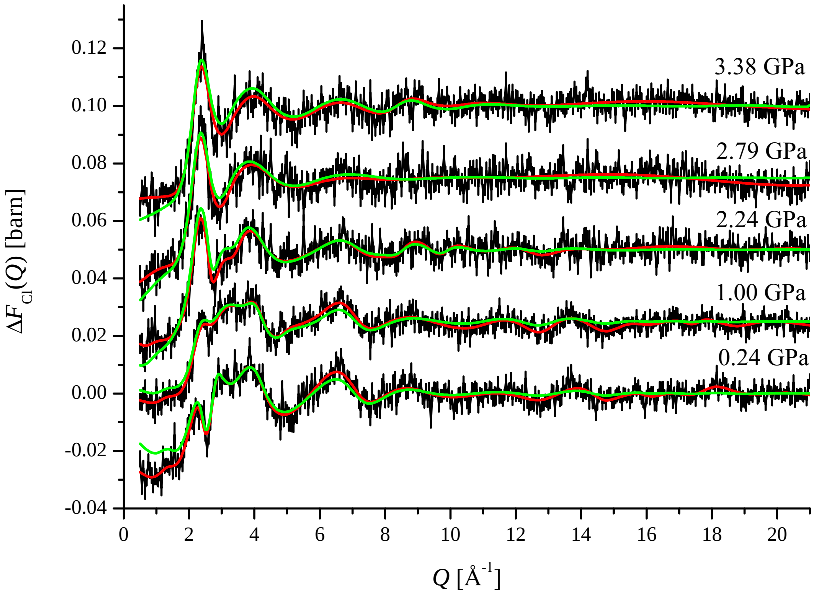

Figure 6-10: The pressure dependence of the first-order difference function $\Delta F_{\mathrm{Cl}}(Q)$ for a 5 molal NaCl – D_2O solution. The solid black curves with vertical error bars are the measured datasets, and the solid green curves are the back Fourier transforms of the $\Delta G_{\mathrm{Cl}}(r)$ functions shown by the solid curves in figure 6-11. The solid red curves are Harwell spline fits to the measured datasets. The curves are offset vertically for clarity of presentation.

As these first order difference functions were obtained by taking the difference between the two measured intensities $I(\theta)$, it was necessary to ensure that the total structure factors and the difference functions have the same normalisation. This means

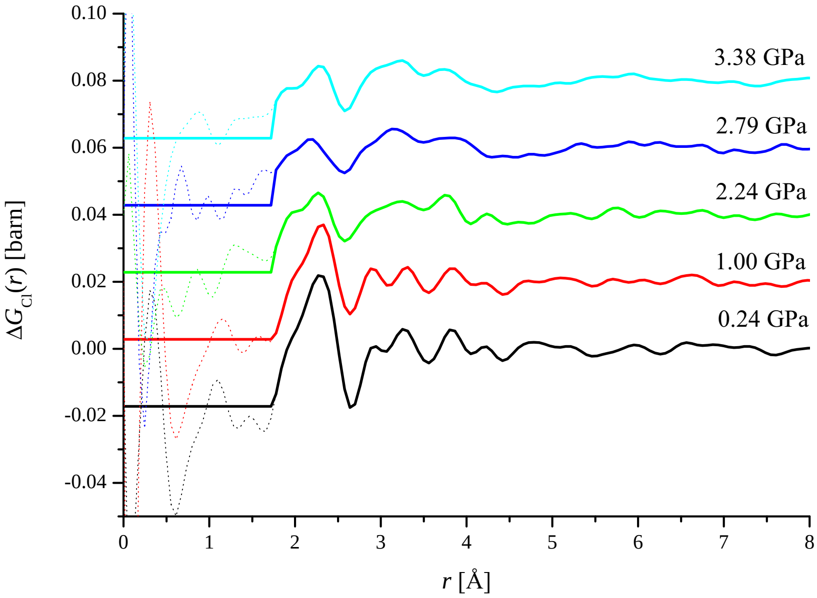

Figure 6-11: The pressure dependence of the first-order difference function $\Delta G_{\rm Cl}(r)$ for a 5 molal NaCl – D_2O solution. The solid curves were obtained by Fourier transforming the spline fitted $\Delta F_{\rm Cl}(Q)$ functions given in figure 6-10 after truncation at $Q_{\rm max} = 21$ Å^{-1} using a Lorch modification function. The low-r oscillations (dashed lines) have been set to their theoretical $\Delta G_{\rm Cl}(r \rightarrow 0)$ limit. The curves are offset vertically for clarity of presentation.

that the number of sample scattering centres illuminated by the incident neutron beam $N_{\rm S}$ (see equation 6.10) is the same for both the total structure factors and the difference functions. The number of scattering centres $N_{\rm S}$ is calculated using the dimensions of the sample, which is constrained by the dimensions of its gasket, and the atomic number density at the required pressure.

Table 6.6: The pressure dependence of the chlorine - deuterium bond distance r_{ClD} and coordination number $\bar{n}_{\mathrm{Cl}}^{\mathrm{D}}$ as obtained from the first peak in the measured $\Delta G_{\mathrm{Cl}}(r)$ functions shown in figure 6-11. The weighted peak position $\bar{r}_{\mathrm{ClD}}$, as defined by equation 6.5, is also given.

Pressure /GPa	$\bar{n}_{\mathrm{Cl}}^{\mathrm{D}}$	r_{ClD} /Å	$\bar{r}_{\mathrm{ClD}}$ /Å
0.24(5)	7.1(5)	2.29(4)	2.21(4)
1.00(5)	6.9(5)	2.31(4)	2.23(4)
2.24(5)	6.5(5)	2.27(4)	2.18(4)
2.79(5)	6.1(5)	2.20(4)	2.16(4)
3.38(5)	6.3(5)	2.29(4)	2.18(4)

Table 6.7: The pressure dependence of the chlorine - deuterium bond distance r_{ClD} and coordination number $\bar{n}_{\mathrm{Cl}}^{\mathrm{D}}$ as obtained from the first peak in the measured $\Delta G_{\mathrm{Cl}}(r)$ functions shown in figure 6-12. The weighted peak position $\bar{r}_{\mathrm{ClD}}$, as defined by equation 6.5, is also given.

Pressure /GPa	$\bar{n}_{\mathrm{Cl}}^{\mathrm{D}}$	r_{ClD} /Å	$\bar{r}_{\mathrm{ClD}}$ /Å
0.24(5)	7.0(5)	2.29(4)	2.21(4)
1.00(5)	6.9(5)	2.30(4)	2.23(4)
2.24(5)	6.5(5)	2.25(4)	2.18(4)
2.79(5)	6.1(5)	2.20(4)	2.16(4)
3.38(5)	6.4(5)	2.29(4)	2.18(4)

Table 6.8: The pressure dependence of the chlorine - deuterium bond distance r_{ClD} and coordination number $\bar{n}_{\mathrm{Cl}}^{\mathrm{D}}$ as obtained from the first peak in the measured $\Delta G_{\mathrm{Cl}}(r)$ functions shown in figure 6-13. The weighted peak position $\bar{r}_{\mathrm{ClD}}$, as defined by equation 6.5, is also given.

Pressure /GPa	$\bar{n}_{\mathrm{Cl}}^{\mathrm{D}}$	r_{ClD} /Å	$\bar{r}_{\mathrm{ClD}}$ /Å
0.24(5)	6.9(5)	2.23(4)	2.21(4)
1.00(5)	6.8(5)	2.20(4)	2.22(4)
2.24(5)	6.8(5)	2.13(4)	2.17(4)
2.79(5)	6.7(5)	2.16(4)	2.15(4)
3.38(5)	6.7(5)	2.15(4)	2.17(4)

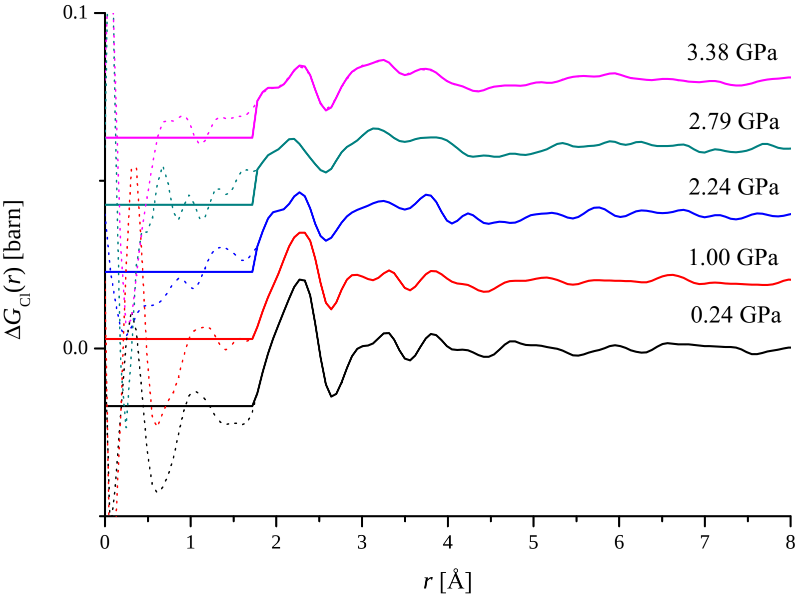

Figure 6-12: The pressure dependence of the first-order difference function $\Delta G_{\mathrm{Cl}}(r)$ for a 5 molal NaCl – D_2O solution. The solid curves were obtained by Fourier transforming the spline fitted $\Delta F_{\mathrm{Cl}}(Q)$ functions given in figure 6-10 after truncation at $Q_{\mathrm{max}} = 18$ Å^{-1} using a Lorch modification function. The low-r oscillations (dashed lines) have been set to their theoretical $\Delta G_{\mathrm{Cl}}(r \to 0)$ limit. The curves are offset vertically for clarity of presentation.

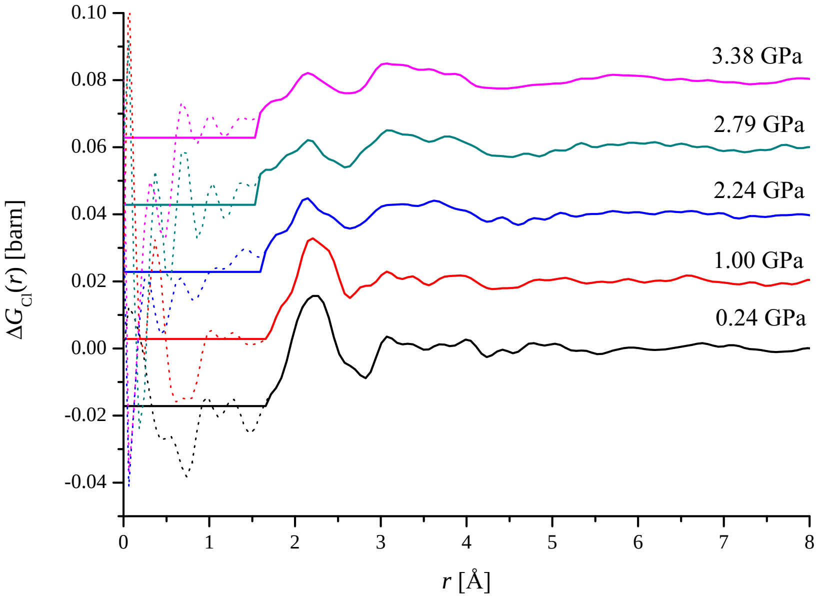

Figure 6-13: The pressure dependence of the first-order difference function $\Delta G_{\mathrm{Cl}}(r)$ for a 5 molal NaCl – D_2O solution. The solid curves were obtained by Fourier transforming the spline fitted $\Delta F_{\mathrm{Cl}}(Q)$ functions given in figure 6-10 after truncation at $Q_{\mathrm{max}} = 12$ Å^{-1} using a Lorch modification function. The low-r oscillations (dashed lines) have been set to their theoretical $\Delta G_{\mathrm{Cl}}(r \to 0)$ limit. The curves are offset vertically for clarity of presentation.

6.5 Discussion

The total structure factors $F(Q)$ given in figures 6-6 and 6-7 show a sharpening and shift to higher-Q value of the principal peak at $Q_{\rm PP} \simeq 2.2$ Å^{-1}. There is good agreement at most Q-values between the measured $F(Q)$ functions and the back Fourier transforms, except for the region between 4 and 6 Å^{-1}. This is likely to originate from the correction procedure used for the inelasticity slope, i.e. the 5th order polynomial fitted to the data does not produce the correct slope in this region. However, the low-Q data points ($\leq$ 1 Å^{-1}) in the back Fourier transforms agree with the measured data points, indicating that the $F(Q)$ functions are correctly normalised.

The first peak in the $G(r)$ functions (figures 6-8 and 6-9) decreases in height and broadens with increasing pressure. Each peak gives a coordination number $\bar{n}_{\rm O}^{\rm D} = 2$, consistent with the presence of D_2O water molecules. The intra-molecular O-D distance $r_{\rm OD}$ found from the position of the first peak in $G(r)$ also remains constant with pressure, and is consistent with the value $r_{\rm OD} = 0.96(2)$ Å found from neutron diffraction measurements on D_2O at ambient pressure [15] and at pressures in the range from 0.24 – 3.38 GPa [119].

Figure 6-10 shows that the first peak in the $\Delta F_{\rm Cl}(Q)$ functions at ~ 2.3 Å^{-1} becomes sharper as the pressure is increased. Previous ambient pressure and temperature work on a 5.32 molal aqueous solution of $\rm NaCl - D_2O$ by Soper *et al* [117] and on a 3.62 molal aqueous solution of $\rm NaCl - D_2O$ by Barnes *et al* [123], both show the beginnings of a first peak at ~ 2.3 Å^{-1}. There is difficulty in fully eliminating the Ti-Zr gasket scattering from the measured $\Delta F_{\rm Cl}(Q)$ functions. For example, in the $\Delta F_{\rm Cl}(Q)$ functions at 0.24 and 1.00 GPa, there is feature at $Q = 14$ Å^{-1} that may originate from a trough in the measured diffraction pattern for Ti-Zr, and there is an unphysical slope beyond $Q =$ 18 Å^{-1} in the $\Delta F_{\rm Cl}(Q)$ function for 2.79 GPa. Nevertheless, the $r_{\rm ClD}$ peak position is consistent with the value $r_{\rm OD} = 2.27$ Å found from previous experiments [123], and there is no evidence in the $\Delta G_{\rm Cl}(r)$ functions of the intra-molecular O-D peak, which is a prominent feature in the $G(r)$ functions.

Figure 6-11 shows the pressure dependence of real space first-order difference functions $\Delta G_{\rm Cl}(r)$, which were obtained by Fourier transforming the Harwell spline fitted $\Delta F_{\rm Cl}(Q)$ functions shown in figure 6-10 after the application of a Lorch modification function with $Q_{\rm max} = 21$ Å^{-1}. The use of a Lorch function produces a smoother $\Delta G_{\rm Cl}(r)$ function at all r-values, but does lead to a loss in resolution of the first r-space peak. The first peak in the $\Delta G_{\rm Cl}(r)$ functions is asymmetric, with a low-r shoulder that becomes more distinct with increasing pressure. Figures 6-12 and 6-13 show the $\Delta G_{\rm Cl}(r)$ functions obtained by Fourier transforming the Harwell spline fitted $\Delta F_{\rm Cl}(Q)$ functions after truncation at $Q_{\rm max} = 18$ Å^{-1} and at $Q_{\rm max} = 12$ Å^{-1} with a Lorch modification function, respectively. These $\Delta G_{\mathrm{Cl}}(r)$ functions give a first Cl-D peak that is broader and more distorted than seen in figure 6-11, which may indicate that there are still some small background features in the $\Delta F_{\mathrm{Cl}}(Q)$ functions at lower-Q values that are due to Ti-Zr gasket scattering.

The position r_{ClD} of the first Cl-D peak in $\Delta G_{\mathrm{Cl}}(r)$ is given in table 6.6, along with the weighted peak position $\bar{r}_{\mathrm{ClD}}$. As the peak is asymmetric, the weighted peak position provides a more representative Cl-D bond distance. Figures 6-14 and 6-15 show the decrease in peak position and weighted peak position with increasing pressure, respectively. The Cl-D peak position $\bar{r}_{\mathrm{ClD}}$ becomes shorter as the pressure is increased changing from 2.21(4) Å at 0.24 GPa to 2.18(4) Å at 3.38 GPa. Yamaguchi *et al* [124] measured $\Delta F_{\mathrm{Cl}}(Q)$ for solutions of LiCl – D_2O and CsCl– D_2O in the temperature range 298 – 300 K and pressure range 0.1 – 169 MPa. They observed a first Cl-D peak at 2.3 Å, a Cl-O peak at 3.2 Å, and a second Cl-D peak at 3.5 Å, which all decreased in amplitude with increasing temperature. Cummings *et al* [125] measured a 5.32 molal aqueous solution of NaCl – D_2O under ambient conditions. They obtained a coordination number $\bar{n}_{\mathrm{Cl}}^{\mathrm{D}} = 5.5(4)$ at a distance of $r_{\mathrm{ClD}} = 2.26(3)$ Å. Cummings *et al* also observed the Cl – O peak at $r_{\mathrm{ClO}} = 3.20(5)$ Å.

Figure 6-16 shows the Cl-D coordination numbers obtained for the $\Delta G_{\mathrm{Cl}}(r)$ functions as shown in figures 6-11, 6-12 and 6-13, respectively. The coordination numbers for the top three pressure points obtained from the first peak in the $\Delta G_{\mathrm{Cl}}(r)$ functions shown in figure 6-13 are larger than those found from the $\Delta G_{\mathrm{Cl}}(r)$ functions shown in figures 6-11 and 6-12. In the present work, the Cl-D coordination number is found to decrease with increasing pressure, from $\bar{n}_{\mathrm{Cl}}^{\mathrm{D}} = 7.1(5)$ at 0.24 GPa to $\bar{n}_{\mathrm{Cl}}^{\mathrm{D}} = 6.3(5)$ at 3.38 GPa. At first sight, this is an unexpected result because coordination numbers usually increase with density. This effect does not appear to result from increased ion-pairing between Na^+ and Cl^- that displaces water molecules, as shown by figure 6-1 the dielectric constant of water increases with pressure at least over the range from ambient to 0.5 GPa.

The Cl-O peak in $\Delta G_{\mathrm{Cl}}(r)$ was observed in previous work under ambient conditions [123, 125] and under pressures [124] in the range 3.20 – 3.32 Å. Molecular dynamics simulations by Regan *et al* [115], at temperatures of 177 °C – 727 °C and pressures up to 250 bar, suggest that the first Na-Cl peak should also occur in the region of 3.20 – 3.32 Å. The Na – Cl peak position for contact ion pair can also be estimated at ambient conditions using the Shannon ionic radii [127] which gives $r_{\mathrm{ClNa}} = 2.83$ Å. This suggests that the second peak in the measured $\Delta G_{\mathrm{Cl}}(r)$ function consists of overlapping Cl-O, Na-Cl and Cl-D correlations [125]. Further simulations are required to help solve this issue.

Although the structure of the NaCl – D_2O system has been simulated under high

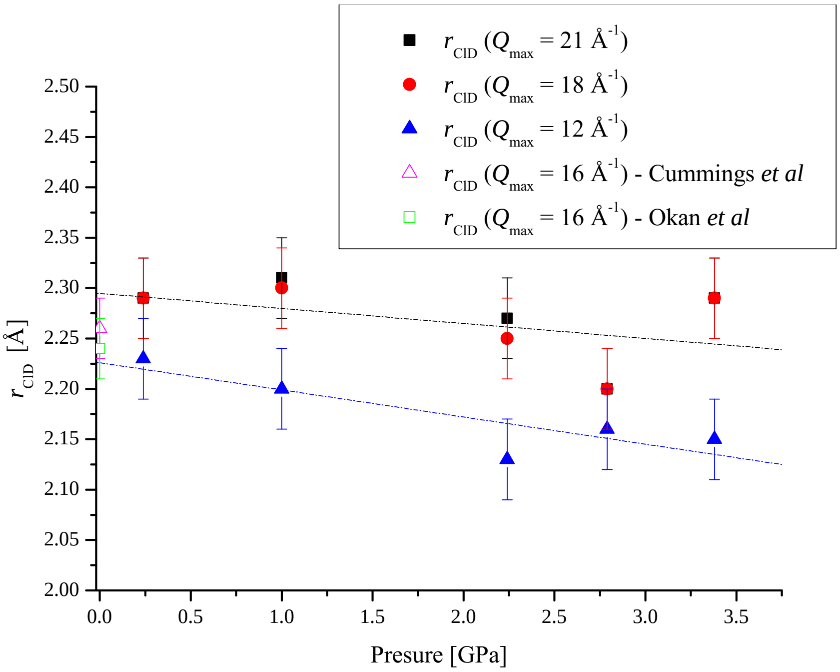

Figure 6-14: The pressure dependence of the chlorine - deuterium peak position r_{ClD} obtained from the first peak in the $\Delta G_{\mathrm{Cl}}(r)$ functions shown in figures 6-11, 6-12 and 6-13. The points with vertical error bars correspond to the $\Delta G_{\mathrm{Cl}}(r)$ functions that were obtained from $\Delta F_{\mathrm{Cl}}(Q)$ by truncation using a Lorch function at $Q_{\mathrm{max}} = 21$ Å^{-1} (black squares), at $Q_{\mathrm{max}} = 18$ Å^{-1} (red circles) or $Q_{\mathrm{max}} = 12$ Å^{-1} (blue triangles). The black dotted line is a linear fit to the dataset truncated at $Q_{\mathrm{max}} = 21$ Å^{-1} and the blue dotted line is a linear fit to the dataset truncated at $Q_{\mathrm{max}} = 12$ Å^{-1}. The green open square with vertical error bars is r_{ClD} at ambient from Okan *et al* [126] for a 3.62 molal solution of NaCl in D_2O. The magenta open triangle with vertical error bars is r_{ClD} at ambient from Cummings *et al* [125] for a 5.32 molal solution of NaCl in D_2O.

temperature and/or high temperature conditions [107, 108, 114, 115], these studies have been limited to pressures ≤ 0.1 GPa. In comparison, the experimental results presented in this chapter correspond to a higher pressure regime of 0.24 – 3.38 GPa. These experimental results provide new information on the structure of the NaCl – D_2O system, and will hopefully stimulate the development of new molecular dynamics models for this and other geological fluids.

6.6 Conclusion

In summary, it has been shown that the NDIS method can be used to help resolve the structural complexity of the NaCl – D_2O system under high pressure conditions at 150°C. The O-D bond distances and coordination numbers $\bar{n}_{\mathrm{O}}^{\mathrm{D}}$ of the water molecule

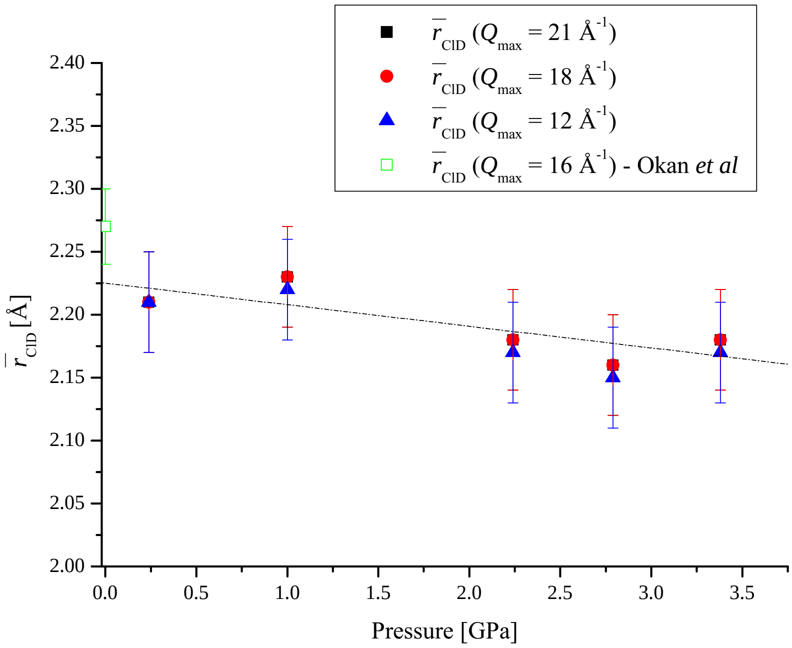

Figure 6-15: The pressure dependence of the chlorine - deuterium weighted peak position $\bar{r}_{\mathrm{ClD}}$ obtained from the first peak in the $\Delta G_{\mathrm{Cl}}(r)$ functions shown in figures 6-11, 6-12 and 6-13. The points with vertical error bars correspond to the $\Delta G_{\mathrm{Cl}}(r)$ functions that were obtained from $\Delta F_{\mathrm{Cl}}(Q)$ by truncation using a Lorch function at Q_{max} = 21 Å^{-1} (black squares), at Q_{max} = 18 Å^{-1} (red circles) or Q_{max} = 12 Å^{-1} (blue triangles). The black dotted line is a linear fit to the dataset truncated at Q_{max} = 21 Å^{-1}. The green open square with vertical error bars is $\bar{r}_{\mathrm{ClD}}$ at ambient from Okan *et al* [126] for a 3.62 molal solution of NaCl in D_2O.

remain constant over the measured pressure range, where the measured bond distances are in agreement with previous measurements made at ambient [15] and under pressure [119]. The first-order difference functions give the first Cl-D bond distance and coordination number $\bar{n}^{\mathrm{D}}_{\mathrm{Cl}}$. As the pressure increases the value of $\bar{n}^{\mathrm{D}}_{\mathrm{Cl}}$ decreases from 7.1(5) to 6.3(5), as the Cl-D peak position $\bar{r}_{\mathrm{ClD}}$ decreases from 2.21(4) Å to 2.18(4) Å. These measurements on the structure of the NaCl – D_2O system under high pressure conditions may help in the development of models for geological fluids.

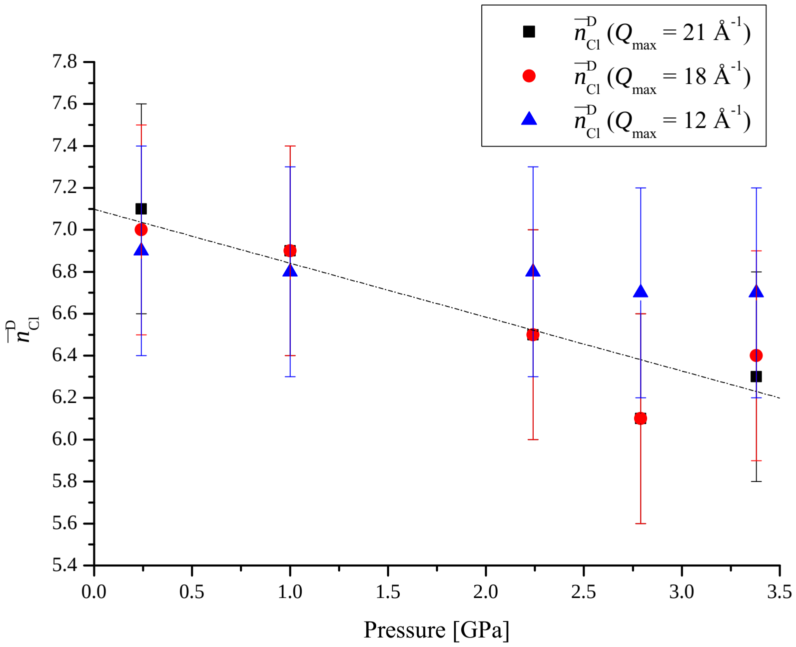

Figure 6-16: The pressure dependence of the chlorine - deuterium coordination number $\bar{n}_{\mathrm{Cl}}^{\mathrm{D}}$ obtained from the first peak in the $\Delta G_{\mathrm{Cl}}(r)$ functions shown in figures 6-11, 6-12 and 6-13, respectively. The points with vertical error bars correspond to the $\Delta G_{\mathrm{Cl}}(r)$ functions that were obtained from $\Delta F_{\mathrm{Cl}}(Q)$ by truncation using a Lorch function at Q_{max} = 21 Å^{-1} (black squares), Q_{max} = 18 Å^{-1} (red circles) or at Q_{max} = 12 Å^{-1} (blue triangles). The black dotted line is a linear fit to the dataset truncated at Q_{max} = 21 Å^{-1}.

7. Overall Conclusions

The method of neutron diffraction with isotope substitution was used to measure the full set of partial structure factors for crystalline ice-Ih, glassy $GeSe_3$ and glassy $GeSe_4$, and it has also been used to measure the Cl^- ion coordination environment in a 5 molal solution of NaCl in D_2O under pressure.

In chapter 4 the full set of partial structure factors were measured for ice-Ih at 15 K and 123 K. The hydrogen bond network in ice-Ih was characterised using first inter-molecular O-H peak position and coordination number $\bar{n}_{\mathrm{O}}^{\mathrm{H}} = 2$, indicating that the oxygen molecules are hydrogen bonded to two others with a distribution of hydrogen bond lengths. The intra-molecular H-H peak and first inter-molecular O-H peak are both asymmetric, and this asymmetry is seen at both temperatures 15 K and 123 K, showing the proton disorder in ice-Ih that is not seen in crystallographic measurements. This proton disorder is observed in both ice-Ih and low density amorphous ice. The intra-molecular O-H distances of 0.961(3) Å at 123 K and 0.965(12) Å at 15 K for the $g_{\mathrm{OH}}(r)$ function are considerably shorter than the published crystallographic value of 0.987(5) Å. This is probably due to residual inelasticity corrections, as the intra-molecular O-H peak position of 0.981(3) Å at 15 K from the $\Delta G_{\mathrm{no\ HH}}(r)$ difference function agrees with the crystallographic value within the random error. Calculations using the intra-molecular and first inter-molecular O-H bond distances and first O-O bond distance with the cosine rule suggest that the hydrogen bond is bent with a bond angle of $160.1(4.4)^\circ$ at 15 K and $177.2(2.4)^\circ$ at 123 K. However, if the intra-molecular O-H peak position from the $\Delta G_{\mathrm{no\ HH}}(r)$ difference functions are used, then the O-H$\cdots$O angle is $153.4(4.4)^\circ$ at 15 K and $164.0(2.4)^\circ$ at 123 K.

In chapter 5 the NDIS method was used to measure the full set of partial structure factors for glassy $GeSe_3$ and glassy $GeSe_4$. The measured coordination numbers for both $GeSe_3$ and $GeSe_4$ are consistent with a chemically ordered continuous random network (COCRN) model [1]. A comparison of glassy $GeSe_3$ and $GeSe_4$ with previous measurements on glassy $GeSe_2$ [16] provides insight into the compositional dependence of the chemical ordering. Further complementary information could be obtained via simulations of the glasses, providing additional information on *e.g.* the proportions of different structural configurations. However, the current first principles molecular dynamics simulations of glassy $GeSe_3$ and $GeSe_4$ [17–19] do not accurately reproduce all of the features in the measured pair-distribution functions. In particular, the Ge-Ge partial structure factor is not well reproduced by the simulations.

In chapter 6 the results from *in situ* high pressure neutron diffraction experiments on a 5 molal solution of NaCl in D_2O at 150°C were presented. Accurate total structure factors were measured in the pressure range of 0.24 GPa – 3.38 GPa for two isotopically enriched solutions using $Na^{35}Cl$ and $Na^{Mix}Cl$. The O-D bond distances and coordination numbers obtained from the measured total pair-distribution functions remain constant over the measured pressure range, and are in agreement with previous measurements of the O-D peak position in D_2O under ambient [15] and high pressure [119] conditions. The measured difference functions $\Delta F_{Cl}(Q)$ show that as the pressure increases the Cl-D coordination number decreases from 7.1(5) to 6.3(5), as the Cl-D distance decreases from 2.21(4) Å to 2.18(4) Å.

It would be interesting to use the information contained in the measured partial structure factors for ice-Ih to produce accurate 3-D models of the system using e.g. the reverse Monte-Carlo method. This would provide additional information on the structure of the crystal such as bond angle distributions and clarify the nature of the proton disorder. There is also room to improve in the current first principles molecular dynamics simulations of glassy $GeSe_3$ and $GeSe_4$ [17–19], and the partial structure factors presented in this thesis provide the experimental data required to test the assumptions used in these simulations. Finally it will be useful to extend the investigation of a 5 molal solution of NaCl in D_2O to the pressure range of 0.01 – 0.1 GPa, thus making contact with the state of this aqueous solution under ambient conditions. Such experiments could be made using a Ti-Zr pressure cell [128]. Looking further ahead, the results from the planned experiment on the structure of the CO_2 – NaCl – D_2O system under pressure [128] will build on the results presented here, and will provide information that is relevant to CO_2 sequestration.

Bibliography

[1] S. R. Elliott. *Physics of Amorphous Materials.* Longman Group UK, Essex, 2nd. edition, 1990.

[2] A. Feltz. *Amorphous Inorganic Materials and Glasses.* Wiley-VCH, New York, 1993.

[3] P. Boolchand. *Insulating and Semiconducting Glasses.* World Scientific, Singapore, 2000.

[4] J. S. Sanghara, I. D. Aggarwal, L. B. Shaw, L. E. Busse, P. Thielen, V. Nguyen, P. Pureza, S. Bayya, and F. Kung. Applications of chalcogenide glass optical fibers at nrl. *J. Optoelec. Adv. Mat.*, 3:627, 2001.

[5] A. Zakery and S. R. Elliott. Optical properties and applications of chalcogenide glasses: a review. *Journal of Non-Crystalline Solids*, 330:1–12, 2003.

[6] B. J. Eggleton, B. Luther-Davies, and K. Richardson. Chalcogenide photonics. *Nature Phot.*, 5:141, 2011.

[7] D. L. Anderson. *New theory of the Earth.* Cambridge University Press, Cambridge, UK, 2007.

[8] J. P. Poirier. *Introduction to the physics of the Earth's interior.* Cambridge University Press, Cambridge, 1991.

[9] F. Paesani and G. A. Voth. The properties of water: Insights from quantum simulations. *Journal of Physical Chemistry B*, 113:5702, 2009.

[10] F. Franks. *Water: A matrix of Life.* Cambridge University Press, Cambridge, UK, 2nd edition edition, 2000.

[11] Takeshi Egami and Simon J. L. Billinge. *Underneath the Bragg Peaks: Structural Analysis of Complex Materials*, volume 7 of *Pergamon Materials Series.* Pergamon, The Boulevard, Langford Lane, Kidlington, Oxford, OX5 1GB, 2003.

[12] W. F. Kuhs and M. S. Lehmann. The structure of Ice-Ih. In Felix Franks, editor, *Water Science Reviews: Crystalline hydrates.* Cambridge University Press, The Pitt building, Trumpington Street, Cambridge, CB2 1RP, UK, 1986.

[13] H. E. Fischer, A. C. Barnes, and P. S. Salmon. Neutron and x-ray diffraction studies of liquids and glasses. *Rep. Prog. Phys.*, 69:233, 2006.

[14] J. E. Enderby, D. M. North, and P. A. Egelstaff. The partial structure factors of liquid Cu-Sn. *Philosophical Magazine*, 14(131):961, 1966.

[15] A. Zeidler. *Ordering in amorphous binary systems.* PhD thesis, University of Bath, 2009.

[16] P. S. Salmon and I. Petri. Structure of glassy and liquid $GeSe_2$. *Journal of Physics: Condensed Matter*, 15:S1509, 2003.

[17] M. Micoulaut, A. Kachma, M. Bauchy, S. LeRoux, C. Massobrio, and M. Boero. Structure, topology, rings and vibrational and electronic properties of Ge_xSe_{1-x} glasses across the rigidity transition: A numerical study. *Physical Review B*, 88:054203, 2013.

[18] A. Bouzid, S. Le Roux, G. Ori, C. Tugéne, M. Boero, and C. Massobrio. *Molecular Dynamics Simulations of Disordered Materials: Chapter 12: First-Principles Modeling of Binary Chalcogenides: Recent Accomplishments and New Achievements.* Springer International Publishing, Springer International Publishing, Gewerbestrasse 11, 6330 Cham, Switzerland, 1st edition, 2015.

[19] A. Bouzid, S. Le Roux, G. Ordi, M. Boero, and C. Massobrio. Origin of structural analogies and differences between the atomic structures of $GeSe_4$ and GeS_4 glasses: A first principles study. *The Journal of Chemical Physics*, 143:034504, 2015.

[20] D. S. Sivia. *Elementary Scattering Theory For X-ray and Neutron Users.* Oxford University Press, Great Clarendon Street, Oxford OX2 6DP, 2011.

[21] G. L. Squires. *An Introduction to the Theory of Thermal Neutron Scattering.* Cambridge University Press, Cambridge, 1978.

[22] A. C. Wright and R. N. Sinclair. Neutron scattering from vitreous silica: III. elastic diffraction. *Journal of Non-Crystalline Solids*, 76(2-3):351, 1985.

[23] Keiron James Pizzey. *Glasses under extreme conditions.* PhD thesis, University of Bath, 2015.

[24] J. W. E. Drewitt. *Structure of Copper Halide Melts, Rare Earth Chalcogenide Glasses and Glassy Germania at High Pressure.* PhD thesis, University of Bath, 2009.

[25] G. Placzek. The scattering of neutrons by systems of heavy nuclei. *Phys. Rev.*, 86(3):377, 1952.

[26] T. E. Faber and J. M. Ziman. A theory of the electrical properties of liquid metals III. the resistivity of binary alloys. *Philosophical Magazine*, 11(109):153 – 173, 1965.

[27] J. R. Westlake. *A Handbook of Numerical Matrix Inversion and Solution of Linear Equations.* Wiley, Garsington Road, Oxford OX4 2DQ, 1968.

[28] A. Zeidler, P. S. Salmon, R. A. Martin, T. Usuki, P. E. Mason, G. J. Cuello, S. Kohara, and H. E. Fischer. Structure of liquid and glassy $ZnCl_2$. *Physical Review B*, 82:104208, 2010.

[29] Richard A. Martin, Philip S. Salmon, Henry E. Fischer, and Gabriel J. Cuello. Structure of dysprosium and holmium phosphate glasses by the method of isomorphic subsitution in neutron diffraction. *Journal of Physics: Condensed Matter*, 15:8235–8252, 2003.

[30] D. I. Grimley and R. N. Wright, A. C. Sinclair. Neutron scattering from vitreous silica. *Journal of Non-Crystalline Solids*, 119:49, 1990.

[31] David A. Keen. A comparison of various commonly used correlation functions for describing total scattering. *Journal of Applied Crystallography*, 34(2):172, 2001.

[32] http://www.ill.eu/reactor-environment-safety/high-flux-reactor/technical-characteristics/.

[33] H. E. Fischer, G. J. Cuello, P. Palleau, D. Feltin, A. C. Barnes, Y. S. Badyal, and J. M. Simonson. D4c: A very high precision diffractmeter for disordered materials. *Applied Physics A: Materials Science & Processing*, 74:S160, 2002.

[34] William G. Marshall and Duncan J. Francis. Attainment of near-hydrostatic compression conditions using the Paris-Edinburgh cell. *Journal of Applied Crystalography*, 35:122, 2002.

[35] S. Klotz, T. Strässle, A. L. Cornelius, J. Philippe, and V. Pomjakushin. Elastic properties of α-iron at high temperatures by high-pressure neutron scattering. *Journal of Physics D: Applied Physics*, 44:055406, 2011.

[36] Anita Zeidler, Malcolm Guthrie, and Philip S. Salmon. Pressure-dependant structure of the null-scattering alloy $\mathrm{Ti}_{0.676}\mathrm{Zr}_{0.324}$. *High pressure research: An international journal*, 35:239–246, 2015.

[37] Philip S. Salmon and Anita Zeidler. Networks under pressure: the development of in situ high-pressure neutron diffraction for glassy and liquid materials. *Journal of Physics: Condensed Matter*, 27:133201, 2015.

[38] H. H. Paalman and C. J. Pings. Numerical evaluation of x-ray absorption factors for cylindrical samples and annular sample cells. *J. Appl. Phys.*, 33(8):2635–2639, 1962.

[39] A. K. Soper and P. A. Egelstaff. Multiple scattering and attenuation of neutrons in concentric cylinders. *Nuc. Inst. Meth.*, 178(2-3):415, 1980.

[40] P. S. Salmon and C. J. Benmore. Structure of melt-quenched chalcogenide glasses using the method of isotope substitution in neutron diffraction. In W. S. Howells. and A. K. Soper, editors, *Recent Developments in the Physics of Fluids*, pages F225–F232, Adam Hilger: Bristol, 1992.

[41] Prae Chirawatkul. *Structure of liquid and glassy materials: from ambient to extreme conditions: a multiprobe arpproach.* PhD thesis, University of Bath, 2010.

[42] Peter Jenniskens and David F Blake. Structural transitions in amorphous water. *Science*, 265:753, 1994.

[43] T. Bartels-Rausch, V. Bergeron, J. Cartwright, R. Escribano, J. H. Finney, H. Grothe, P. Gutiérrez, J. Haapala, W. F. Kuhs, J. B. C. Pettersson, S. D. Price, I. Sainz-Diaz, D. J. Stokes, G. Strazzulla, E. S. Thomson, H. Trinks, and N. Uras-Aytemiz. Ice structures, patterns, and processes: A view across the icefields. *Reviews of Modern Physics*, 84:885, 2012.

[44] J. H. Finney. Ice: the laboratory in your freezer. *Interdisciplinary Science Reviews*, 29:339, 2004.

[45] V. F. Petrenko and R. W. Whitworth. *Physics of Ice.* Oxford University Press, Great Clarendon Street, Oxford, OX2 6DP, 1999.

[46] G. J. Morris and E. Acton. Controlled ice nucleation in cryopreservation - A review. *Cryobiology*, 66:85–92, 2013.

[47] Andrzej Falenty, Thomas C. Hansen, and Werner F. Kuhs. Formation and properties of ice XVI obtained by emptying a type sII clathrate hydrate. *Nature*, 516:232, 2014.

[48] G. Algara-Siller, O. Lehtinen, F. C. Wang, R. R. Nair, U. Kaiser, H. A. Wu, A. K. Geim, and I. V. Grigorieva. Square ice in graphene nanocapillaries. *Nature*, 519:443, 2015.

[49] Tamsin L. Malkin, Benjamin J. Murray, Andrey V. Brukhno, Jamshed Anwar, and Christoph G. Salzmann. Structure of ice crystallized from supercooled water. *Proceedings of the National Academy of Sciences*, 109:1041–1045, 2012.

[50] W. F. Kuhs and M. S. Lehmann. Oxygen disorder and the geometry of the water molecule in Ice-Ih. volume 37, pages 75–82. Colston Research Society. Symposium G, Adam Hilger, Bristol, 1985.

[51] J. D. Bernal and R. H. Fowler. A theory of water and ionic solution, with particular reference to hydrogen and hydroxyl ions. *Journal of Chemical Physics*, 1:515, 1933.

[52] Bo Berglund, Jan Lindgren, and Jörgen Tegenfelt. O-H and O-D stretching vibrtions in isotopically diluted HDO molecules in some solid hydrates. *Journal of Molecular Structures*, 43:179, 1978.

[53] Léon van Hove. Correlations in space and time and Born approximation scattering systems of intereacting particles. *Physical Review*, 95:249, 1954.

[54] V. F. Sears. Neutron scattering lengths and cross sections. *Neutron News*, 3(3):27, 1992.

[55] D. J. Hughs and J. A. Harvey. *Neutron Cross Sections Report : BNL 325*. Brookhaven National Lab, Brookhaven National Lab., Upton, NY. USA, 1955.

[56] W. F. Kuhs and M. S. Lehmann. The geometry and orientation of the water moleule in ice-Ih. *Journal du Physique*, 3:48, 1987.

[57] P. S. Salmon, I. Petri, P. H. K. de Jong, P. Verkerk, H. E. Fischer, and W. S. Howells. Structure of liquid lithium. *Journal of Physics: Condensed Matter*, 16:195, 2004.

[58] P. A. Egelstaff. Static and dynamic structure of liquids and glasses. *Journal of Non-Crystalline Solids*, 156-158(Part 1):1 – 8, 1993.

[59] A. S. Fortes, I. G. Wood, D. Grigoriev, M. Alfredsson, S. Kipfstuhl, K. S. Knight, and R. I. Smith. No evidence for large-scale proton ordering in antartic ice from powder neutron diffraction. *The Journal of Chemical Physics*, 120:11376, 2004.

[60] http://www.ill.eu/sites/fullprof/.

[61] S. Le Roux and V. Petkov. ISAACS - interactive structure analysis of amorphous and crystalline systems. *Journal of Applied Crystalography*, 43:181–185, 2010.

[62] L. B. Skinner, C. J. Benmore, J. C. Neuefeind, and J. B. Parise. The structure of water around the compressibility minimum. *The Journal of Chemical Physics*, 141:214507, 2014.

[63] K. Röttger, A. Endriss, J. Ihringer, S. Doyle, and W. F. Kuhs. Lattice constants and thermal expansion of H_2O and D_2O Ice-Ih between 10 and 265 K. *Acta Crystallogr.*, B50:644–648, 1994.

[64] J. G. Powles and J. C. Dore. Coherent neutron scattering by light water (H_2O) and a light-heavy water mixture (64 per cent H_2O / 36 per cent D_2O). *Molecular Physics*, 24:1025–1037, 1972.

[65] J. G. Powles. Slow neutron scattering by molecules v. recoil corrections for any molecule. *Molecular Physics*, 37:623–641, 1979.

[66] M. A. Floriano, D. D. King, E. Whalley, E. C. Svensson, V. F. Sears, and E. D. Hallman. Direct determination of the intramolecular O-D distance in ice-Ih and Ic by neutron diffraction. *Nature*, 329:821–823, 1987.

[67] D. T. Edmonds and A. L. Mackay. The pure quadrupole resonance of the deuteron in ice-Ih. *Journal of Magnetic Resonance*, 20:515–519, 1975.

[68] Kozo Kuchitsu. Average values of bond angles. *Bulletin of the Chemical society of Japan*, 44:96–99, 1971.

[69] W.S. Benedict, N. Gailar, and E. K. Plyler. Rotation-vibration spectra of deuterated water vapour. *The Journal of Chemical Physics*, 24:1139–1165, 1956.

[70] Anita Zeidler, Philip S. Salmon, Henry E. Fischer, Jörg C. Neuefeind, J. M. Simonson, Hartmut Lemmel, Helmut Rauch, and Thomas E. Markland. Oxygen as a site specific probe of the structure of water and oxide materials. *Physical Review Letters*, 107:145501, 2011.

[71] Lawrie B. Skinner, Congcong Huang, Daniel Schlesinger, Lars G. M. Patterson, Anders Nilsson, and Chris J. Benmore. Benchmark oxygen-oxygen pair-distribution function for ambient water from x-ray diffraction measurements with a wide Q-range. *The Journal of Chemical Physics*, 138:074506, 2013.

[72] A. B. Seddon and M. J. Laine. Chalcogenide glasses for acousto-optic devices. II. As-Ge-Se systems. *Journal of Non-Crystalline Solids*, 213 & 214:168–173, 1997.

[73] J. T. Gopinath, M. Soljačić, E. P. Ippen, V. N. Fuflyigin, W. A. King, and M. Shurgalin. Third order nonlinearities in Ge-As-Se based glasses for telecommunications applications. *Journal of Applied Physics*, 96:6931, 2004.

[74] J. Troles, V. Shiryaev, M. Churbanov, P. Houizot, L. Brilland, F. Desevedavy, F. Charpentier, T. Pain, G. Snopatin, and J. L. Adam. $GeSe_4$ glass fibers with low optical losses in the mid-IR. *Optical Materials*, 32:212–215, 2009.

[75] Philip S. Salmon. Structure of liquids and glasses in the Ge-Se binary system. *J. Non-Cryst. Solids*, 353:2959–2974, 2007.

[76] M. F. Thorpe and F. L. Galeener. Network dynamics. *Physical Review B*, 22(6):3078, 1980.

[77] M. F. Thorpe, D. J. Jacobs, M. V. Chubynsky, and J. C. Phillips. Self-organisation in network glasses. *Journal of Non-Crystalline Solids*, 266-269:859–866, 2000.

[78] J. C. Phillips. Topology of covalent non-crystalline solids I: Short-range order in chalcogenide alloys. *Journal of Non-Crystalline Solids*, 34(2):153, 1979.

[79] P. Boolchand, J. Grothaus, M. Tenhover, M. A. Hazle, and R. K. Grasselli. Structure of $GeSe_2$ glass: Spectroscopic evidence for broken chemical order. *Physical Review B*, 33:5421, 1986.

[80] P. Boolchand, X. Feng, and W. J. Bresser. Rigidity transitions in binary Ge-Se glasses and the intermediate phase. *Journal of Non-Crystalline Solids*, 348:293, 2001.

[81] E. L. Gjersing, S. Sen, and B. G. Aitkin. Structure, connectivity, and configurations entropy of Ge_xSe_{100-x} glasses: Results from ^{77}Se MAS NMR spectroscopy. *Journal of Physical Chemistry C*, 114:8601, 2010.

[82] R. M. White. Random network model for amorphous alloys. *Journal of Non-Crystalline Solids*, 13:387–398, 1974.

[83] K. S. Liang. Local atomic arrangement and bonding studies in amorphous As_2Se_3-As_4Se_4. *J. Non-Cryst. Solids*, 18:197, 1975.

[84] W. H. Zachariasen. The atomic arrangement in glass. *J. Am. Chem. Soc*, 54:3841, 1932.

[85] P. Lucas, E. A. King, O. Gulbiten, J. L. Yarger, E. Soignard, and B. Bureau. Bimodal phase percolation model for the structure of Ge-Se glasses and the existance of the intermediate phase. *Physical Review B*, 80:214114, 2009.

[86] S. Hosokawa, W-C. Pilgrim, J. F. Berar, and S. Kohara. Recent developments of anomalous x-ray scattering for non-crystalline materials with help of reverse Monte Carlo modeling: The example of $GeSe_2$ glass. *Physica Status Solidi (a)*, 208(11):2544, 2011.

[87] C. Massobrio, M. Celino, P. S. Salmon, R. A. Martin, M. Micoulaut, and A. Pasquarello. Atomic structure of the two intermediate phase glasses $SiSe_4$ and $GeSe_4$. *Phys. Rev. B*, 79(17):174201, 2009.

[88] Hiroshi Watanabe. Spectral Database for Organic Compounds (SDBS) http://sdbs.db.aist.go.jp. Spectroscopy Databases. Fourier transform infrared spectrum (FT-IR) SDBS No 40411.

[89] J. A. Savage and S. Nielsen. Chalcogenide glasses transmitting in the infrared between 1 and 20 μ - a state of the art review. *Infrared Physics*, 5:195–204, 1965.

[90] L. B. Skinner, C. J. Benmore, S. Antao, E. Soignard, S. A. Amin, E. Bychkov, E. Rissi, J. B. Parise, and J. L. Yarger. Structural changes in vitreous $GeSe_4$ under pressure. *The Journal of Physical Chemistry C*, 116(3):2212, 2012.

[91] Von G. Dittmar and H. Schäfer. Die kristallstruktur von germaniumdiselenid. *Acta Crystallogr*, 32:2726–2728, 1976.

[92] B. Kalkan, R. P. Dias, C. S. Yoo, S. M. Clark, and S. Sen. Polyamorphism and pressure induced matalization at the rigidity percolation threshold in densified $GeSe_4$ glass. *The Journal of Chemical Physics*, 118:5110, 2014.

[93] Philip S. Salmon and Anita Zeidler. *Molecular Dynamics Simulations of Disordered Materials: Chapter 1: The Atomic-scale structure of network glass-forming materials.* Springer International Publishing, Springer International Publishing, Gewerbestrasse 11, 6330 Cham, Switzerland, 1st edition, 2015.

[94] P. S. Salmon. The structure of tetrahedral network glass forming systems at intermediate and extended length scales. *Journal of Physics: Condensed Matter*, 19:455208, 2007.

[95] P. S. Salmon, R. A. Martin., P. E. Mason, and G. J. Cuello. Topological versus chemical ordering in network glasses at intermediate and extended length scales. *Nature*, 435:75 – 78, 2005.

[96] P. S. Salmon. Decay of the pair correlations and small-angle scattering for binary liquids and glasses. *Journal of Physics: Condensed Matter*, 18:11443, 2006.

[97] S. A. Wood. The aqueous geochemistry of the rare-earth elements and yttrium 2. theoretical predictions of speciation in hydrothermal solution to 300°C at saturation water pressure. *Chemical Geology*, 88:99–123, 1990.

[98] M. Blunt, F. J. Fayers, M. Franklin, and J. R. Orr. Carbon dioxide in enchanced oil recovery. *Energy Conversion and Management*, 34:9–11, 1993.

[99] M. Hirschmann and D. Kohlstedt. Water in earth's mantle. *Physics Today*, March Edn.:40 – 41, 2012.

[100] R. J. Bodnar, C. W. Burnham, and S. M. Sterner. Synthetic fluid inclusions in natural quartz. III. Determination of phase equilibrium properties in the system H_2O - NaCl to 1000°C and 1500 bars. *Geochimica et Cosmochimica Acta*, 49:1861–1873, 1985.

[101] H. Bureau and H. Keppler. Complete miscibility between silicate melts and hydrous fluid in the upper mantle: experimental evidence and geochemical implications. *Earth and Planetary Science Letters*, 165:187–196, 1999.

[102] S. Bachu. Sequestration of CO_2 in geological media: criteria and approach for site selection in response to climate change. *Energy Conversion and Management*, 41:953–970, 2000.

[103] S. Bachu. Screening and ranking of sedimentary basins for sequestration of CO_2 in geological media in response to climate change. *Environmental Geology*, 44:277–289, 2003.

[104] T. Xu, J. A. Apps, and K. Pruess. Numerical simulation of CO_2 disposal by mineral trapping in deep aquifers. *Applied Geochemistry*, 19:917–936, 2004.

[105] R. A. Mayanovic, A. J. Anderson, W. A. Bassett, and I. M. Chou. On the formation and structure of rare-earth element complexes in aqueous solution under

hydrothermal conditions with new data on gadolinium aqua and chloro complexes. *Chemical Geology*, 239:266–283, 2007.

[106] H . C. Helgeson, D. H. Kirkham, and G. C. Flowers. Theoretical prediction of the thermodynamic behavior of aqueous electrolytes at high pressures and temperatures: IV. calculations of activity coefficients and apparent molal amd standard and relative molal properties to 600°C and 5 Kb. *American Jounal of Science*, 281:1249–1516, 1981.

[107] K. S. Pitzer and J. C. Pelper. Thermodynamic properties of aqeuous sodium chloride solutions. *J. Phys. Chem. Ref. Data.*, 13:1 – 102, 1984.

[108] P. Debye and E. Hückel. The theory of electrolytes. I. lowering the freezing point and related phenomena. *Physikalische Zeitschrift*, 24:185–206, 1923.

[109] A. Liebscher. Aqueous ffluid at elevated pressure and temperature. *Geofluids*, 10:3–19, 2010.

[110] C. A. J. Appelo, D. L. Parkhurst, and V. E. A. Post. Equations for calculating hydrogeochemical reactions of mineral and gases such as CO_2 at high pressures and temperatures. *Geochimica et Cosmochimica Acta*, 125:49 – 67, 2014.

[111] A. A. Chialvo and J. M. Simonson. Aqueous Na^+Cl^- pair association from liquidlike to steamlike densities along near-critical isotherms. *Journal of Chemical Physics*, 118:7921–7929, 2003.

[112] E. H. Oelkers and H. C. Helgeson. Calculation of dissociation constant and the relative stabilities of polynuclear clusters of 1:1 electrolytes in hydrothernal solutions at supercritical pressures and temperatures. *Geochimica et Cosmochimica Acta*, 57:2673–2697, 1993.

[113] A. Rabenau. The role of hydrothermal synthesis in preparative chemistry. *Angewandte Chemie, International Edition*, 24:1026–1040, 1985.

[114] D. M. Sherman and M. D. Collings. Ion association in concentrated NaCl brines from ambient to supercritical conditions: results from classical molecular dynamics simulations. *Geochem. Trans.*, 3:102 – 107, 2002.

[115] M. T. Reagan, J. G. Harris, and J. W. Tester. Molecular simulations of dense hydrothermal NaCl - H_2O solutions from subcritical to supercritical conditions. *Journal of Physical Chemistry B*, 103:7935 – 7941, 1999.

[116] J. P. Brodholt. Molecular dynamics simulations ofsolutions NaCl solutions at high pressures and temperatures. *Chemical Geology*, 151:11–19, 1998.

[117] A. K. Soper, G. W. Neilson, J. E. Enderby, and R. A. Howe. A neutron diffraction study of hydration effects in aqueous solutions. *Journal of Physics C: Solid State Physics*, 10:1793 – 1801, 1977.

[118] A. Jenkins. *IUPAC. Compendium of Chemical Terminology, 2nd ed. (the "Gold Book").* Blackwell Scientific Publications, Oxford, 1997. XML on-line corrected version: http://goldbook.iupac.org.

[119] A. Zeidler. Private communication. August 2015.

[120] C. W. F. T. Pistorius, E. Rapoport, and J. B. Clark. Phase diagrams of H_2O and D_2O at high pressure. *The Journal of Chemical Physics*, 48:5509 – 5514, 1968.

[121] S. Klotz. Private communication, September 2010.

[122] R. W. Potter and D. A. Brown. The volumetric properties of aqueous sodium chloride solutions from 0° to 500° at pressures up to 2000 bars based on a regression of avaliable data in the literature. *United States Geological Survey Bulletin*, 1421-C:1 – 36, 1977.

[123] A. C. Barnes., J. E. Enderby., J. Breen, and J. C. Leyte. The water structure around the chloride ion in aqueous polyethylene oxide solutions. *Chemical Physics Letters*, 142:405 – 408, 1987.

[124] T. Yamaguchi, H. Ohzono, M. Yamagami, K. Yamanaka, K. Yoshida, and H. Wakita. Ion scattering in aqueous solutions of lithium chloride, nickel chloride and caesium chloride in ambient to supercritical water. *Journal of Molecular Liquids*, 153:2 – 8, 2010.

[125] S. Cummings, J. E. Enderby, G. W. Nielson, and J. R. Newsome. Chloride ions in aqeous solution. *Nature*, 287:714 – 716, 1980.

[126] S. E. Okan and P. S. Salmon. A neutron diffraction study on the structure of Cl^- solutions in hydrogen-bonded molecular solvents. *Journal of Physics: Condensed Matter*, 6:3839–3848, 1994.

[127] London Materials Department of Imperial College. Database of ionic radii.

[128] A. Polidori. Private communication. September 2015.